UNIVERSITÉ DE STRASBOURG

N° d'ordre :

École Doctorale Mathématiques, Sciences de l'Information et de l'Ingénieur

UdS – INSA – ENGEES

THÈSE

présentée pour obtenir le grade de

Docteur de l'Université de Strasbourg
Discipline : Physique
Spécialité Photovoltaïque

par

Marek BASTA

Low-energy photovoltaic conversion in MIND structures

Soutenue publiquement le 5 septembre 2013

Membres du jury

Directeur de thèse : M. Zbigniew KUZNICKI, professeur, UFR de Physique, Université de Strasbourg
Co-Directeur de thèse : M. Jan MISIEWICZ, professeur, Université Technique de Wroclaw
Rapporteur externe : M. Uli LEMMER, professeur, Karlsruhe Institut de Technologie, Karlsruhe
Rapporteur externe : M. Laurent BIGUE, professeur, Université Haute Alsace
Examinateur : M. Marek GODLEWSKI, professeur, Institut de Physique de l'Académie Polonais des Sciences
Examinateur : M. Patrick MEYRUEIS, professeur, Laboratoire ICube, Strasbourg

Low-energy photovoltaic conversion in MIND structures

To my wife and daughter

Acknowledgements

This work was conducted in cooperation between University of Strasbourg (Alsace, France) and Wroclaw University of Technology (Wroclaw, Poland). I would like to express my gratitude to the French Embassy in Poland and the Regional Parliament of Lower Silesia Province for financial support.

I would also like to express my deepest gratitude to the Director of my thesis Prof. Zbigniew T. KUZNICKI for his supervision, inspiration and encouragement during my research. It has been a privilege for me, to be a student of him.

I would like to express my gratitude and sincere appreciation to my co-Director Prof. Jan MISIEWICZ for help and guidance and for monitoring my research.

I am greatly honored by the kind acceptance of Prof. Uli LEMMER, Prof. Laurent BIGUE, Prof. Marek GODLEWSKI and Prof. Patrick MEYRUEIS as members of the jury for my thesis and would like to thank them for serving as my advisory committee.

Special thanks to Prof. Yoshitate TAKAKURA for his incredible introduction to rigorous treatment of electromagnetic propagation and Dr. Sylvain LECLER for his support with numerical calculations. I would like to extend my gratitude to Dr. Victorien RAULOT for the structural measurements and Dr. Bartlomiej WITKOWSKI for the electron microscopy measurements.

I would like to give special thanks to my friend, Mikael HOSATTE for all the help and support I received from him. I would like to thank all my friends from the laboratory: Marc BEURET and Cedric PERRETON for their constant help and our great discussions.

Lastly, I would like to thank the invited members of the committee, Prof. Marie-Catherine PALAU and M. Federico SPRENG from Astrium Space Transportation, for their interest and encouragement.

.

Table of contents

General introduction

The history of mankind is also a history of human energy usage. Both progressed from human muscle power and firewood in the prehistoric times, and later, thanks to agricultural surpluses, also from animal power. Humanity was slowly crawling out from the stage of barbarism, harnessing the power of wind and water, which allowed our history to advance more rapidly, up to the pre-industrial era. At some point in our history we fully harnessed the power from the fossil fuels: coal, gas and oil, thanks to the invention of steam engine; those are the times of Industrial Revolution. Over that period, roughly from 1750 until 1850, world's population increased sixfold, resulting in even more dramatic energy demand. Before that period, 70% of total work was delivered by human muscles, most of the rest by domestic animals, but in the times of Industrial Revolution, fossil fuels were the only present energy source that could fulfill the constantly increasing demand. Coal fueled the industrial revolution in the 18th and 19th century. With the advent of the automobile, airplanes and the spreading use of electricity, oil became the dominant fuel during the twentieth century. The growth of oil as the largest fossil fuel was further enabled by steadily dropping prices from 1920 until 1973.

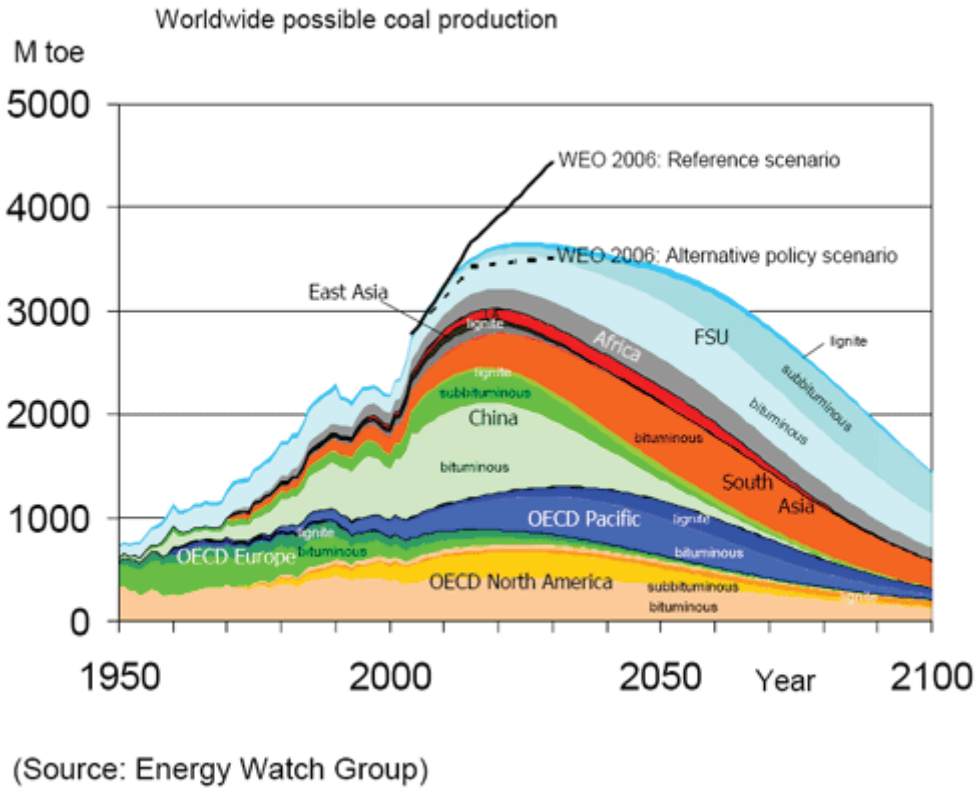

Figure 1. Worldwide possible coal production. Predicted production peak will occur in late 2020s.

Today, in the post-industrial era, our consumption of fossil fuels and electricity is enormous. On one hand fossil fuels are abundant, effective and easy to transport and those features

allowed us to reach such an incredible level, but on the other hand humanity used more energy in the 20th century only than is used in all of the rest of human history. From that perspective an obvious conclusion makes itself apparent; fossil fuels cannot and will not last forever, therefore a new energy source must be implemented in their place, if we humans want to maintain the same life-style and civilization level. There have been several initiatives taken and several candidates are present, notably the atomic power, which is by far the most

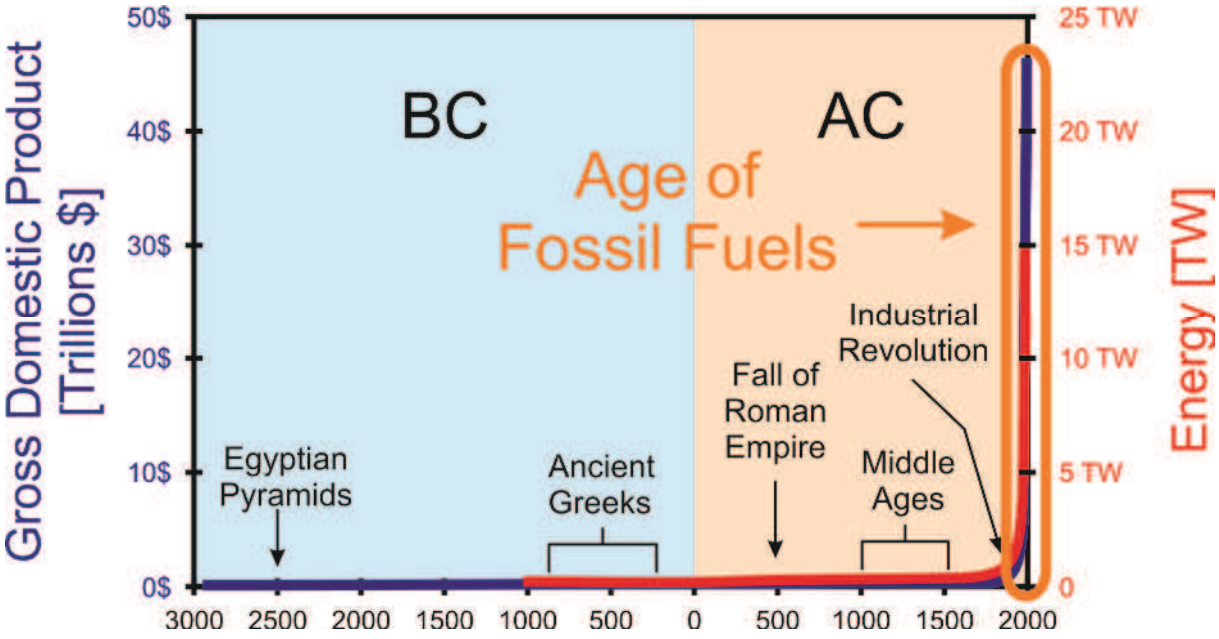

Figure 2. World Gross Domestic Product (GDP) and energy consumption for the whole recorded history. The explosion in 19th century is linked with industrial revolution.

efficient way of producing electricity, but is also the one that causes the most trouble. Even now, when we do not rely fully on it, one relatively small malfunction of the atomic reactor in a power plant, such as the one that happened in Chernobyl on 26 April 1986, or the one at Fukushima in 2011, could have catastrophic effects. The renewable energy sources offer the unique possibility of electric power production without any major drawback and renewable energy sources are abundant enough to live up to the constantly increasing world's energy demand.

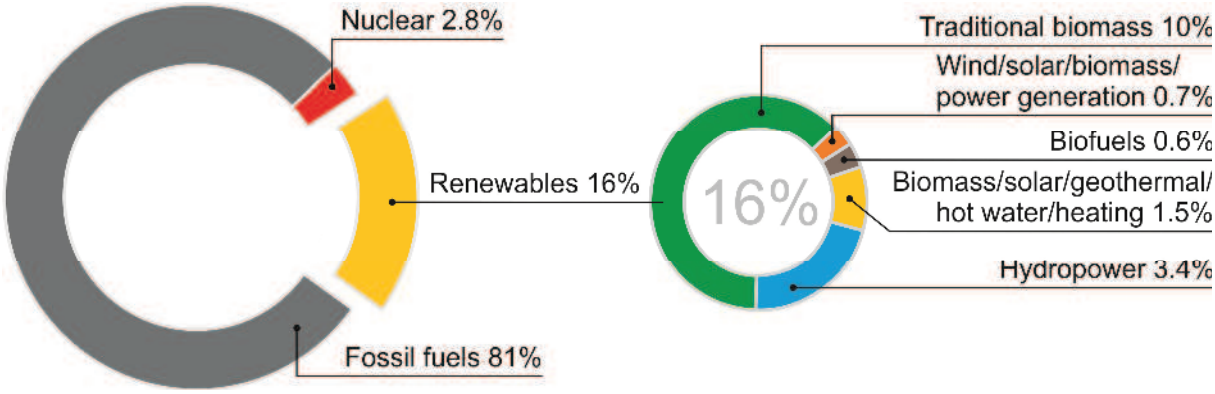

Figure 3. World energy consumption. Only 16% is supplied from renewable sources and only 1.5% from solar energy.

Today world's energy consumption is somewhere above 19 TW, while the potential of renewable sources is: 32 TW geothermal, 870 TW wind power and 86 000 TW solar power. It is easy to note that any of those energy sources is capable of fulfilling the world's need now and in the near future, with solar power being the most abundant and most accessible.

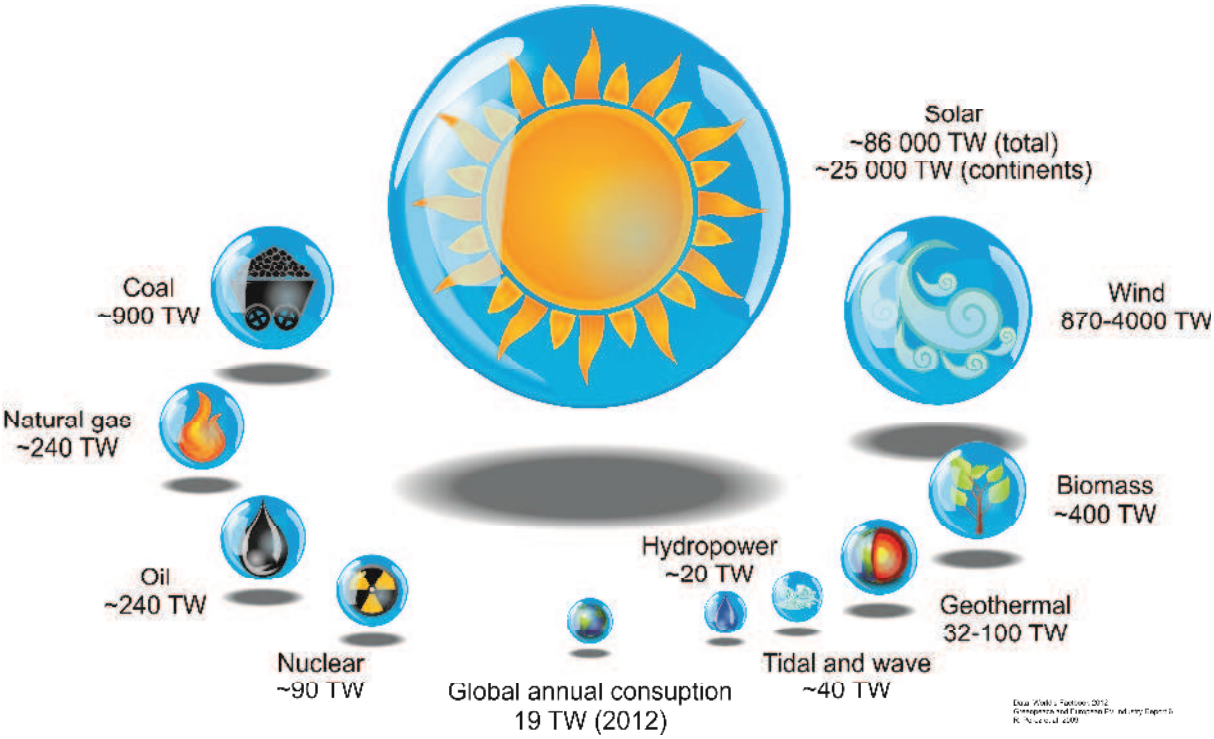

Figure 4. Potential global availability of renewable energy sources and global annual energy consumption. Sun power offers more than 5600 times energy than global needs of today.

The Sun is an average star. It has been burning for more than 4-bilion years and will burn at least that long before turning into red giant, engulfing the Earth in the process. The Sun is responsible for nearly all the energy available on Earth. The exceptions are attributable to

moontides, radioactive material and the Earth's residual internal heat. Everything else is converted form of a Sun's energy: Hydropower is made possible by evaporation-transpiration due to solar radiant heat; the winds are caused by Sun's uneven heating of Earth's atmosphere; fossil fuels are remnants of organic life previously nourished by the Sun; and photovoltaic electricity is produced directly from sunlight by converting the energy in sunlight into free charged particles within certain kinds of materials

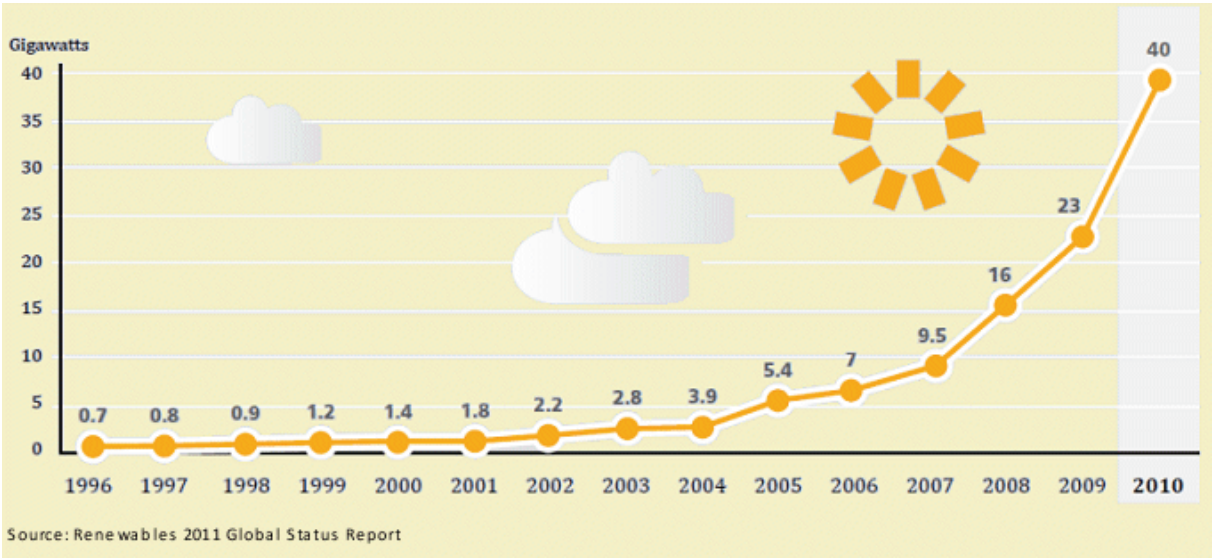

Figure 5. Global photovoltaic market. A rapid growth in production is observed for the past few years.

In theory, with today's knowledge, humanity has all the necessary tools in hand to rely completely on renewable energy sources while maintaining the highly developed civilization and current growth rate. It can be argued that, even if the fossil fuels triggered the events that allowed for such a dramatic changes that occurred in 19th and 20th century, regarding technological advancement, transformation of the society and rapid increase in human population, those fossil sources are not capable to upkeep this tendency and if no other energy source is found, human civilization will collapse and reverse a couple of hundreds of years in development. Therefore there are two fundamental reasons to study intensively the potential of renewable energy sources and solar power in general. The first is to maintain the current state of civilization and development while the second reason is related directly to our current status on the Kardashev scale. The Kardashev scale is a method of measuring a civilization's level of technological advancement, based on the amount of energy a civilization is able to utilize. The scale has three designated categories called Type I, II, and III. A Type I civilization uses all available resources impinging on its home planet, Type II harnesses all

the energy of its star, and Type III of its galaxy. At the present state, the humanity is a type 0 civilization, but according to some scientist, like Prof. Michio Kaku and Prof. Steven Hawking, we will experience the transfer to a planetary, type I civilization in the next 50 years. If this is to happen and if we are to ensure our further growth in technological advancement, there is no other long term choice than to embrace, accept and utilize the immense amount of energy the Sun is giving us every day.

Chapter I

Theory of the photovoltaic conversion

1. The Sun. Solar Energy.

The Sun is the star at the center of our planetary system. It is almost perfectly spherical and consists of a hot plasma interwoven with magnetic fields. It has a diameter of about 1 392 000 km, about 109 times that of the Earth, and its mass (about 2×10^{30} kilograms, 330 000 times that of the Earth) accounts for about 99.86% of the total mass of the Solar System. Chemically, about three quarters of the Sun's mass consists of hydrogen, while the rest is mostly helium. The remaining (1.69%, which nonetheless equals 5 628 times the mass of Earth) consists of heavier elements, including oxygen, carbon, neon and iron, among others. The mean distance of the Earth from the Sun in about 149.6 million kilometers, which is equal to 1 AU. At the average distance, light travels from the Sun to the Earth in about 8 minutes 19 seconds. In the stellar classification, the Sun is a G2V class star, meaning that the major part of its radiation is in the yellow-green portion of the spectrum, has surface temperature about 5778 K and is a main-sequence star, generating its energy through nuclear fusion of hydrogen into helium. The total power emitted by sun equals 3.846×10^{26} W, which corresponds to a mean intensity of 2.009×10^{7} $W\cdot m^{-2}\cdot sr^{-1}$ [1].

The Sun releases 95% of its output as light, while the remaining 5% consists of highly energetic X-rays and radio signals. Since the peak of radiation is in the green portion of the visible spectrum, most plants and the human eye function best in green light through adaptation to the nature of the sunlight reaching them.

1.1. Solar spectrum.

The spectrum of the Sun's solar radiation is close to that of a black body with a temperature of about 5778 K. The Sun emits EM radiation across most of the electromagnetic spectrum. Although the Sun produces Gamma rays as a result of the nuclear fusion process, these very high energy photons are converted to lower energy photons before they reach the Sun's surface. Therefore the Sun emits electromagnetic radiation in the X-ray, UV, visible, infrared range and also radio waves. Most of the high energy photons are absorbed by the Earth's atmosphere before they reach the Earth’s surface, such as the most UV light.

The spectrum of electromagnetic radiation striking the Earth's atmosphere spans a range of 100 nm to about 1 mm. It can be divided into five regions in increasing order of wavelengths:

- Ultraviolet or UV, divided into three parts: C: 100 to 280 nm, B: 280 to 315 nm and A: 315 to 400 nm. UVC and UVB radiation is greatly absorbed by the atmosphere and is responsible for the photochemical reaction leading to the production of the ozone layer. The least dangerous part of the UV light is the UVA, which is often used for tanning and treatment of various skin diseases.
- Visible range commonly referred to as light spans 380 to 780 nm. It is the only part of the spectrum that is visible to the naked human eye.
- Infrared or IR, divided also into three parts: A: 700 nm to 1400 nm, B: 1400 nm to 3000 nm and C: 3000 nm to 10^6 nm. It is responsible for an important part of the electromagnetic radiation reaching the Earth.

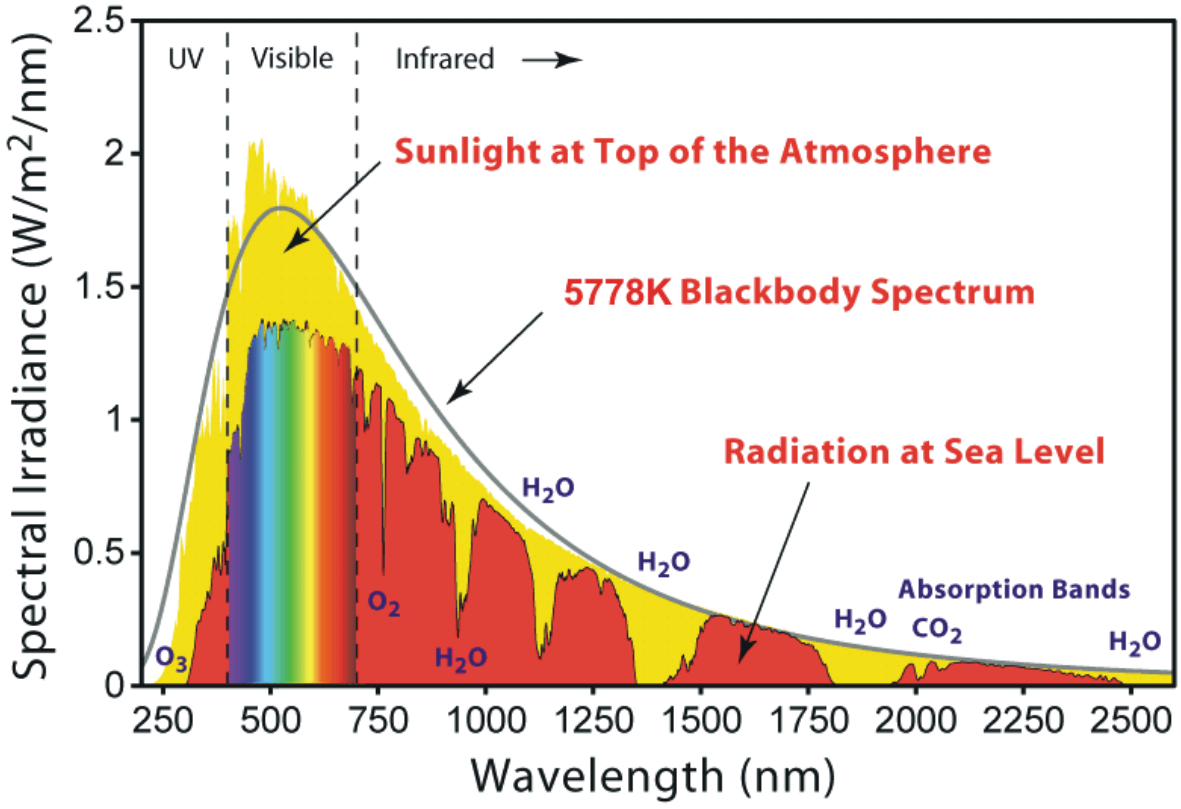

Figure I.1. Solar spectrum at the top of the atmosphere, at the sea level and the radiation of a black body with temperature $T = 5778$ K [2].

The Total Sun Irradiation (TSI) upon the Earth, measured by the Solar Radiation and Climate Experiment (SORCE) satellite is estimated to be around 1361 W/m² [3].

1.2. Energy fluxes and concentration.

To understand the origin of sunlight one can consider the Sun as a black body with a temperature T_s = 5778 K [4], since this is the temperature of the Sun's surface. The number of photons emitted by a unit of volume of such a black body can be expressed by the Planck's law:

$$dn_{ph}(\hbar\omega) = u(\omega, T) \cdot d\hbar\omega = \frac{(\hbar\omega)^2}{4\pi^3\hbar^3c^3} \cdot \frac{d\Omega}{exp\left(\frac{\hbar\omega}{kT}\right) - 1} \cdot d\hbar\omega \quad \text{(I.1.1)}$$

where $u(\omega,T)$ is the spectral density, $\hbar$ is the reduced Planck constant, c is the speed of light and k is the Boltzmann constant. Energy of photons emitted by a unit of volume is described by:

$$de_{ph}(\hbar\omega) = \hbar\omega \cdot dn_{ph} \cdot d\hbar\omega = \frac{(\hbar\omega)^3}{4\pi^3\hbar^3c^3} \cdot \frac{d\Omega}{exp\left(\frac{\hbar\omega}{kT}\right) - 1} \cdot d\hbar\omega \quad \text{(I.1.2)}$$

So the total energy emitted by a given volume is expressed by:

$$e_{ph} = \int_0^\infty \frac{(\hbar\omega)^3}{4\pi^3\hbar^3c^3} \cdot \frac{d\hbar\omega}{exp\left(\frac{\hbar\omega}{kT}\right) - 1} \cdot \int_0^{4\pi} d\Omega \quad \text{(I.1.3)}$$

$$e_{ph} = \frac{\pi^2k^4}{15\hbar^3c^3}T^4 \quad \text{(I.1.4)}$$

The total number of photons emitted is then given by:

$$n_{ph} = 2.40411\frac{k^3}{\pi^2\hbar^3c^3}T^3 \quad \text{(I.1.5)}$$

and their mean energy is equal to:

$$\langle\hbar\omega\rangle = \frac{e_{ph}}{n_{ph}} = 2.701kT \quad \text{(I.1.6)}$$

For the Sun, at the temperature T_s = 5778 K we obtain:

$$\langle\hbar\omega\rangle_{Sun} = 1.3442\ eV \quad \text{(I.1.7)}$$

If $e_{ph\Omega}$ is the energy density for a unit of a solid angle, then the energy flux emitted by a surface element dA of a solid angle comprising a source would be:

$$dI_E = \frac{e_{ph}}{4\pi} \cdot c \cdot dA \cdot d\Omega \tag{I.1.8}$$

Surface elements of the energy emitter (Sun) dA_S and the energy receiver dA_E are presented on figure I.2.

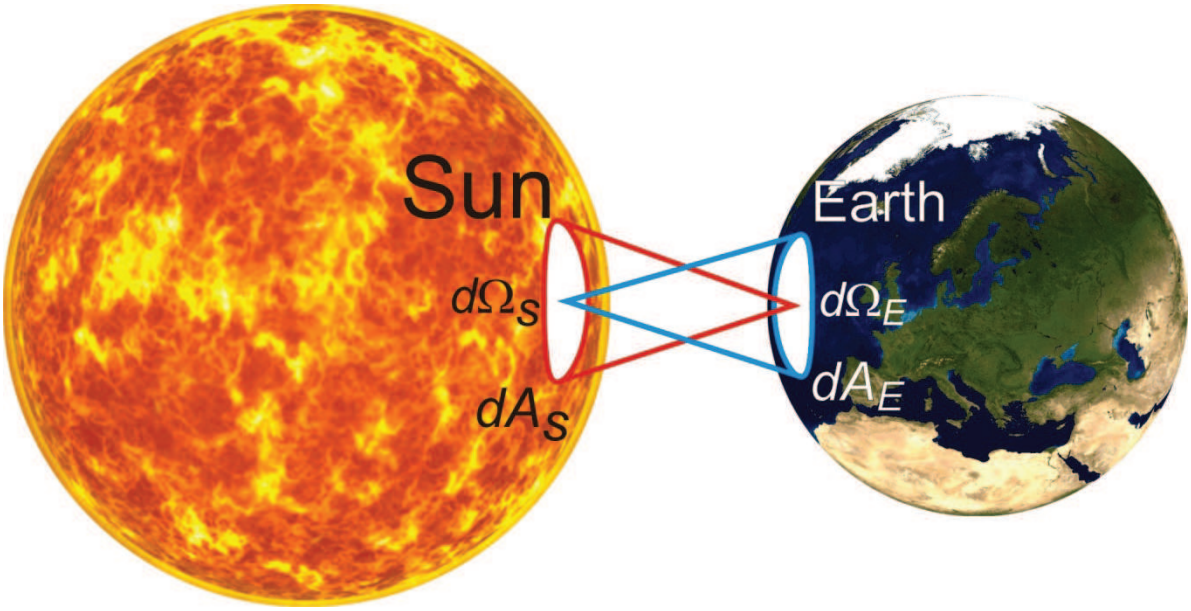

Figure I.2. Surface elements dA_S and dA_E of the source (Sun) and receiver (Earth) of energy, respectively.

If the distance between the Sun and the Earth is R_{SE}, the solid angle is defined by:

$$d\Omega_{S,E} = \frac{dA_{S,E}}{R_{SE}^2} \tag{I.1.9}$$

Assuming all the energy emitted by the Sun reaches the Earth, the energy density per solid angle emitted by the Sun is equal the energy density per solid angle received by the Earth:

$$e_{phS\Omega} = e_{phE\Omega} \tag{I.1.10}$$

$$j_{e\Omega} = c \cdot e_{ph\Omega} \tag{I.1.11}$$

and energy density is equal to:

$$j_e = j_{e\Omega} \cdot d\Omega \tag{I.1.12}$$

If we approximate the Sun as a perfect sphere, the total energy flux emitted by the Sun in the solid angle $d\Omega$ is equal:

$$I_{eS} = j_{e\Omega} \cdot d\Omega \cdot \pi \cdot \mathrm{R_S^2} \tag{I.1.13}$$

where $\mathrm{R_S}$ is the radius of the Sun. Following the Stefan-Boltzmann law, the total power emitted per unit area of the surface of a black body is directly proportional to the fourth power of its absolute temperature:

$$j^* = \sigma T^4 \tag{I.1.14}$$

so the total power emitted by the Sun in given by:

$$P_S = 4\pi \mathrm{R_S^2} \sigma T_S^4 \tag{I.1.15}$$

Since the Sun emits that power evenly in all directions, the fraction of power that strikes the Earth is then given by the following expression:

$$P_{SE} = P_S \frac{\pi \mathrm{R_E^2}}{4\pi \mathrm{R_{SE}^2}} \tag{I.1.16}$$

where $\mathrm{R_E}$ is the radius of the Earth. Every real planet reflects part of the incident radiation. The amount of power reflected by the planet is described by its albedo α. In other words, Earth absorbs a fraction 1 - α of the Sun's light and reflects the rest. The power absorbed is given by:

$$P_{abs} = (1 - \alpha) P_{SE} \tag{I.1.17}$$

even if the planet absorbs only a circular area, it emits equally as a sphere. When a planet, considered as a black body, is thermal equilibrium with its surroundings, it emits exactly the same amount of energy it receives from the Sun. The planet emits mainly in the IR part of the spectrum, since its temperature is much lower than that of the Sun. In this frequency range it emits $\bar{\epsilon}$ of the radiation that a black body would emit, where $\bar{\epsilon}$ is the average emissivity in the IR range. The power emitted by the planet is then given:

$$P_{emt} = \bar{\epsilon} 4\pi \mathrm{R_P^2} \sigma T_P^4 \tag{I.1.18}$$

Substituting the expressions for solar and planet power in equations I.1.14-I.1.18 and simplifying yields, the estimated temperature of the planet, ignoring the greenhouse effect is given by:

$$T_P = T_S \sqrt{\frac{R_S \sqrt{\frac{1-\alpha}{\bar{\epsilon}}}}{2R_{SE}}} \tag{I.1.19}$$

Assuming $\alpha = 0.306$ [5], $R_S = 6.98 \cdot 10^8$ m, $R_{SE} = 1.496 \cdot 10^{11}$ m [6], simplifying $\bar{\epsilon}$ to 1 and ignoring the greenhouse effect, the average temperature of the Earth is:

$$T_P = 254.356K = -18°C \tag{I.1.20}$$

The difference between the real and estimated temperature is mainly due to the greenhouse effect.

For several applications, solar power concentrated with the help of lenses and mirrors might be used. Fulfilling the assumptions of the energy balance, we have:

$$4\pi R_S^2 j_S = 4\pi R_E^2 j_E \tag{I.1.21}$$

which comes from the second law of the thermodynamics, stating that the radiative temperature of the concentrated light cannot exceed the radiative temperature of the Sun. The above expression with the concentration becomes:

$$C j_E = \sigma T_C^4 \geq \sigma T_S^4 = j_S \tag{I.1.22}$$

Therefore the maximum concentration becomes:

$$C_{max} = \frac{j_S}{j_E} = \left(\frac{R_S}{R_E}\right)^2 = 46164 \tag{I.1.23}$$

1.3. Air Mass.

The amount of light that reaches the ground is influenced by both the elliptical orbit and the Earth's atmosphere. The extraterrestrial solar illuminance E_{ext}, corrected for the elliptical orbit by using the day number of the year is given by the following expression [7]:

$$E_{ext} = E_{sc}\left(1 + \gamma \cdot cos\left(2\pi \frac{day - 3}{365}\right)\right) \tag{I.1.24}$$

and

$$\gamma = \sqrt{\frac{R_{ph}}{R_{ah}}} = 0.033412 \tag{I.1.25}$$

being the ratio between Earth's perihelion and aphelion squared. The *day-3* term in equation (I.1.24) comes from the fact that in modern times Earth's perihelion occurs around January 3rd each year. The solar illuminance constant $E_{sc} = 128 \cdot 10^3$ lx, the direct normal illuminance E_{dn}, corrected for the attenuating effects of the atmosphere is given by:

$$E_{dn} = E_{ext} e^{-cm} \tag{I.1.26}$$

where c is the atmospheric extinction coefficient and m is the relative optical air mass. The term air mass normally indicates relative air mass, the path length relative to that at the zenith at the sea level, so by definition, at the sea level air mass is equal to 1. With increasing angle between the source and the zenith, the air mass increases also, reaching the value of approximately 38 at the horizon. Air mass can be less than one at the elevation greater than the sea level, but most of the closed form expressions do not include that effect. In some disciplines the air mass is indicated by an acronym AM; additionally the value is given by appending the value to the acronym, AM1 indicates an air mass of 1 and so on. The region above the Earth's atmosphere, where there is no atmospheric attenuation is considered to have air mass 0 (AM0).

2. Silicon as a semiconductor.

Silicon (latin: *silicium*) is the chemical element that has the symbol **Si** and atomic number 14 (column 4). A tetravalent metalloid, silicon is less reactive than its chemical analog carbon. Silicon is the eighth most abundant element in universe by mass. It occasionally occurs in nature as the free element, but is more widely distributed in dusts, planetoids and planets as various forms of silicon dioxide and silicates. Silicon is the second most common element of the Earth's crust, making up 25.7% of its mass.

Silicon has found many applications in industry, especially in electronics. The use of silicon in semiconductor devices demands a much greater purity than afforded by metallurgical grade silicon. Very pure silicon (>99.9%) can be extracted directly from solid silica or other silicon compounds by molten salt electrolysis. Though this method was known as early as in 1854, the rapid expansion of silicon technology and especially silicon solar technology has been

made available thanks to Czochralski method in 1916. To this day this method is the one most widely used in industrial scale silicon production and is the cheapest one available. Elemental silicon is the principal component of most semiconductor devices such as photodiodes, integrated circuits or microchips. Silicon is also the most frequently used semiconductor, because unlike many other semiconductors it maintains its properties over a wide temperature range. Another reason for using this semiconductor is that its native grown dioxide can be easily obtained in a furnace and creates a very good semiconductor-dielectric interface and electronic passivation surface.

In the form of silica (silicon dioxide) it forms various glasses, ceramics and cements, which are used in many branches of the industry. It can also be used for the creation of synthetic glass-like compounds, containing silicon, carbon, oxygen and hydrogen, named silicones.

Silicon is also an essential element in the living world. While it is mainly required by plants, only small traces of it appear to be needed by animals.

Silicon is an elemental semiconductor. There is no simple definition of semiconductors, but one can apply the name to materials whose electrical conductivity σ lies between 10^{-9} to 10^{2} $\Omega^{-1}cm^{-1}$. Different from metals, where the conductivity decreases with temperature, the conductivity of semiconductors for some temperatures increases exponentially. This is caused by the exponential increase of carrier concentration with temperature (thermal generation), as predicted by equations (I.2.22) and (I.2.23). Apart from that, the conductivity of semiconductors depends strongly on additional effects like doping or illumination.

Considering band structure, it is assumed that the band gap for semiconductors lies between 0 and 3 eV. Materials for which the band gap is greater than 3 eV (while conductivity is lower than 10^{-9} $\Omega^{-1}cm^{-1}$) are called insulators. This is a limited definition, because for different reasons one can call diamond-structured carbon a semiconductor, which has band gap of 6eV, or semi-insulator GaAs. The reason these materials are considered semiconductors is due to the type of conductivity. Metals have only electrons, semiconductors have electrons and holes, but lack ionic conductivity, visible in dielectrics. In semiconductors the most important role is always played by electron-hole conductivity, before the ionic one. On the other hand, semiconductors with 0 eV effective bang gap are called semimetals.

2.1. Properties of crystalline silicon.

At T = 298 K (room temperature) silicon exists in the solid state. It can exist in other phases such as crystalline, amorphous and polycrystalline. The melting point for silicon is at T = 1687 K and its boiling point is at T = 3173 K.

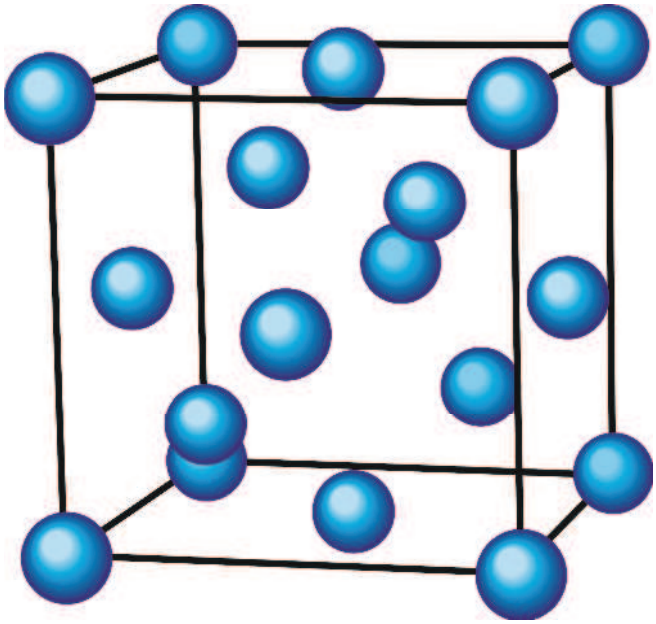

Figure I.3. Crystalline silicon forms in a diamond structure, space group Fd-3m.

The cell parameters for Si are 543.09 pm (picometre). The electronic configuration of silicon is [**Ne**].**3s**^{2}.**3p**^{2} where [Ne] stands for structure of neon [8].

To understand the origin of properties of crystalline silicon one must consider a silicon crystal extended to infinity in all three dimensions. Properties of such a crystal can then be analyzed by the Bloch's theorem [9], which states that the eigenstates ψ of the one-electron Hamiltonian:

$$H = -\hbar^2 \frac{\nabla^2}{2m} + U(r) \tag{I.2.1}$$

where $U(r+R) = U(r)$ for all R in a Bravais lattice, can be chosen to have the form of the plane waves times a function with the periodicity of the Bravais lattice:

$$\psi_{nk}(r) = e^{ik \cdot r} u_{nk}(r) \tag{I.2.2}$$

where $u_{nk}(r+R) = u_{nk}(r)$ for all R in the Bravais lattice. the equations (I.2.1) and (I.2.2) imply that:

$$\psi_{nk}(r+R) = e^{ik\cdot R}\psi_{nk}(R) \tag{I.2.3}$$

By imposing appropriate boundary conditions, such as Born-von Karman conditions [9], we can demonstrate that the *k* vector must be real and arrive at a condition restricting the values of *k*. If we are working with the case where the primitive cell is no longer cubic, we can generalize the boundary conditions as follows:

$$\psi(r+N_i a_i) = \psi(r), i = 1,2,3 \tag{I.2.4}$$

where the a_i are three primitive vectors and the N_i are all integers of order $N^{1/3}$, where $N = N_1N_2N_3$ is the total number of primitive cells in the crystal. Applying Bloch's theorem (I.2.3) to the boundary condition (I.2.4) we find that:

$$\psi_{nk}(r+N_i a_i) = e^{iN_i k\cdot a_i}\psi_{nk}(r) \tag{I.2.5}$$

which requires that:

$$e^{iN_i k\cdot a_i} = 1, i = 1,2,3 \tag{I.2.6}$$

When *k* has the form:

$$k = x_1 b_1 + x_2 b_2 + x_3 b_3 \qquad \text{where } b_j \cdot a_j = 2\pi\delta_{ij} \tag{I.2.7}$$

and a_j, b_j are the normal and reciprocal lattice vectors, respectively, equation (I.2.6) requires the following:

$$e^{2\pi i N_i x_i} = 1 \tag{I.2.8}$$

and consequently we must have:

$$x_i = \frac{m_i}{N_i} \tag{I.2.9}$$

m_i integral. Therefore the general form for allowed Bloch wave vectors is:

$$k = \sum_{i=1}^{3} \frac{m_i}{N_i} b_i \tag{I.2.10}$$

The volume of a reciprocal lattice primitive cell is $(2\pi^3)/v$, where $v = V/N$ is the volume of a direct lattice primitive cell, so the volume Δk of *k*-space allowed value of k can be expressed as follows:

$$\Delta k = \frac{2\pi^3}{V} \tag{I.2.11}$$

The ground state on N Bloch electrons is constructed by occupying all Bloch levels labeled by the quantum numbers *n* and *k*, but, unlike the free electron case, $\varepsilon_n(k)$ does not have a simple explicit free-electron form and *k* must be confined to a single primitive cell of a reciprocal lattice if each level is to be counted only once. When the lowest of these levels are filled by a specified number of electrons, two quite distinct types of configuration can result:

- A certain number of bands may be completely filled, all others remain empty. The difference in energy between the highest occupied level and the lowest unoccupied level is known as the *band gap*. We shall find that solids with a band gap greatly in excess of k_BT (T near the room temperature) are insulators. If the band gap is comparable to k_BT, the solid is known as an intrinsic semiconductor. Because the number of levels in a band is equal to the number of primitive cells in the crystal and because each level can accommodate two electrons (one of each spin), a configuration with a band gap *can* arise only if the number of electrons per primitive cell is even.
- A number of bands may be partially filled. When this occurs, the energy of the highest occupied level, the Fermi energy ε_F, lies within the energy range of one or more bands. For each partially filled band there will be a surface in *k*-space that separates occupied from the unoccupied levels. The set of all such surfaces is known as the Fermi surface and is the generalization to Bloch electrons of the free electron Fermi sphere. The parts of the Fermi surface arising from individual partially filled bands are known as branches of the Fermi surface. A solid has metallic properties provided that a Fermi surface exists.

One must very often calculate quantities that are weighted sums over the electronic levels of various on-electron properties. Such quantities are of the form:

$$Q = 2\sum_{n,k} Q_n(k) \tag{I.2.12}$$

where for each *n* the sum is over all allowed *k* giving physically distinct levels.

In the limit of a large crystal the allowed values of *k* get very close together, and the sum may be replaced by an integral. Since the volume of *k*-space per allowed *k* has the same value as in the free electron case, the prescription for the free-electron model case remains valid and we find that:

$$q = \lim_{V\to\infty} \frac{Q}{V} = 2\sum_{n} \int \frac{dk}{(2\pi)^3} Q_n(k) \tag{I.2.13}$$

where the integral is over the primitive cell. If $Q_n(k)$ depends on *n* and *k* only through the energy $\varepsilon_n(k)$, then in further analogy to the free electron case one can define a density of states per unit volume $g(\varepsilon)$ so that *q* has the form:

$$q = \int d\varepsilon_g(\varepsilon) Q(\varepsilon) \tag{I.2.14}$$

Comparing equations (I.2.13) and (I.2.14) we find that:

$$N(\varepsilon) = \sum_{n} N_n(\varepsilon) \tag{I.2.15}$$

where $N_n(\varepsilon)$, the density of states in the n^{th} band is given by:

$$N_n(\varepsilon) = \int \frac{dk}{4\pi^3} \delta(\varepsilon - \varepsilon_n(k)) \tag{I.2.16}$$

where the integral is over any primitive cell.

In an intrinsic semiconductor, the number of occupied conduction band levels is given by [10]:

$$n = \int_{\varepsilon_C}^{\varepsilon_{top}} N(\varepsilon) F(\varepsilon) d\varepsilon \tag{I.2.17}$$

where ε_C is the energy at the bottom of the conduction band and ε_{top} is the energy at the top. The density of states $N(\varepsilon)$ can be approximated by the density near the bottom of the conduction band for low-enough carrier densities and temperatures (the so called parabolic band approximation):

$$N(\varepsilon) = M_c \frac{\sqrt{2}}{\pi^2} \frac{(\mathcal{E} - \mathcal{E}_C)^{\frac{1}{2}}}{\hbar^3} (m_{de})^{3/2} \tag{I.2.18}$$

where M_C is the number of equivalent minima in the conduction band and m_{de} is the density of state effective mass for electrons:

$$m_{de} = (m_1^* m_2^* m_3^*)^{1/3} \tag{I.2.19}$$

where m_1^*, m_2^* and m_3^* are the effective masses along the principal axes of the ellipsoidal energy surface. The Fermi-Dirac distribution function $F(\varepsilon)$ is given by:

$$F(\varepsilon) = \frac{1}{1 + exp\left(\frac{\mathcal{E} - \mathcal{E}_F}{k_B T}\right)} \tag{I.2.20}$$

where k_B is the Boltzmann constant, T absolute temperature and ε_F the Fermi energy. The integral in the equation (I.2.17) can be evaluated to be:

$$n = N_C \frac{2}{\sqrt{\pi}} F_{1/2}\left(\frac{\mathcal{E}_F - F_C}{k_B T}\right) \tag{I.2.21}$$

where N_C is the effective density of states in the conduction band and is given by:

$$N_C = 2\left(\frac{2\pi m_{de} k_B T}{h^2}\right)^{3/2} M_C \tag{I.2.22}$$

and $F_{1/2}(\eta_f)$ is the Fermi-Dirac integral. For the Boltzmann statistics case, that is for the Fermi level several $k_B T$ below E_C in non-degenerate semiconductors, the integral approaches $\sqrt{\pi} e^{\eta_f}/2$ and equation (I.2.21) becomes:

$$n = N_C exp\left(-\frac{\mathcal{E}_C - \mathcal{E}_F}{k_B T}\right) \tag{I.2.23}$$

Similarly, we can obtain the hole density near the top of the valence band:

$$p = N_V \frac{2}{\sqrt{\pi}} F_{1/2}\left(\frac{\mathcal{E}_V - \mathcal{E}_F}{k_B T}\right) \tag{I.2.24}$$

where N_v is the effective density of states of the valence band and is given by:

$$N_V = 2\left(\frac{2\pi m_{dh} k_B T}{h^2}\right)^{3/2} \tag{I.2.25}$$

where m_{dh} is the density of state effective mass of the valence band:

$$m_{dh} = (m_{lh}^{*\frac{3}{2}} + m_{hh}^{*\frac{3}{2}})^{2/3} \tag{I.2.26}$$

where subscripts refer to light and heavy holes, respectively. Under non-degenerate conditions we obtain:

$$p = N_V exp\left(\frac{\mathcal{E}_V - \mathcal{E}_F}{k_B T}\right) \tag{I.2.27}$$

As can be seen from the above equations, knowledge about the density of states is vital for calculating the real number of free-carriers in given conditions.

Equations (I.2.22) and (I.2.25) provide good approximation for the points in the band maxima and minima and their surroundings, but often more detailed description is needed. Such description can be provided by the Density Functional Theory methods or the Local Density Approximation [11,12].

Having determined the Density of States one can try to estimate the position of Fermi level in intrinsic semiconductors. In such materials, at finite temperatures continuous thermal agitation exists, which results in excitations of electrons from the valence band to the conduction bands and leaves an equal number of holes in the valence band, that is, $n = p = n_i$, where n_i is the intrinsic carrier density. This process is balanced by recombination of the electrons in the conduction band with holes in the valence band.

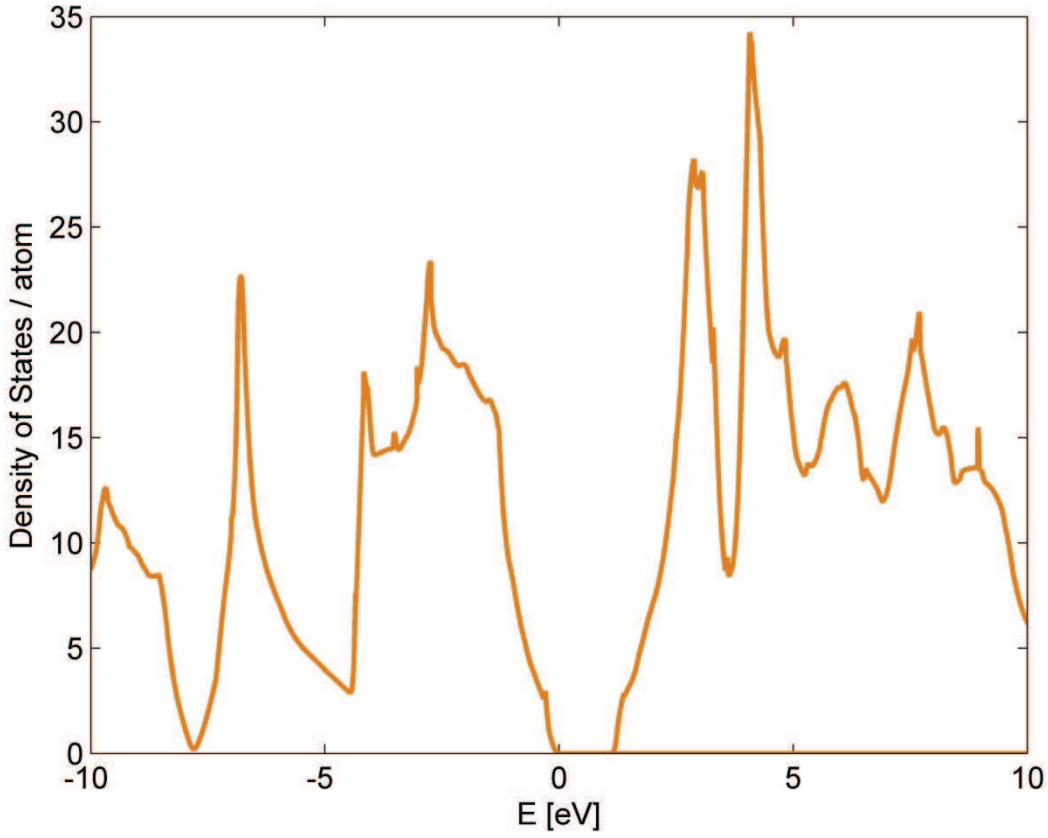

Figure I.4. The Electronic Density of States of crystalline silicon calculated by ab initio method within the frames of Local Density Approximation. Characteristic van Hove singularities can be seen.

The Fermi level for an intrinsic semiconductor is then obtained by equating (I.2.23) and (I.2.27):

$$\varepsilon_F = \varepsilon_i = \frac{\mathcal{E}_C - \mathcal{E}_V}{2} + \frac{k_B T}{2} ln\left(\frac{N_V}{N_C}\right) = \frac{\mathcal{E}_C - \mathcal{E}_V}{2} + \frac{3k_B T}{4} ln\left(\frac{m_{dh}}{m_{de} M_c^{2/3}}\right) \quad \text{(I.2.28)}$$

Hence the Fermi level for an intrinsic semiconductor (for T close to 293 K) generally lies very close to the middle of the band gap.

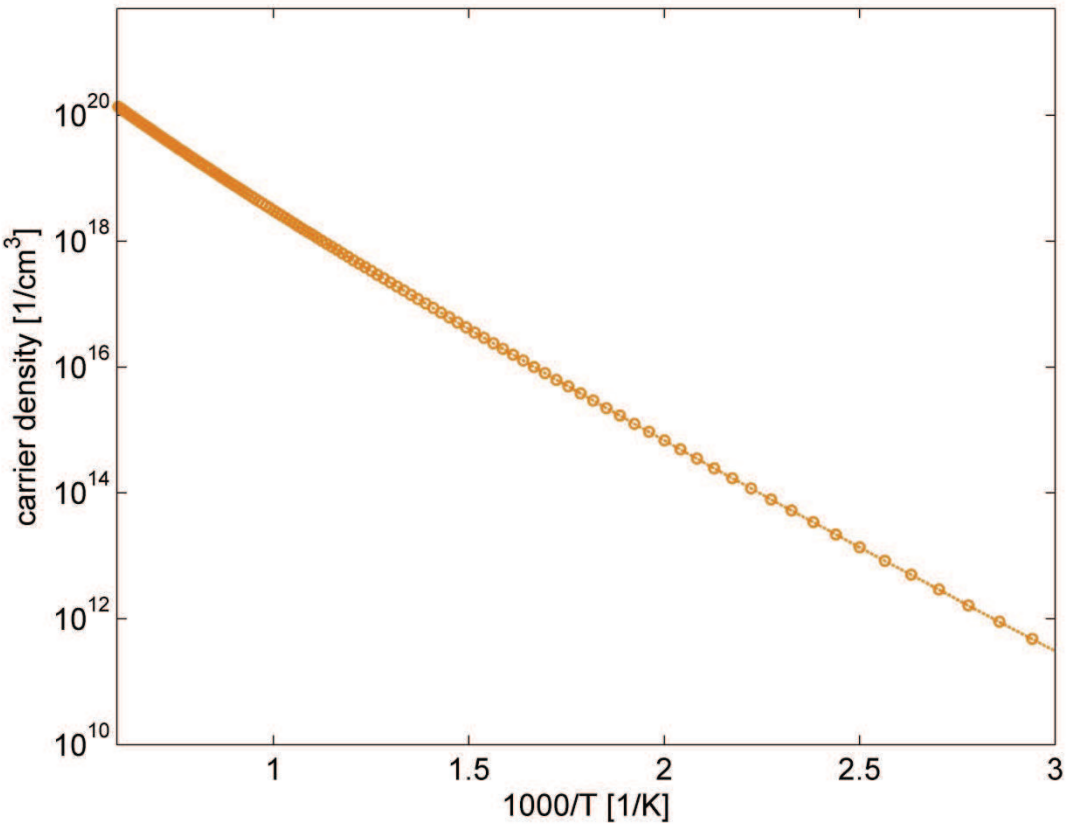

Figure I.5. Intrinsic carrier density in silicon vs *T*, calculated using the density of states presented in figure I.4.

One can gain a substantial insight into the structure imposed on the electronic levels by a periodic potential, if that potential is rather weak. There are two main reasons behind that: the electron-ion interaction is the strongest at small separations, but the conduction electrons are forbidden from entering the immediate neighborhood of the ions by the Pauli principle, since this region is already occupied. Second reason is that in the area where the conduction electrons are allowed, their mobility further diminishes the net potential any single electron experiences, for they can screen the fields of positively charged ions.

When the periodic potential $U = 0$, the solution to the Schrodinger's equation are plane waves. The wave function of a Bloch level with crystal momentum *k* can be written as follows:

$$\psi_k(r) = \sum_k c_{k-K} e^{i(k-K)\cdot r} \tag{I.2.29}$$

where the coefficients c_{k-K} and the energy levels ε are determined by the set of equations:

$$\left[\frac{\hbar^2}{2m}(k-K)^2 - \varepsilon\right] c_{k-K} + \sum_{K'} U_{K'-K} c_{k-K'} = 0 \tag{I.2.30}$$

The sum in (I.2.29) is over all reciprocal lattice vectors K, and for any fixed k there is an equation of the form (I.2.30) for each reciprocal lattice vector K. The infinitely many solutions of equation (I.2.30) are labeled with band index n.

When periodic potential U is zero and we are dealing with free electron case, the solution divides naturally into two possibilities: the non-degenerate case, where there is only one K vector for which the equation (I.2.30) is satisfied:

$$\varepsilon = \varepsilon^0_{k-K}, \psi_k \propto e^{i(k-K)\cdot r} \tag{I.2.31}$$

and the degenerate case, if there is a group of reciprocal lattice vectors $K_1,\ldots,K_m$ satisfying:

$$\varepsilon^0_{k-K_1} = \cdots = \varepsilon^0_{k-K_m} \tag{I.2.32}$$

Situation becomes more complex when U is no longer 0, but very small. There are two possible scenarios:

Scenario 1. We fix k and consider such reciprocal lattice vector K_1 that:

$$\left|\varepsilon^0_{k-K_1} - \varepsilon^0_{k-K}\right| \gg U, \quad \text{for fixed } k \text{ and all } K \neq K_1 \tag{I.2.33}$$

and we wish to investigate the effect of U on free-electron level given by:

$$\varepsilon = \varepsilon^0_{k-K_1}, c_{k-K} = 0, \quad K \neq K_1 \tag{I.2.34}$$

Setting $K = K_1$ we have:

$$\left(\varepsilon - \varepsilon^0_{k-K_1}\right) c_{k-K_1} = \sum_K U_{k-K_1} c_{k-K} \tag{I.2.35}$$

Because we chose the additive constant in the potential energy so that $U_K = 0$ when $K = 0$, only terms with $K \neq K_1$ appear on the right-hand side of equation (I.2.35). We consider a case where c_{k-K} vanishes when $K \neq K_1$ in the limit of vanishing U, so writing equation (I.2.30) for $K \neq K_1$ we obtain:

$$c_{k-K} = \frac{U_{K_1-K} c_{k-K_1}}{\varepsilon - \varepsilon^0_{k-K}} + \sum_{K \neq K_1} \frac{U_{K\prime-K} c_{k-K\prime}}{\varepsilon - \varepsilon^0_{k-K}} \tag{I.2.36}$$

Therefore, provided that there is no near degeneracy (which could cause some of the denominators in (I.2.36) to be of order of U and resulting in additional terms in the sum to be comparable to the term $K = K_1$) we can write:

$$c_{k-K} = \frac{U_{K_1-K} c_{k-K_1}}{\varepsilon - \varepsilon^0_{k-K}} + O(U^2) \tag{I.2.37}$$

Combining this with (I.2.35) we find:

$$\left(\varepsilon - \varepsilon^0_{k-K_1}\right) c_{k-K_1} = \sum_K \frac{U_{K_1-K} U_{K-K_1}}{\varepsilon - \varepsilon^0_{k-K}} c_{k-K_1} + O(U^3) \tag{I.2.38}$$

Thus, as expected the perturbed energy level ε differs from the free-electron value $\varepsilon^0_{k-K_1}$ only by the order of U^2. To solve equation (I.2.38) for ε, it suffices to replace the appearing ε in the denominator on the right-hand side by $\varepsilon^0_{k-K_1}$ leading to the following expression, correct to second order in U:

$$\varepsilon = \varepsilon^0_{k-K_1} + \sum_K \frac{\left|U_{K-K_1}\right|^2}{\varepsilon^0_{k-K_1} - \varepsilon^0_{k-K}} + O(U^3) \tag{I.2.39}$$

Equation (I.2.39) asserts that weakly perturbed, non-degenerate bands repel each other, for every energy level ε^0_{k-K} that lies below $\varepsilon^0_{k-K_1}$ contributes a term that raises the value of ε, while every energy level that lies above $\varepsilon^0_{k-K_1}$ contributes a term that lowers the value of ε. Also, in the case of no near degeneracy, the shift in energy from the case of the free-electron value is second order of U.

Scenario 2. We suppose that the value of k is such that there are reciprocal lattice vectors $K_1, \ldots, K_m$ and corresponding energy states $\varepsilon^0_{k-K_1}, \ldots, \varepsilon^0_{k-K_m}$ all within order U of each other, but far apart from other energy states ε^0_{k-K} on the scale of U:

$$\left|\varepsilon^0_{k-K} - \varepsilon^0_{k-K_i}\right| \gg U, \quad i = 1, \ldots, m, \quad K \neq K_1, \ldots, K_m \tag{I.2.40}$$

In this scenario we must treat separately all m equations of type (I.2.30) for any given K equal to $K = K_1, \ldots, K_m$. In these m equations we separate from the sum all the terms containing

coefficients c_{k-Kj}, j = 1... m, which need to be small in the limit of vanishing interaction, from the remaining c_{k-K} that will be at most of the order of U. We obtain:

$$\left(\varepsilon - \varepsilon^0_{k-K_i}\right)c_{k-K_i} = \sum_{j=1}^{m} U_{K_j-K_i}c_{k-K_j} + \sum_{K\neq K_{1,\ldots,}K_m} U_{k-K_i}c_{k-K} \tag{I.2.41}$$

for $i = 1, \ldots, m$. If we assume the same separation in the sum, we obtain:

$$c_{k-K} = \frac{1}{\varepsilon - \varepsilon^0_{k-K}}\left(\sum_{j=1}^{m} U_{K_j-K}c_{k-K_j} + \sum_{K\neq K_{1,\ldots,}K_m} U_{K'-K}c_{K-K'}\right) \tag{I.2.42}$$

for $K \neq K_1,\ldots, K_m$, which corresponds to the equation (I.2.36) in the non-degenerated case. Knowing that c_{k-K} will be at most of the order of U for any $K \neq K_1,\ldots, K_m$, equation (I.2.42) becomes:

$$c_{k-K} = \frac{1}{\varepsilon - \varepsilon^0_{k-K}}\sum_{j=1}^{m} U_{K_j-K}c_{k-K_j} + O(U^2) \tag{I.2.43}$$

substituting equation (I.2.43) into (I.2.41) we find that:

$$\left(\varepsilon - \varepsilon^0_{k-K_i}\right)c_{k-K_i} = \sum_{j=1}^{m} U_{K_j-K}c_{k-K_j} + \sum_{j=1}^{m}\left(\sum_{K\neq K_{1,\ldots,}K_m} \frac{U_{K_1-K}U_{K-K_1}}{\varepsilon - \varepsilon^0_{k-K}}\right)c_{k-K_j} + O(U^3) \tag{I.2.44}$$

We found that the shift in m nearly degenerate levels reduces to the solution of m coupled equations for c_{k-Kj}. Since coefficients in the second term on the right-hand side are of the higher order than those in the first, one can find the leading corrections in U are:

$$\left(\varepsilon - \varepsilon^0_{k-K_i}\right)c_{k-K_i} = \sum_{j=1}^{m} U_{K_j-K}c_{k-K_j} \tag{I.2.45}$$

for $i = 1, \ldots, m$, which are just set of equations for a system of m quantum levels.

The quantum structure of real solids is usually so complex that the nearly free-electron model is rarely valid [9]. One obvious observation that arises is the complete disregard of bands arising from ion-core levels. Several methods exist that allow rigorous analysis of core levels and resulting bands, the most-widely used one being the Tight-Band method. Nevertheless, cases where the interest is directed towards either deep core or highly excited, near free-

electron states are rather rare. Therefore several combined methods have been introduced that allow accurate representation of band structure for both areas of interest. Methods that gained most attention are: Independent Electron Approximation, Cellular Method, Muffin-Tin Potential, Augmented Plane Wave Method, Green's Function Method, Orthogonalized Plane Wave Method and Pseudopotential Method [13]. It is not the aim of this work to review all these methods, therefore we will focus briefly only on the Pseudopotential [14,15] method. The interested reader is referred to the information present in the literature [9,13].

Let us now describe the exact wave function for a valence band as a linear combination of Orthogonalized Plane Waves:

$$\psi_k = \sum_K c_k \phi_{k+K} \tag{I.2.46}$$

and let ϕ_k^v be the plane-wave part of this expansion:

$$\phi_k^v(r) = \sum_K c_K e^{i(k+K)\cdot r} \tag{I.2.47}$$

we also keep in mind that for core levels:

$$\phi_k = e^{ik\cdot r} + \sum_c b_c \, \psi_k^c(r) \tag{I.2.48}$$

where $b_c = -\int dr \psi_k^{c*}(r)\, e^{ik\cdot r}$, then we can rewrite the expansions (I.2.48) and (I.2.46) as:

$$\psi_k^v(r) = \phi_k^v(r) - \sum_c \left(\int dr' \psi_k^{c*}(r') \psi_k^v(r') \right) \psi_k^c(r) \tag{I.2.49}$$

Since ψ_k^v is an exact valence wave function, it satisfies Schrodinger's equation with eigenvalue ε_k^v:

$$H\psi_k^v = \varepsilon_k^v \psi_k^v \tag{I.2.50}$$

Substitution of (I.2.50) into (I.2.49) gives:

$$H\phi_k^v - \sum_c \left(\int dr' \psi_k^{c*} \phi_k^v \right) H\psi_k^c = \varepsilon_k^v \left(\phi_k^v - \sum_c \left(\int dr' \psi_k^{c*} \phi_k^v \right) \psi_k^c \right) \tag{I.2.51}$$

If we note that $H\psi_k^c = \varepsilon_k^c \psi_k^c$ for the exact core levels, then we can rewrite (I.2.51) as:

$$(H + V^R)\phi_k^v = \varepsilon_k^v \phi_k^v \tag{I.2.52}$$

where most of the cumbersome terms are confined within the operator V^R, defined by:

$$V^R\psi = \sum_c (\varepsilon_k^v - \varepsilon_c)\left(\int dr'\psi_k^{c*}\psi\right)\psi_k^c \tag{I.2.53}$$

The pseudopotential is defined to be the sum of the actual periodic potential U and V^R:

$$H + V^R = -\frac{\hbar^2}{2m}\nabla^2 + V^{pseudo} \tag{I.2.54}$$

We assume that the pseudopotential is sufficiently small to justify the nearly free-electron calculation of the valence levels. One can see a hint that this might be so from the fact that actual periodic potential is attractive near the ion cores and thus $(\psi, U\psi) = \int dr\psi^*(r)U(r)\psi(r)$ is negative, the corresponding matrix element of the potential V^R is, according to (I.2.53):

$$(\psi, V^R\psi) = \sum_C (\varepsilon_k^v - \varepsilon_k^c)\left|\int dr\psi_k^{c*}\psi\right|^2 \tag{I.2.55}$$

Since valence energies are above core energies, this is always positive. Thus adding V^R to U provides at least partial cancellation, and one might hope for it to lead to a potential weak enough to do nearly free electron calculations for ϕ_k^v, treating the pseudopotential as weak perturbation.

In three dimensions the structure of energy bands is often presented by plotting ε vs. k along straight lines connecting particular high-symmetry points in the Brillouin zone. Such curves are generally shown in a reduced zone-scheme, because for general directions in k-space they are not periodic. An example of accurately calculated band structure for crystalline silicon is shown in figure I.6. The calculation was performed within the Density Functional Theory (DFT) [16,17], the Local Density Approximation (LDA) [11] [18] and Pseudopotential models. The electronic band gap for bulk crystalline Si (c-Si) is E_g = 1.12 eV. The optical band gap for bulk silicon is E_g = 1.17 eV [13].

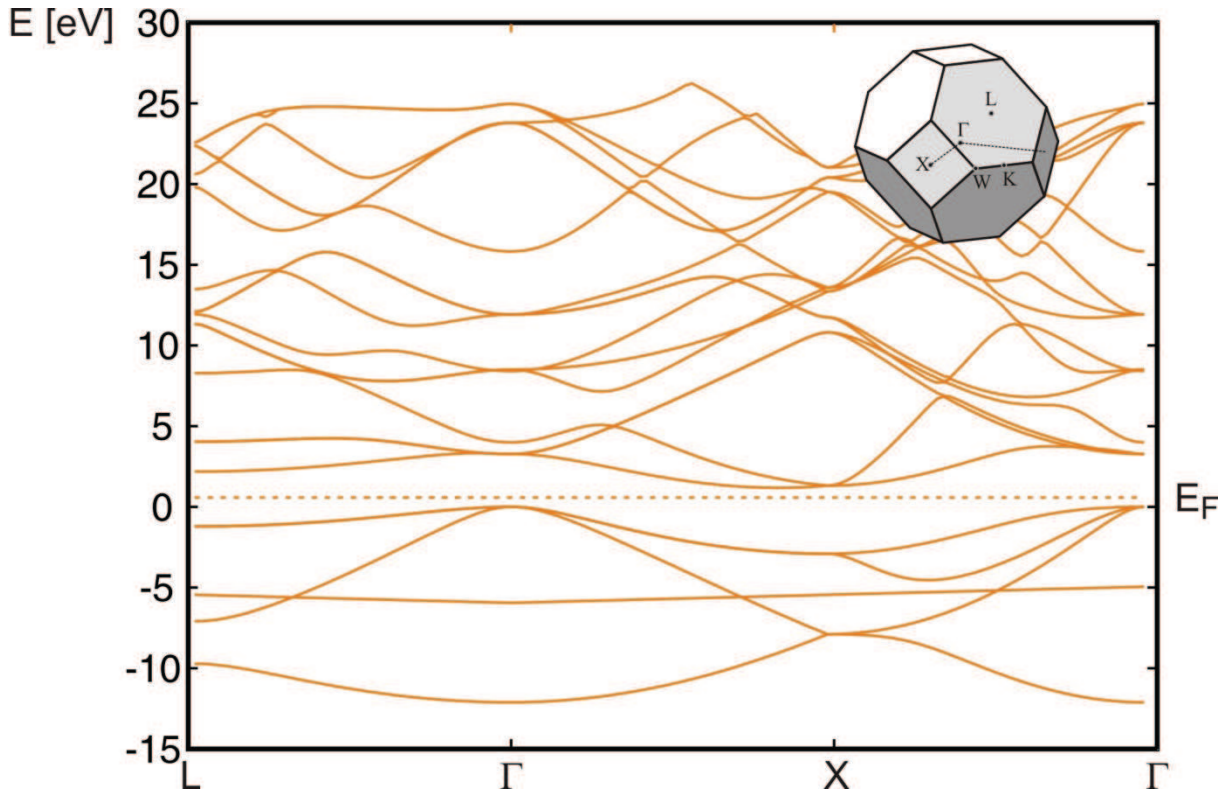

Figure I.6. Electronic band structure of crystalline silicon calculated by *ab initio* method within LDA and DFT frames. High symmetry points are indicated on the first Brillouin zone, while the Γ point ($k = 0$) lies in the middle.

2.2. Impurity and defects in Si.

By a crystalline defect one generally means any region where the microscopic arrangement of ions differs drastically from that of a perfect crystal. Defects are called point, line or surface, depending on whether the imperfect region is bounded on the atomic scale to one, two or three dimensions. Particular kinds of defects that found a broad application in semiconductors are dopants (doping impurities). When a dopant is introduced in a semiconductor, electronic density and potential often introduced by that defect is often quite different than that of the surrounding ions (figure I.7). The periodic potential of a crystal is locally disturbed, resulting in additional states that appear somewhere in the energy spectrum. Depending on the nature of the defects, some of those extra states can be beneficial. Another effect that appears is that the neighboring atoms usually are no longer in their local energy minima, and the crystalline network relaxes around the defect (figure I.8). The force resulting from the introduction of a phosphorous atom and subsequent relaxation imposes a strain on the neighboring atoms. As

within the frames of DFT-LDA approximation by *ab initio* method, this pressure is equal p = 1.34904 GPa for a cell consisting of a total of eight atoms [19].

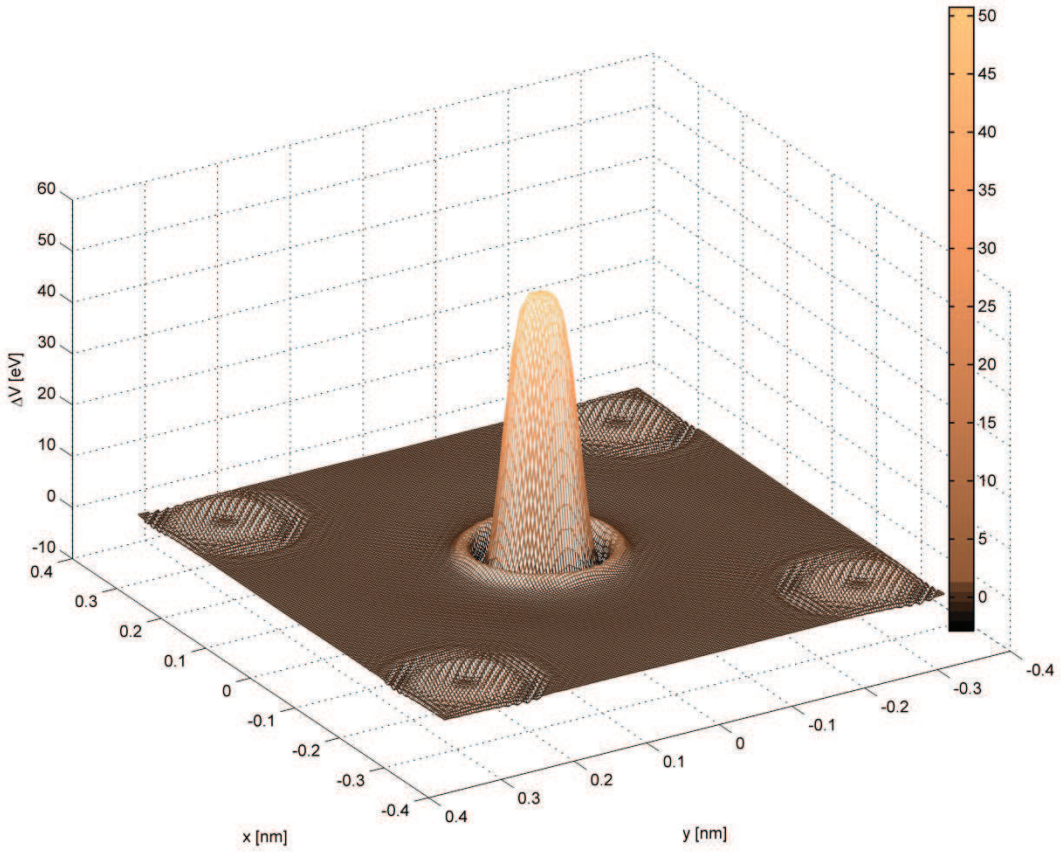

Figure I.7. Changes in the potential ΔV around a phosphorous atom substituted in Si, in regard to the potential of undoped silicon. The potential is plotted in a plane passing through the P atom and after the relaxation of crystalline network.

When a semiconductor is doped with donor and/or acceptors, impurity energy levels are introduced. A donor level is defined as being neutral when occupied, and positive when empty. Likewise, an acceptor level is defined as negative when occupied and neutral when empty. The simplest calculation of impurity energy levels is based on the hydrogen-atom model. The ionization energy for the hydrogen atom is:

$$\varepsilon_H = \frac{m_0 q^4}{32\pi^2 \varepsilon_0^2 \hbar^2} = 13.6eV \qquad \text{(I.2.56)}$$

where ε_0 is the free-space permittivity.

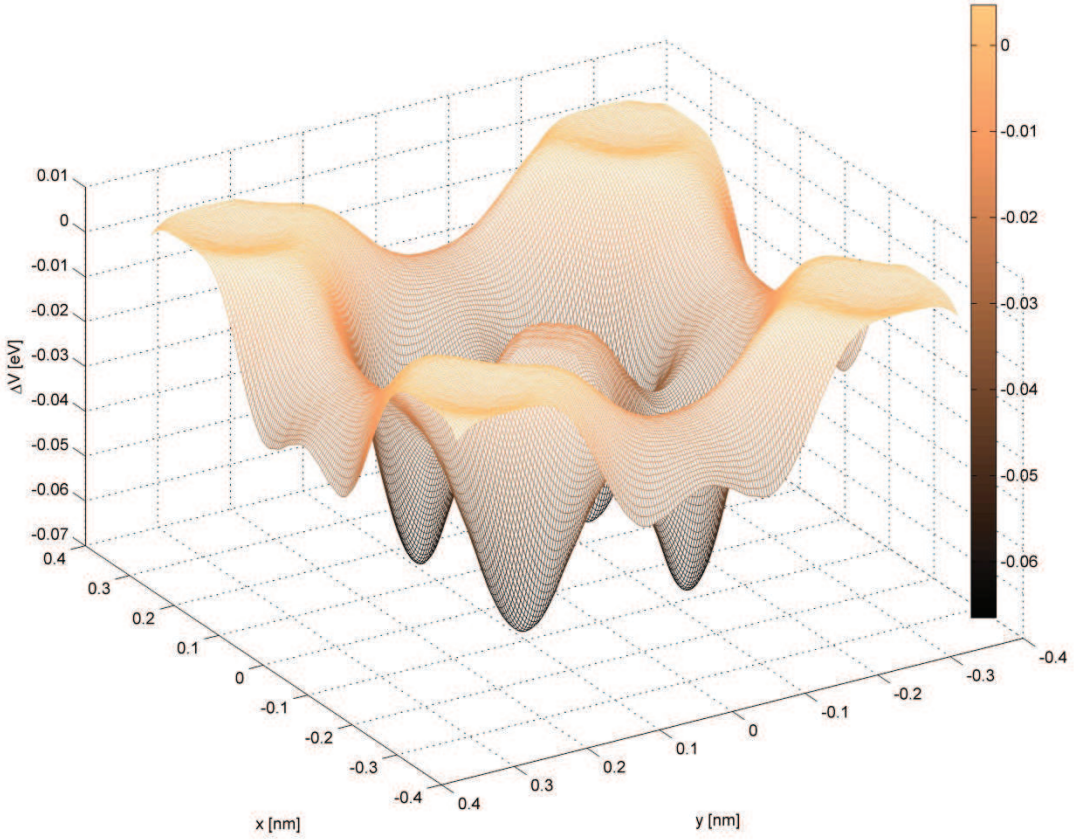

Figure I.8. Changes in the potential ΔV around a phosphorous atom occupying an interstitial position in Si, after relaxation of the crystalline network. The potential is plotted in a plane passing through the P atom.

The ionization energy for the donor ε_d can be obtained by replacing m_o by the conductivity effective mass of electrons:

$$m_{cc} = 3\left(\frac{1}{m_1^*} + \frac{1}{m_2^*} + \frac{1}{m_3^*}\right)^{-1} \tag{I.2.57}$$

and by replacing by the permittivity of the semiconductor ε_s in (I.2.56):

$$\mathcal{E}_d = \left(\frac{\varepsilon_0}{\varepsilon_s}\right)^2 \left(\frac{m_{cs}}{m_0}\right) \varepsilon_H \tag{I.2.58}$$

The ionization energy for donors calculated from (I.2.58) is 0.006 eV for Ge, 0.025 eV for Si, and 0.007 eV for GaAs [10]. The hydrogen-atom calculation for the ionization level for the acceptors is similar to that for the donors. We consider the unfilled valence band as a filled band plus an imaginary hole in the central force field of a negatively charged acceptor. The calculated acceptor ionization energy (measured from the valence-band edge) is 0.015 eV for

Ge, 0.05 eV for Si, and about 0.05 eV for GaAs. The simple hydrogen-atom model given above certainly cannot account for the details of ionization energy, particularly the deep levels in semiconductors. However, the calculated values do predict the correct order of magnitude of the true ionization energies for shallow impurities. It is possible for a single atom to have many levels; for example gold in Ge has three acceptor levels and one donor level in the forbidden energy gap.

The Fermi level for the intrinsic semiconductor (I.2.28) lies very close to the middle of the band gap. Figure I.9 depicts this situation, showing schematically from left to right the simplified band diagram, the density of states $N(\varepsilon)$, the Fermi-Dirac distribution function $F(\varepsilon)$, and the carrier concentrations. The shaded area in the conduction band and the valence band are the same; indicating that $e = p = n$; for the intrinsic case. When impurity atoms are introduced, the Fermi level must adjust itself to preserve charge neutrality (figure I.9 *b* and *c*). Consider the case shown in figure I.9 *b*, where donor impurities with a concentration N_D (cm^{-3}) are added to the crystal. To preserve electrical neutrality the total negative charges (electrons and ionized acceptors) must equal the total positive charges (holes and ionized donors), or for the present case:

$$n = N_D^+ + p \tag{I.2.59}$$

where n is the electron density in the conduction band, p is the hole density in the valence band, and N_D^+ is the number of ionized donors, given by:

$$N_D^+ = N_D \left[1 - \frac{1}{1 + \frac{1}{g} \cdot exp\left(\frac{\mathcal{E}_D - \mathcal{E}_F}{k_B T}\right)} \right] \tag{I.2.60}$$

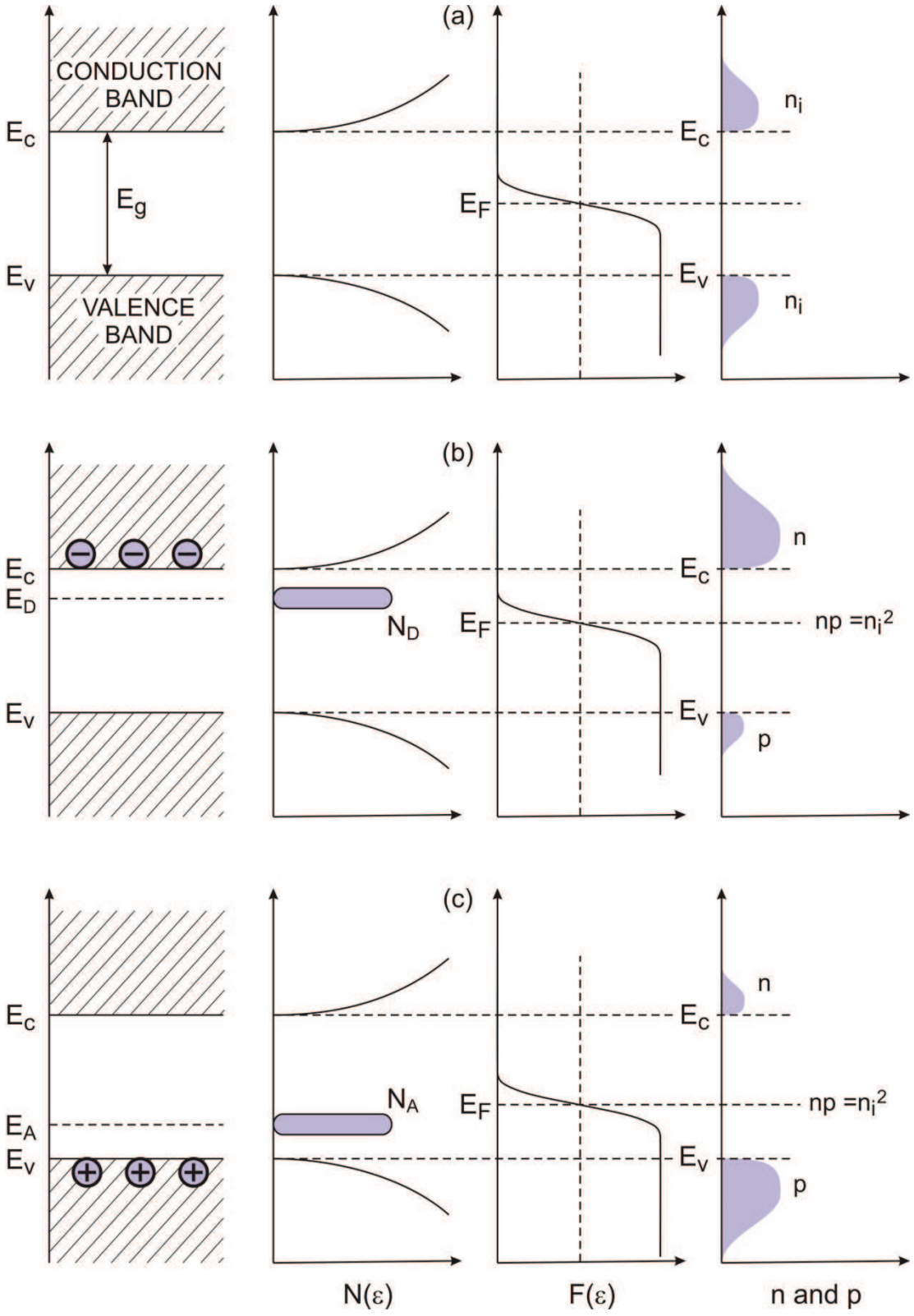

Figure I.9. Schematic band diagrams, density of states, the Fermi-Dirac distribution, and the carrier concentration for: a) intrinsic, b) n-type and c) p type semiconductor at thermal equilibrium.

where g is the ground-state degeneracy of the donor impurity level and equals 2 because of the fact that a donor level can accept one electron with either spin or can have no electron. When acceptor impurities of concentration N_A are added to a semiconductor crystal, a similar expression can be written for the charge neutrality condition and the expression for ionized acceptors is:

$$N_A^- = \frac{N_A}{1 + g \cdot exp\left(\frac{\mathcal{E}_A - \mathcal{E}_F}{k_B T}\right)} \tag{I.2.61}$$

where the ground-state degeneracy factor g is 4 for acceptor levels. The value is 4 because in Ge, Si. and GaAs each acceptor impurity level can accept one hole of either spin and the impurity level, is doubly degenerate as a result of the two degenerate valence bands at $k = 0$. Rewriting the neutrality condition (I.2.59), we obtain:

$$\int_{\varepsilon_C}^{\varepsilon_{top}} N(\varepsilon)F(\varepsilon)d\varepsilon = N_D\left[1 - \frac{1}{1 + \frac{1}{g} \cdot exp\left(\frac{\mathcal{E}_D - \mathcal{E}_F}{k_B T}\right)}\right] + \int_{\varepsilon_{bottom}}^{\varepsilon_V} N(\varepsilon)(1 - F(\varepsilon))d\varepsilon \tag{I.2.62a}$$

or simply:

$$N_C exp\left(-\frac{\mathcal{E}_C - \mathcal{E}_F}{k_B T}\right) = N_D\left[1 - \frac{1}{1 + \frac{1}{g} \cdot exp\left(\frac{\mathcal{E}_D - \mathcal{E}_F}{k_B T}\right)}\right] + N_V exp\left(\frac{\mathcal{E}_V - \mathcal{E}_F}{k_B T}\right) \tag{I.2.62b}$$

For a set of given N_C, N_V, N_D, E_C, E_V, E_D, and T, the Fermi level E_F can be uniquely determined from (I.2.62). In the case shown in figure I.9 b (with $N_D = 10^{16}$ cm^{-3}, $T = 300$ K) the Fermi level is close to the conduction band edge and adjusts itself so that almost all donors are ionized. As the temperature is lowered sufficiently, the Fermi level rises toward the donor level (for n-type semiconductors) and the donor level is partially filled with electrons. The approximate expression for the electron density is then:

$$n = \left(\frac{N_D - N_A}{2N_A}\right) N_D exp\left(-\frac{E_d}{k_B T}\right) \tag{I.2.63}$$

for a partially compensated semiconductor and for:

$$N_A \gg \frac{1}{2} N_C exp\left(-\frac{E_d}{k_B T}\right)$$

where $E_d = E_C - E_D$, or:

$$n = \frac{1}{\sqrt{2}} (N_D N_C)^{1/2} exp\left(-\frac{E_d}{k_B T}\right) \quad \text{(I.2.64)}$$

Figure I.10 shows a typical example, where n is plotted as a function of reciprocal temperature. At high temperatures we have the intrinsic range since $n = p > N_D$. At very low temperatures most impurities are not ionized and the slope is given by (I.2.63) or (I.2.64), depending on the compensation conditions. The electron density, however, remains essentially constant over a wide range of temperatures (T ~ 200 to 500 K in figure I.10).

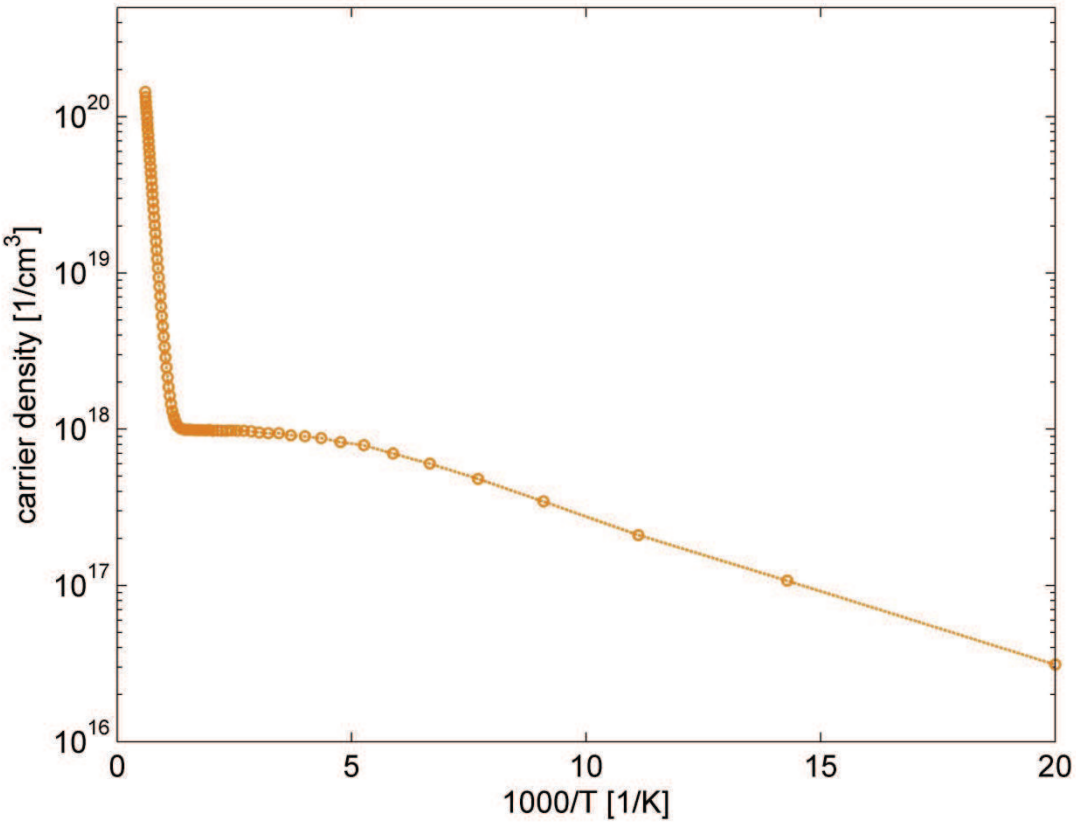

Figure I.10. Carrier density vs T in P-doped silicon for a doping concentration $N_d = 10^{18}$ cm^{-3}, calculated using the density of states presented in figure I.4.

When doping impurity atoms are added, the up product is still given by:

$$np = N_C N_V exp\left(-\frac{E_g}{k_B T}\right) \quad \text{(I.2.65)}$$

which is called the mass-action law, and the product is independent of the added impurities. At relatively elevated temperatures, most donors and acceptors are ionized, so the neutrality condition can be approximated by:

$$n + N_A = p + N_D \quad \text{(I.2.66)}$$

This analysis gives the basic insight for the charge neutrality principle and calculation of the Fermi level in semiconductors, as well as an estimation of the number of free carriers for intrinsic and doped semiconductors and their evolution with temperature.

3. Theoretical limits of photovoltaic conversion

The thermodynamic efficiency of the energy conversion of radiation into other forms of energy is of wide interest and has been much discussed [20,21]. The efficiency of a solar cell is defined as the ratio between incident power P_S and output power of a photovoltaic device P_D. The upper limit can be determined either by analyzing the thermodynamic limits of the two interacting bodies or by a detailed analysis of all the generation and recombination mechanisms, without taking into account the exact structure of the device.

3.1. Thermodynamical limit of solar energy conversion.

Here we shall consider a system consisting of two large reservoirs called pump (P) and sink (S) together with a converter (C). The last interacts with the pump by an interchange of isotropic radiation and with the sink by isotropic radiation and possibly by other means so as to exchange work and heat. If the converter takes in black-body radiation at temperature T_P from the pump and rejects black-body radiation at a temperature marginally above the sink temperature T_S, then an upper limit to the conversion efficiency is [22,23]:

$$n_L = 1 - \frac{4}{3}\frac{T_S}{T_P} + \frac{1}{3}\left(\frac{T_S}{T_P}\right)^4 \qquad \text{(I.3.1)}$$

We assume that that the converter (C) of the temperature T_C is encircled by two reservoirs: the Sun, which acts as a pump (P) of the temperature T_P and the environment which acts as a sink (S) of the temperature T_S [24]. We consider the exchange of energy and entropy C → S and C → P, and we mark $j_{e,XY}$ and $j_{s,XY}$ as energy and entropy fluxes from point X to Y, where $X,Y = P, S, C$. The schematic representation of the system considered here is shown in figure I.11.

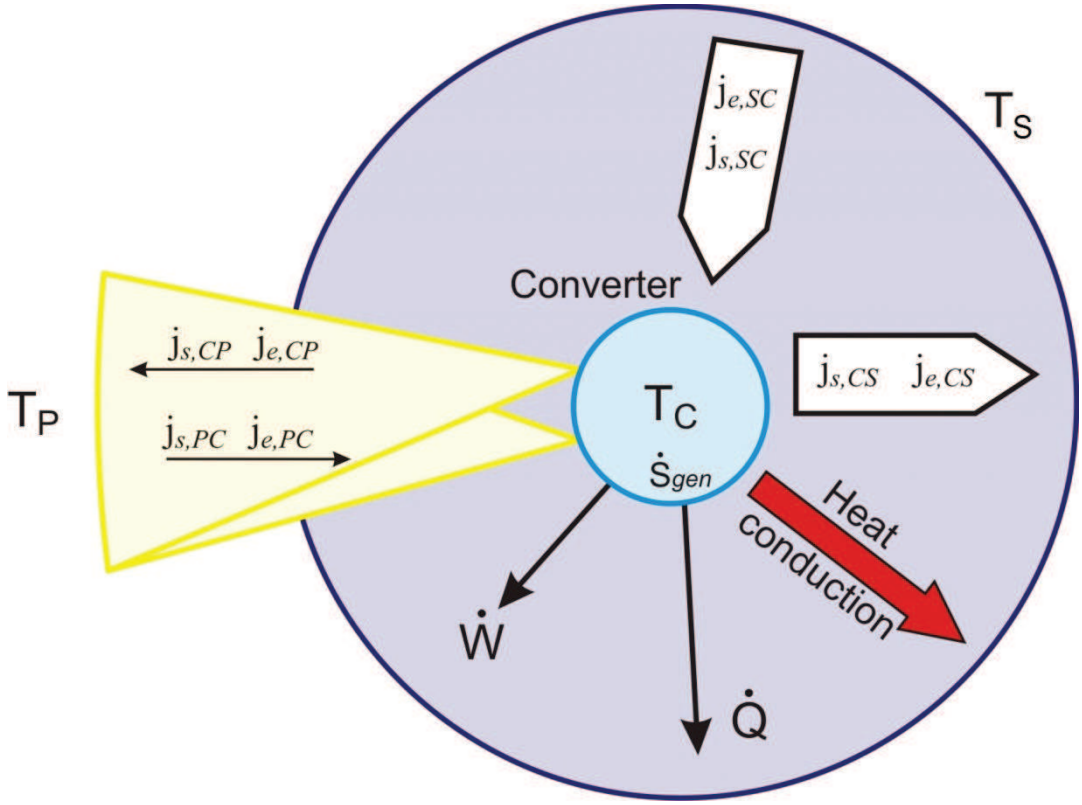

Figure I.11. System Pump - Converter - Environment (PCE) with different energy and entropy fluxes and the direction of their flow. The heat conduction is not considered here, but is shown for complete description.

The transfer of the heat $\dot{Q}$, which is done and temperature T_Q ($T_S < T_Q < T_P$) from the converter to the environment is associated to the transfer of entropy. W is the collectible work provided by the converter and $\dot{S}$ is the generation of entropy by the unit of surface inside the converter. The balance between energy and entropy fluxes is then:

$$j_{e,net} = j_{e,PC} - j_{e,CP} + j_{e,SC} - j_{e,CS} - \dot{Q} - \dot{W}$$
$$j_{s,net} = j_{s,PC} - j_{s,CP} + j_{s,SC} - j_{s,CS} - \dot{S}_{gen} - \frac{\dot{Q}}{T_Q} \quad \text{(I.3.2)}$$

The efficiency of the conversion is described as follows:

$$\eta = \frac{\dot{W}}{j_{e,PC}} = \frac{(j_{e,PC} - T_Q j_{s,PC}) - (j_{e,CS} - T_Q j_{s,CS}) + (j_{e,SC} - T_Q j_{e,SC})}{j_{e,PC}} + \frac{-(j_{e,CP} - T_Q j_{s,CP}) - (j_{e,net} - T_Q j_{s,net}) - T_Q \dot{S}_{gen}}{j_{e,PC}} \quad \text{(I.3.3)}$$

The terms $j_{e,net}$ and $j_{s,net}$ are often neglected. Since the Sun is visible from the Earth under a solid angle Ω, a following assumption is justified:

$$j_{e,XY} = \iint K_{\omega X} \cdot \cos\theta_{XY} \cdot d\hbar\omega \cdot d\Omega_{XY}$$
$$j_{s,XY} = \iint L_{\omega X} \cdot \cos\theta_{XY} \cdot d\hbar\omega \cdot d\Omega_{XY} \quad \text{(I.3.4)}$$

with [21]:

$$K_{\omega X} = \frac{l_X \cdot (\hbar\omega)^3}{8\pi^3\hbar^3c^2} \cdot n_{\omega X}$$
$$L_{\omega X} = \frac{l_X \cdot k \cdot (\hbar\omega)^2}{8\pi^3\hbar^3c^2} \cdot [(1+n_{\omega X}) \cdot \ln(1+n_{\omega X}) - n_{\omega X} \cdot \ln n_{\omega X}] \quad \text{(I.3.5)}$$

where $n_{\omega X}$ is the number of photons at frequency $\nu = 2\pi\omega$ emitted by X. Θ_{XY} is the angle that emits incident radiation normal to the surface of Y, where $X, Y = S, C, P$. The parameters $l_X = 1$ for polarized light and $l_X = 2$ for non-polarized light. If $K_{\omega X}$ and $L_{\omega X}$ are angle-independent, we can write:

$$j_{e,XY} = B_{XY} \int_0^\infty K_{\omega X} \cdot d\hbar\omega$$
$$j_{s,XY} = B_{XY} \int_0^\infty L_{\omega X} \cdot d\hbar\omega \quad \text{(I.3.6)}$$

where:

$$B_{XY} = \int_{\Omega_{XY}} \cos\theta_{XY} \cdot d\Omega_{XY} \quad \text{(I.3.7)}$$

In the case of the PCE system, $B_{tot} = B_{CP} + B_{CS}$ represents the whole solid angle accessible to the system. We therefore obtain the following relations:

$$B_{XY} = B_{YX} \quad \text{(I.3.8)}$$

$$\frac{B_{PC}}{B_{tot}} = \frac{C}{C_{max}} \quad \text{(I.3.9)}$$

Assuming that $n_{\omega X}(\hbar\omega)$ depends on parameter $z = \frac{\hbar\omega}{kT_x}$, and that X is a black body of temperature T_X, we can obtain:

$$j_{e,XY} = \frac{15\sigma}{2\pi^5} B_{XY} \cdot l_X \cdot T_X^4 \cdot I(n_X)$$
$$j_{s,XY} = \frac{15\sigma}{2\pi^5} B_{XY} \cdot l_X \cdot T_X^3 \cdot J(n_X) \quad \text{(I.3.10)}$$

where σ=5,670·10^{-8} [W·m^{-2}·K^{-4}] is the Stefan constant, and $n_X = n_{\omega X}(z)$. Additionally:

$$I(n_X) = \int_0^\infty z^3 \cdot n_X \cdot dz$$
$$J(n_X) = \int_0^\infty z^2 \cdot \left[\ln(1 + n_X) + n_X \cdot \ln\left(1 + \frac{1}{n_X}\right)\right] \cdot dz \quad \text{(I.3.11)}$$

If the Pump (Sun) and the Sink (environment) are considered black bodies at temperatures T_P and T_S respectively, and upon assuming the same polarization factor l_X for all components we obtain:

$$n_X = \frac{1}{exp\left(\frac{\hbar\omega}{k_B T_X}\right) - 1} = \frac{1}{exp(z) - 1} \quad \text{(I.3.12)}$$

we can also introduce an integral $G(u,v)$ defined as a Debye function [25]:

$$G_n(u,v) = \int_u^\infty \frac{z^n}{exp(z - v) - 1} \cdot dz \quad \text{(I.3.13)}$$

now, we find that $I(n_X)$ and $J(n_X)$ can be expressed as:

$$I(n_X) = G_3(0,0) = \frac{\pi^4}{15}$$
$$J(n_X) = \frac{4}{3} G_3(0,0) = \frac{4\pi^4}{45} \quad \text{(I.3.14)}$$

The conversion efficiency η becomes finally:

$$\eta = \left[1 - \frac{4}{3}\cdot\frac{T_Q}{T_P} - \left(\frac{T_S}{T_P}\right)^4 + \frac{4}{3}\cdot\frac{T_Q}{T_P}\left(\frac{T_S}{T_P}\right)^3\right] - \left(\frac{C_{max}}{C}\right)\left[\left(\frac{T_C}{T_P}\right)^4 - \frac{4}{3}\cdot\frac{T_Q}{T_P}\left(\frac{T_C}{T_P}\right)^3 - \left(\frac{T_S}{T_P}\right)^4 + \frac{4}{3}\cdot\frac{T_Q}{T_P}\left(\frac{T_S}{T_P}\right)^3\right] - \frac{2\pi^5\cdot T_S\cdot \dot{S}_{gen}}{15\sigma\cdot B_{PC}\cdot l_P\cdot T_P^4\cdot I(n_P)} \quad \text{(I.3.15)}$$

In the case when $T_Q = T_S$ we obtain:

$$\eta = \left[1 - \frac{4}{3}\cdot\frac{T_S}{T_P} + \frac{1}{3}\cdot\left(\frac{T_S}{T_P}\right)^3\right] - \left(\frac{C_{max}}{C}\right)\left[\left(\frac{T_C}{T_P}\right)^4 - \frac{4}{3}\cdot\frac{T_E}{T_P}\left(\frac{T_C}{T_P}\right)^3 + \frac{1}{3}\cdot\left(\frac{T_S}{T_P}\right)^3\right] - \frac{2\pi^5\cdot T_S\cdot \dot{S}_{gen}}{15\sigma\cdot B_{PC}\cdot l_P\cdot T_P^4\cdot I(n_P)} \quad \text{(I.3.16)}$$

The maximum conversion efficiency η_L corresponds to the efficiency obtained by Landsberg and co-workers [21]. It is obtained under following conditions:

- the converter is totally encircled by the Sun
- the converter is in equilibrium with the surrounding environment
- there is no generation of entropy inside the cell

Therefore:

$$\eta \le \eta_L = 1 - \frac{4}{3}\cdot\frac{T_S}{T_P} + \frac{1}{3}\cdot\left(\frac{T_S}{T_P}\right)^3 \quad \text{(I.3.17)}$$

as in (I.3.1). It is worth noting that this efficiency is somewhat below the Carnot efficiency

$$\eta_{Carnot} = 1 - \frac{T_S}{T_P} \quad \text{(I.3.18)}$$

Other authors [26] proved that this difference comes from the generation of entropy when the light traverses the space between the Sun and the Earth.

Another model that represents a more realistic approach to the Pump - Converter - Sink system is shown in figure I.12. This endoreversible converter takes into account irreversibility of heat transfer between different points of the system. Because of that, the maximal efficiency in that approach is always below the one obtained by Landsberg approach. The Carnot engine (CENG), coupled with a radiator (R) of the temperature T_C is encircled with by

the Sun, which again acts as a pump (P) at the temperature T_P, and by the environment, which acts as the sink (S) of the temperature T_S.

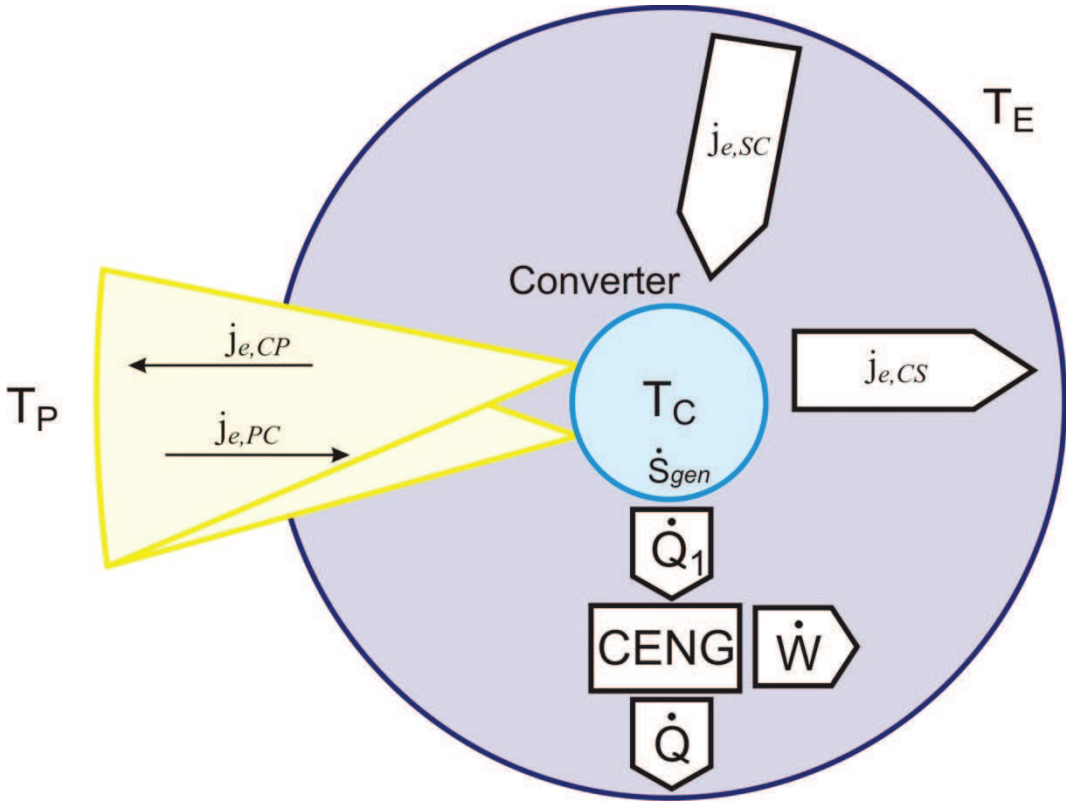

Figure I.12. System Pump - Converter - Environment (PCE) and a Carnot engine representing the endoreversible converter system.

In this case the conversion efficiency is expressed as:

$$\eta = \frac{\dot{W}}{j_{e,PC}} = \left(1 - \frac{T_S}{T_P}\right) \cdot \frac{j_{e,PC} - j_{e,CP} + j_{e,SC} - j_{e,CS}}{j_{e,PC}} \tag{I.3.19}$$

by using the same notations as in previous model, we obtain:

$$\eta = \left(1 - \frac{T_S}{T_C}\right)\left[1 - \left(\frac{T_S}{T_P}\right)^4 + \left(\frac{C_{max}}{C}\right) \cdot \left(\left(\frac{T_S}{T_P}\right)^4 - \left(\frac{T_C}{T_P}\right)^4\right)\right] \tag{I.3.20}$$

For thermal equilibrium $T_C = T_E = T_P$ the efficiency is self-cancelling, for $T_C = T_E$ and $T_C = T_{C0}$. T_{C0} corresponds to the situation where the work extracted from the converter is $W = 0$. Therefore we can write:

$$T_{C0} = T_P \sqrt[4]{\left(\frac{T_S}{T_P}\right)^4 + \left[1 - \left(\frac{T_S}{T_P}\right)^4\right] \cdot \left(\frac{C}{C_{max}}\right)} \tag{I.3.21}$$

also, we have:

$$\eta = \left(1 - \frac{T_S}{T_C}\right) \cdot \frac{C_{max}}{C} \cdot \left(\frac{T_{C0}^4 - T_C^4}{T_P^4}\right) \tag{I.3.22}$$

The maximal efficiency is obtained for the temperature T, satisfying the following relation:

$$\frac{\partial \eta}{\partial T_C}(T = T_{Cm}) = 0 \leftrightarrow \frac{4T_{Cm}^5}{T_{C0}^4 + 3T_{Cm}^4} = \frac{T_S}{T_P} \tag{I.3.23}$$

for the maximal concentration C_{max} we obtain:

$$\eta = \left(1 - \frac{T_S}{T_C}\right) \cdot \left(1 - \frac{T_C^4}{T_P^4}\right) \tag{I.3.24}$$

the maximal efficiency η as a function of the ratio T_C/T_P for different values of concentration C is shown in figure I.13.

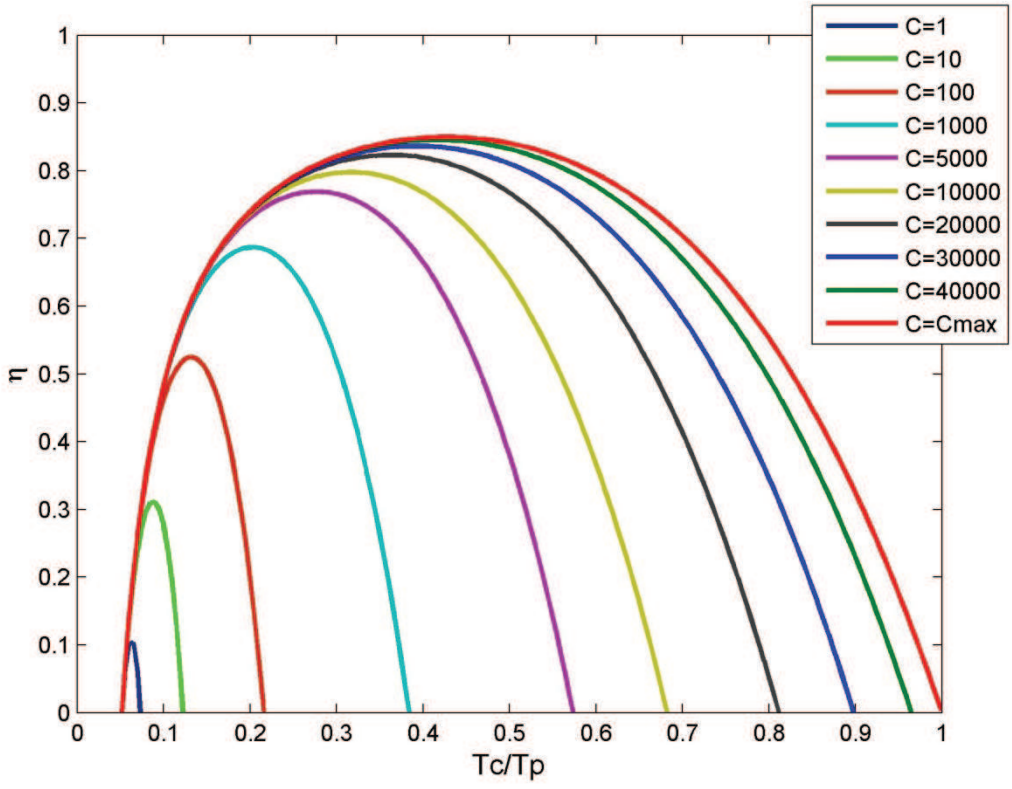

Figure I.13. Conversion efficiency calculated from equation (I.3.20) for different concentration ratios and different converter temperature T_C. T_P = 5800 K and T_S = 300 K.

3.2. Efficiency limit in a quantum converter.

The maximum efficiency for $C = 1$ for an endoreversible converter is around 12%, which is much the below obtained efficiency for real solar cells. This is due to the fact that

semiconductor solar cells are using only a part of the spectrum, but at elevated efficiency. To determine the efficiency in the case of a quantum converter with defined band gap, such as a semiconductor, we must take into account the quantum nature of light-matter interactions in such a system. In such case, the absorbed flux of photons is given by the Kirchoff's law of thermal radiation [27]:

$$dj_{e,abs}(\hbar\omega) = \frac{(\hbar\omega)^3}{4\pi^3\hbar^3c^2} \cdot \frac{a(\hbar\omega)d\Omega}{exp\left(\frac{\hbar\omega}{k_BT}\right) - 1} \cdot d(\hbar\omega) \tag{I.3.25}$$

$a(\hbar\omega)$ is the absorption degree. For a sufficiently thick cell, we assume that $a = 0$ for any $\hbar\omega < E_g$ and $a = 1$ for all other wavelengths. Photons with energy inferior to the band gap are not absorbed by the converter. Photons emitted by the Sun and environment have a chemical potential equal to zero, while photons emitted by the converter have a chemical potential equal to qV. Therefore we obtain:

$$\begin{aligned} j_{e,XY} &= \frac{15\sigma}{2\pi^5} B_{XY} \cdot l_X \cdot T_X^4 \cdot I(n_X) \\ j_{s,XY} &= \frac{15\sigma}{2\pi^5} B_{XY} \cdot l_X \cdot T_X^3 \cdot J(n_X) \end{aligned} \tag{I.3.26}$$

with:

$$n_P = \frac{1}{exp\left(\frac{\hbar\omega}{k_BT_P}\right) - 1} \tag{I.3.27}$$

and:

$$n_S = \frac{1}{exp\left(\frac{\hbar\omega}{k_BT_S}\right) - 1} \tag{I.3.28}$$

as well as:

$$n_C = \frac{1}{exp\left(\frac{\hbar\omega}{k_BT_C}\right) - 1} \tag{I.3.29}$$

upon assuming that $u = \frac{E_g}{kT_P}$, $v = \frac{qV}{kT_S}$ and recalculating equations (I.3.11) and neglecting $\dot{S}_{gen}$ we find the maximum output efficiency:

$$\eta_{max} = \frac{\dot{W}}{P_{in}} = \frac{\left(j_{e,PC} - T_Q j_{s,PC}\right) + \left(j_{e,SC} - T_Q j_{e,SC}\right) - \left(j_{e,CP} - T_Q j_{s,CP}\right) - \left(j_{e,CS} - T_Q j_{s,CS}\right)}{P_{in}} \tag{I.3.30}$$

or incorporating the function G (equation I.3.13) we get:

$$\begin{aligned}\eta_{max} = \frac{15}{\pi^4}\Bigg\{&\left(1 - \frac{4}{3}\cdot q\right)\cdot G_3(u,0) - \frac{q\cdot u^3}{3}\cdot \ln(1-e^{-u}) \\ &+ \left(1 - \frac{C_{max}}{C}\right)\frac{l_S}{l_P}a^4\left[\left(1 - \frac{4}{3}\frac{q}{a}\right)G_3\left(\frac{u}{a},0\right) - \frac{q}{3a}\left(\frac{u}{a}\right)^3 \ln\left(1-e^{-\frac{u}{a}}\right)\right] \\ &- \frac{C_{max}}{C}\frac{l_C}{l_P}b^4\left[\left(1 - \frac{4}{3}\frac{q}{b}\right)G_3\left(\frac{u}{b},\frac{v}{b}\right) - \frac{q}{3b}\left(\frac{u}{b}\right)^3 \ln\left(1-e^{-\frac{v-u}{b}}\right)\right. \\ &\left. + \frac{qv}{b^2}G_3\left(\frac{u}{b},\frac{v}{b}\right)\right]\Bigg\}\end{aligned} \tag{I.3.31}$$

Even more accurate description that includes the degree of polarization and reflectivity for any photon absorbed or emitted by the converter is given by Badescu and Landsberg [28].

We have shown that, quite surprisingly, efficiency of an endoreversible photovoltaic converter under normal, natural irradiation ($C = 1$) is only 11.7%. It has been shown that real solar cells have largely exceeded this value [29]. The difference comes from different mode of conversion employed. In the endoreversible thermodynamical converter the whole spectrum is absorbed and used, while in the photovoltaic converter absorption is selective and only photons with energy $E \geq E_g$ are absorbed and converted, but with different efficiency.

In 1961, Shockley and Queisser first introduced the idea of detailed balance limit analysis for a solar cell [30], by assuming several hypotheses:

- Solar cell is transparent for any photon with energy below the band gap E_g,
- All photons with energy higher or equal to E_g are always absorbed and always create one electron-hole pair,
- Carrier mobility is infinite,
- There are two possible types of recombination: radiative and non-radiative. The parameter ρ is defined as:

$$\rho = \frac{radiative\ recombination\ rate}{total\ recombination\ rate} \tag{I.3.32}$$

In such case, the total current density *J* flowing through a photovoltaic cell is given by the difference between carriers generated by external illumination and recombination inside the cell. The detailed balance equation is then gives as:

$$\frac{J}{e} = j_{n,PC} + j_{n,SC} - R_C \tag{I.3.33}$$

where $j_{n,PC}$ is the number of photons emitted by the pump (Sun) and absorbed by the cell, $j_{n,SC}$ is the number of photons emitted by the sink (Environment) and absorbed by the cell, R_C is the total recombination rate and *e* is elemental charge. In our case we assume the both pump and sink can be considered as black bodies, therefore we obtain:

$$\begin{aligned} j_{n,PC} &= \frac{C}{C_{max}} \cdot \frac{2\pi}{\hbar^3 c^2} k_B^3 T_P^3 \cdot G_2\left(\frac{E_g}{k_B T_P}, 0\right) \\ j_{n,SC} &= \left(1 - \frac{C}{C_{max}}\right) \cdot \frac{2\pi}{\hbar^3 c^2} k_B^3 T_C^3 \cdot G_2\left(\frac{E_g}{k_B T_C}, 0\right) \end{aligned} \tag{I.3.34}$$

Contrary to the endoreversible converter case, the integration is done over $E \in < E_g, \infty >$. Total recombination rate is given by:

$$R_C = \frac{1}{\rho} \cdot j_{n,C} \tag{I.3.35}$$

after generalized Planck's law we obtain:

$$j_{n,C} = \frac{2\pi}{\hbar^3 c^2} k_B^3 T_C^3 \cdot G_2\left(\frac{E_g}{k_B T_C}, \frac{qV}{k_B T_C}\right) \tag{I.3.36}$$

conversion efficiency is then expressed as follows:

$$\eta = \frac{I \cdot V}{\Pi_{in}} \tag{I.3.37}$$

where Π_{in} is expressed as:

$$\Pi_{in} = \frac{C}{C_{max}} \cdot \frac{2\pi}{\hbar^3 c^2} k_B^4 T_P^4 \cdot G_3(0,0) \tag{I.3.38}$$

by substituting $\gamma = \rho \frac{C}{C_{max}}$, we can express the Shockley-Queisser efficiency (SQ) for the case in which the pump and the sink are considered black bodies:

$$\eta_{SQ} = \frac{15}{\pi^4} \cdot \frac{eV}{k_B T_P} \left[G_2\left(\frac{qV}{k_B T_P}, 0\right) - \left(\frac{T_C}{T_P}\right)^3 G_2\left(\frac{E_g}{k_B T_C}, 0\right) - \frac{1}{\gamma}\left(\frac{T_C}{T_P}\right)^3 \left(G_2\left(\frac{E_g}{k_B T_C}, \frac{eV}{k_B T_C}\right) - G_2\left(\frac{E_g}{k_B T_C}, 0\right)\right)\right] \quad \text{(I.3.39)}$$

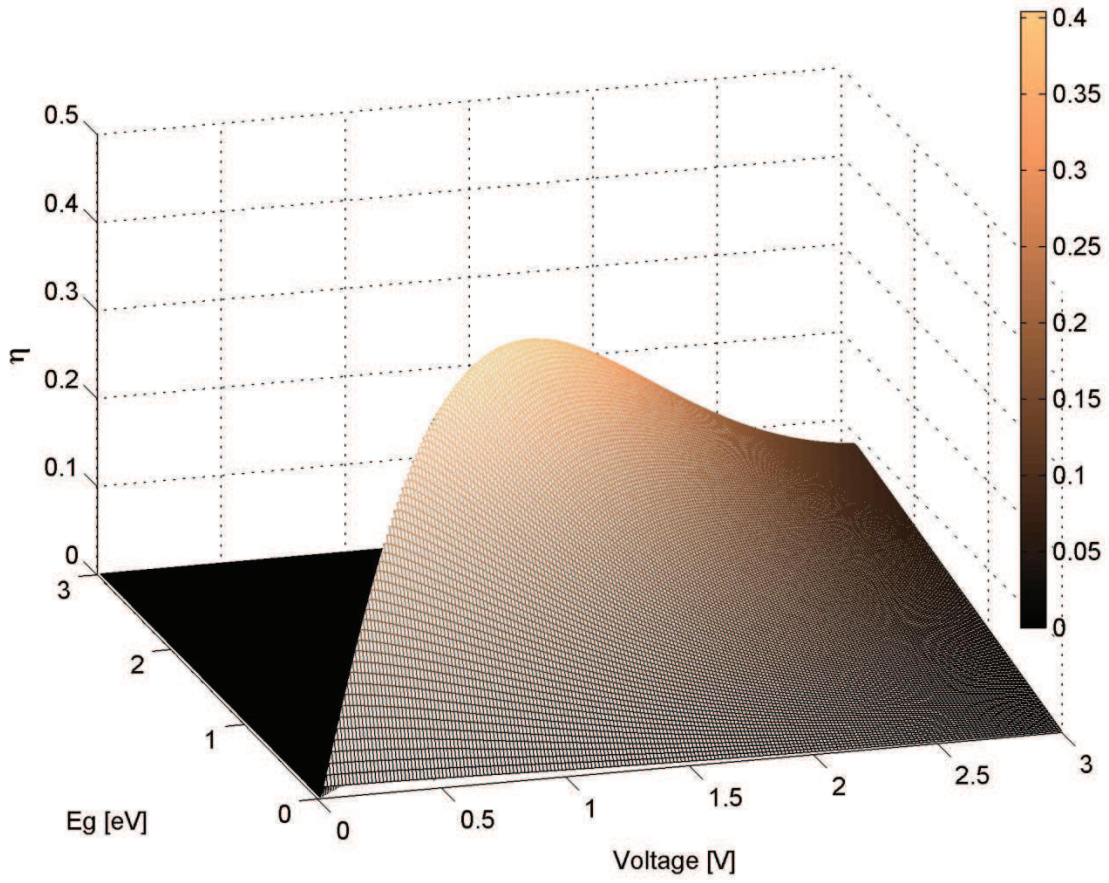

Figure I.14. The photovoltaic efficiency surface $\eta(E_g, V)$. Pump (Sun) at $T_P = 5800$ K, concentration factor $C_{max} = 46000$, radiative efficiency $\rho = 1$, cell temperature $T_C = 300$ K.

The above integrals converge only when $E_g > eV$, which is also consistent with the assumption that $\rho = 1$. For E_g-$eV \approx k_B T_C$, equation (I.3.39) can yield V_{oc} higher than E_g/e, which is obviously incorrect for Boltzmann statistics since the electronic populations are degenerate. Key assumptions are no longer valid; stimulated emission can take place in real material. Estimation of the Shockley-Queisser efficiency limit as a function of band gap energy E_g and applied voltage V is shown in figure I.14.

4. Semiconductor solar converters

The photovoltaic effect, the direct generation of electric power by light in a solid material, was discovered by British scientists: W. G. Adams and his student R. E. Day in the 1870s using selenium. An important breakthrough was made in the 1950s by G. Pearson, D. Chapin, and C. Fuller at Bell Labs. Using silicon, they demonstrated a solar cell of efficiency 5.7%, ten times greater than that of the selenium solar cell. Solar cells first found applications in space. The efficiency of silicon cells has been improved to about 24% in the early 2000s, very close to the theoretical limit of 28%. To date, semiconductor solar cells account for roughly 90% of the market share. Silicon solar cells account for more than 85% of the solar cell market. Thin film solar cells, especially those based on CIGS (copper–indium–gallium–selenide) and CdTe-CdS, are second to silicon solar cells in market share.

4.1. Properties of a p-n junction.

When a *p*-type semiconductor and an *n*-type semiconductor are brought together, a *built-in potential* is established. Because the Fermi level of a *p*-type semiconductor is close to the top of the valence band and the Fermi-level of an *n*-type semiconductor is close to the bottom of the conduction band, there is a difference between the Fermi levels of the two sides. When the two pieces are combined to form a single system, the Fermi levels must be aligned. As a result, the energy levels of the two sides must undergo a shift with a potential V_0. Letting E_{cp} be the energy level of the bottom of the conduction band for the *p*-type semiconductor versus the Fermi level and E_{cn} that for the *n*-type semiconductor, the built-in potential is:

$$qV_0 = E_{cp} - E_{cn} \tag{I.4.1}$$

Because concentration of holes is low in the *n*-region, the holes diffuse from the *p*-region to the *n*-region (so called Fermi pressure). After a number of holes move to the *n*-region, an electrical field is formed to drive the holes back to the *p*-region. At equilibrium, the net current $J_p(x)$ must be zero:

$$J_p(x) = q\left[\mu_p p(x)E_x(x) - D_p\frac{dp(x)}{dx}\right] = 0 \tag{I.4.2}$$

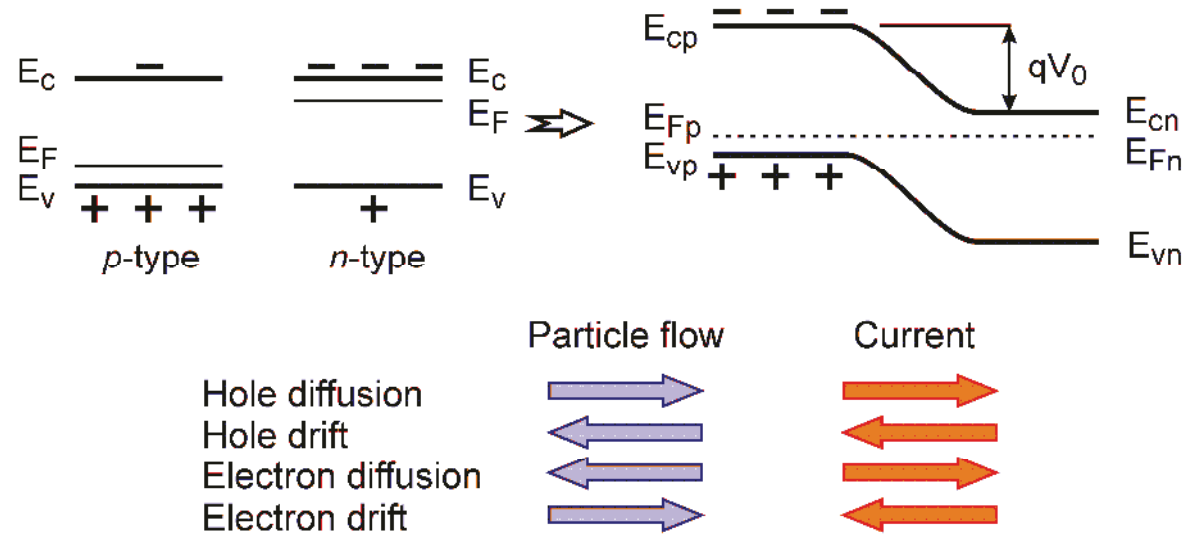

Figure I.15. Formation of a p-n junction. When two pieces of semiconductor are brought together, the Fermi level must align. To achieve this, the holes in the p-side move to the n-side, and electrons on n-side move to the p-side thus forming a double charged layer, until a dynamic equilibrium is established.

where μ_p is the mobility of the holes, $p(x)$ is the concentration of holes as a function of x, $E_x(x)$ is the x-component of electric field intensity as a function of x, and D_p is the diffusion coefficient of the holes. Using Einstein's relation:

$$\frac{D_p}{\mu_p} = \frac{k_B T}{q} \tag{I.4.3}$$

and the relation between the potential $V(x)$ and electric field intensity, $E_x(x) = -dV(x)/dx$, Eq. (I.4.2) becomes:

$$-\frac{q}{k_B T}\frac{dV(x)}{dx} = \frac{1}{p(x)}\frac{dp(x)}{dx} \tag{I.4.4}$$

Integrating Eq. (I.4.4) over the entire transition region yields:

$$-\frac{q}{k_B T}\left(V_n - V_p\right) = \ln\frac{p_n}{p_p} \tag{I.4.5}$$

Since V_n-$V_p = V_0$, therefore we obtain:

$$p_n = p_p exp\left(-\frac{qV_0}{k_B T}\right) \tag{I.4.6}$$

and a similar expression for electrons:

$$n_p = n_n exp\left(-\frac{qV_0}{k_B T}\right) \quad \text{(I.4.7)}$$

A very effective and fairly accurate model is based on the depletion approximation. Under such an approximation, in the p-region near the junction boundary there is a layer of thickness x_p where all the holes are removed and the charge density ρ_p is determined by the density of the acceptors N_A which are negatively charged:

$$\rho_p = -qN_A \quad \text{(I.4.8)}$$

The electrostatic potential Φ in this region is given by the Poisson's equation:

$$\frac{d^2\phi}{dx^2} = \frac{1}{\varepsilon_0} qN_A = -\frac{dE_x}{dx} \quad \text{(I.4.9)}$$

Similarly, there is a slab of thickness x_n where all the free electrons are removed, and the charge density ρ_n is determined by the density of the donors, N_D, which are positively charged:

$$\rho_n = qN_D \quad \text{(I.4.10)}$$

gives:

$$\frac{d^2\phi}{dz^2} = -\frac{1}{\varepsilon_0} qN_D = -\frac{dE_x}{dx} \quad \text{(I.4.11)}$$

The boundary conditions for the p-n junction are as follows; the charge neutrality of the entire transition region requires that:

$$N_D x_n = N_A x_p \quad \text{(I.4.12)}$$

Second, outside the transition region, the electric field should be zero:

$$E_x = 0 \; for \; x \leq -x_p \; and \; x \geq x_n \quad \text{(I.4.13)}$$

Third, the electrostatic potential should match the values at the boundaries of the transition region:

$$\phi = 0, at \; x = -x_p$$
$$\phi = V_0, at \; x = x_n \quad \text{(I.4.14)}$$

The solution to equations (I.4.9), (I.4.11) with boundary conditions (I.4.14) is as follows:

$$E_x = -\frac{qN_A}{\varepsilon_0}(x + x_p), for - x_p \leq x < 0$$
$$E_x = \frac{qN_A}{\varepsilon_0}(x - x_n), for\ 0 < x \leq x_n \quad \text{(I.4.15)}$$

Using the above boundary conditions and the definition of the width of the transition region $W = x_n + x_p$ the following relation is obtained:

$$V_0 = \frac{q}{2\varepsilon_0}\frac{N_A N_D}{N_A + N_D}W^2 \quad \text{(I.4.16)}$$

and from it the transition region W as a function of V_0 can be estimated:

$$W = \sqrt{\frac{2\varepsilon_0 V_0}{q}\left(\frac{1}{N_A} + \frac{1}{N_D}\right)} \quad \text{(I.4.17)}$$

and the junction capacitance:

$$C = \frac{\varepsilon_0}{W} \quad \text{(I.4.18)}$$

The properties and carrier concentration of a *p*-*n* junction change when a bias voltage V is applied. By applying a forward bias, the potential difference across a p-n junction becomes V_0-V. The electron concentration in the p-region, n_p, changes:

$$n_p \rightarrow n_n exp\left(-\frac{q(V_0 - V)}{k_B T}\right) \quad \text{(I.4.19)}$$

Comparing with equation (I.4.6), one finds an excess free-electron concentration at the border of the neutral *p*-region:

$$\delta n_p(x = 0) = n_p\left[exp\left(\frac{qV}{k_B T}\right) - 1\right] \quad \text{(I.4.20)}$$

Similarly, the external forward bias voltage V generates an excess hole concentration at the border of the neutral *n*-region:

$$\delta p_n(x = 0) = p_n\left[exp\left(\frac{qV}{k_B T}\right) - 1\right] \quad \text{(I.4.21)}$$

The excess carrier concentrations generate an excess diffusion current, which is the main part of the forward-bias current of a diode.

Diffusion of excess minority carriers is the origin of junction current. However, there is a competing process which limits the junction current. The excess minority carriers are surrounded by a sea of majority carriers which are constantly courting for recombination. Because the concentration of majority carriers, p_p or n_n, is several orders of magnitude greater than the concentration of excess minority carriers, even with recombination, p_p or n_n is virtually a constant. The rate of decay of excess minority carriers is thus proportional to its concentration, which can be characterized by a lifetime. The combined effect of diffusion and lifetime of the excess minority carriers can be summarized in the following equations. For free electrons:

$$\frac{\partial \delta n_p(x,t)}{\partial t} = -\frac{\delta n_p(x,t)}{\tau_n} + D_n \frac{\partial^2 \delta n_p(x,t)}{\partial x^2} \tag{I.4.22}$$

where D_n is the diffusion coefficient, and τ_n is the lifetime of free electrons. For holes:

$$\frac{\partial \delta p_n(x,t)}{\partial t} = -\frac{\delta p_n(x,t)}{\tau_p} + D_p \frac{\partial^2 \delta p_n(x,t)}{\partial x^2} \tag{I.4.23}$$

where D_p is the diffusion coefficient and τ_p is the lifetime of holes. At equilibrium, the concentration of carriers is independent of time. For example equation (I.4.22) becomes:

$$D_n \frac{d^2 \delta n_p(x)}{dx^2} = \frac{\delta n_p(x)}{\tau_n} \tag{I.4.24}$$

and the calculated diffusion current of electrons is:

$$I_n = qD_n \frac{d\delta n_p(x)}{dx} = q\sqrt{\frac{D_n}{\tau_n}}\delta n_p(x) \tag{I.4.25}$$

At $x = 0$ the junction current of electrons is:

$$I_n(x_p = 0) = -q\sqrt{\frac{D_n}{\tau_n}} n_p \left[exp\left(\frac{qV}{k_B T}\right) - 1\right] \tag{I.4.26}$$

and for holes:

$$I_p(x_n = 0) = q\sqrt{\frac{D_p}{\tau_p}} p_n \left[exp\left(\frac{qV}{k_B T}\right) - 1\right] \tag{I.4.27}$$

The total junction current is then:

$$I = q\left(\sqrt{\frac{D_n}{\tau_n}}n_p + \sqrt{\frac{D_p}{\tau_p}}p_n\right)\left[exp\left(\frac{qV}{k_BT}\right) - 1\right] \quad \text{(I.4.28)}$$

Furthermore, using the approximate relations:

$$p_n = \frac{n_i^2}{N_D}, n_p = \frac{n_i^2}{N_A} \quad \text{(I.4.29)}$$

Equation (I.4.28) can be also expressed as follows:

$$I = qn_i^2\left(\frac{1}{N_A}\sqrt{\frac{D_n}{\tau_n}} + \frac{1}{N_D}\sqrt{\frac{D_p}{\tau_p}}\right)\left[exp\left(\frac{qV}{k_BT}\right) - 1\right] \quad \text{(I.4.30)}$$

Denoting a constant:

$$I_0 = qn_i^2\left(\frac{1}{N_A}\sqrt{\frac{D_n}{\tau_n}} + \frac{1}{N_D}\sqrt{\frac{D_p}{\tau_p}}\right) \quad \text{(I.4.31)}$$

equation (I.4.30) is simplified to the well-known form of the diode equation, also known as the *Shockley* equation:

$$I = I_0\left(exp\left(\frac{qV}{k_BT}\right) - 1\right) \quad \text{(I.4.32)}$$

It is also worth noting that the minimum value of dark current I_0 is given by:

$$I_0 = \frac{q}{k_B}\frac{15\sigma}{\pi^4}T^3\int_u^\infty \frac{x^2}{e^x - 1}dx, u = \frac{E_g}{k_BT} \quad \text{(I.4.32)}$$

4.2. Principles of operation.

A solar cell is an electronic device which converts sunlight directly into electricity. Light shining on the solar cell produces both a current and a voltage to generate electric power. This process requires a material in which the absorption of light raises an electron to a higher energy state and allows the movement of this higher energy electron from the solar cell into an external circuit. Typical silicon solar cells are constructed as follows: the base is a piece of *p*–type silicon, a fraction of a millimeter thick, lightly doped with boron. The emitter is

formed by doping the surface area of the cell (about 1 µm thick) with phosphorous and creating n-type region by compensation. At the border of two regions, a p-n junction is formed, which acts as a membrane separating the electrons and holes [31,32].

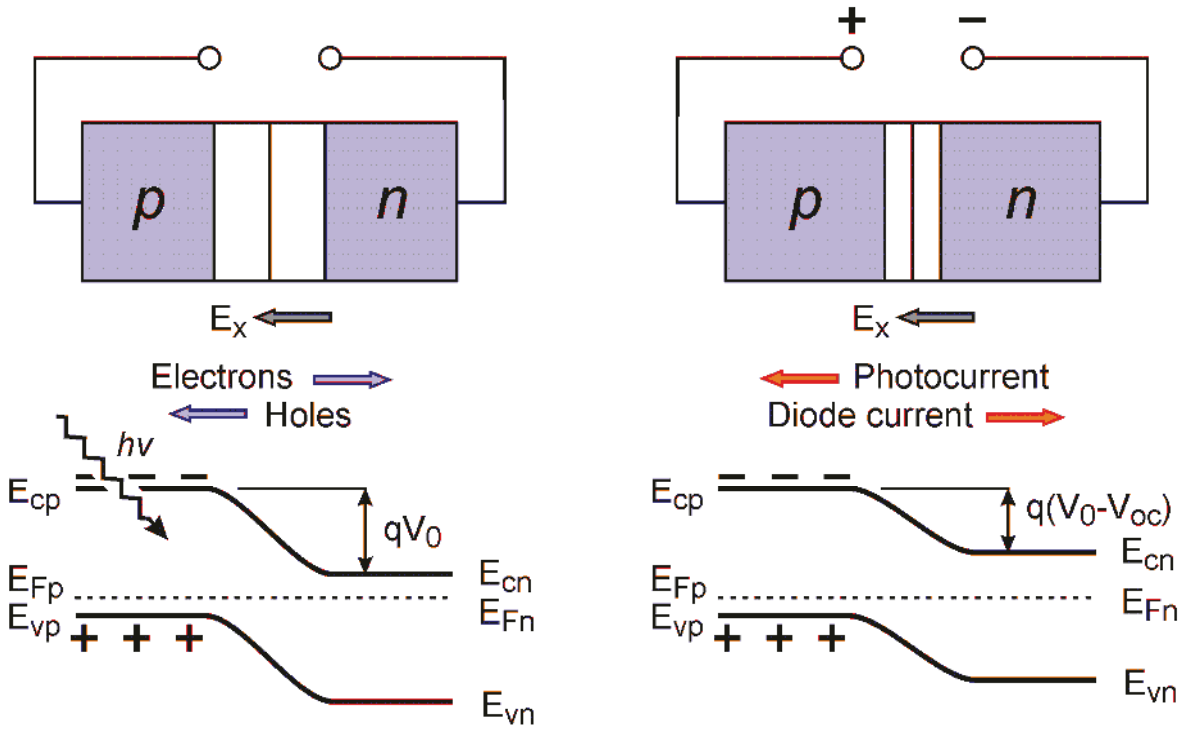

Figure I.16. Separation of holes and electrons in a solar cell. (a) an incident photon is absorbed and generates an electron-hole pair. (b) If the terminals are not connected, the electrons migrate to the n–type region. At equilibrium, an open-circuit voltage is established.

According to the theory of quantum transitions a stream of photons (or radiation) interacts with a semiconductor through absorption or spontaneous emission. A photon with energy greater than the gap energy of the semiconductor material can be absorbed and create an electron–hole pair. An electron–hole pair can recombine and emit a photon of energy roughly equal to the energy gap of the semiconductor. According to the principle of detailed balance the probabilities of the two processes should be equal. This fact has a significant consequence to the efficiency of solar cells.

A typical solar cell can be represented as source of current connected in parallel to a diode. The current source in this case is the photocurrent generated by incident sunlight, and the diode equation (I.4.32) is changed to:

$$I = I_0\left(exp\left(\frac{qV}{kT}\right) - 1\right) - I_{SC} \quad \text{(I.4.33)}$$

which is a fundamental equation for solar cells in a format consistent with the Shockley equation. The open circuit voltage is when the current is zero, is defined by the condition:

$$I_0\left(exp\left(\frac{qV}{kT}\right) - 1\right) = I_{SC} \quad \text{(I.4.34)}$$

V_{oc} is then expressed by following:

$$V_{oc} = \frac{kT}{q}\ln\left(\frac{I_{SC}}{I_0} - 1\right) \quad \text{(I.4.35)}$$

because $I_{sc}/I_0 >> 1$, (I.4.35) can be simplified to:

$$V_{oc} = \frac{kT}{q}\ln\left(\frac{I_{SC}}{I_0}\right) \quad \text{(I.4.36)}$$

The output power of a solar cell is determined by the product of the voltage and current $P = I \cdot V$. The maximum power peak P_{max} occurs for some I_{max} and V_{max} different from I_{SC} and V_{OC}. In general, the condition for maximum power is:

$$dP = IdV + VdI = 0 \quad \text{(I.4.37)}$$

According to the solar cell equation (I.4.33), the output power as a function of the output voltage V is:

$$P = IV = \left[I_{SC} - I_0\left(exp\left(\frac{qV}{kT}\right) - 1\right)\right] \quad \text{(I.4.38)}$$

From figure I.17 we observe that V_{max} is only slightly smaller than V_{OC}. By introducing a voltage offset $v = V_{OC} - V_{max}$, we can simplify equation (I.4.38) to:

$$P \approx I_{SC}(V_{OC} - v)\left(1 - exp\left(-\frac{qV}{kT}\right)\right) \quad \text{(I.4.39)}$$

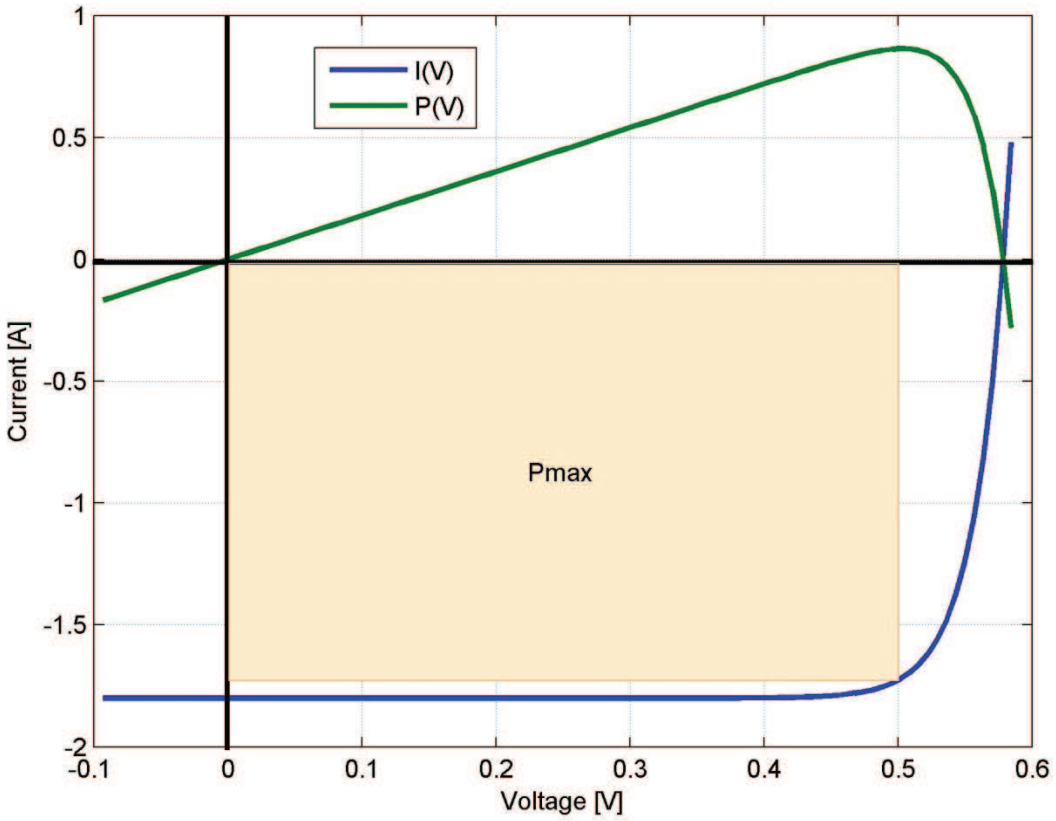

Figure I.17. An example of a current-voltage characteristic described by the Shockley equation. The rectangle determines the maximum power point. Green curve represents power output from the cell.

Taking the derivative of P with respect to v, we obtain:

$$exp\left(\frac{qV}{kT}\right) = 1 + \frac{qV_{OC}}{kT} \tag{I.4.40}$$

with help of equation (I.4.36) we can simplify equation (I.4.39) to:

$$exp\left(\frac{qV}{kT}\right) = 1 + \ln\left(\frac{I_{SC}}{I_0}\right) \tag{I.4.41}$$

Because $I_{SC} >> I_0$, we find:

$$v = \frac{k_B T}{q} \ln\ln\left(\frac{I_{SC}}{I_0}\right) \tag{I.4.42}$$

Therefore the voltage at the maximum power is:

$$V_{max} = V_{OC} - v = V_{OC}\left(1 - \frac{\ln\ln\left(\frac{I_{SC}}{I_0}\right)}{\ln\left(\frac{I_{SC}}{I_0}\right)}\right) \quad \text{(I.4.43)}$$

and the current at maximum power:

$$I_{max} = I_{SC}\left(1 - exp\left(-\frac{qV}{kT}\right)\right) = I_{SC}\left(1 - \frac{1}{\ln\left(\frac{I_{SC}}{I_0}\right)}\right) \quad \text{(I.4.44)}$$

It is easy to see that the maximum power P_{max} is roughly equal to:

$$P_{max} = V_{max}I_{max} = V_{OC}I_{SC}\left(1 - \frac{\ln\ln\left(\frac{I_{SC}}{I_0}\right)}{\ln\left(\frac{I_{SC}}{I_0}\right)}\right) \quad \text{(I.4.45)}$$

The fill factor n_{FF}, is defined as follows:

$$n_{FF} = \frac{V_{max}I_{max}}{V_{OC}I_{SC}} \quad \text{(I.4.46)}$$

Typically, for crystalline Si solar cells the fill factor n_{FF} is 0.8-0.85. In a real device, the ideal characteristic described by equation (I.4.33) is modified to include the series resistance R_s from ohmic loss in the front surface and the shunt resistance R_{sh} from leakage currents. The IV curve for a real device, including both effects is then given by:

$$\ln\left(\frac{I + I_L}{I_0} - \frac{V - IR_s}{I_0R_{sh}} + 1\right) = \frac{q}{nk_BT}(V - IR_s) \quad \text{(I.4.47)}$$

where n is the diode ideality factor, usually ranging from 1 to 2, for Si solar cells.

4.3. Theoretical efficiency limits in Si solar cell.

Introduced in §3.2, the detailed balance limit, first presented by Shockley and Queisser in 1961 [30], allows for a correct treatment of semiconductor solar cells.

The efficiency is defined as the ratio of power delivered to a matching load versus the incident radiation power on the solar cell. Three parameters are involved: the temperature of the pump (Sun), T_P the temperature of the cell, T_C and the energy gap of the semiconductor, E_g. Actually, efficiency only depends on two dimensionless ratios:

$$x_P = \frac{E_g}{kT_P} \tag{I.4.47a}$$

and:

$$x_C = \frac{E_g}{kT_C} \tag{I.4.47b}$$

The assumptions introduced in this approach listed in §3.2 are satisfied by the great majority of conventional solar cells and the limit is well verified by experiments, unless one of the assumptions is explicitly broken, such as in the case of concentrated sunlight or a tandem cell. First we will consider the effect of band gap. Assuming that solar radiation is proportional to black body radiation of temperature T_P the power spectrum on the surface of the Sun is:

$$u(\varepsilon, T_P)d\varepsilon = \frac{2\pi q^4}{c^2h^3}\frac{\varepsilon^3}{exp\left(\frac{\varepsilon}{kT_P}\right)-1}d\varepsilon \tag{I.4.48}$$

At the surface of the Earth, the spectral power density is diluted by a factor f defined as:

$$f = \left(\frac{r_S}{A_S}\right)^2 = 2.15 \cdot 10^{-5} \tag{I.4.49}$$

We assume that all photons with energy above the E_g are absorbed with 100% probability and all photons with energy below E_g are not absorbed at all. This allows us to evaluate the radiative recombination rate ρ introduced earlier. Also, any excess energy above E_g is quickly lost due to thermalization. The power of thus generated electron-hole pairs is expressed by:

$$P_{ep} = \frac{2\pi q^4 E_g f}{c^2h^3}\int_{E_g}^{\infty}\frac{\varepsilon^2 d\varepsilon}{exp\left(\frac{\varepsilon}{kT_P}\right)-1} = \frac{2\pi q^4 f(k_BT_P)^4}{c^2h^3}x_P\int_{x_P}^{\infty}\frac{x^2dx}{e^x-1} \tag{I.4.50}$$

on the other hand, the incident radiation power is:

$$P_P = \frac{2\pi q^4 f}{c^2h^3}\int_0^{\infty}\frac{\varepsilon^3}{exp\left(\frac{\varepsilon}{kT_P}\right)-1}d\varepsilon = \frac{2\pi q^4 f(k_BT_P)^4}{c^2h^3}\frac{\pi^4}{15} \tag{I.4.51}$$

Therefore the efficiency as a function of x_P is defined as follows:

$$\eta_u(x_P) = \frac{P_{ep}}{P_P} = \frac{15}{\pi^4}x_P\int_{x_P}^{\infty}\frac{x^2dx}{e^x-1} \tag{I.4.52}$$

Figure I.18 shows the ultimate efficiency as a function of band gap energy E_g. A qualitative explanation of the result is as follows. If the band gap is small, the range of photon absorption is large. For a large band gap, the range of spectral absorption is reduced.

The ultimate efficiency determines the maximum open-circuit current of a solar cell. If the solar radiation power received by a solar cell is P_S, the power of the electron–hole pairs generated by the solar radiation is $\eta_u P_S$. It corresponds to the maximum short-circuit current of the solar cell:

$$I_{SC} = \frac{q}{E_g}\eta_u P_P \tag{I.4.53}$$

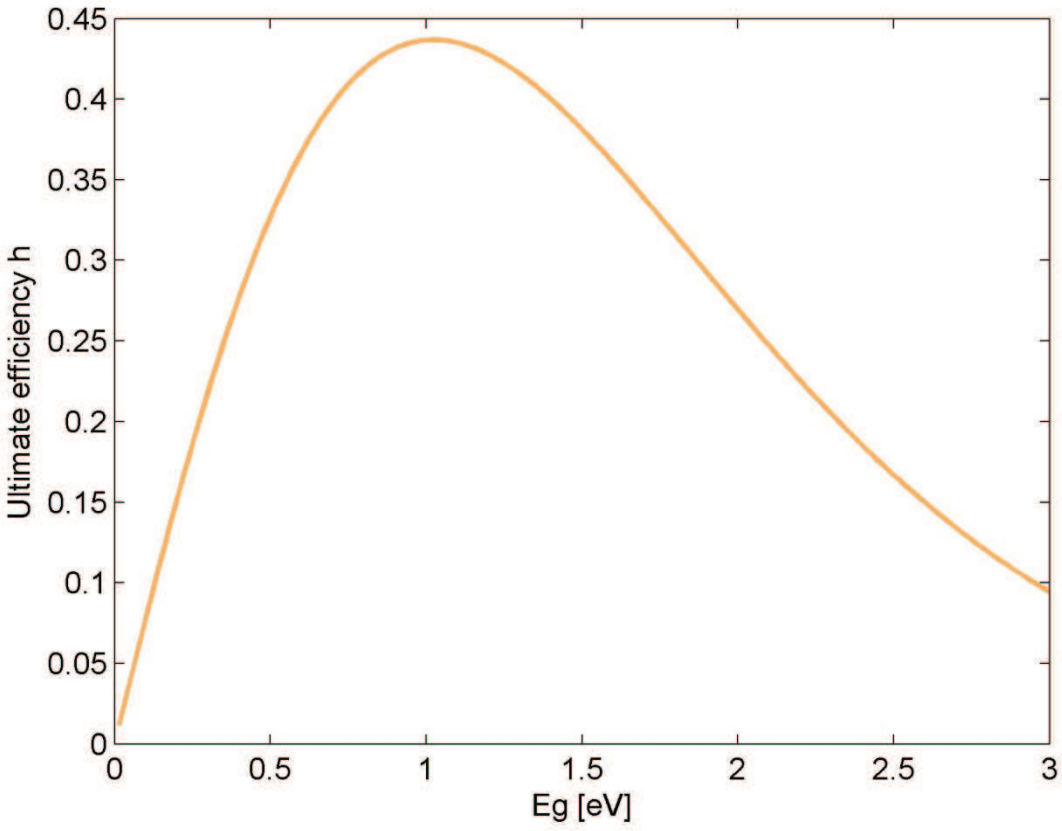

Figure I.18. Ultimate efficiency of solar cells as derived by Shockley and Queisser. The absolute maximum is $\eta_u = 44\%$ for the band gap energy $E_g = 1.1$ eV. For comparison, for crystalline silicon $E_g = 1.12$ eV.

The open-circuit voltage at the terminals of the solar cell is determined by the diode equation (I.4.35). Combining (I.4.35) with equation (I.4.53), we have the nominal power, defined as the product of the short-circuit current and the open-circuit voltage:

$$P_{no} = I_{SC}V_{OC} = \frac{\eta_u(x_P)}{x_P}\ln\left(\frac{I_{SC}}{I_0} - 1\right)P_P \tag{I.4.54}$$

Clearly, the *reverse saturation current* of a *p-n* junction, I_0 is the limiting factor, determined by equation (I.4.31):

$$I_0 = qn_i^2\left(\frac{1}{N_A}\sqrt{\frac{D_n}{\tau_n}} + \frac{1}{N_D}\sqrt{\frac{D_p}{\tau_p}}\right) \tag{I.4.55}$$

The reverse saturation current I_0 can be estimated using actual real semiconductors data. An obvious observation arises from analysis of equation (I.4.55). If the recombination time increases the reverse saturation current I_0 increases, limiting the open-circuit voltage V_{oc}. The role of recombination time was found to be the main limiting factor for a detailed balance treatment. The number of electron–hole pairs generated per unit area per unit time on a surface perpendicular to the sunlight is expressed by the power of the electron–hole pair:

$$F_P = \frac{P_{ep}}{E_g} = \frac{2\pi q^4 f}{c^2h^3}\int_{E_g}^{\infty}\frac{\varepsilon^2 d\varepsilon}{exp\left(\frac{\varepsilon}{kT_P}\right) - 1} \tag{I.4.56}$$

Many factors that contribute to recombination, such as those related to defects or surfaces, can be reduced or avoided. The radiative recombination F_C, however, is a process which sets a fundamental limit on the efficiency of solar cells. The principle of detailed balance requires that the generation rate must equal the recombination rate, which satisfies the Kirchoff's Law. The rate of radiative electron–hole recombination can be calculated using an integral similar to equation (I.4.56) but at the environment temperature T_C:

$$F_{c0} = \frac{2\pi q^4}{c^2h^3}\int_{E_g}^{\infty}\frac{\varepsilon^2 d\varepsilon}{exp\left(\frac{\varepsilon}{kT_C}\right) - 1} \tag{I.4.57}$$

With sunlight, excess carriers are generated, but the change in population is usually significant for minority carriers. For bulk type semiconductor under illumination, the equilibrium electron concentration is changed to:

$$n_p = n_{p0}exp\left(\frac{qV}{kT_C}\right) \tag{I.4.58}$$

Thus the radiative recombination rate is changed to:

$$F_C(V) = F_{c0} exp\left(\frac{qV}{kT_C}\right) \quad \text{(I.4.59)}$$

In a steady state, the rate of electron–hole pair generation must equal the rate of radiative recombination plus the rate of electron consumption due to the current *I* drawn by the external circuit:

$$F_P = F_C(V) + \frac{I}{q} \quad \text{(I.4.60)}$$

By shorting the terminals together, the voltage *V* is zero, and short-circuit current I_{sc} is:

$$I_{SC} = q(F_P - F_{c0}) \quad \text{(I.4.61)}$$

Using equation (I.4.59) the current on the external load *I*, is given as:

$$I = I_{SC} + qF_{c0}\left(1 - exp\left(\frac{qV}{kT_C}\right)\right) \quad \text{(I.4.62)}$$

Defining the reverse saturation current I_0 as

$$I_0 = qF_{c0} \quad \text{(I.4.63)}$$

equation (I.4.62) becomes:

$$I = I_{SC} + I_0\left(1 - exp\left(\frac{qV}{kT_C}\right)\right) \quad \text{(I.4.64)}$$

The open-circuit voltage can be obtained by setting $I = 0$:

$$V_{OC} = \frac{kT_C}{q}\ln\left(\frac{I_{SC}}{I_0} - 1\right) \quad \text{(I.4.65)}$$

Because $F_P >> F_{c0}$, above equation can be simplified to:

$$V_{OC} = \frac{kT_C}{q}\ln\left(\frac{F_P}{F_{c0}} - 1\right) \quad \text{(I.4.66)}$$

Shockley and Queisser defined the nominal efficiency as:

$$\eta_n = \frac{V_{OC}I_{SC}}{P_P} \quad \text{(I.4.67)}$$

nominal efficiency η_n can be expressed as a function of ultimate efficiency η_u and detailed balance efficiency η_d:

$$\eta_n = \eta_u \eta_d \tag{I.4.68}$$

where the η_d is defined as:

$$\eta_d = \frac{qV_{OC}}{E_g} = \frac{1}{x_C} \ln\left(\frac{F_P}{F_{c0}} - 1\right) \tag{I.4.69}$$

Using equation (I.4.56) and (I.4.57), we obtain:

$$x_C = \frac{E_g}{kT_C} 9.45 \tag{I.4.70}$$

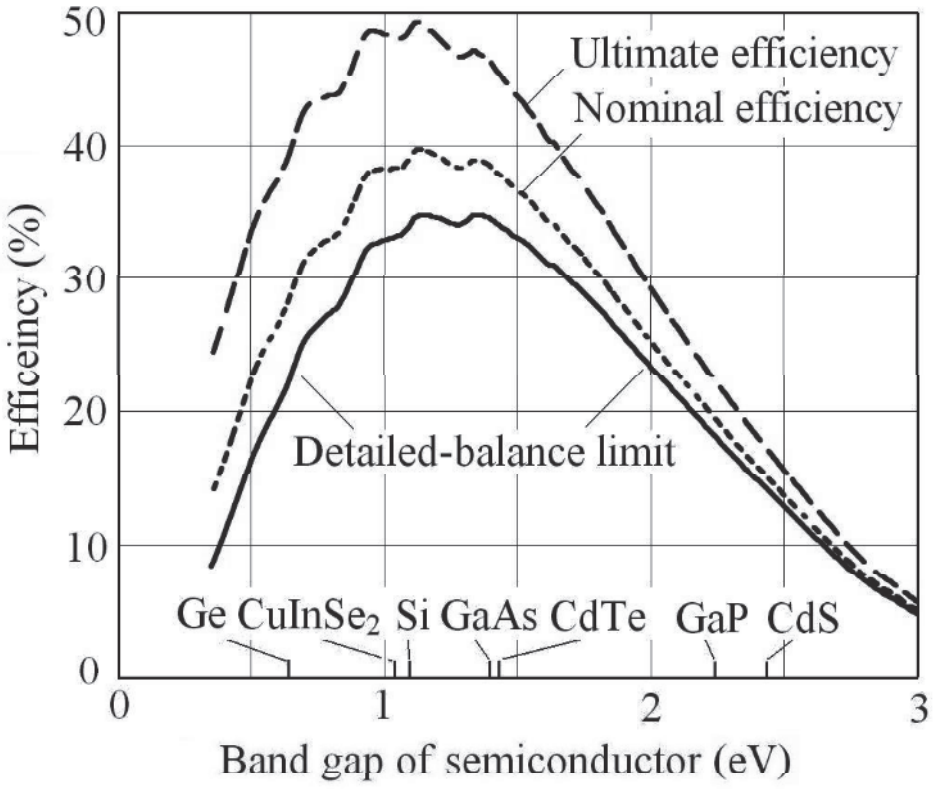

Figure I.19. Shockley-Queisser efficiencies η_u η_d and η_n as a function of band gap energy for AM1.5 spectrum [33]. Several real semiconductors and their band gap energies are marked also.

The detailed balance limit is the ultimate upper limit of the ratio of the open-circuit voltage and the band gap of the semiconductor. It also depends on the temperature of the cell. If $T \rightarrow 0$, $x_C \rightarrow \infty$ and we obtain:

$$\eta_d \rightarrow \frac{1}{x_C} \ln(Ce^{x_C}) \rightarrow \frac{x_C + \ln C}{x_C} \rightarrow 1 \tag{I.4.71}$$

With a load of matched impedance, the output power of a solar cell can be maximized. As was shown before, the maximum power is related to the nominal power by a fill factor n_{FF}:

$$\eta_{SQ} = \eta_u \eta_d n_{FF} \tag{I.4.72}$$

The Shockley-Queisser limit is based solely on the thermodynamics of radiative recombination of electron–hole pairs. There are several other recombination mechanisms and factors that could limit solar-cell efficiency. Some of the factors are intrinsic and others can be mitigated or avoided by a better cell design and manufacturing. The most serious limiting factor to solar cell efficiency is the recombination rate of electrons and holes that affects the opening voltage in the following manner:

$$V_{OC} = const + \frac{kT}{2q} \ln \tau \tag{I.4.73}$$

If there are several recombination processes, the rate is additive, and thus the inverse of the recombination time is additive, leading to even greater decrease in V_{OC}. Some most common recombination processes include:

- Auger recombination - after the creation of an e-h pair, its energy E_g is transferred into either a free electron near the conduction band edge E_C, or a free hole near the valance band edge E_V. Then the excited electron quickly loses its excess energy to the lattice as phonons
- trap-state recombination - the impurities in a semiconductor create states in the energy gap. The gap states are effective intermediate media for a two-step recombination process, therefore the higher the concentration of impurities, the more the gap states, and thus the shorter the electron–hole pair lifetime
- surface recombination - the ultimate defect from the point of view of the crystal periodicity is its surface. It is then justified to expect high density of surface-trap associated states that facilitate recombination of electron-hole pairs.

The other factors limiting the efficiency of a solar cell are for example the metal contacts that further reduce the V_{OC} as well as introduce potential barriers and contact resistance if their work function is not matched exactly with the work function of each side of the cell.
Shockley and Queisser estimated that the maximum efficiency for single-junction solar cells is around $\eta = 29.7\%$.

4.4. Next generation of light-to-electricity converters.

Surpassing the Shockley-Queisser limit was, and still is, a main goal for many solar cell physicists. There are several approaches up to date that all fall into one category of 3rd generations solar cells. Another reason for such high interest in this area is driven by the need of reduction so called efficiency/material ratio. Most solar cells presently on the market are based on silicon wafers, the so-called "first generation" technology. As this technology has matured, costs have become increasingly dominated by material costs, mostly those of the silicon wafer, the strengthened low-iron glass cover sheet, and those of other encapsulants. Recently, the price of silicon wafer has decreased tenfold thanks to increased interest in this particular branch of industry exhibited by Chinese companies. Studies show that if the Si-based photovoltaic market reached 500 MW/year mass production, volume costs would account for over 70% of the total manufacturing costs [34]. This opens up new path for more efficient approaches or material-limiting approaches, such as 2nd generation solar cells. Regardless of semiconductor, thin-films offer prospects for a major reduction in material costs by eliminating the silicon wafer. Thin-films also offer other advantages, particularly the increase in the unit of manufacturing from a silicon wafer (~100 cm^2) to a glass sheet (~1m^2), about 100 times larger. In terms of energy conversion efficiency, thin-film technology so far has not reached the first generation achievements (15%, whereas the announced record for first generation Si solar cell is 25.47% [35]). Nevertheless there have been some spectacular advancements in the field of thin-film manufacturing itself, such as the recent Twin-Creeks Hyperion line dedicated for manufacturing ultra-thin Si films [36]. To progress further, conversion efficiency needs to be increased substantially. The Carnot limit on the conversion of sunlight to electricity is 95% as opposed to the theoretical upper limit of 33% for a standard solar cell, as shown in §4.3. This suggests the performance of solar cells could be improved 2–3 times if different concepts are to be used to produce the 'next generation' of high-performance, low-cost photovoltaic product.

Before we address the problem in detail, we shall analyze different limiting factors and their quantitative influence on the total device performance. Figure I.20 shows efficiency losses in standard solar cell. A key loss is process 1, whereby the photoexcited pair quickly loses energy in excess of the band gap. In this case, a low-energy red photon is just as effective as a much higher energy blue photon. Balancing this loss with the loss of low-energy photons passing straight through the device alone limits conversion efficiency of a cell η_u to about ~44%. Another important loss is recombination of the photoexcited electron–hole pairs (process 4). This can be kept to a minimum by using material with high lifetimes for the photogenerated carriers, ensured by good control of the defects. The lifetime is then determined by radiative recombination in the cell, the inverse to photoexcitation. As shown by Shockley and Queisser in 1961, this symmetry between light absorption and light emission can be used to derive quite fundamental limits on achievable solar cell performance. This approach revisits "black body radiation", the topic that stimulated the birth of quantum mechanics. By relating the light emitted by an ideal cell to that emitted by a blackbody, Shockley and Queisser showed that the performance of a standard cell was limited to η_d~29.7% efficiency for an optimal cell with a band gap E_g = 1.3 eV. This is less than the 44% efficiency previously mentioned since the output voltage of the cell is less than the band gap potential, with the difference made up by voltage drops at the contact and junction (figure I.20).

These drops can be reduced if sunlight is focused to increase the photon density striking the cell. Under the maximum possible sunlight concentration C_{max}, the limiting efficiency increases to 40.8%. However, only direct (non-diffused) sunlight can be efficiently focused in this way. As the efficiency under maximal concentration gives the highest numerical value and also applies to the conversion of direct light even when non-concentrated, this efficiency is a useful figure for comparing the ultimate potential of any given approach. This efficiency is also more directly comparable with results from classical thermodynamics.

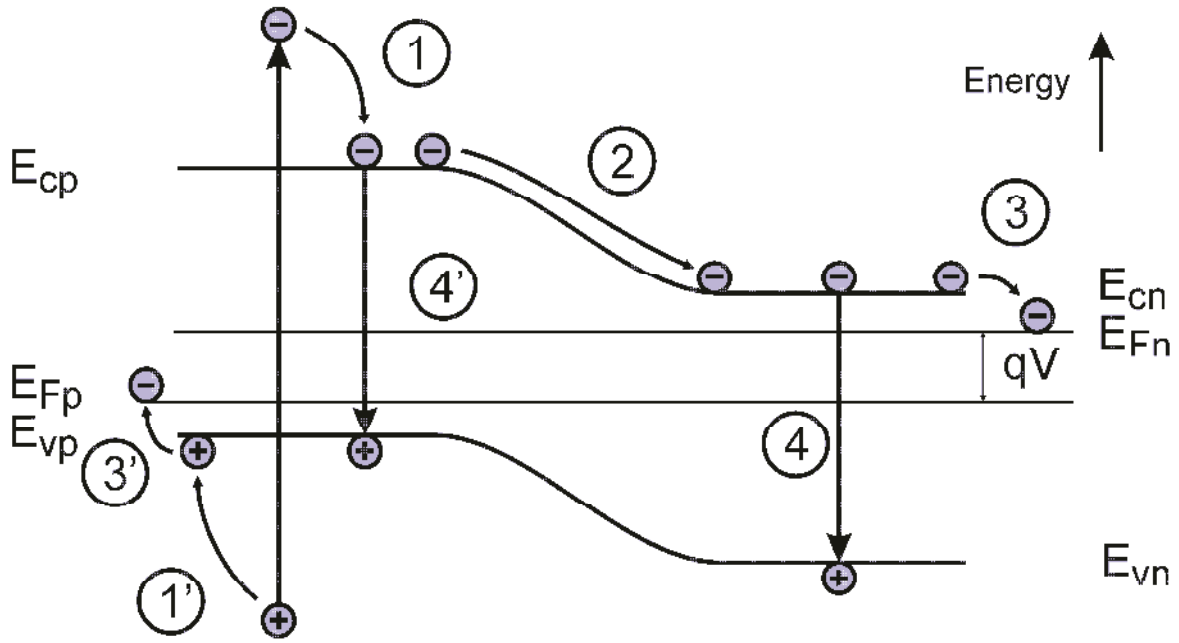

Figure I.20. Loss processes in a standard solar cell: (1) thermalization; (2) and (3) junction and contact voltage; (4) recombination.

The key loss process of recombination (4) can be largely eliminated if the energy of the absorbed photon is just a little higher than the cell band gap. This leads to the tandem cell concept, where multiple cells are used each with a different band gaps and each converting a narrow range of photon energies close to its band gap. Fortunately, just stacking the cells with the highest band gap cell uppermost as in figure I.21, automatically achieves the desired filtering. Under maximum concentration C_{max}, each cell has its proper contribution V_i to total V and W_i to total work W:

$$W_i = \frac{2\pi}{c^2 h^3} eV_i \left[\int_{E_{gi}}^{E_{gi+1}} \frac{(\hbar\omega)^2}{exp\left(\frac{\hbar\omega}{kT_P}\right) - 1} d\hbar\omega + \frac{1}{2} \int_{E_{gi-1}}^{\infty} \frac{(\hbar\omega)^2}{exp\left(\frac{\hbar\omega - qV_{i-1}}{kT_P}\right) - 1} d\hbar\omega \right.$$
$$+ \frac{1}{2} \int_{E_{gi}}^{\infty} \frac{(\hbar\omega)^2}{exp\left(\frac{\hbar\omega - qV_{i+1}}{kT_P}\right) - 1} d\hbar\omega \qquad \text{(I.4.74)}$$
$$\left. - \int_{E_{gi}}^{\infty} \frac{(\hbar\omega)^2}{exp\left(\frac{\hbar\omega - qV_i}{kT_P}\right) - 1} d\hbar\omega \right]$$

Second and third term in above equation result from emission of radiation from cells indexed by *i-1* and *i+1*. In the ideal case, the difference between band gaps approaches 0, and we obtain:

$$dW = \frac{2\pi}{c^2 h^3} eV(E_g) \left[\frac{{E_g}^2}{exp\left(\frac{E_g}{kT_P}\right) - 1} - \frac{{E_g}^2}{exp\left(\frac{E_g - qV}{kT_P}\right) - 1} \right] \quad \text{(I.4.75)}$$

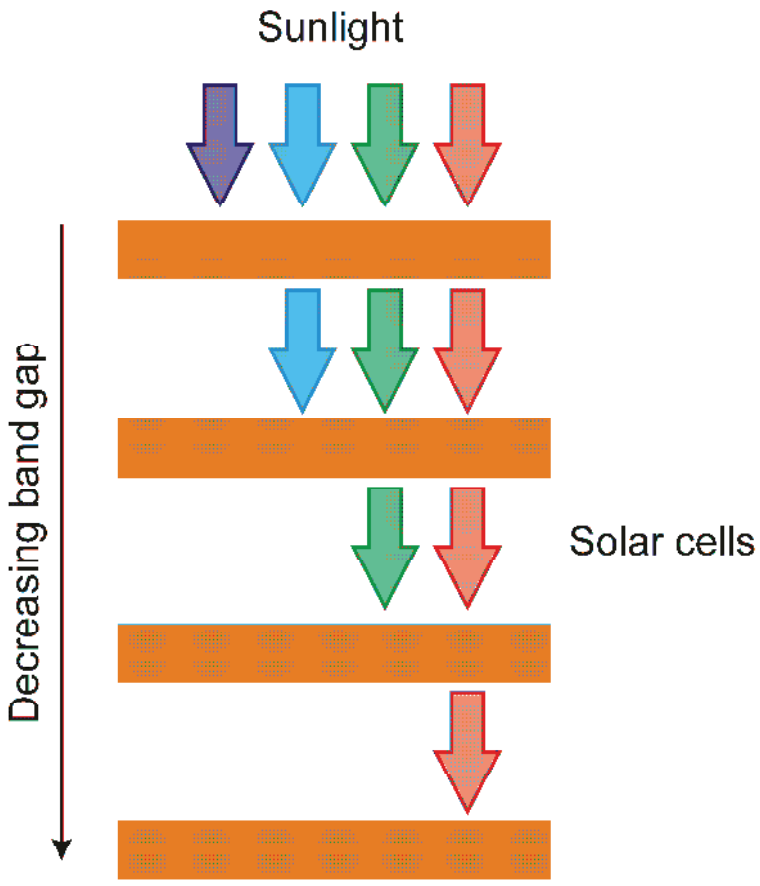

Figure I.21. Stack of different converters forming a tandem cell, where each cell in the stack has lower band gap energy than the previous cell.

Total work is then given by:

$$W = \int_0^\infty dW = \frac{2\pi}{c^2 h^3} e \int_0^\infty V(E_g) \left[\frac{{E_g}^2}{exp\left(\frac{E_g}{kT_P}\right) - 1} - \frac{{E_g}^2}{exp\left(\frac{E_g - qV}{kT_P}\right) - 1} \right] dE_g \quad \text{(I.4.76)}$$

Performance increases as the number of cells in the stack increases, with a direct sunlight conversion efficiency $\eta = 86.8\%$ [37] calculated for an infinite stack of independently operated cells [38].

The independent operation of each cell proves to be technically challenging, therefore in tandem cells the current output from each cell is designed to match with other cells, so the whole stack can be connected in series. This constraint reduces performance and renders the tandem cell extremely sensitive to the spectral content of the sunlight. Tandem cells are now in commercial production with a record efficiency reported to be $\eta = 43.5\%$ for a three-junction solar cell under concentrated light $C = 418$ [39].

A somewhat similar approach is the multiband cell approach, where an additional band is introduced to increase efficiency. The work of *Luque et al*. has shown advantages if a third band, nominally an impurity band, is included in the analysis [40]. This theory has been extended to an n-band cell and additional implementation approaches discussed. These include using excitations between minibands in superlattices, if phonon relaxation processes can be controlled, the use of semiconductors with multiple narrow bands, such as those reported for I–VII and I_3–VI compounds or the use of high concentrations of impurities such as rare earths to form multiple impurity bands in wide band gap semiconductors. The limiting efficiency for an *n*-band cell is identical to the 86.8% figure for a large stack of tandem cells, but it may be more tolerant to spectral variations of sunlight. A realization of an n-band structure can be done with the exploit of multiple-quantum well based solar cells as shown schematically on figure I.22. The excess energy of a high-energy electron–hole pair could be used to create additional carriers as allowed by energy conservation. If the excess energy can be transformed into additional non-equilibrium carriers, instead of being given up as heat, a higher efficiency would be possible. Evidence for the creation of more than one collectable e-h pair by high-energy photons is documented [41], has been attributed to impact ionization by the photoexcited carriers.

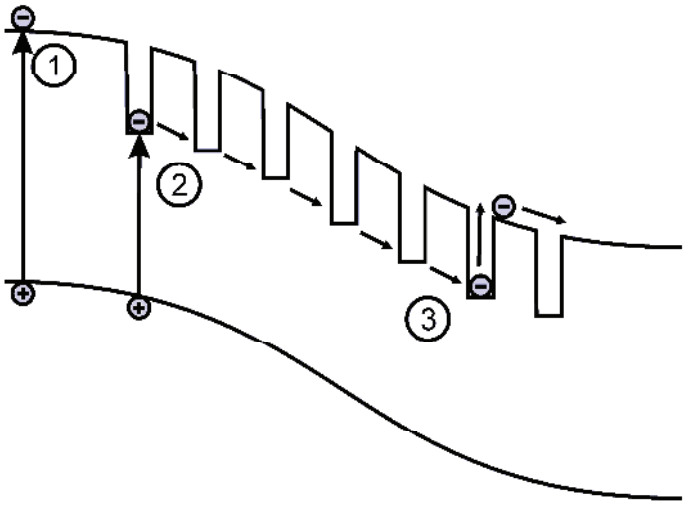

Figure I.22. Concept of multiple quantum well solar cells meeting the constraints of n-band theory.

The group of Brendel [42] calculated the thermodynamic efficiency limit for such cell using the detailed balance treatment. Assuming infinite mobility, perfect absorption and ideal collection, for a device where the multiplication is allowed between *VB→CB* in the whole volume we have:

$$CE(\hbar\omega) = m\left(E_g, m_{max}, \hbar\omega\right) = \begin{cases} m \quad if \quad mE_g \le \hbar\omega \le (m+1)E_g \quad (m = 1, \dots, m_{max} - 1) \\ m_{max} \quad if \quad m_{max}E_g \le \hbar\omega \end{cases} \tag{I.4.77}$$

Where m_{max} is the maximal multiplication. The relation between electron generation and photon absorption is the following:

$$\gamma \leftrightarrow m\left(E_g, m_{max}, \hbar\omega\right)eh \tag{I.4.78}$$

The inverse reaction of multiple recombination would result in photon emission. The energy of such a photon is given by:

$$\mu_\gamma = m\left(E_g, m_{max}, \hbar\omega\right)\mu_{eh} = m\left(E_g, m_{max}, \hbar\omega\right)qV \tag{I.4.79}$$

In this case the total current extracted under maximum concentration C_{max} is given by:

$$\frac{I}{e}=\frac{2\pi}{c^2h^3}\left[\int_{E_g}^{\infty} m\left(E_g,m_{max},\hbar\omega\right)\frac{(\hbar\omega)^2 d\hbar\omega}{exp\left(\frac{\hbar\omega}{kT_P}\right)-1}\right.$$
$$\left.-\int_{E_g}^{\infty} m\left(E_g,m_{max},\hbar\omega\right)\frac{(\hbar\omega)^2 d\hbar\omega}{exp\left(\frac{\hbar\omega-m\left(E_g,m_{max},\hbar\omega\right)qV}{kT_P}\right)-1}\right] \quad \text{(I.4.80)}$$

For maximum concentration and maximum multiplication $m_{max} > 200$ and band gap $E_g = 0.048$ eV the maximal efficiency is $\eta = 85.4\%$. For non-concentrated light and band gap $E_g = 0.758$ eV the maximal efficiency becomes $\eta = 43.6\%$.

In principle, if collisions with lattice can be avoided during the time it takes a photogenerated carrier to traverse the cell; the energy loss associated with process (1), of figure I.20 can be avoided. The various time constants can be appreciated by imagining a direct band gap cell illuminated by a short pulse of monochromatic light ie. laser light. Such a pulse would create electrons in the conduction band and holes in the valence band of distinct energy and momentum. Collisions of these carriers occur in less than a picosecond, tending to smear this distribution. The peaked distributions will become broader and tend towards a Boltzmann type of distribution. Elastic collisions do not change the energy of a population. The temperature distribution of the hot carriers will be determined by the total number of carriers created by the laser pulse and the total energy given to each carrier type. Different temperatures are possible for electrons and holes unless they are efficient in sharing their energy. In the next phase, collisions with lattice atoms become important. These result in energy loss (phonon emission). During this phase, the number of electrons and the number of holes remain constant, but the average energy and carrier temperature decrease due to this loss. The temperature of electrons and holes equalize and both reduce towards that of the host lattice. Finally, recombination in the semiconductor becomes important. The distribution of electrons and holes retain the same general shape, determined by the ambient temperature, but the number of carriers at each energy reduces until finally reaching the levels prior to the laser pulse. A standard cell is designed to collect the carriers before they get too far into the latter recombination stage of this decay sequence. A converter based on hot carrier effects has to catch them before the carrier cooling stage. Carriers either have to traverse the cell very quickly or cooling rates have to be slowed significantly. Special contacts to prevent the

carriers from cooling may also be required. The limiting efficiency of this approach is 86.8% as for an infinite tandem cell stack; however, to reach this limiting efficiency, carrier cooling has to be reduced sufficiently or radiative recombination rates sufficiently have to be accelerated in such a way that the latter was faster than the former. Particular band structure and cell architecture also is required.

References:

[1] D. R. Williams, Sun Fact Sheet, NASA (2004). Retrieved 2010-09-27.

[2] American Society for Testing and Materials (ASTM) Terrestrial Reference Spectra for Photovoltaic Performance Evaluation.

[3] G. Kopp; J. Lean, *A new, lower value of total solar irradiance: Evidence and climate significance,* Geophys. Res. Lett. L, 2011, L01706.

[4] G. B Rybicki, A. P Lightma, *Radiative Processes in Astrophysics*, John Wiley & Sons 1979.

[5] G. Cole, M. Woolfson, *Planetary Science: The Science of Planets Around Stars,* Institute of Physics Publishing, 380–382, 2002, 36–37.

[6] http://solarsystem.nasa.gov/planets.

[7] C. Kandilli and K. Ulgen, *Solar Illumination and Estimating Daylight Availability of Global Solar Irradiance,* Energy Sources 30, 2008, 1127-1140.

[8] http://webelements.com, University of Sheffield.

[9] N. W. Ashcroft, N. D. Mermin, *Solid State Physics*, Saunders College Publishing, 1976.

[10] S. M. Sze, *Physics of semiconductor devices*, John Wiley & Sons 1981.

[11] R. M. Martin, *Electronic Structure. Basic Theory and Practical Methods,* Cambridge University Press 2004.

[12] M. C. Payne, M. P. Teter, D. C. Allan, T. A. Arias, and J. D. Joannopoulos, *Iterative minimization techniques for ab initio total-energy calculations: molecular dynamics and conjugate gradients,* Rev. Mod. Phys. 64, 1992, 1045-1097.

[13] C. Kittel, *Introduction to Solid State Physics*, 7th edition, John Wiley & Sons 1995.

[14] E. Antoncik, *Approximate formulation of the orthogonalized plane-wave method*, J. Phys. Chem Solids 10, 1959, 314-320.

[15] J. C. Phillips, L. K. Kleinman, *Crystal Potential and Energy Bands of Semiconductors. I. Self-Consistent Calculations for Diamond*, Phys. Rev. 116, 1959, 880-884.

[16] P. Hohenberg, W. Kohn, *Inhomogeneous electron gas*, Phys. Rev. 136, 1964, 864-871.

[17] W. Kohn, L. Sham, *Self-Consistent Equations Including Exchange and Correlation Effects*, Phys. Rev. A 140, 1965, 1133.

[18] M. C. Payne, M. P. Teter, D. C. Allan, T. A. Arias, and J. D. Joannopoulos, *Iterative minimization techniques for ab initio total-energy calculations: molecular dynamics and conjugate gradients*, Rev. Mod. Phys. 64, 1992, 1045-1097.

[19] M. Servidori Z. Soulek, S. Solmi, *Some aspects of damage annealing in ion-implanted silicon: Discussion in terms of dopant anomalous diffusion*, J. Appl. Phys. 62, 1987, 1723.

[20] A. de Vos, H. Pauwels, *On thermodynamic limit of photovoltaic energy conversion, Appl. Phys. A Mat. Sci. Eng.* 25, 1981, 119-125.

[21] P. T. Landsberg, G. Tonge, *Thermodynamic energy conversion efficiencies*, J. Appl. Phys. 51, 1980, R1-R20.

[22] P. T. Landsberg ,J. R. Mallinson, *Thermodynamic constraints, effective temperatures and solar cells*, Coll. Int. sur I'Electricitie Solaire (Toulouse: CNES) 1976, 27-35.

[23] P. T. Landsberg, *A note on the thermodynamics of energy conversion in plants*, Photochem. Photobiol. 26, 1977, 313-314.

[24] P. T. Landsberg and P. Baruch, *The thermodynamics of the conversion of radiation energy for photovoltaics*, J. Phys. A: Math. Gen. 22, 1989, 1911-1926.

[25] M. Abramovitz, I. Stegun, *Handbook of mathematical functions*, Dover Publishing 1964.

[26] A. de Vos, P. T. Landsberg, P. Baruch, J. E. Parott, *Entropy fluxes, endoreversibility and solar conversion*, J. Appl. Phys., 74, 1993, 3631-3627.

[27] Kirchhoff, G., *On the relation between the radiating and absorbing powers of different bodies for light and heat*, Philosophical Magazine, 4, 1860, 1-21.

[28] V. Badescu, P.T. Landsberg, *Statistical thermodymamics foundation for photovoltaic and photothermal conversion. II. Application to photovoltaic conversion*, J. Appl. Phys., 78, 1995, 2793-2802.

[29] M. A. Green, K. Emery, Y. Hishikawa, W. Warta, E. D. Dunlop, *Solar cell efficiency tables (version 39)*, Prog. Phot. Res. Appl. 20, 2012, 12-20.

[30] W. Shockiey, H.J. Queisser , *Detailed balance limit of efficiency of p-n junction solar cells*, J.App1 Phys. 32, 1961, 510-519.

[31] Z. T. Kuznicki, *L-H interface improvement for ultra-high-efficiency Si solar cells*, J.App1 Phys. 74, 1993, 2058.

[32] Z. T. Kuznicki, *Low-high homojunction in the stationary state*, J.App1 Phys. 69, 1991, 6526.

[33] L. M. Peter, *Towards sustainable photovoltaics: the search for new materials*, Phil. Trans. R. Soc. A 369, 2011, 1840-1856.

[34] T. M. Bruton, G. Luthardt, K-D. Rasch, K. Roy, I. A. Dorrity, B. Garrard, L. Teale, J. Alonso, U. Ugalde, K. Declerq, J. Nigs, J. Szlufcik, A. Rauber, W. Wettling, A. Vallera, *A study of the manufacture at 500 MWp p.a. of crystalline silicon photovoltaic modules*, Conference Record, 14th EU PVSEC, Barcelona, June, 1997, 11–16.

[35] *Silicon Solar Cell Efficiency World Record Set in Analytical Test by Solar3D*, January 3rd, 2012, CleanTechnica.

[36] Twin-Creeks introduces Hyperion, March 13th, 2012. San Jose, California.

[37] A. de Vos, *Detailed balance limit of the efficiency of tandem solar cells*, J. Phys. D: Appl. Phys., 13, 1980, 839-846.

[38] A. Marti and G. L. Araujo, *Limiting efficiencies for photovoltaic energy conversion in multigap systems*, Sol. Energy Mater. Sol. Cells 43, 1996, 203–222.

[39] *NREL confirms world-record 43.5% efficiency on Solar Junction's CPV cell*, PV Tech, 14 April 2011.

[40] A. Luque, A. Marti, *Increasing the Efficiency of Ideal Solar Cells by Photon Induced Transitions at Intermediate Levels*,Phys. Rev. Lett. 78, 1997, 5014.

[41] O. E. Semonin, J. M. Luther, S. Choi, H.-Y. Chen, J. Gao, A. J. Nozik, M. C. Beard, *Peak external photocurrent quantum efficiency exceeding 100% via MEG in a Quantum Dot Solar Cell*, Science 334, 2011, 1530-1533.

[42] R. Brendel, J. H. Werner, H. J. Queisser, *Thermodynamic efficiency limits for semiconductor solar cells with carrier multiplication*, Sol. En Mater. Sol. Cells, 41/42, 1996, 419-425.

Chapter II

Concept of MIND structures

Contents

Abstract

A theoretical approach to alternative mechanisms for increasing efficiency is described. The concepts of Luque for a cell incorporating intermediate band with a modification for non-radiative inverse Auger recombination are discussed. The fabrication of test structures is briefly mentioned, with key points highlighted. Finally, the working concept of a structure exhibiting non-classical effect is presented.

1. Basic principles and device architecture

An original idea of combining sub-band gap absorption and carrier multiplication was proposed by Kuznicki in the beginning of 1990s. [1, 2]. An increase of photocurrent due to electron multiplication with characteristic energy smaller than the band gap was discussed [3]. We consider a semiconducting material with band gap E_g in which an additional band or levels E_t exist closely below the conduction band (CB). We introduce the value $E_\delta = E_C - E_t$. As opposed to the multi-band cell introduced by Luque [4] supposing a semiconductor with a large band gap, we assume that the transitions between different bands are not always radiative and that the generation of Auger type is possible between an intermediate band and the conduction band. Figure II.1 shows schematically the principle of such process.

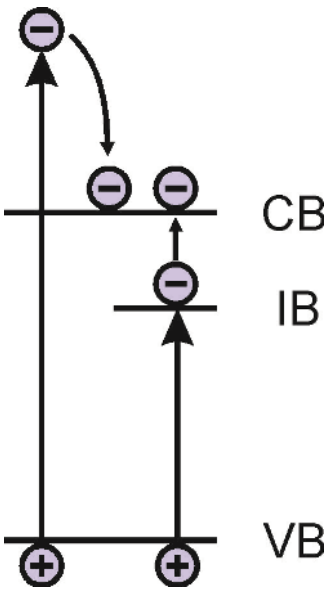

Figure II.1. Principle of operation of the MIND (Multi-interface Novel Device) cell based on carrier multiplication.

Like in the concept of Luque, the transitions between the valence band, the conduction band and impurities can be induced by photon absorption; in our approach we assume that part of those transitions can have a mixed, phonon-photon origin. For each of these radiative generation processes G^R there exist an inverse process of radiative recombination R^R.

In the concept we are presenting here, we suppose that the transitions between the intermediate impurity band and the conduction band can also occur by impact ionization. We introduce a fraction θ of radiative generation between the intermediate impurity band and the conduction band. The value of θ is smaller as the impurity band is farther from CB, due to

lesser photons with correct energy in solar spectrum. We assume that all the excess photon energy above the band gap energy is transferred to an electron. E_δ is the minimum additional energy a carrier must have to trigger the multiplication process. We also assume that there is no multiplication for holes, because their optical mass is much greater (which is the case for Si) and that the entire excess energy is usually transferred to the electron only.

1.1. Theoretical conversion limit

As in the case of other third generation solar cells, we will try to calculate the maximal theoretical efficiency allowed by the laws of thermodynamics. However we will not optimize the band gap of the material, but it will be set to the Si band gap energy E_g = 1.12 eV.
We also associate a respective Fermi level with each of the three bands, which describes their free carrier populations. E_{fC}, E_{fV}, and E_{fI} are the Fermi energies for CB, VB and impurity band (IB). Metallic contacts were optimized only for extraction of holes from VB and electrons from CB. The chemical potential of e-h pairs is then given by:

$$eV = E_{fC} - E_{fV} = \mu_{CV} \qquad \text{(II.1.1)}$$

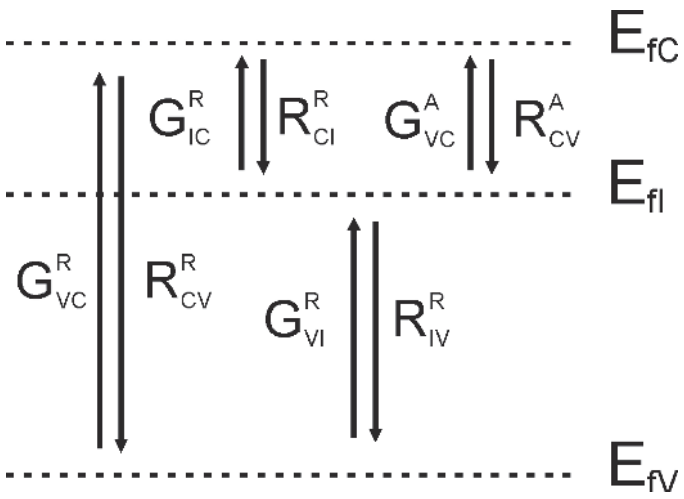

Figure II.2. Radiative and non-radiative transitions in the three band model.

There are two stages to second generation that occur after absorption of a high energy photon:

- *primary generation* of a hot electron by a photon
- *secondary generation* by electron multiplication due to the presence of IB

Absorption of a photon with energy $E \geq E_g+E_\delta$ allows for generation of one secondary electron, $E \geq E_g+2E_\delta$ allows two secondary electrons and so on. The energy E_δ is the characteristic energy of the multiplication process.

We can derive formulas that govern the processes occurring between three different bands, and establish continuity equations for the population of electrons, holes and electrons in the impurity band [4]:

$$\frac{\partial n}{\partial t}(x) = G_{VC}^{R}(x) + \theta G_{IC}^{R}(x) + (1-\theta)G_{IC}^{A}(x) - R_{CV}^{R}(x) - \theta R_{CI}^{R}(x) - (1-\theta)R_{CI}^{A}(x) + \frac{1}{e}\nabla j_n(x) = 0 \quad \text{(II.1.2)}$$

$$\frac{\partial p}{\partial t}(x) = G_{VC}^{R}(x) + G_{VI}^{R}(x) - R_{CV}^{R}(x) - R_{IV}^{R}(x) - \frac{1}{e}\nabla j_p(x) = 0 \quad \text{(II.1.3)}$$

$$\frac{\partial n_I}{\partial t}(x) = \theta R_{CI}^{R}(x) + (1-\theta)R_{CI}^{A}(x) - G_{VI}^{R}(x) - \theta G_{IC}^{R}(x) - (1-\theta)G_{IC}^{A}(x) - R_{IV}^{R}(x) = 0 \quad \text{(II.1.4)}$$

$j_n(x)$ and $j_p(x)$ are current densities for electrons and holes respectively. R is the index designating the radiative processes and A is the index designating the Auger process (impact ionization of IB or Auger recombination), n is the electron density in CB and p is hole density in VB. n_I is the number of occupied states in the IB. All these phenomena are shown in Figure II.2.

By introducing the parameter θ one can generalize the models introduced by Luque ($\theta = 1$) and Brendel [5] ($\theta = 0$, equating $E_\delta = E_g$). If NI is the total number of states in the IB, the number of the secondary generation centers is given by:

$$\rho(x) = e\big(p(x) - n(x) + N_I - n_I(x)\big) = 0 \quad \text{(II.1.5)}$$

for donors, and:

$$\rho(x) = e\big(p(x) - n(x) - n_I(x)\big) = 0 \quad \text{(II.1.6)}$$

for acceptors. The quasi-Fermi energy levels allow us to write the following relations [6]:

$$np = n_0 p_0 \exp\left(\frac{\mu_{CV}}{kT_C}\right) \quad \text{(II.1.7)}$$

$$n = n_0 \exp\left(\frac{\mu_{CI}}{kT_C}\right) \quad \text{(II.1.8)}$$

$$p = p_0 \exp\left(\frac{\mu_{IV}}{kT_C}\right) \quad \text{(II.1.9)}$$

where n_0, n_{I0} and p_0 are the populations in the dark when all three quasi-Fermi levels meet and are equal to the E_F.

The ratio of primary generation is proportional to the number of absorbed photons that excite electrons from VB to CB:

$$G_{VC}^{R}(x) = \frac{2\pi}{c^2h^3}\sin^2\nu \cdot \int_{E_g}^{\infty} g(\hbar\omega, x)CE(x)\frac{(\hbar\omega)^2}{\exp\left(\frac{\hbar\omega}{kT_P}\right)-1}d\hbar\omega \quad \text{(II.1.10)}$$

where ν is the angle corresponding to the concentration $0.266° < \nu < 90°$ and CE is the Collection Efficiency, which defines the probability with which a pair of generated carriers in a given point in space will be collected in an external circuit. Radiative recombination between CB and VB can be derived with the generalized Planck's law:

$$R_{VC}^{R}(x) = r_{CV}np = \frac{2\pi}{c^2h^3}\int_{E_g}^{\infty} g(\hbar\omega, x)CE(x)\frac{(\hbar\omega)^2}{\exp\left(\frac{\hbar\omega - qV}{kT_C}\right)-1}d\hbar\omega \quad \text{(II.1.11)}$$

r_{CV} is the coefficient of radiative recombination that can be deduced by analyzing detailed balance for a solar cell in the dark, when there is no current extracted from the cell, and under illumination for $T_C = T_E$. In the latter case, we have a unique Fermi level ε_F:

$$G_{VC0}^{R}(x) = \frac{2\pi}{c^2h^3}\int_{E_g}^{\infty} g(\hbar\omega, x)CE(x)\frac{(\hbar\omega)^2}{\exp\left(\frac{\hbar\omega}{kT_C}\right)-1}d\hbar\omega \quad \text{(II.1.12)}$$

$$r_{CV} = \frac{G_{VC0}^{R}}{n_i^2} \quad \text{(II.1.13)}$$

$$R_{VC}^{R}(x) \approx G_{VC0}^{R}\frac{np}{n_i^2} = G_{VC0}^{R}\exp\left(\frac{qV}{kT_C}\right) \quad \text{(II.1.14)}$$

Equation (II.1.14) represents an approximation to the exact formula (equation II.1.12). In the same manner, we describe radiative transitions between VB and IB and between CB and IB:

$$G_{VI}^{R}(x) = \frac{2\pi}{c^2h^3}\sin^2\nu\int_{E_g-E_\delta}^{E_a} g(\hbar\omega, x)CE(x)\frac{(\hbar\omega)^2}{\exp\left(\frac{\hbar\omega}{kT_P}\right)-1}d\hbar\omega \quad \text{(II.1.15)}$$

$$G_{IC}^{R}(x) = \frac{2\pi}{c^2h^3}\sin^2\nu\int_{E_\delta}^{E_b} g(\hbar\omega, x)CE(x)\frac{(\hbar\omega)^2}{\exp\left(\frac{\hbar\omega}{kT_P}\right)-1}d\hbar\omega \quad \text{(II.1.16)}$$

We assume that an energetic photon will induce the highest radiative transition possible. Therefore we can distinguish two cases:

$$E_\delta < \frac{E_g}{2}: E_a = E_g \quad \text{and} \quad E_b = E_g - E_\delta \quad \text{(II.1.17)}$$

$$E_\delta > \frac{E_g}{2}: E_a = E_\delta \quad \text{and} \quad E_b = E_g \quad \text{(II.1.18)}$$

The term describing radiative recombination between IB and VB is expressed by:

$$R_{IV}^{R}(x) = r_{IV} n_I p = \frac{2\pi}{c^2 h^3} \int_{E_g - E_\delta}^{E_a} g(\hbar\omega, x) CE(x) \frac{(\hbar\omega)^2}{\exp\left(\frac{\hbar\omega - \mu_{IV}}{kT_C}\right) - 1} d\hbar\omega \quad \text{(II.1.19)}$$

$$R_{CI}^{R}(x) = r_{CI} n(N_I - n_I) = \frac{2\pi}{c^2 h^3} \int_{E_\delta}^{E_b} g(\hbar\omega, x) CE(x) \frac{(\hbar\omega)^2}{\exp\left(\frac{\hbar\omega - \mu_{IC}}{kT_C}\right) - 1} d\hbar\omega \quad \text{(II.1.20)}$$

The yield of secondary generation is proportional to the number of absorbed photons having excess energy $\hbar\omega \geq E_g + E_\delta$ and is given as an integral over secondary generation terms:

$$G_{CI}^{A}(x) = \frac{2\pi}{c^2 h^3} \sin^2 \nu \int_{E_g + E_\delta}^{\infty} d(\hbar\omega, x) g(\hbar\omega, x) CE(x) \frac{(\hbar\omega)^2}{\exp\left(\frac{\hbar\omega}{kT_P}\right) - 1} d\hbar\omega \quad \text{(II.1.21)}$$

$d(\hbar\omega,x)$ represents the average number of secondary electrons generated by a hot electron created by a photon with the energy $\hbar\omega$ between x and $x+dx$. We introduce the probability σ_k of generation of a k^{th} secondary electron by a hot electron that has already generated k-1 secondary electrons. We then have for m = 1,2,…:

$$d(\hbar\omega, x) = \sigma_1 + \sigma_1\sigma_2 + \cdots + \sigma_1 \cdot \ldots \cdot \sigma_{max} \; if \; E_g + mE_\delta \leq \hbar\omega \leq E_g + (m+1)E_\delta \quad \text{(II.1.22)}$$

In general, we have $\sigma_1 \geq \sigma_2 \geq \sigma_3 \geq \ldots$

If the probability of secondary generation is independent of stage (i.e., whether it is the second, third, fourth etc.) the probability is constant and equal to σ. Therefore we obtain:

$$d(\hbar\omega, x) = \sum_{i=1}^{m} \sigma^i \; if \; E_g + mE_\delta \leq \hbar\omega \leq E_g + (m+1)E_\delta \quad \text{(II.1.23)}$$

$$G_{CI}^{A}(x) = \frac{2\pi}{c^2 h^3} \sin^2 \nu \sum_{m=1}^{\infty} \int_{E_g + mE_\delta}^{E_g + (m+1)E_\delta} \left(\sum_{i=1}^{m} \sigma^i \right) g(\hbar\omega, x) CE(x) \frac{(\hbar\omega)^2}{\exp\left(\frac{\hbar\omega}{kT_P}\right) - 1} d\hbar\omega \quad \text{(II.1.24)}$$

which could be also presented as follows:

$$G_{CI}^{A}(x) = \frac{2\pi}{c^2 h^3} \sin^2 \nu \sum_{i=1}^{m} \left[\sigma^i \int_{E_g + iE_\delta}^{\infty} g(\hbar\omega, x) CE(x) \frac{(\hbar\omega)^2}{\exp\left(\frac{\hbar\omega}{kT_P}\right) - 1} \right] d\hbar\omega \quad \text{(II.1.25)}$$

We have the following relation: $d(\hbar\omega,x) = \beta(\hbar\omega) n_I^m(x)$, where β is the coefficient of secondary generation proportional to $n_\delta^{-m/2}$ [7]. In the ideal case (σ= 1), we have: $d(\hbar\omega,x) = m$, if $E_g + mE_\delta \leq \hbar\omega \leq E_g + (m+1)E_\delta$. However, for hot carriers generated in the zone without multiplication, we have $d(\hbar\omega,x) = 0$.

The inverse mechanism is the sum of non-radiative recombination mechanisms of Auger type between the valence band and the impurity band. For reversibility reasons in the energy interval $<E_g+mE_\delta;\ E_g+(m+1)E_\delta>$, we assume that the number of electrons from the CB participating in the process is n^m and that $(N_I-n_I)^m$ empty states are in the IB. We can therefore write:

$$R_{CI}^A(x) = \sum_{m=1}^{\infty} \int_{E_g+mE_\delta}^{E_g+(m+1)E_\delta} r_{CI}(\hbar\omega) n^{m+1} (N_I + n_I)^m \, d\hbar\omega \tag{II.1.26}$$

As for the radiative terms, the calculation of $r_{CI}(\hbar\omega)$ is done for the relation $R_{CI}^A = G_{CI}^A$ in the dark for an initial photon energy given by $E_g+mE_\delta \leq \hbar\omega \leq E_g+(m+1)E_\delta$:

$$r_{CI}(\hbar\omega) n_0^{m+1} (N_I + n_{I0})^m = d\hbar\omega \frac{2\pi}{c^2 h^3} g(\hbar\omega, x) CE(x) \frac{(\hbar\omega)^2}{\exp\left(\frac{\hbar\omega}{kT_C}\right)} \tag{II.1.27}$$

$$r_{CI}(\hbar\omega) = \frac{d\hbar\omega}{n_0^{m+1}(N_I + n_{I0})^m} \frac{2\pi}{c^2 h^3} g(\hbar\omega, x) CE(x) \frac{(\hbar\omega)^2}{\exp\left(\frac{\hbar\omega}{kT_C}\right)} \tag{II.1.28}$$

$$r_{CI}(\hbar\omega) = \beta(\hbar\omega) \frac{n_{I0}^m}{n_{I0}^m (N_I + n_{I0})^m} \frac{1}{n_0} \frac{2\pi}{c^2 h^3} g(\hbar\omega, x) CE(x) \frac{(\hbar\omega)^2}{\exp\left(\frac{\hbar\omega}{kT_C}\right)} \tag{II.1.29}$$

Keeping in mind that:

$$\frac{n_{I0}^m}{(N_I + n_{I0})^m} = \left[\exp\left(\frac{\varepsilon_F - E_t}{kT_C}\right)\right]^m \text{ and } n_0^m = \left[N_C \exp\left(\frac{\varepsilon_F - E_C}{kT_C}\right)\right]^m \tag{II.1.30}$$

As a consequence:

$$r_{CI}(\hbar\omega) \sim \exp\left(\frac{E_\delta}{kT_C}\right) \tag{II.1.31}$$

Therefore:

$$R_{CI}^A(x) = \sum_{m=1}^{\infty} \int_{E_g+mE_\delta}^{E_g+(m+1)E_\delta} d(\hbar\omega, x) \frac{n^{m+1}(N_I + n_I)^m}{n_0^{m+1}(N_I + n_{I0})^m} \frac{2\pi}{c^2 h^3} g(\hbar\omega, x) CE(x) \frac{(\hbar\omega)^2}{\exp\left(\frac{\hbar\omega}{kT_C}\right)} d\hbar\omega \tag{II.1.32}$$

Supposing that the density of states in the intermediate band is large enough that its quasi-Fermi density does not change under illumination, we have:

$$(N_I + n_{I0}) = (N_I + n_I) \tag{II.1.33}$$

We obtain:

$$R_{CI}^{A}(x) =$$

$$\frac{2\pi}{c^2h^3}\sum_{m=1}^{\infty}\int_{E_g+mE_\delta}^{E_g+(m+1)E_\delta}\sum_{i=1}^{m}\sigma^i\exp\left(\frac{(m+1)\mu_{CI}}{kT_C}\right)g(\hbar\omega,x)CE(x)\frac{(\hbar\omega)^2}{\exp\left(\frac{\hbar\omega}{kT_C}\right)}d\hbar\omega \quad \text{(II.1.34)}$$

The current density traversing the cell is given by detailed balance:

$$I = e\int_0^W\Big(G_{VC}^{R}(x)+\theta G_{IC}^{R}(x)+(1-\theta)G_{IC}^{A}(x)-R_{CV}^{R}(x)-\theta R_{CI}^{R}(x)- (1-\theta)R_{CI}^{A}(x)\Big)dx \quad \text{(II.1.35)}$$

Therefore, the current is given as a difference between the generation and recombination currents going through the cell in opposite directions:

$$I = I_{GEN} - I_{REC} \quad \text{(II.1.36)}$$

with:

$$\frac{I_{GEN}}{e} = \frac{2\pi}{c^2h^3}\int_{E_g}^{\infty}IQE_{VC}(\hbar\omega)\frac{(\hbar\omega)^2}{\exp\left(\frac{\hbar\omega}{kT_P}\right)-1}d\hbar\omega + \theta\frac{2\pi}{c^2h^3}\int_{E_\delta}^{E_g}IQE_{IC}(\hbar\omega)\frac{(\hbar\omega)^2}{\exp\left(\frac{\hbar\omega}{kT_P}\right)-1}d\hbar\omega + (1-\theta)\frac{2\pi}{c^2h^3}\int_{E_g+E_\delta}^{\infty}IQE_{IC}^{A}(\hbar\omega)\frac{(\hbar\omega)^2}{\exp\left(\frac{\hbar\omega}{kT_P}\right)-1}d\hbar\omega \quad \text{(II.1.37)}$$

$$\frac{I_{REC}}{e} =$$

$$\frac{2\pi}{c^2h^3}\int_{E_g}^{\infty}IQE_{VC}(\hbar\omega)\frac{(\hbar\omega)^2}{\exp\left(\frac{\hbar\omega-qV}{kT_C}\right)-1}d\hbar\omega + \theta\frac{2\pi}{c^2h^3}\int_{E_\delta}^{E_g}IQE_{IC}(\hbar\omega)\frac{(\hbar\omega)^2}{\exp\left(\frac{\hbar\omega-\mu_{CI}}{kT_C}\right)-1}d\hbar\omega + (1-\theta)\frac{2\pi}{c^2h^3}\int_{E_g+E_\delta}^{\infty}IQE_{IC}^{A}(\hbar\omega)\exp\left(\frac{(d(\hbar\omega,x)+1)\mu_{CI}}{kT_C}\right)\frac{(\hbar\omega)^2}{\exp\left(\frac{\hbar\omega}{kT_C}\right)-1}d\hbar\omega \quad \text{(II.1.38)}$$

We have therefore defined the Internal Quantum Efficiency (IQE):

$$IQE_{CV}(\hbar\omega) = \int_{E_g}^{\infty} g(\hbar\omega, x)CE(x) \tag{II.1.39}$$

$$IQE_{IC}(\hbar\omega) = \int_{E_\delta}^{E_g} g(\hbar\omega, x)CE(x) \tag{II.1.40}$$

$$IQE_{IC}^{A}(\hbar\omega) = \int_{E_g+E_\delta}^{\infty} g(\hbar\omega, x)CE(x) \tag{II.1.41}$$

In the ideal case the following conditions are realized;

- collection of photogenerated carriers is perfect: $CE(x) = 1$
- the thickness of the cell is large enough to allow total absorption of the incident light, $\int_0^W g(\hbar\omega, x)\, dx = 1$
- light concentration is maximal $C_{max} = \pi/2$
- multiplication is possible in the whole cell with the maximal probability, $\sigma = 1$.

$$d(\hbar\omega, x) = m \;\; if \; E_g + mE_\delta \leq \hbar\omega \leq E_g + (m+1)E_\delta \tag{II.1.42}$$

Indeed, for the ideal case we have:

$$IQE_{CV}(\hbar\omega) = 1 \tag{II.1.43}$$

$$IQE_{IC}(\hbar\omega) = 1 \tag{II.1.44}$$

$$IQE_{IC}^{A}(\hbar\omega) = m \quad if \quad E_g + mE_\delta \leq \hbar\omega \leq E_g + (m+1)E_\delta \tag{II.1.45}$$

We can estimate the energy converted by the multiplication:

$$E_{conv} = FF_{max}E_g N_{prim} + E_{sec} \tag{II.1.46}$$

where N_{prim} is the number of primary electrons corresponding to the number of absorbed photons. In the above conditions we have:

$$N_{prim} = \frac{2\pi}{c^2h^3} \int_{E_g}^{\infty} IQE_{CV}(\hbar\omega) \frac{(\hbar\omega)^2}{\exp\left(\frac{\hbar\omega}{kT_P}\right) - 1} d\hbar\omega \tag{II.1.47}$$

E_{sec} is the energy used for the secondary generation, which would normally be lost to heat:

$$E_{sec} = E_\delta \frac{2\pi}{c^2h^3} \int_{E_g}^{\infty} IQE_{IC}^{A}(\hbar\omega) \frac{(\hbar\omega)^2}{\exp\left(\frac{\hbar\omega}{kT_P}\right) - 1} d\hbar\omega \tag{II.1.48}$$

E_{sec} is non-linearly dependent on the energy E_{δ}. The open circuit voltage is taken as a parameter varying between 0 and E_g. We have the following relation between the fill factor and the open and circuit voltage [8]:

$$FF \approx \frac{\frac{qV_{OC}}{kT_C} - \ln\left(1 + \frac{qV_{OC}}{kT_C}\right)}{1 + \frac{qV_{OC}}{kT_C}} \; and \; FF_{max} \approx \frac{\frac{qE_g}{kT_C} - \ln\left(1 + \frac{qE_g}{kT_C}\right)}{1 + \frac{qE_g}{kT_C}} = 89\% \tag{II.1.49}$$

In such a case, the convertible energy is given by:

$$E_{sec} = E_{\delta}\frac{2\pi}{c^2h^3}\int_{E_g}^{\infty} IQE_{IC}^{A}(\hbar\omega)\frac{(\hbar\omega)^2}{\exp\left(\frac{\hbar\omega}{kT_P}\right) - 1}d\hbar\omega \tag{II.1.50}$$

Obviously this approximation represents only a very generic efficiency limit. To obtain more accurate representation of the secondary generation problem, one must turn to the detailed balance method, taking into account all the recombination and generation currents in the cell and the energy of absorbed photons. The generation current was discussed by Kuznicki and others in 1988 [9], for threshold energies greater than the band gap. A detailed study on this problem was conducted by Marc Ley and is presented in his thesis [10].

A final formula describing the maximum efficiency is then:

$$\eta = \frac{15}{\pi^4}\frac{eV}{k^4T_P^4}\left[\int_{E_g}^{\infty} IQE_{CV}(\hbar\omega)\frac{(\hbar\omega)^2}{\exp\left(\frac{\hbar\omega}{kT_P}\right)-1}d\hbar\omega + \theta\int_{E_\delta}^{E_g} IQE_{IC}(\hbar\omega)\frac{(\hbar\omega)^2}{\exp\left(\frac{\hbar\omega}{kT_P}\right)-1}d\hbar\omega + (1-\theta)\int_{E_g+E_\delta}^{\infty} IQE_{IC}^{A}(\hbar\omega)\frac{(\hbar\omega)^2}{\exp\left(\frac{\hbar\omega}{kT_P}\right)-1}d\hbar\omega\right] +$$

$$\frac{15}{\pi^4}\frac{eV}{k^4T_P^4}\left(\frac{1}{\sin^2 v}-1\right)\left[\int_{E_g}^{\infty} IQE_{CV}(\hbar\omega)\frac{(\hbar\omega)^2}{\exp\left(\frac{\hbar\omega}{kT_C}\right)-1}d\hbar\omega + \theta\int_{E_\delta}^{E_g} IQE_{IC}(\hbar\omega)\frac{(\hbar\omega)^2}{\exp\left(\frac{\hbar\omega}{kT_C}\right)-1}d\hbar\omega + (1-\theta)\int_{E_g+E_\delta}^{\infty} IQE_{IC}^{A}(\hbar\omega)\frac{(\hbar\omega)^2}{\exp\left(\frac{\hbar\omega}{kT_C}\right)-1}d\hbar\omega\right] +$$

$$\frac{15}{\pi^4}\frac{eV}{k^4T_P^4}\frac{1}{\sin^2 v}\left[\int_{E_g}^{\infty} IQE_{CV}(\hbar\omega)\frac{(\hbar\omega)^2}{\exp\left(\frac{\hbar\omega-qV}{kT_C}\right)-1}d\hbar\omega + \theta\int_{E_\delta}^{E_g} IQE_{IC}(\hbar\omega)\frac{(\hbar\omega)^2}{\exp\left(\frac{\hbar\omega-\mu_{CI}}{kT_C}\right)-1}d\hbar\omega + (1-\theta)\int_{E_g+E_\delta}^{\infty} IQE_{IC}^{A}(\hbar\omega)\exp\left(\frac{(d(\hbar\omega,x)+1)\mu_{CI}}{kT_C}\right)\frac{(\hbar\omega)^2}{\exp\left(\frac{\hbar\omega}{kT_C}\right)-1}d\hbar\omega\right] \quad \text{(II.1.51)}$$

1.2. Conversion limit for realistic device architecture

It is however not possible to create a silicon wafer that would allow low-energy multiplication everywhere in its volume. The necessary conditions for this process occur only in specific areas that are deeply transformed from silicon's initial, monocrystalline properties. Multiplication in the whole active region is also not necessary from the point of view of a working device, as the high energy photons are absorbed closer to the surface. In a realistic

device operating with multiplication properties, the area capable of multiplication should be located only close to the surface.

In this realistic but nonetheless approximate model developed here, we assume that the multiplication is localized only in an area called *the active sub-structure*, and it is positioned close to the crystal structure, as can be seen in Figure II.3. We can also safely assume that the active area will have slightly different optical and electrical properties than the monocrystalline Si, due to the introduction of planar nanostructures and combination of their properties with the initial Si properties.

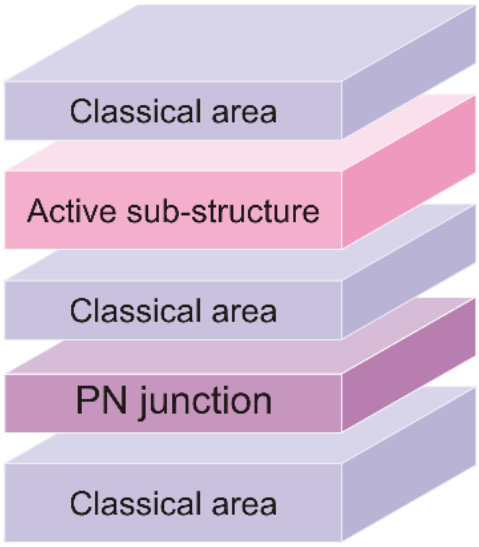

Figure II.3. A MIND test device with an active sub-structure, allowing carrier multiplication.

In an ideal device IQE and CE are independent of position. However, for understanding of a multilayered structure, it is imperative to know the exact flux penetrating inside each layer. In our case, we assume that the classical zones will have the same optical properties as monocrystalline Si, while the active sub-structure will have an enhanced absorption coefficient, similar to the absorption coefficient of amorphous Si. Distribution of the field and power inside the multi-layered structures will be discussed in detail in the following chapters of this work.

The cell presented above consists of three layers:

- a classical area, dominated by crystalline Si (cSi), where multiplication does not occur, abbreviated W_C
- zone with multiplication, that has optical properties of amorphous Si (aSi), abbreviated W_A
- PN junction is located 1µm below the surface of the sample.

We assume that CE is equal to unity in each classical area (defined before) of the device, which means that every carrier generated in this area can be collected in the external circuit with 100% efficiency. On the other hand, in the area where multiplication is possible, *CE* is a function of the incident wavelength λ. Therefore the complete expression for *CE* is given by:

$$CE(\hbar\omega, x) = \begin{cases} CE_{classical} = 1 & if \quad x \in W_C \\ m(\hbar\omega) & if \quad x \in W_A \end{cases} \tag{II.1.52}$$

where *m* is the multiplication order (number of extra electrons), as was defined earlier.

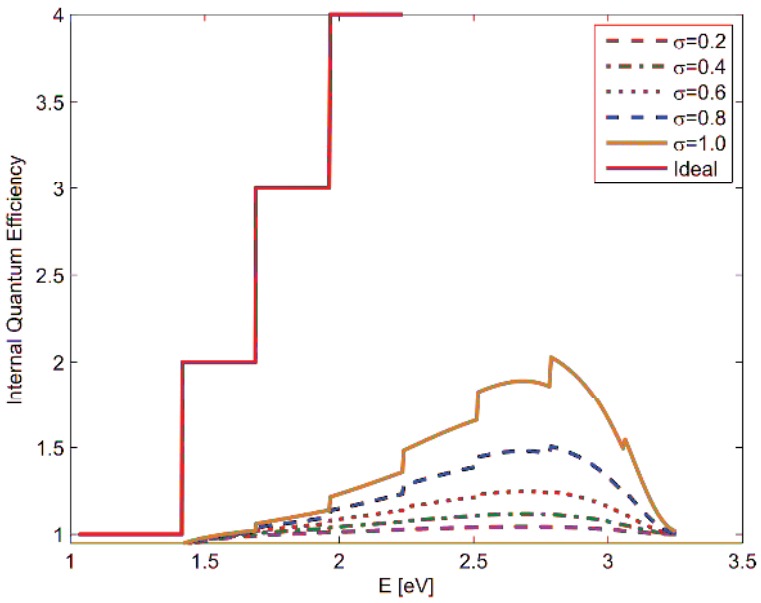

Figure II.4. Increase in *IQE* for different multiplication probabilities σ in a structure where the 12 nm thick active area is localized 165 nm below the surface of Si, in comparison with the ideal case. Characteristic energy E_δ = 0.274 eV.

The exact number of additional electrons given by multiplication and the resulting increase in IQE depends on the position of the active sub-structure. We would like to consider the most probable case, where the active area is confined to the amorphous layer and does not extend to the whole emitter. As a model structure we consider one with a 12 nm thick active area located 165 nm below the surface of silicon. Figure II.4 shows the changes in the *IQE* induced by the introduction of the active area in this region in comparison with the ideal case.

Since we assume that multiplication occurs in a layer where optical properties differ from the classical area, we can no longer assume that the generation function *G* follows a simple exponential resulting from absorption in crystalline material. Because each layer has a different refractive index and extinction coefficient, a change in optical impedance occurs when light traverses the interface, which in turn causes multiple internal reflections. Due to

that reason, the distribution of energy and the number of photons changes depending whether the interferences are constructive or destructive. Therefore to achieve any reasonable level of precision, we must turn to the energy distribution, expressed by $|S|$, and the energy density u, which can provide the information about the exact number of photons at any point in space. Keeping to the assumption that only radiative transitions are possible and that every absorbed photon creates an exciton, we can try to estimate the increase in efficiency of a quantum converter incorporating the active sub structure. For the sake of simplicity, we will also assume that the reflectivity is null and there is no transmission for all wavelengths, due to the back mirror. We will consider a multiplication probability $\sigma = 1$ for each case.

The formalism behind the calculation of S and u will be presented in Chapter III. We assume that the active sub-structure is localized in the emitter for obvious reasons, and may vary in thickness. We will consider three cases:

1. The sub-structure covers the whole emitter.
2. Only two areas can be distinguished in the emitter, with the classical one closer to the surface.
3. The sub-structure is located somewhere in the middle, with classical areas bordering it on both sides.

The quantities we will look at are the increase in current density j_{SC} and estimated conversion efficiency η calculated using the diode equation and assuming that the I_0 takes the minimum value possible (see Chapter I for the appropriate equations).

Case 1

We start with a classical silicon device, which incorporates an amorphous layer located 100 nm from the surface and the cell thickness is limited to 1 mm. In the classical case, there is no multiplication and we assume CE = 1 everywhere in the cell. For a Si solar cell, with band gap equal to $E_g = 1.17$ eV, the maximum efficiency should be close to the Shockley-Queisser limit. This is indeed the case, and we obtain the efficiency $\eta = 33.71\%$ and short-circuit current density $j_{SC} = 41.1434$ mA/cm^2.

If we now turn the whole emitter (that is everything between the surface and the PN junction) into an area capable of multiplication and set the characteristic energy $E_\delta = 0.274$ eV and multiplication probability $\sigma = 1$, we find an efficiency $\eta = 89.59\%$ and short-circuit current density $j_{SC} = 106.3767$ mA/cm^2. Note: this is an overestimation since it does not take into

account the mechanism necessary for recharging of the multiplication centers, which plays crucial role in energy conservation and effectively lowers the probability of multiplication.

Case 2

One cannot expect that the whole area of the emitter can be turned into a cSi zone with enabled low-energy multiplication. To maintain such sub-structure properties, it is necessary to sandwich it between two layers of crystalline Si. Let us define a ratio $W_A = total\ amorphous\ layer\ thickness/W$, where $W = 1$ μm is the total emitter length. To maintain a certain level of physical accuracy, we will consider that only half of the upper emitter might be converted into an area where multiplication can actively and efficiently participate in the generation process.

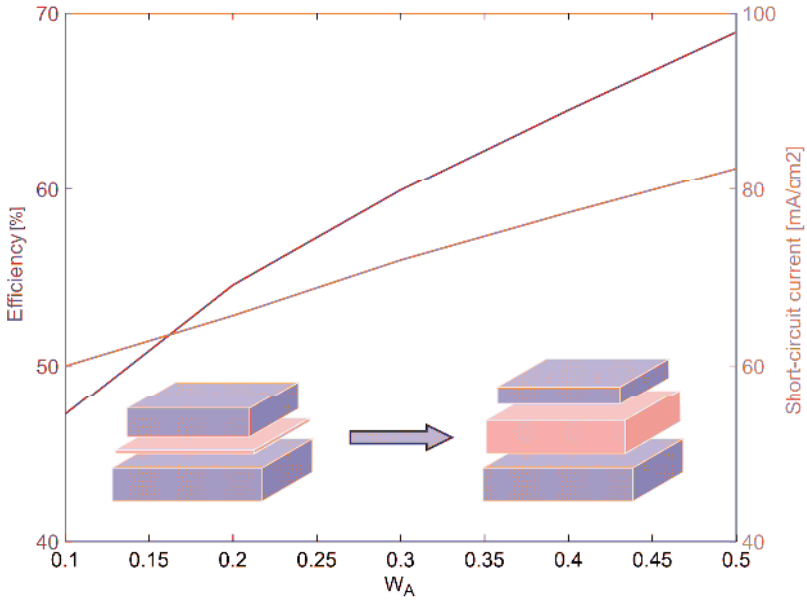

Figure II.5. Changes in I_{SC} and η for different thicknesses of amorphous layer described by parameter W_A as in case 2.

Therefore our ratio W_A will change only between 0.1 and 0.5. The amorphous layer will always begin at the PN junction and extends towards the surface. A result of this study is shown in Figure II.5.

Case 3

We will intentionally put the middle of the amorphous layer precisely 165 nm below the surface of the sample and analyze changes in η and I_{SC} as the amorphous layer expands in both directions. We will also redefine W_A to express only the thickness of amorphous layer, not the ratio.

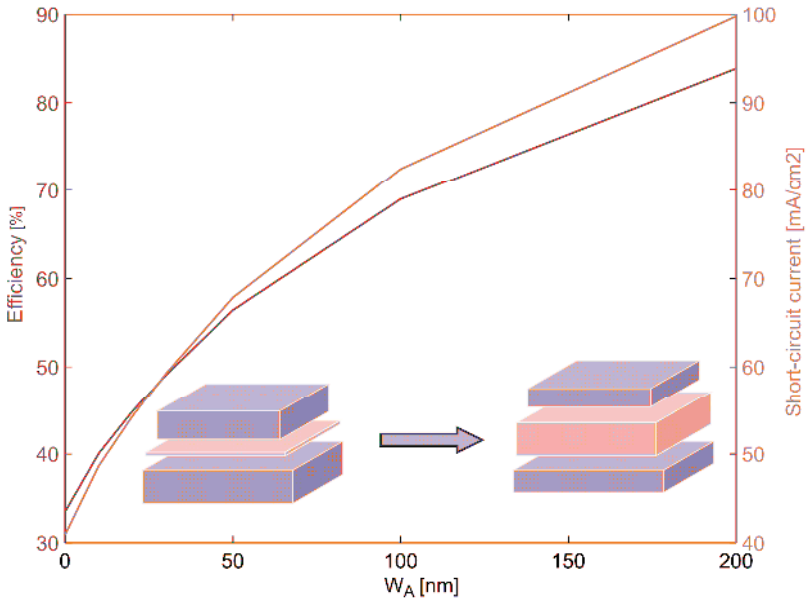

Figure II.6. Changes in I_{SC} and η for different thickness of amorphous layer described by parameter W_A as described in case 3. W_A here is the thickness of amorphous layer in nm, where its middle point is 165 nm below the surface.

As expected: the efficiency and short-circuit current increases much faster now than it did in the case 2, where amorphous layer was buried deeper inside the emitter. The absolute changes in their values are also higher for smaller thicknesses of active area. Both of these effects can be associated only with the penetration depth of high energy photons, which is very short in silicon. This result is probably more realistic than in the *case 2*, since the absolute thicknesses of active areas are smaller and the aSi layer is sandwiched between cSi layers. Those features arguably could provide just the right conditions for efficient multiplication to occur.

2. Realization of test devices

We have shown that for a material with an optical band gap similar to the one of crystalline silicon, a significant improvement can be obtained if such material possesses also a region where low-energy multiplication is possible. Such a feature requires modification of the material on the nanometric scale and introduction of extrinsic multiplication centers.

In the previous paragraph, we assumed the existence of two phases of silicon in the cell, one having properties of amorphous Si (especially optical) and other being the crystalline Si. One possibility of realization of such structure is offered by combining ion implantation followed by thermal annealing [11]. The concept of modification of silicon solar cells on the

nanometric scale and introduction of the multiplication centers results in so-called MIND (Multi-interface Novel Devices) [1].

In this paragraph we will study several experimental results of nanometric modifications in the model cells. Although fabrication of these cells was not the purpose of this work and was conducted and extensively described elsewhere [10], we will focus on the most important features and results for the purpose of clarity.

These cells were not intended to be complete devices, optimized for maximum conversion efficiency, but rather aimed at demonstrating the evidence of potential new effects.

2.1. Fabrication stages

Choice of base material

High-efficiency solar cells require good quality base materials with lowest possible number of impurities [12]. The material of choice for MIND cells was boron doped float-zone Si wafers, supplied by TOPSIL. Parameters of the wafers are shown in Table 1.1.

Diameter	4”
Thickness	525 ± 35 μm
Orientation	100
Type	P
Doping	Boron
Resistivity	4.0-10.0 Ωcm
Base doping density	$5 \cdot 10^{5}$ cm^{-3}
Front face	Polished
Rear face	Polished

Table 2.1. Initial characteristics of the substrate used for fabrication of test devices.

Ion implantation

Ion implantation is a method that allows changing of physical, chemical and mechanical properties of the material. It relies on introduction of different atomic species and controlled energy deposition, in the surface region of a treated solid substrate. This is done by bombardment with ions having energy of the order between keV and MeV. In microelectronics, this method is used to obtain reproducible and precise doping profiles.

Mean ion penetration depth depends on the implantation energy, while the density of the introduced ions depends on the implantation current and duration of the bombardment. When an amorphization appears its volume depends on the energy deposited.

In the case of MIND structures, ion implantation served two distinctive purposes and was divided into two steps. Step 1 consisted of bombarding with P ions at an energy of 180 keV and a dose of $6\text{-}10 \cdot 10^{14}$ cm^{-2}. This created partial buried amorphization of sub-surface zone in implanted structures. Step 2 consisted of bombarding with P ions of 25 keV at a dose of $5 \cdot 10^{14}$ cm^{-2} that created an inhomogeneous doping profile in the emitter.

Some of the samples were implanted only once after they were exposed to initial doping by diffusion. In these cases the main purpose of the P implantation was to create a buried amorphous region in the emitter.

Formation of the emitter

The thermal treatment partially recrystallized the amorphous zones of Si and helped creating sharp interfaces between the crystalline and amorphous part of the emitter. Annealing temperature of the process was set at 500˚C. The thermal treatment also allowed moving interstitial P atoms into electrically active sites. This stage is responsible for formation of the PN junction, which secures proper functionality of the device. The details concerning exact process parameters are confidential and cannot be discussed here. Interested reader is directed to the following work [10, chapter III, 1]. After annealing, Secondary Ion Mass Spectroscopy (SIMS) analysis was performed in order to extract information about the distribution of P ions inside the emitter for both types of samples, which is shown in figure II.7. Estimated positions of PN junctions for both sample types, extracted from Spreading Resistance Profiling are at 500 nm for double–implanted samples and at 1 μm for diffused–implanted samples.

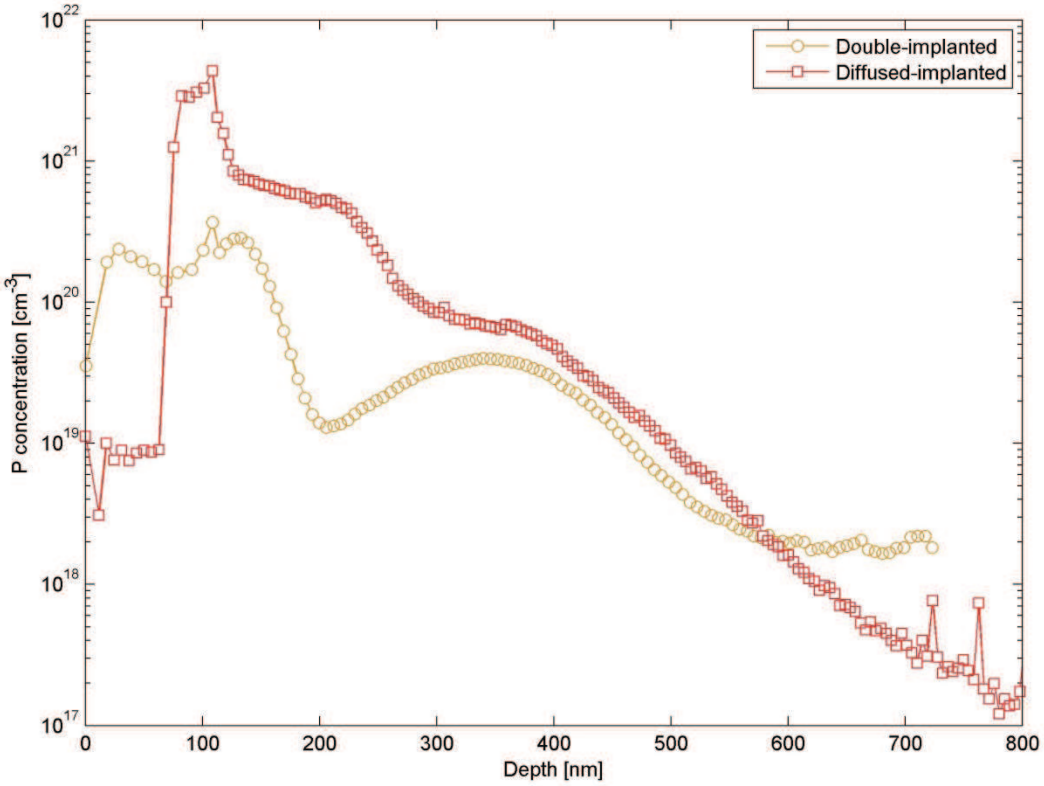

Figure II.7. P profile as obtained by SIMS measurement. It is clearly seen that the diffused – implanted samples have a one order higher doping concentration than double implanted, reaching solubility limit in Si [13].

Passivation layer

Surface recombination can have a major impact both on the short-circuit current and on the open-circuit voltage. High recombination rates at the top surface have a particularly detrimental impact on the short-circuit current since the top surface also corresponds to the highest generation region of carriers in the solar cell. Lowering the high top surface recombination is usually accomplished by reducing the number of dangling silicon bonds at the top surface through depositing a passivation layer of SiO_2 on the top surface, which also plays the role of a simple anti-reflection coating. To obtain a good quality interface between SiO_2 and Si, a 100 nm thick thermal oxide layer was first grown on both sides of the wafer. On the back side of the sample, low-energy boron implantation created a back surface field (BSF) [14] was done through that layer. On the front face, the thermally grown SiO_2 layer was etched by hydrofluoric acid solution to a thickness of 5 nm for the samples that were double-implanted. For the diffused-implanted samples, the 100 nm thick oxide layer composed of P_2O_5 was removed chemically. In both cases, the resulting thickness of the

passivation layer after etching was 5 nm. Most of the samples were then covered by SiO_2 deposited by LPCVD (Low Pressure Chemical Vapor Deposition), after deposition of metal electrodes.

Back surface field

To reduce recombination of the minority carriers on the back surface of the sample and therefore to increase their diffusion length, a back surface field was introduced. It was obtained by introducing acceptor dopants (in this case boron) close to the p contact of the cell. The implantation process was done through the 100 nm thick thermal oxide layer, and was therefore calibrated to produce the maximum concentration at the oxide/semiconductor interface. The energy of the ion beam was 20 keV and the dose was 10^{15} cm^{-2}.

Metal electrodes

Metal contacts were evaporated on the surface of Si after etching of the thermally grown oxide layer. The electrode thickness is 1 µm with a width of 100 µm. On the front face, a bilayer contact made of Ti/Au or Ti/Ag was deposited, on the back face an Al contact was deposited. On both sides of the sample the contacts were deposited in a form of grid with 0.9 mm spacing. The rear grid was then covered by an Al layer, which acts also as a back mirror.

2.2. Process key points

The fabrication process of the test MIND structures consisted of several steps that are listed in the Table 2.2 below. The main goal, which was to create an amorphized layer of Si buried below the surface of the emitter, was achieved with good accuracy. We will discuss the properties of this layer in the following chapters. The resulting structure architecture is shown in Figure II.8.

Stage 1	Thermal oxidation
Stage 2	Realization of the back surface field
Stage 3	Realization of the emitter (either double-implanted or diffused-implanted
Stage 4	Thermal annealing
Stage 5	Rear contacts
Stage 6	Front contacts
Stage 7	Surface passivation by LPCVD

Table 2.2. Summary of the fabrication stages in chronological order.

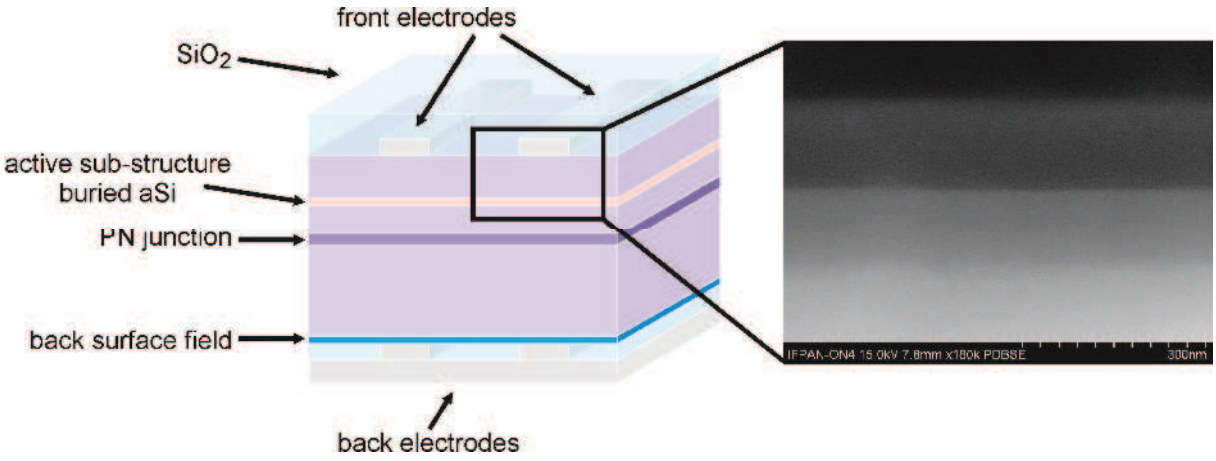

Figure II.8. Architecture of test devices (left) and Backscattered Electron Microscopy image (right) of the buried sub–structure. Picture shows fully completed sample after all the fabrication steps.

Note: It is important to stress that the process parameters were not optimized for maximum efficiency of the final device. The goal was rather the laboratory-scale test structures.

3. Conclusions

As a summary of this chapter, we highlight the most important points. First, a new kind of silicon-based structures was created, with the objective of showing that the principle of low energy multiplication can be experimentally confirmed. This multiplication mechanism involves, unlike other similar concepts, also non-radiative transitions, namely photon-electron and electron-electron. The approach to this concept was resolved technically by introducing a buried active sub-structure in the emitter of a test device. The purpose of the test structures was to obtain confirmation of the new effect and to gain deeper insight into the phenomenon.

References:

[1] Z. T. Kuznicki, J.-J. Grob, J.-C. Mueller, H. E. Strazynska-Kuznicki, French patent 94 98885, 13th June 1994

[2] Z. T. Kuznicki, *Quantum Efficiencies exceeding unity in amorphized silicon layers*, 23th IEEE Photovoltaic Specialists Conference, May 1996, Washington, USA

[3] Z. T. Kuznicki, S. de Unamuno, F. Villaume, internal report 1998

[4] A. Luque, A. Marti, *Increasing the efficiency of ideal solar cells by photon induced transmission at intermediate levels*, Phys. Rev. Lett., 78, 1997, 5014-5017

[5] R. Brendel, J. H. Werner, H. J. Queisser, *Thermodynamic efficiency limit for semiconductor solar cell with carrier multiplication*, Sol. En. Mat. Sol. Cells, 41/42, 1996, 419-425

[6] A. Luque, A. Marti, *A metallic intermediate band high efficiency solar cell,* Prog. Photovolt. Res. Appl., 9, 2001, 73-86

[7] B. K. Ridley, *Quantum processes in semiconductors*, Fourth Edition, Oxford Science Publications, 1999

[8] A. de Vos, *The fill factor of a solar cell from the mathematical point of view*, Solar Cells, 8, 1983, 283-296

[9] Z. T. Kuznicki, F. Capot, S. de Unamuno, *Photovoltaic conversion with multiplication: thermodynamic limits for any impact energy*, 2nd World Conference and Exhibition on Photovoltaic Energy Conversion, 6 – 10 July, 1998, Vienna, 180-183

[10] M. Ley, *Cellule photovoltaique MIND – amelioration du rendement quantique interne a l'aide d'une sous – structure active enterree dans l'emetteur,* PhD thesis, Universite de Strasbourg, 2002, 78-84

[11] Z. T. Kuznicki, *Multi-interface Novel Devices Part I. Limits, modeling and design; Part II. Elements of realization*, E-MRS First Polish-Ukrainian Symposium "New Photovoltaic Materials for Solar Cells", Cracow, Poland, October 21-22, 1996, Proceedings 58-98

[12] J. R. Davis, A. Rohatgi, R. H. Hopkins, P. D. Blais, P. Rai-Choudhury, J. R. McCormick, H. C. Mollenkopf, *Impurities in silicon solar cells*, IEEE Trans. Elec. Dev., ED-27, 1980, 677-687

[13] G. E. Jellison, S. P. Withrow, J. W. McCamy, J. D. Budai, D. Lubben and M. J. Godbole, *Optical functions of ion-implanted, laser-annealed heavily doped silicon*, Phys. Rev. B 50 (20), 1995, 14607-14614

[14] Z. T. Kuznicki, Low-high homojunction in the stationary state, J. Appl. Phys. 69, 6526 (1991)

Chapter III

Numerical simulations

Contents

Abstract

A theoretical analysis of MIND structures, their optical, electrical and photovoltaic properties is laid out in this chapter. We begin with analyzing silicon as a host material from a microscopic point of view. With *ab initio* calculations, we extract information about the silicon crystal lattice disturbed with P dopants, its density of states, potential and strain.

Further in the chapter we focus on various models of dielectric functions, analyzing their strengths and weaknesses. When an appropriate approximation is chosen, that will accurately describe the material properties in respect with the problem determined beforehand (small changes in the properties in the emitter, inhomogeneous doping distribution), we will present the optical model chosen to represent planar MIND structures, namely the Transition Matrix Approximation (TMA).

Another approximation, the Effective Medium Theory (EMT) used to describe the interface between crystalline and amorphized phase of the material, is then presented. The MATLAB code that summarizes earlier theoretical introduction is shown. As a last point in this chapter, we present some of the possible results obtainable through our modeling.

1. *Ab initio* calculations of some properties of silicon.

To gain further insight into properties of crystalline Si, we performed some basic *ab initio* simulations of both crystalline and doped silicon using ABINIT software [1,2].

Quantum mechanics and electromagnetism are widely perceived as leading to a "first-principles" approach to materials and nanosystems: if the needed software applications and corresponding hardware were available, these properties could be obtained without any adjustable parameter (nuclei characteristics being given). However, such first-principles equations (e.g. the N-body Schrodinger equation) are too complex to be handled directly. Indeed, fundamental quantities, like the wavefunctions for N particles, cannot be represented faithfully on the hardware available nowadays, for N over about a dozen. Different methodologies to address this problem have been proposed. The approach we used, implemented in the ABINIT package, focuses on the Density Functional Theory (DFT), proposed in 1964-65 by Hohenberg and Kohn [3] and Kohn and Sham [4] (KS), and the Many-Body Perturbation Theory, in particular the so-called GW approximation (GWA) of L. Hedin [5]. Both significantly reduce the complexity of the first-principles approach at the expense of some approximations. On the basis of such methodologies in the 1980s, it became clear that numerous properties of materials, like total energies, electronic structure, and dynamical, dielectric, mechanical, magnetic, vibrational properties, can be obtained with an accuracy that can be considered as truly predictive (e.g. a few percent uncertainty on bond lengths, a fraction of an eV for electronic energies...). Many research groups implemented the DFT methodology, using different representations (planewaves, augmented waves, muffin-tin orbitals). The interested reader is encouraged to read the comprehensive book by R. M. Martin [6]). However, it is hardly possible for one research group to gather the expertise to address such a wide range of properties. As for drawbacks, the DFT in the usual LDA or GGA approximations does not describe correctly the interaction between electrons, and contains moreover a spurious self-interaction. As a consequence, it is not able to describe strongly correlated systems which contain partially filled *d* or *f* shells.

We concentrated mainly on calculating the density of states, the band structure and the strain introduced by a P atom substituting for a Si atom in the crystal network, as well as the usual ground state output information (electronic density and Kohn-Sham potential).

Part of the results concerning crystalline silicon was already presented in Chapter I, §2 of this work. Here we will focus on the rest of the results for crystalline Si and heavily doped Si:P.

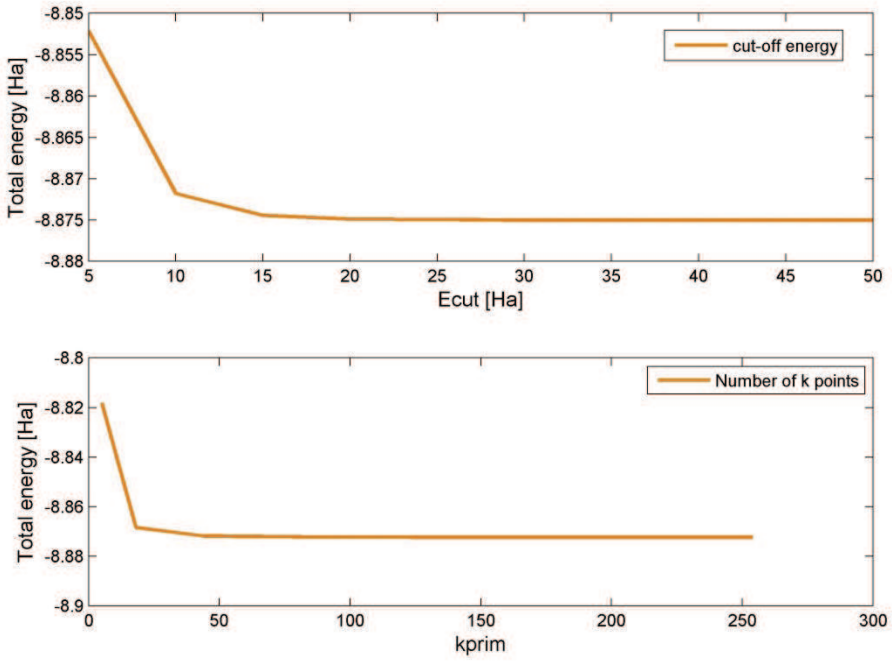

Figure III.1. Convergence tests for primitive Si cell. Plane wave cut-off energy E_{cut} is presented on the upper graph and the number of k points in the Brillouin zone on the lower. 1 Ha = 27.21138386 eV.

A typical ground state *ab initio* calculation requires at first the determination of atom positioning inside the cell as well as a proper choice of pseudopotential functions, Local Density Approximation (LDA) or Generalized Gradient Approximation (GGA). In our calculation we used the pseudopotential functions provided by the ABINIT package [7] that are based on Troullier-Martins pseudopotentials for both Si and P atoms [8]. Then, the convergence tests were conducted, which are presented in figure III.1. We obtained stable results for cut-off energy for plane waves E_{cut} = 30 Ha and number of k points in Brillouin zone k_{prim} = 50. The cell length was found to be a = 539.6509 pm which is in good agreement with crystallographic data a_{crys} = 543.09 pm [9].

Ab initio calculations provide the variety of results, ranging from total energy and its derivatives, electronic density and the density of states. It is worth noting that even if some of those physical quantities are flawed by the approximations used and by the model itself, their quality is still good enough to allow predictions of real materials. There are several quantities such as the total energy and the electronic density that are exact analogs of the real quantities in our physical world. They do not suffer from approximations. Changes in Kohn-Sham

potential however, even if often very similar to changes in the real potential, differ significantly and cannot be used to accurately estimate the response of real systems.

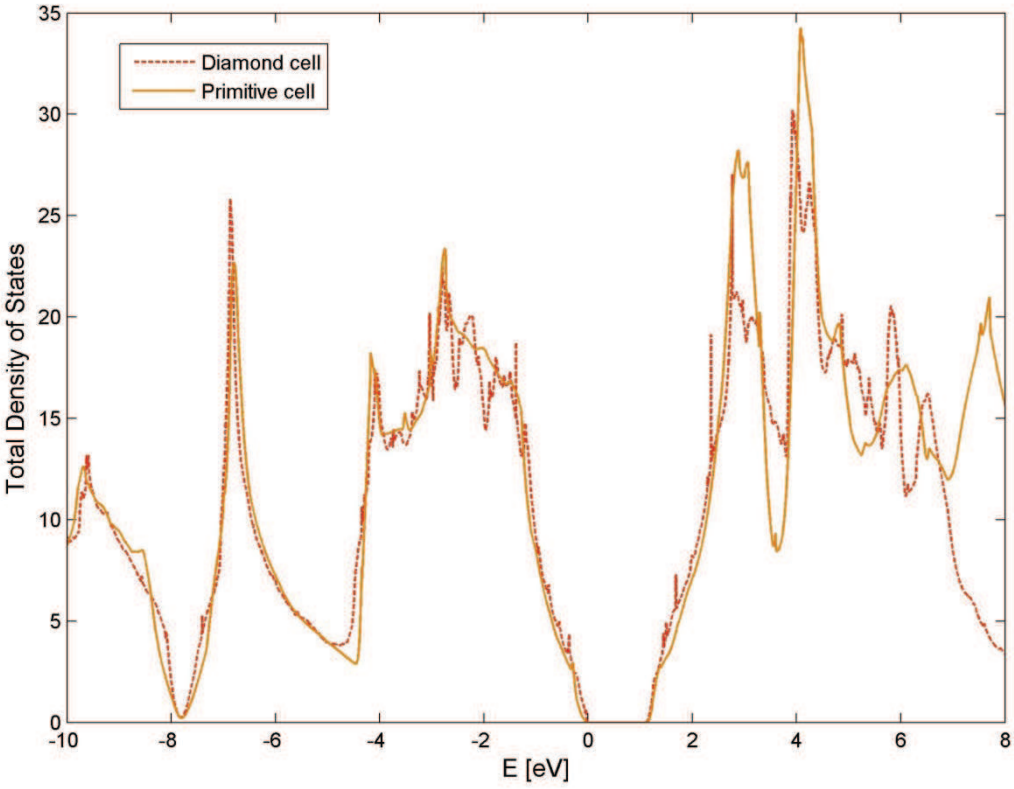

Figure III.2. Comparison of Total Density of States per atom calculated by ABINIT software for a primitive cell (solid line) and for a diamond cell (dashed line) of crystalline silicon.

We began by investigating the influence of cell determination (primitive or diamond), after all convergence test were conducted, on the Total Density of States (TDOS) for crystalline silicon. The result of TDOS / atom for both cells is presented in figure III.2. Both curves were corrected for the band gap energy that normally is underestimated in this approach due to lack of electron screening. It is easy to note that there are some significant differences that appear especially for the high energy range. These differences arise from limitations of our computing machine that was not able to handle the calculations for the diamond cell (consisting of 8 atoms) for converged number of *k* points. Nevertheless, in the energy range covered by the solar spectrum, the simulation of TDOS for both cells provided similar and comparable results.

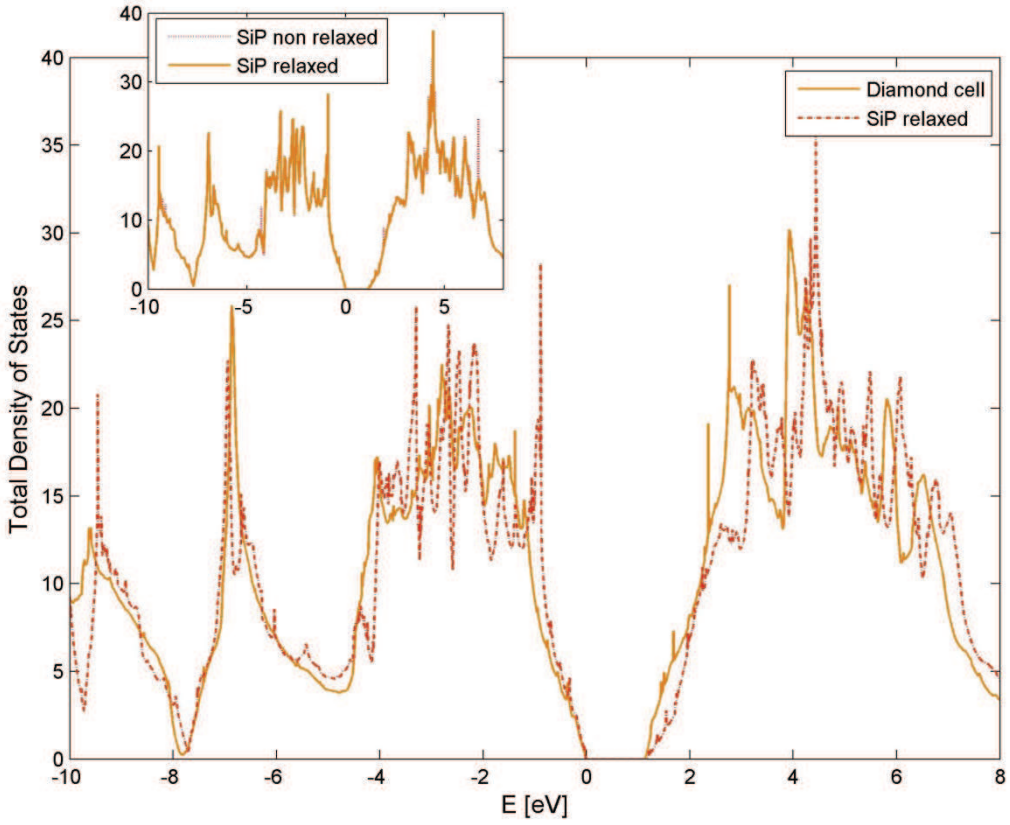

Figure III.3. Comparison of Total Density of States per atom calculated by ABINIT software for crystalline (solid line) and the diamond cell Si with one atom substituted by P (dashed line). The inset shows the changes in TDOS after cell relaxation following atomic substitution.

Simulation for the diamond cell was necessary to study TDOS changes when a Si atom is substituted by a P atom. Phosphorous doping, besides being the most common method of introducing donors in crystalline Si, plays also a crucial role in the concept of MIND structures. The strain imposed by the substituting atom is one of key factors that allow formation and persistence of the PV metamaterial. To be able to study the changes that P substitution introduces in cSi network, we replaced one Si atom in a diamond cell. Since phosphorous has different atomic radius than silicon, we allowed the cell and neighboring atoms to find their global minima again. The stress tensor resulting from substitution of Si atom by P was found to be:

$$\sigma = \begin{bmatrix} 1.34904045 & 0 & 0 \\ 0 & 1.34904045 & 0 \\ 0 & 0 & 1.34904045 \end{bmatrix} GPa \qquad \text{(III.1.1)}$$

Although there were no significant changes in TDOS before and after relaxation, the situation changes dramatically when we compare TDOS for crystalline Si and P-doped Si. Both results

are shown in figure III.3. This result should be understood as follows: when a Si atom is substituted by P in the crystal network, it introduces additional states in the electronic structure. In an *ab initio* calculation we performed, due to the periodic boundary conditions, it is difficult to determine the exact number of states introduced by a P – dopant, because the site wavefunction extends well over the host and neighboring cell. In such a case, we can only compare the number of states introduced by a dopant per atom in its nearest neighborhood, which can be later used to estimate the real difference in TDOS for any given amount of doping. From figure III.3 it can be easily seen that the most significant changes in the density of states occur in the conduction band for energies around 3-4 eV above the band minimum. Nevertheless, it can be extrapolated from figure III.3 that for low doping densities ($N_d \sim 10^{14}$-10^{16} [1/cm^3]), the changes in TDOS are very small and in most cases for basic calculations (such as estimation of carrier density of the Fermi level) it is justified and more convenient to use the TDOS for undoped Si.

Another interesting quantity we obtained from ground state calculations is the electronic density. It corresponds to the probability of finding an electron in the real space inside the crystal, and can be used either to visualize atomic bonds and orbitals or to estimate the changes in such bonds and orbitals due to perturbation of the system, by pressure, phase transition or atom displacement.

We calculated the electronic density for crystalline Si and for the relaxed Si:P diamond cell. Results for crystalline Si are shown in figure III.4. The isosurface of constant electronic density $P_N = 0.07$ was chosen to visualize the well-known tetrahedral bonds between Si atoms.

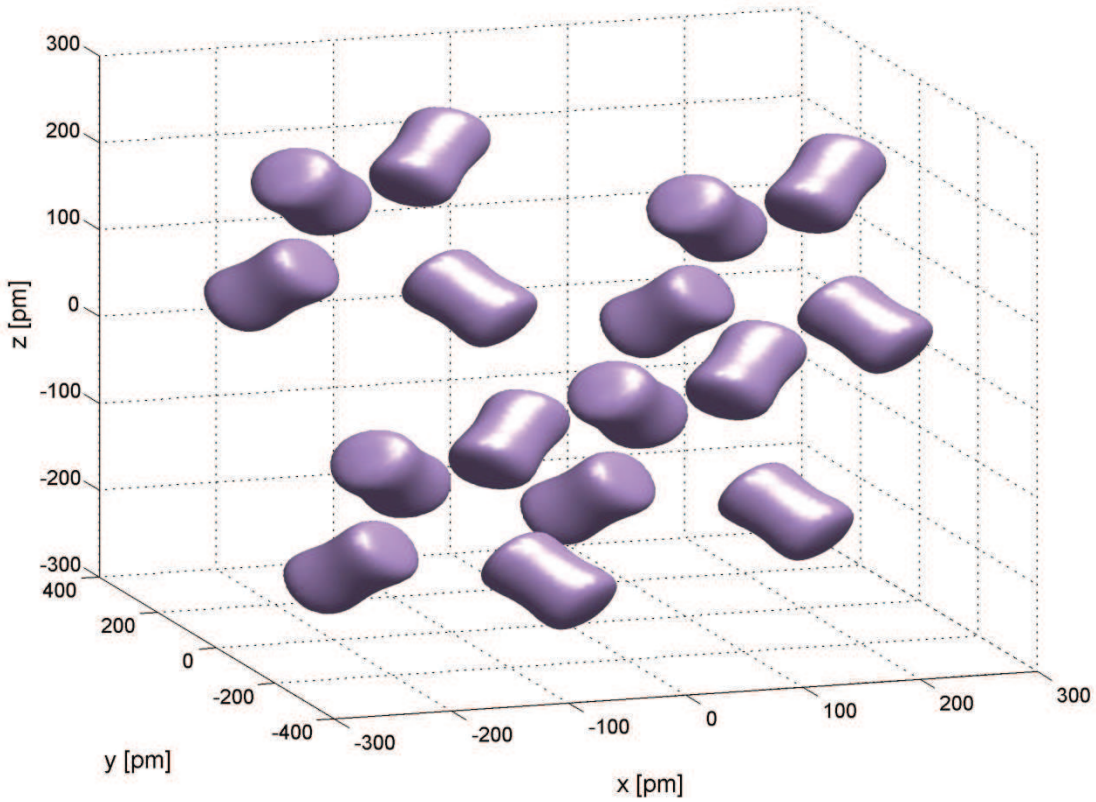

Figure III.4. Electronic density distribution in real space in a silicon cell. The isosurface is drawn along $P_N = 0.07$.

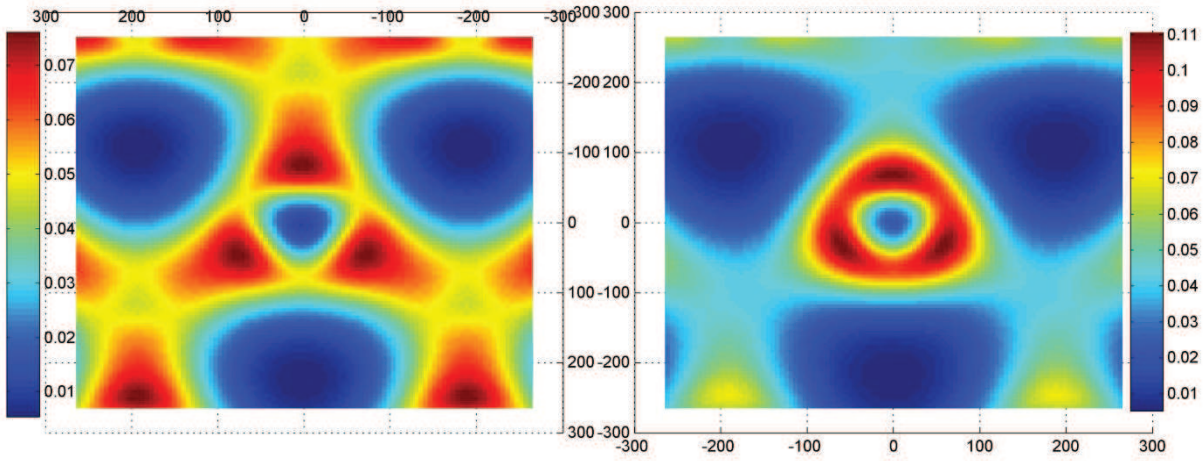

Figure III.5. Electronic density distribution in real space in a Si cell (left) and in a Si:P cell (right). The electronic density is drawn along the 111 crystallographic plane passing through the site of the P atom.

From the data presented in figure III.4, one can find the characteristic positions of the Si atoms in a diamond cell by imagining a Si inside each hollow spot to where the cylindrical-shaped density isosurfaces point. This result shows the well-known property of a Si atom inside a crystal cell, forming four convalescent π – bonds with its neighbors. The situation is different when one Si atom is substituted by P atom. Phosphorous has the valence of five, therefore it forms four covalent bonds with neighboring Si atoms, but one unbound electron in the ground state is delocalized around the P atom, as can be seen in figure III.6 as a tetrahedron – shaped density cloud for $P_N = 0.07$.

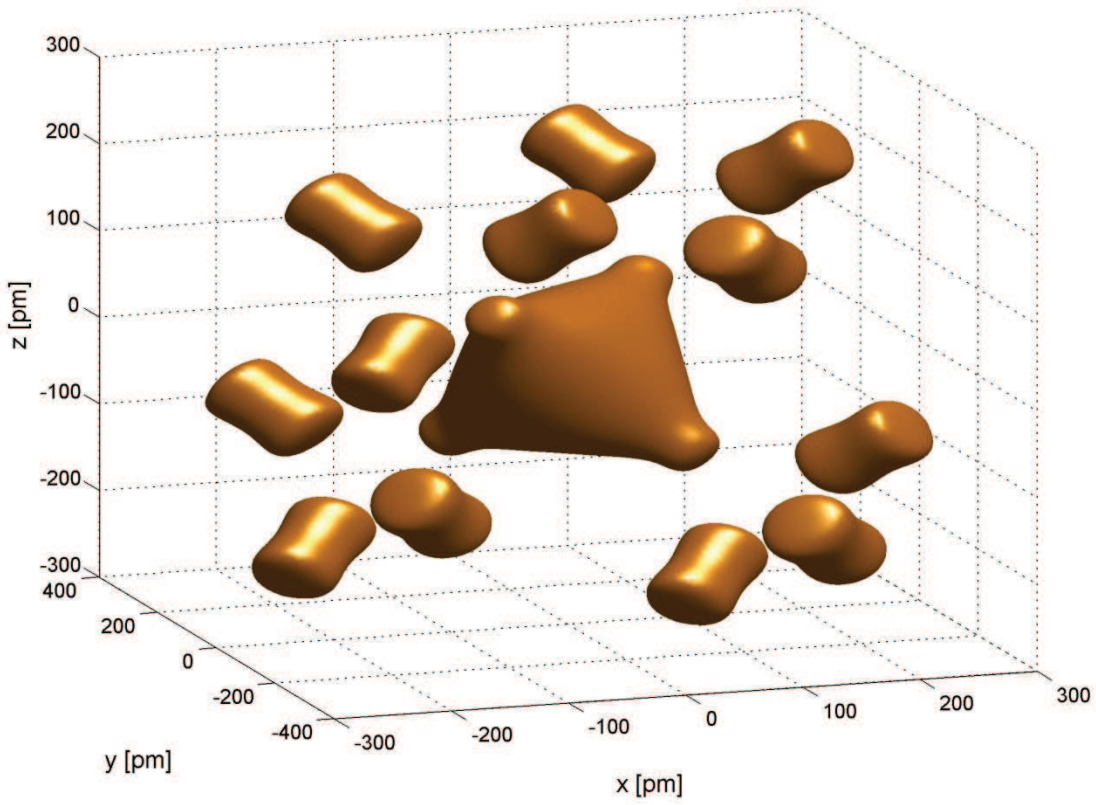

Figure III.6. Electronic density distribution in real space in Si:P diamond cell. The isosurface is drawn along $P_N = 0.07$. Phosphorous atom is placed in the center.

The changes in density introduced by P doping are also presented in figure III.5, where the electron density is represented on a plane parallel to the 111 crystallographic plane, with the P atom placed in the center. In the left panel of the figure, the lower part of the tetrahedron formed around the Si atom is clearly visible and the density is evenly distributed, whereas the density increase coming from the P atom is centered on its site.

Other results obtained in our study, including potential changes and band structure, were presented in Chapter I of this work.

2. Optical functions of crystalline and amorphous Si.

Optical phenomena are usually the interactions between the electromagnetic wave and matter. The energy range usually associated with optical part of the spectrum is from $E = 10^{-3}$ eV (infrared) to $E = 10^{2}$ eV (ultraviolet). Optical phenomena form the base for many applications of semiconductors, such as photovoltaic cells, light-emitting diodes, semiconductor lasers and photodetectors.

Basic processes associated with the light-matter interaction are wave reflection and absorption. Additionally, wave dispersion and luminescence can be observed. When the penetrating light is absorbed and then reemitted with a different frequency, or transformed into heat and reemitted, we deal with photoluminescence. Dispersion is mainly associated with inhomogeneous areas in the medium. If dispersion is associated with acoustic phonons, we have the Brillouin dispersion, and if it is associated with optical photons, it is the Raman dispersion. In the general approach, the strength of such effects (reflection, dispersion, luminescence, etc.) depends on the level of interactions involved. Therefore, the reflection and absorption are usually the strongest, since they depend only on the lowest-level interaction, dispersion and luminescence both depend on two such interactions, and consequently are weaker. Higher level effects, needing even more basic interactions to occur simultaneously, are usually the weakest (such as non-linear interactions).

To understand the interaction between light and matter, we will begin by analyzing the Maxwell equations [10]:

$$\nabla \times \bar{E} = -\frac{\partial \bar{B}}{\partial t} \tag{III.2.1}$$

$$\nabla \times \bar{H} = -\frac{\partial \bar{D}}{\partial t} + \bar{J} \tag{III.2.2}$$

$$\nabla \cdot \bar{B} = 0 \tag{III.2.3}$$

$$\nabla \cdot \bar{D} = \rho \tag{III.2.4}$$

material equations:

$$\bar{D} = \varepsilon\varepsilon_0\bar{E} = (1 + \chi)\bar{D} \tag{III.2.5}$$

$$\bar{B} = \mu\mu_0\bar{H} \tag{III.2.6}$$

and Ohm's law:

$$\bar{j} = \sigma\bar{E} \tag{III.2.7}$$

We assume a non-magnetic media ($\mu = 1$), at least for optical frequencies, and no static charge, $\rho = 0$. In the general case, the dielectric permittivity is a function of frequency, $\varepsilon = \varepsilon(\omega)$, therefore we shall call it the dielectric function. The static dielectric constant is then equal to $\varepsilon_s = \varepsilon(0)$ and $\varepsilon_\infty = \varepsilon(\infty)$ is the high frequency limit of dielectric permittivity.

It is easy to see from equations (III.2.1) to (III.2.4) and (III.2.7) that the wave equation can be expressed as follows:

$$c^2\Delta\bar{E} = \varepsilon\frac{\partial^2\bar{B}}{\partial t^2} + \frac{\sigma}{\varepsilon_0}\frac{\partial\bar{B}}{\partial t} \tag{III.2.8}$$

Assuming the plane wave propagating in the 0X direction, we are looking for the solution of a kind:

$$\bar{E}(t,x) = \bar{E}(\omega,q)e^{i(qx-\omega t)} \tag{III.2.9}$$

where ω is the wave frequency and $q = 2\pi/\lambda$ is the wave number. Upon combining equations (III.2.8) and (III.2.9) we obtain:

$$-c^2q^2\bar{E} = -\left[\varepsilon(\omega)\omega^2 + i\frac{\sigma\omega}{\varepsilon_0}\right] \tag{III.2.10}$$

and the dispersion relation:

$$q^2 = \varepsilon(\omega)\frac{\omega^2}{c^2} + i\frac{\sigma\omega}{\varepsilon_0 c^2} \tag{III.2.11}$$

In the special case of a non-conductive medium we obtain:

$$q^2 = \varepsilon(\omega)\frac{\omega^2}{c^2} \tag{III.2.12}$$

In a conductive medium, equation (III.2.11) can be written in the following manner:

$$q^2 = \left[\varepsilon(\omega) + i\frac{\sigma}{\varepsilon_0\omega}\right]\frac{\omega^2}{c^2} \tag{III.2.13}$$

where the expression in brackets has the meaning of *complex dielectric function*:

$$\tilde{\varepsilon}(\omega) = \varepsilon(\omega) + i\frac{\sigma}{\varepsilon_0\omega} = \varepsilon_1(\omega) + i\varepsilon_2(\omega) \tag{III.2.14}$$

The real and imaginary parts of the complex dielectric function are linked to the Kramers-Kronig relations:

$$\varepsilon_1(\omega) - 1 = \frac{2}{\pi}\left(P\int_0^{\infty} \frac{\omega'\varepsilon_2(\omega')}{\omega'^2 - \omega^2} d\omega' \right) \quad \text{(III.2.15a)}$$

$$\varepsilon_2(\omega) = \frac{-2}{\pi}\left(P\int_0^{\infty} \frac{\varepsilon_1(\omega') - 1}{\omega'^2 - \omega^2} d\omega' \right) \quad \text{(III.2.15b)}$$

and the relation:

$$\int_0^{\infty} \omega\varepsilon_2(\omega) d\omega = \frac{\pi}{2}\omega_p^2 \quad \text{(III.2.16)}$$

where $\omega_p = \sqrt{\frac{Ne^2}{\varepsilon_0 m}}$ is the electronic plasma frequency, n is the electron density and e, m are electron charge and mass. For frequencies $\omega >> \omega'$, from equations (III.2.15a) and (III.2.16) we obtain:

$$\varepsilon_1(\omega) = 1 - \frac{\omega_p^2}{\omega^2} \quad \text{(III.2.17)}$$

The above equation is known as the Drude relation, which describes the modification of ε due to free carriers for metals and non-polar semiconductors.

Introducing the complex refractive index defined as $\tilde{n} = n + i\kappa$ that obeys the following:

$$[\tilde{n}(\omega)]^2 = \tilde{\varepsilon}(\omega) \quad \text{(III.2.18)}$$

we obtain the following expressions for the real and imaginary parts of the dielectric function:

$$n^2 - \kappa^2 = \varepsilon_1 \quad \text{(III.2.19)}$$

$$2n\kappa = \frac{\sigma}{\varepsilon_0\omega} = \varepsilon_2 \quad \text{(III.2.20)}$$

Combining equations (III.2.18) and (III.2.13) and inserting the product to equation (III.2.9) gives:

$$\bar{E}(t,x) = \bar{E}_0 e^{i\left(\frac{\tilde{n}\omega x}{c} - \omega t\right)} = \bar{E}_0 e^{i\left(\frac{n\omega x}{c} - \omega t\right)} e^{-i\left(\frac{\kappa\omega x}{c}\right)} \quad \text{(III.2.21)}$$

The electric field intensity decreases along 0X axis according into the following rule:

$$I \sim \left[\bar{E}_0 e^{-i\left(\frac{\kappa\omega x}{c}\right)}\right]^2 \sim e^{-i\left(\frac{2\kappa\omega x}{c}\right)} \sim e^{-\alpha x} \quad \text{(III.2.22)}$$

where α is the absorption coefficient defined as:

$$\alpha = \frac{2\omega\kappa}{c} = \frac{\omega\varepsilon_2}{cn} = \frac{\sigma}{c\varepsilon_0 n} \quad \text{(III.2.23)}$$

It can be seen that ε_2 is responsible for absorption of the wave, while the connection between ε_2 and real σ indicates that the energy is transferred from the wave to free carriers in the

material. At the border of two materials electromagnetic wave can be reflected or transmitted. We can constitute the amplitude reflection and transmission coefficients for *s* polarization (TE polarization, *E* vector in the *y*-*z* plane):

$$r_s = \frac{n_1 \cos\theta_i - n_2 \cos\theta_t}{n_1 \cos\theta_i + n_2 \cos\theta_t} \quad \text{(III.2.24a)}$$

$$t_s = \frac{2n_1 \cos\theta_i}{n_1 \cos\theta_i + n_2 \cos\theta_t} \quad \text{(III.2.24b)}$$

and for *p* polarization (TM polarization, *H* vector in the *y*-*z* plane):

$$r_p = \frac{n_2 \cos\theta_i - n_1 \cos\theta_t}{n_1 \cos\theta_t + n_2 \cos\theta_i} \quad \text{(III.2.25a)}$$

$$t_p = \frac{2n_1 \cos\theta_i}{n_1 \cos\theta_t + n_2 \cos\theta_i} \quad \text{(III.2.25b)}$$

The power reflection coefficient is linked to the amplitude coefficients in the following way:

$$R = |r^2| \quad \text{(III.2.26)}$$

And since the light travels at a different speed in both media the power transmission coefficient *T* is equal to:

$$T = \frac{n_2 \cos\theta_t}{n_1 \cos\theta_i}|t| \quad \text{(III.2.27)}$$

where θ_i and θ_t are the incident and refracted angle in both media, respectively. The above formulas are known as the Fresnel equations [11].

2.1. Harmonic oscillator approximation.

The Harmonic Oscillator approximation (HMO) or Lorentz model is a classical model which assumes that EM wave travels through a medium composed of oscillating dipoles. All forces are isotropic and the damping strength is proportional to the oscillator amplitude. If an oscillator with mass *m*, charge *e* and resonant frequency ω_g is under the influence of an electric field $E = E_0 e^{i\omega t}$ imposing oscillations in a medium with a damping coefficient Γ, the motion equation of such an oscillator takes the following form:

$$m\ddot{x} + m\gamma\dot{x} + m\omega_g^2 x = eE_0 e^{i\omega t} \quad \text{(III.2.28)}$$

By solving the above equation for *x* we obtain:

$$x = \frac{eE_0}{m}\frac{e^{-i\omega t}}{\omega_g^2 - \omega^2 - i\omega\Gamma} \quad \text{(III.2.29)}$$

The current density resulting from the oscillator's motion is then equal to:

$$j = eN\dot{x} \tag{III.2.30}$$

where N is the number of oscillators in a unit of density. The complex conductivity is then expressed as:

$$\tilde{\sigma} = \frac{j}{E} = \frac{Ne^2}{m}\frac{i\omega}{\omega_g^2 - \omega^2 - i\omega\Gamma} \tag{III.2.31}$$

if separated into real conductivity and electric susceptibility it becomes:

$$\sigma = \frac{Ne^2}{m}\frac{\omega^2\gamma}{\left(\omega_g^2 - \omega^2\right)^2 - (\omega\Gamma)^2} \tag{III.2.32}$$

$$\chi = \frac{Ne^2}{\varepsilon_0 m}\frac{\omega_g^2 - \omega^2}{\left(\omega_g^2 - \omega^2\right)^2 - (\omega\Gamma)^2} \tag{III.2.33}$$

and consequently the complex dielectric function is:

$$\varepsilon = 1 + \frac{Ne^2}{\varepsilon_0 m}\frac{1}{\omega_g^2 - \omega^2 - i\omega\Gamma} \tag{III.2.34}$$

If the medium is composed of many oscillators with different resonant frequencies ω_g, it is necessary to incorporate the addition of each oscillator to the dielectric function:

$$\varepsilon = 1 + \frac{Ne^2}{\varepsilon_0 m}\sum_l \frac{f_l}{\omega_l^2 - \omega^2 - i\omega\Gamma_l} \tag{III.2.35}$$

where N is the number of oscillators and f_l is the strength associated with an oscillator l. The sum of all oscillator strengths must be equal to 1:

$$\sum_l f_l = 1 \tag{III.2.36}$$

In such a case it is often more convenient to express the equation (III.2.35) as follows:

$$\varepsilon = 1 + \sum_l \frac{C_{0l}^2}{\omega_{gl}^2 - \omega^2 - i\omega\Gamma_l} \tag{III.2.35}$$

where C_{0l} is the amplitude of the l^{th} oscillator. The typical behavior of the function ε around its critical energy E_g (or resonant frequency ω_g) is shown in figure III.7.

In the case of Si, there are three possible critical energies between $E = 1.0$ eV to $E = 5.2$ eV. The critical energies are associated with following transitions: $E_{g1} = 3.34$ eV is the direct band gap in Si at the Γ point, $E_{g2} = 3.62$ eV is the energy needed to directly create an electron – hole pair in silicon (including all the average energy losses) [12,13] and $E_{g3} = 4.43$ eV that corresponds to the second direct transition at the Γ point [14].

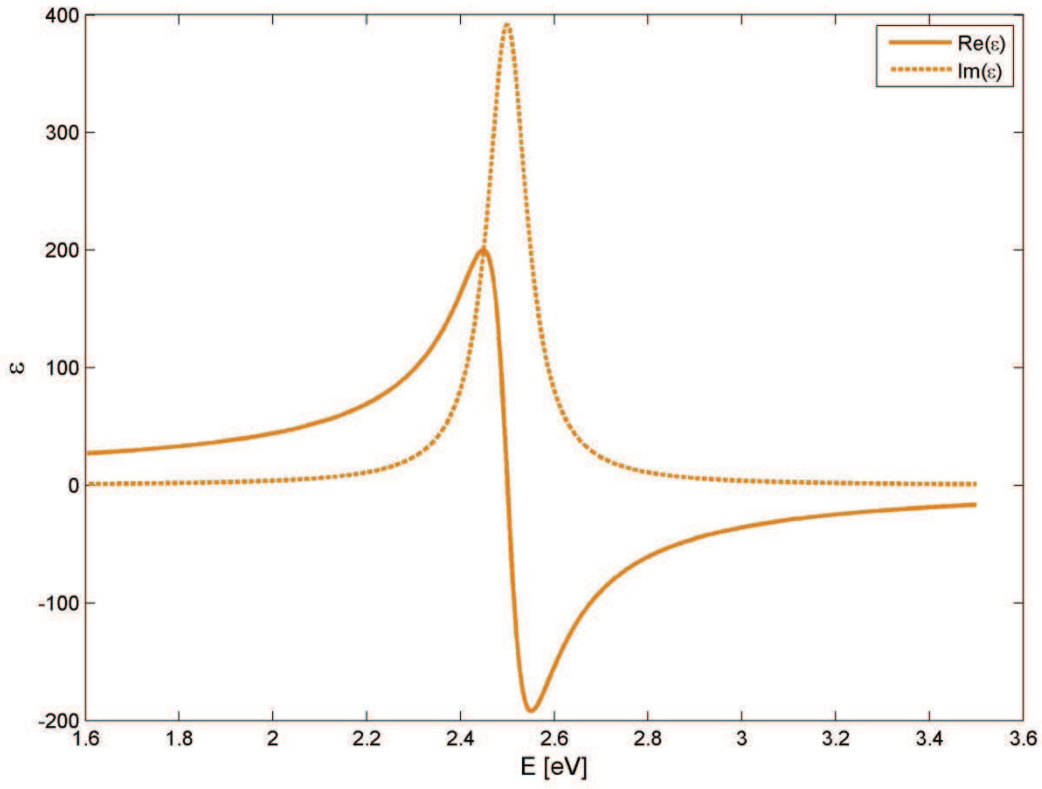

Figure III.7. Real and imaginary parts of a complex dielectric ε function near its critical energy E_g.

The classical Lorentz oscillator, while having the ability to predict qualitative information about the material over the whole energy range, including the fundamental absorption edge, static conductivity and high frequency limit, often does not provide an accurate representation of real semiconductors in a specified energy range. For the case of Si, assuming only three possible critical energies the theoretical representation of experimental data is rather poor. As can be seen in figure III.8, the steep increase of the imaginary part of ε, typical for crystalline Si is not well reproduced. Also the region between $E = 3.5$ and 4.4 eV around second critical energy $E_{g2} = 3.62$ eV is described with low accuracy. Although one may argue that from quantum point of view there are more than three distinct transition energies in the area, resulting from Heisenberg rule and electronic band structure of the crystalline body, the main influence to the experimental dielectric function comes from those three direct transitions. Also, the broadening parameter Γ partially compensates for the additional transitions; therefore use of more than three oscillator energies between 1.5 eV and 5.2 eV has no physical justification.

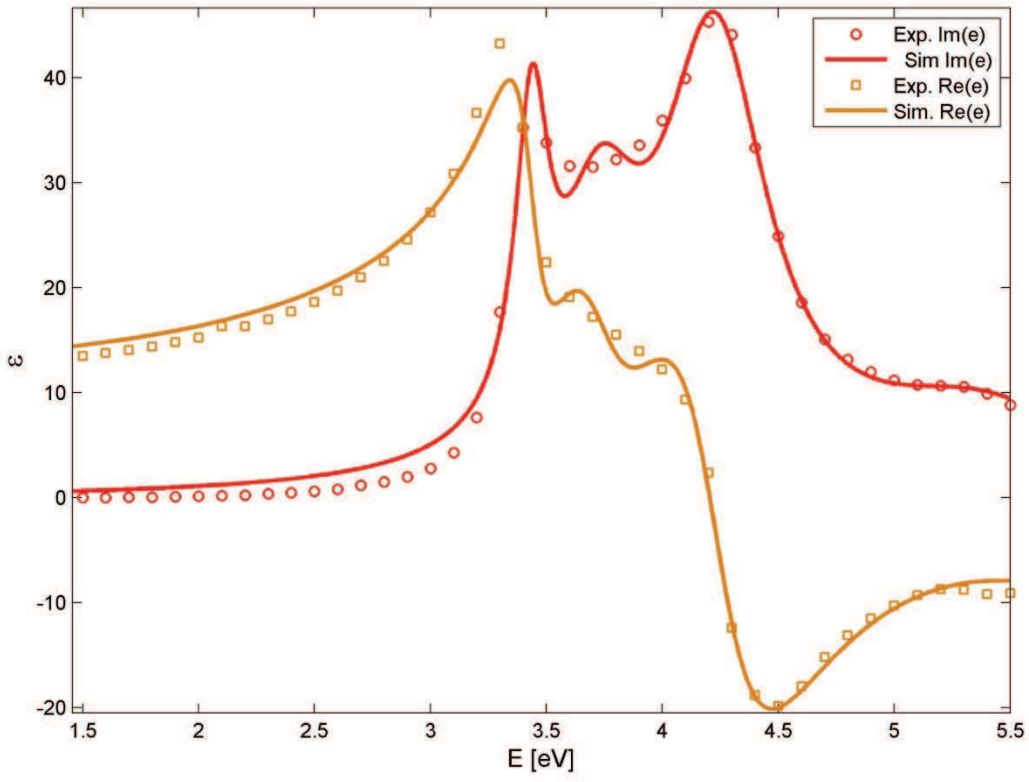

Figure III.8. Classical Lorentz model for silicon in energy range E = 1.5 to 5.2 eV, with three oscillator energies. The classical model offers a good qualitative representation and long-range predictability, but lacks accuracy.

Nevertheless, in most real cases an accurate representation of experimental data is preferred over long-range predictability; therefore we conducted a test where we assumed several more critical frequencies for oscillator transitions. With eight possible transitions at non-physical characteristic energies, the HMO approximation becomes much more accurate, but no longer has its predictive ability in the studied energy range, since some of the parameters C_0, Γ and ω_g no longer can be associated with physical quantities. The critical energies used in the fit shown in the figure III.9 are E_{g1} = 3.369, E_{g2} = 3.47, E_{g3} = 3.605, E_{g4} = 3.779, E_{g5} = 3.988, E_{g6} = 4.238, E_{g7} = 4.452 and E_{g8} = 5.049 eV. As can be seen in figure III.9, even doubling the number of critical energies in the energy range E = 1.5 to 5.2 eV, does not yield the accuracy necessary for precise predictions of device performance. Especially the areas around the first direct band gap are still not represented well enough with plenty of artefacts. Also, the absorption (resulting from ε_2) below E = 3.34 eV is somewhat overestimated, sometimes even doubled.

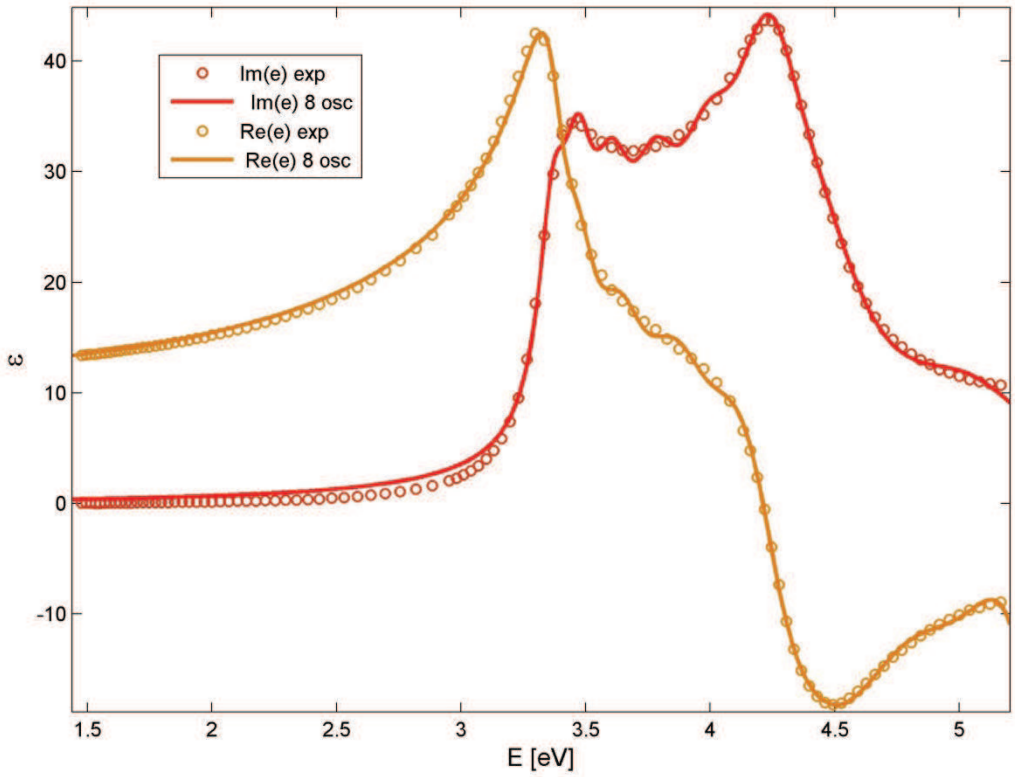

Figure III.9. Eight-oscillator fit of the crystalline Si dielectric function. Even when the number of resonant frequencies is doubled by introducing unphysical transitions, the accuracy of the fit is still poor.

2.2. Drude-Lorentz model in a limited energy range

The MIND structures present a highly P-doped upper emitter, as was shown in Chapter II, with a doping density often reaching the phosphorous solubility level in silicon. In such a case, we make the following three observations:

- free-carrier effects coming from the P-doping cannot be underestimated, and such are not taken into account in classical HMO model
- for a rigorous treatment of the electromagnetic field propagation in such a structure, where the doping level changes by two orders of magnitude over a sub-wavelength range (~200 nm), a predictive model is necessary
- to obtain such level of precision and maintain the predictive capabilities, the classical HMO model is not sufficient.

Free-carrier effects in non-polar semiconductors and metals are usually well approximated by renowned Drude model. In this approximation carriers are treated as non-interacting gas of uncharged particles that can collide only with relatively immobile ions.

In this approximation we are looking for a solution of equation (III.2.28) far away from any transitions, and thus we find:

$$x = \frac{eE_0}{m^*}\frac{e^{-i\omega t}}{\omega^2 + i\omega\Gamma} \tag{III.2.36}$$

The polarization is expressed as:

$$P = -Nex = \frac{-Ne^2}{m^*}\frac{E_0 e^{-i\omega t}}{\omega^2 + i\omega\Gamma} \tag{III.2.37}$$

where N is the free-electron density. Since $P = (\varepsilon\text{-}1)\varepsilon_0 E$, we can write:

$$\tilde{\varepsilon} = 1 - \frac{Ne^2}{m^*\varepsilon_0}\frac{1}{\omega^2 + i\omega\Gamma} \tag{III.2.38}$$

After some rearrangements we find a more convenient formula incorporating the Drude parameters:

$$\tilde{\varepsilon} = 1 - \frac{Ne^2}{\varepsilon_0 m_{opt} m_e \omega^2}\frac{1}{1 + i\frac{1}{\tau_D\omega}} \tag{III.2.39}$$

where τ_D is the Drude damping time, describing the mean time at which electrons collide with immobile ions, m_{opt} is electron optical mass and m_e is the rest mass of the electron [15]. Because in material bodies and at higher densities electron-electron interactions can no longer be neglected, τ_D does not have any physical meaning and is not linked to a real scattering time.

To enhance the accuracy of classical HMO, we followed the approach proposed by the group of Aspnes [16]. First, we will show that equation (III.2.35) can be expressed in the following manner without loss of generality:

$$\varepsilon = 1 + \sum_l \frac{C_{0l}^2}{\left(\omega_{gl} - \omega - i\omega\Gamma_l\right)\cdot\left(\omega_{gl} + \omega + i\omega\Gamma_l\right)} \tag{III.2.40}$$

Given that HMO expressions are known to give reasonable representations of the dielectric response of semiconductors above the fundamental absorption edge [17,18], the main problem to be addressed is the suppression of non-physical optical absorption in the region of transparency or near-transparency. We begin by noting that equation (III.2.40) can be generalized to include the effects of k-space integration on both lineshape and broadening

parameters by changing the orders of the poles and including phase factors. For a single critical point the result is:

$$\varepsilon = \varepsilon_\infty + C_0\left(e^{i\beta}\left(\omega_{gl} - \omega - i\omega\Gamma\right)^{\mu} + e^{-i\beta}\left(\omega_g + \omega + i\omega\Gamma\right)^{\mu}\right) \quad \text{(III.2.41)}$$

where C_0 is the single critical point amplitude, β is the phase of the pole and μ is the pole order. The rest of the parameters retain their usual meaning. The contribution of higher – lying poles is represented by ε_∞. Equation (III.2.41) satisfies causality (all poles lie in the lower half plane), reality $\varepsilon(\omega)=\varepsilon(-\omega)$, and is Kramers – Kronig consistent (converges as $\omega\rightarrow\infty$ as long as $\mu\rightarrow 0$). However, the plasma sum rule is not satisfied since the expression does not approach $-\frac{\omega_p^2}{\omega^2}$ when $\omega\rightarrow\infty$. The latter is not a limitation for a representation intended to be used only over a limited energy range, such as in our case.

After expanding equation (III.2.41) to first order around ω_g we obtain:

$$\varepsilon = \varepsilon_\infty + C_0\left[2Re\left[e^{i\beta}\left(\omega_{gl} - \omega - i\omega\Gamma\right)^{\mu}\right] + 2i\mu\omega Im\left[e^{-i\beta}\left(\omega_g + \omega + i\omega\Gamma\right)^{\mu-1}\right]\right] \quad \text{(III.2.42)}$$

To reduce the effect of Γ for low energies we subtract the second term from equation (III.2.41). After this operation, the resulting equation is no longer Kramers – Kronig consistent as it diverges for $\omega\rightarrow\infty$. If we also subtract the zero-frequency limit of equation (III.2.41) from equation (III.2.42), all contributions are suppressed to second order in ω. This allows the expression to be divided by ω^2, recovering Kramers – Kronig consistency for $\mu < 0$ while retaining suppression of ε_2 in the region of transparency. The complete expression is:

$$\varepsilon = \varepsilon_\infty + \sum_j \frac{C_{0j}}{\omega^2}\Big[e^{i\beta_j}\left(\omega_{gj} - \omega - i\Gamma_j\right)^{\mu_j} + e^{-i\beta_j}\left(\omega_{gj} + \omega + i\Gamma_j\right)^{\mu_j} - 2Re\left(e^{-i\beta_j}\left(\omega_{gj} + i\Gamma_j\right)^{\mu_j}\right) - 2i\mu_j\omega Im\left(e^{-i\beta_j}\left(\omega_{gj} + i\Gamma_j\right)\right)^{\mu_j-1}\Big] \quad \text{(III.2.43)}$$

Equation (III.2.43) has the capability to accurately model optical properties of semiconductors in a limited energy range, with a precision excelling the classical HMO model by several orders of magnitude. The results for crystalline Si are shown in figure III.10.

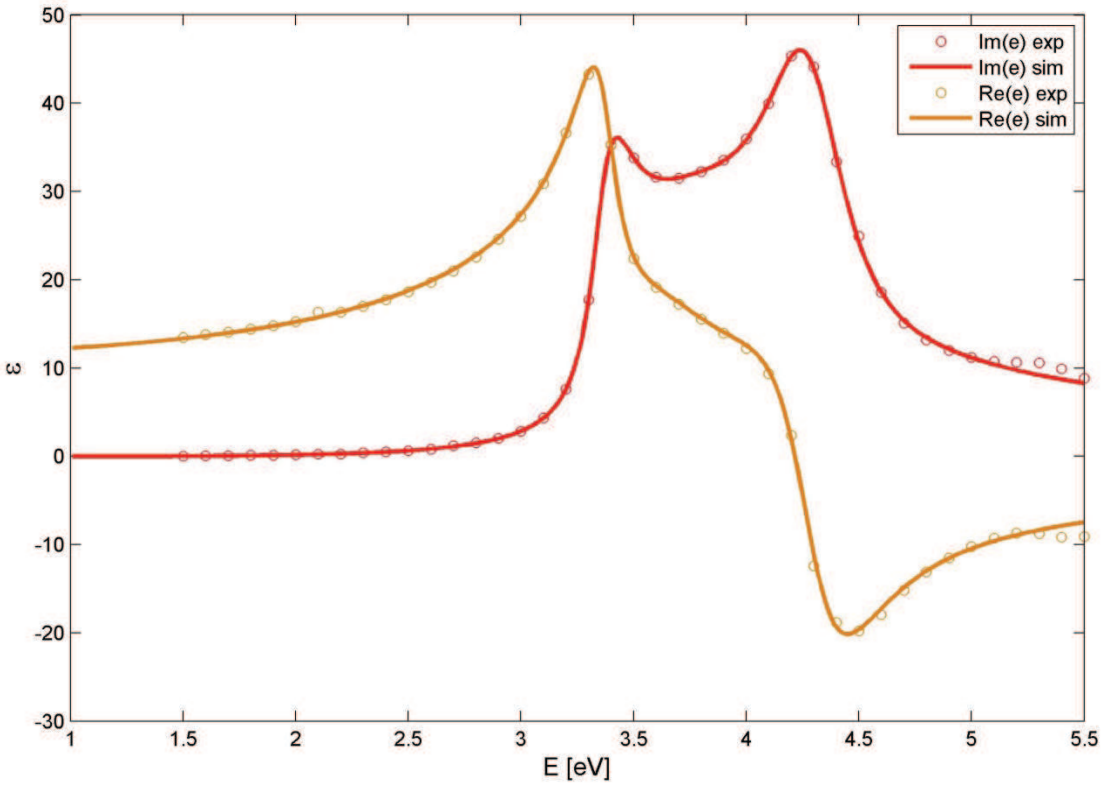

Figure III.10. Modified Lorentz (equation III.2.43) fit for cSi. The goodness for this particular fit was R = 0.9998. Experimental data taken from [19].

To properly address the problem of the inhomogeneous doping distribution in MIND structures, each of the model parameters C_0, Γ, β, m and ω_g must become a function of dopant density N_d and free-carrier effects must be incorporated. In such a case, the complete expression for the dielectric function for any P-doping density between intrinsic and maximum doping level (determined by solubility [19]) becomes:

$$\begin{aligned}\varepsilon(\omega, N_d) = \varepsilon_\infty + \sum_j \frac{C_{0j}(N_d)}{\omega^2}\Big[& e^{i\beta_j(N_d)}\left(\omega_{gj}(N_d) - \omega - i\Gamma_j(N_d)\right)^{\mu_j(N_d)} \\ & + e^{-i\beta_j(N_d)}\left(\omega_{gj}(N_d) + \omega + i\Gamma_j(N_d)\right)^{\mu_j(N_d)} \\ & - 2Re\left(e^{-i\beta_j(N_d)}\left(\omega_{gj}(N_d) + i\Gamma_j(N_d)\right)^{\mu_j(N_d)}\right) \\ & - 2i\mu_j(N_d)\omega Im\left(e^{-i\beta_j(N_d)}\left(\omega_{gj}(N_d) + i\Gamma_j(N_d)\right)^{\mu_j(N_d)-1}\right)\Big] \\ & - \frac{N_{e-h}e^2}{\varepsilon_0 m_{opt} m_e \omega^2}\frac{1}{1 + i\frac{1}{\tau_D \omega}}\end{aligned} \tag{III.2.44}$$

However, determining the functional dependency of model parameters from solid state theory is quite challenging and because of introduced modifications, can only be done to some extent. Therefore we determined the tendency for each parameter, resulting from the changes in physical quantities they represent or are associated with.

Parameters	Doping concentration N_d [1/cm3]					
	$1*10^{14}$	$2.30*10^{19}$	$7.70*10^{19}$	$2.30*10^{20}$	$7.70*10^{20}$	$2.30*10^{21}$
C1	69.56	68.1	65.53	62.1	57	50.62
C2	239.3	316.5	343	335.7	325.3	311.9
C3	92	89	86	83	77	66.88
Γ1	0.09775	0.12	0.1353	0.1582	0.2045	0.3098
Γ2	0.361	0.345	0.3408	0.3396	0.346	0.381
Γ3	0.2316	0.2801	0.3042	0.3264	0.3668	0.4594
β1	0.3582	0.5648	0.63	0.6465	0.596	0.5
β2	0.307	0.089	0.03906	0.03642	0.06536	0.1675
β3	0.004174	0.1891	0.3238	0.4878	0.6708	1.001
|μ1|	0.6976	0.7328	0.7501	0.7685	0.8193	0.9533
|μ2|	0.4398	0.3149	0.2966	0.3108	0.3331	0.3743
|μ3|	1.141	1.244	1.319	1.376	1.447	1.552
Eg1	3.368	3.356	3.351	3.35	3.35	3.35
Eg2	3.654	3.621	3.604	3.592	3.606	3.636
Eg3	4.287	4.285	4.28	4.263	4.239	4.2
R-square	0.9998	0.9999	0.9999	0.9999	0.9999	0.9997
SSE	1.0909	2.2556	1.4831	0.9643	0.8062	0.6568

Table 1. Parameters used in the three-oscillator model for five doping concentrations N_d. Goodness of fit (R) and Sum of Squared Errors (SSE) are presented for each doping density.

The more detailed description of this study can be found in one of our recent papers [20] and will be only briefly mentioned here.

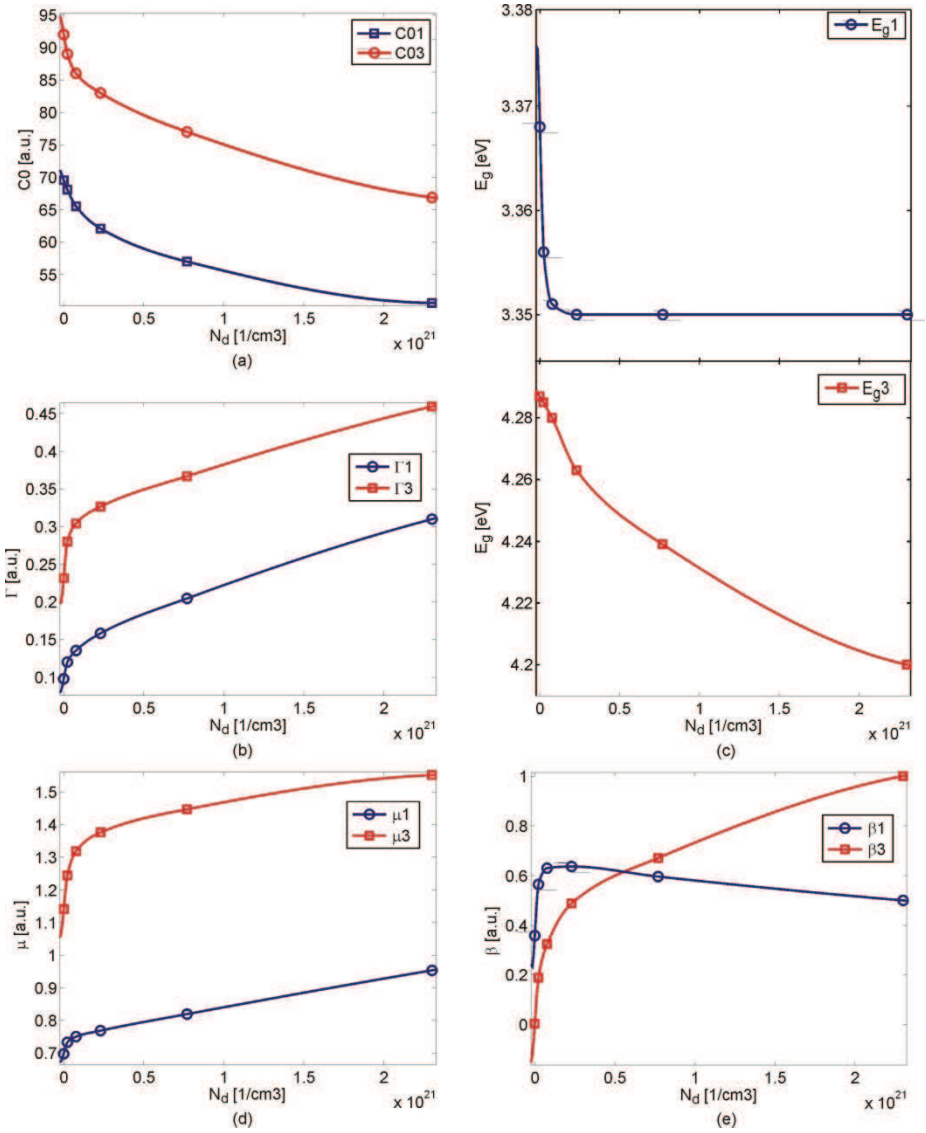

Figure III.11. Evolutions of oscillator amplitude C_0, broadening parameter Γ and critical point energy E_g versus doping density are presented on graphs (a), (b) and (c), respectively. The lower two panels show the changes of the pole order $|\mu|$ (d) and the pole phase factor β (e) versus doping concentration are presented. Tendency lines were obtained by calculating a piece-wise polynomial for each pair of points.

In the most general case, the oscillator amplitude C_0 decreases with increasing doping concentration because of the additional defects and lattice disturbances caused by the introduction of an alien atom, while the broadening parameter Γ tends to increase for the same reasons. The critical point energy E_g (or frequency ω_g) shows a slight shift towards lower energies due to the renormalization of the band structure caused by an additional free-carrier population originating from doping and state-and-band filling. It has been stated before that the condition $\mu < 1$ is necessary to satisfy Kramers – Kronig relations and we expect the pole

order μ to decrease as the doping density increases. This is because the associated oscillator strength becomes relatively weaker, while the phase factor $|\beta|$ should increase with doping concentration due to the increased fraction of Brillouin Zone over which band transitions take place. As can be seen in figure III.11, the parameter $|\mu|$ varies similarly as the corresponding broadening coefficient Γ.

Parameters corresponding to an oscillator with critical energy $E_g \approx 3.62$ eV have a slightly different behaviour than predicted. This might be due to additional mechanisms at this transition that are not present for transitions at $E_g = 3.38$ and 4.29 eV. Parameters of the three-oscillator model (for five different doping densities) are listed in Table 1.

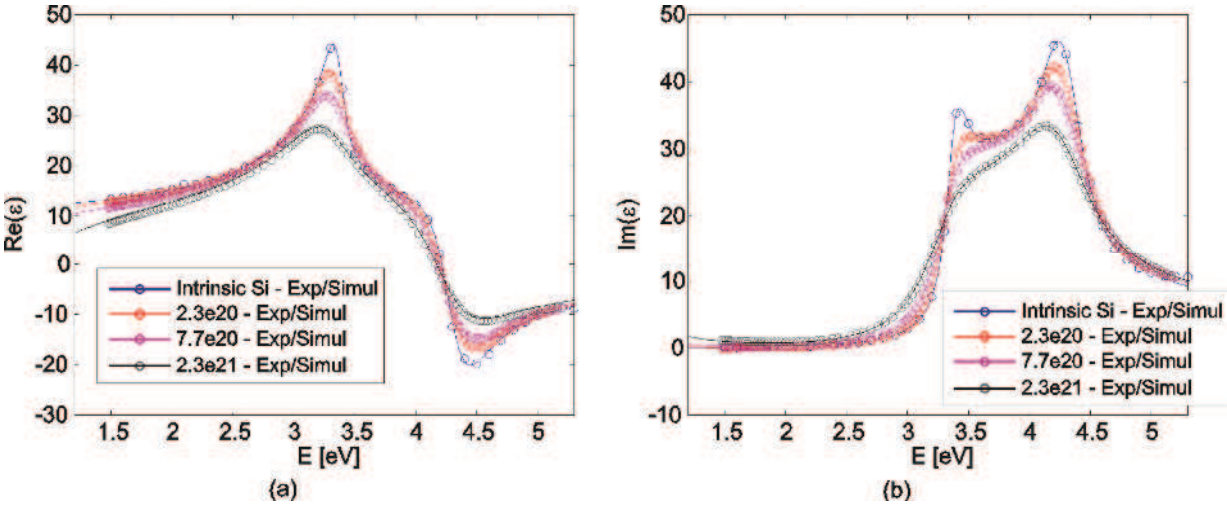

Figure III.12. Simulated (solid line) and experimental (points) data for different P-doping concentrations.

The model reproduces the experimental results from reference [19] very accurately for the whole energy range from $E = 1.0$ to 5.5 eV and for the whole doping density range $N_d = 10^{14}$ to $2.3 \cdot 10^{21}$ cm^{-3}, where the first value corresponds to intrinsic, float-zone Si and the last value is the over-solubility level of P in Si at 300 K, obtained by a special implantation technique presented in the work of Jellison. Comparisons of experimental data with the functions predicted by our model are shown in figure III.12. Determination of parameters evolution and their functional dependence for N_d allows prediction of dielectric function for any given doping concentration, not only those measured experimentally. Results of such predictions are shown in figure III.13.

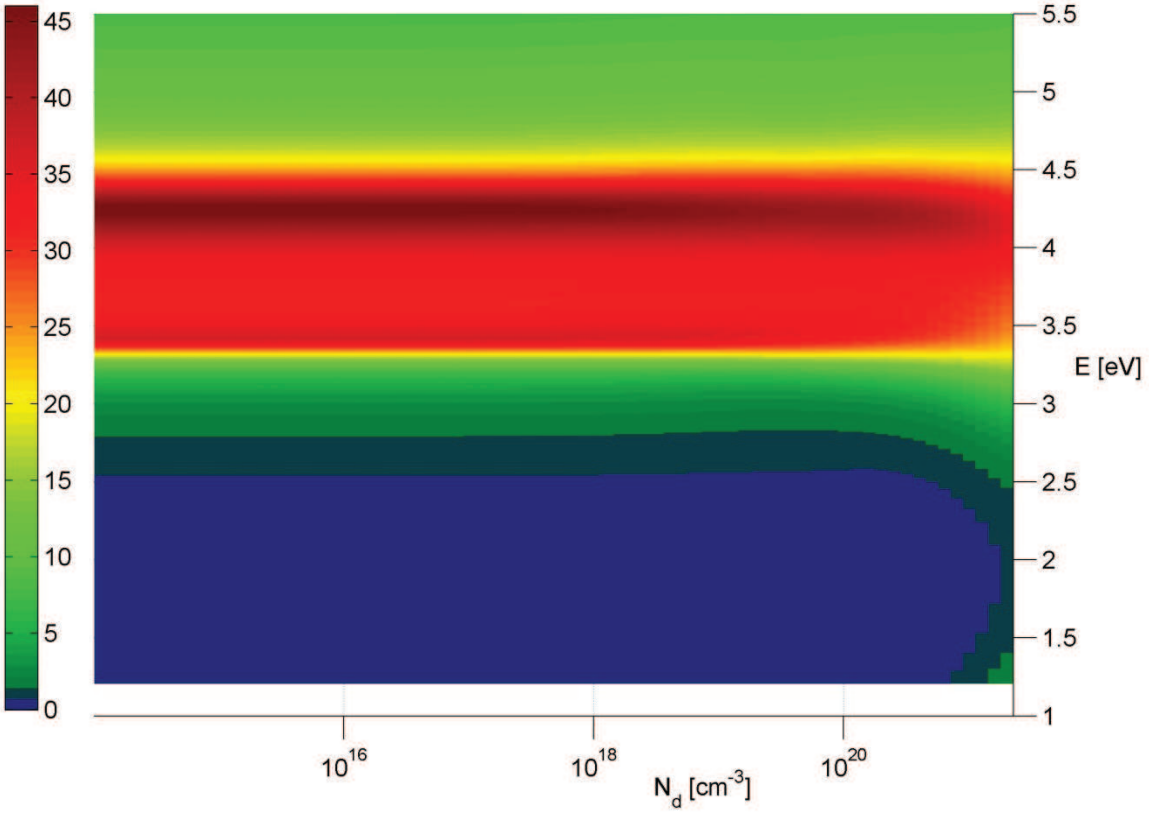

Figure III.13. Imaginary part Im(ε) of complex dielectric function of Si for the whole doping range $N_d = 10^{14}$ to $2.3 \cdot 10^{21}$ cm^{-3}. Free-carrier effects become visible at low energies and for very high doping densities.

The model presented here is able to determine changes in the dielectric function independently of the lattice disturbance, i.e., in the case of injection or excitation of the dense free-carrier gas. As can be seen in figure III.14 (a), the influence of free-carriers on the dielectric function appears mainly at low energies, being negligible in the range around the direct transition peak at $E = 3.4$ eV and above, where the most important role is played by lattice disturbances and effects introduced by doping. In figure III.14 (a), one can clearly see that the free-carrier related Drude part of the dielectric function that is present for energies $E = 1\text{-}3$ eV for the densities studied, is mainly responsible for the changes of reflectivity. However, it has little or no significance around the main transition peaks. For the highest presented density $N = 4 \cdot 10^{21}$ cm^{-3}, one can observe the appearance of the so-called plasma minimum around $E = 1.1$ eV. This minimum in reflectivity depends on carrier density N, carrier optical mass m_{opt} and carrier damping time τ and tends to move towards higher energies when N increases and/or τ and m_{opt} decrease. For higher free-carrier densities,

ultimately near-metallic values, the reflectivity reaches values close to unity. One has to keep in mind that the existence and measurement of such high carrier densities in Si is possible only on a femtosecond-time scale [21, 22].

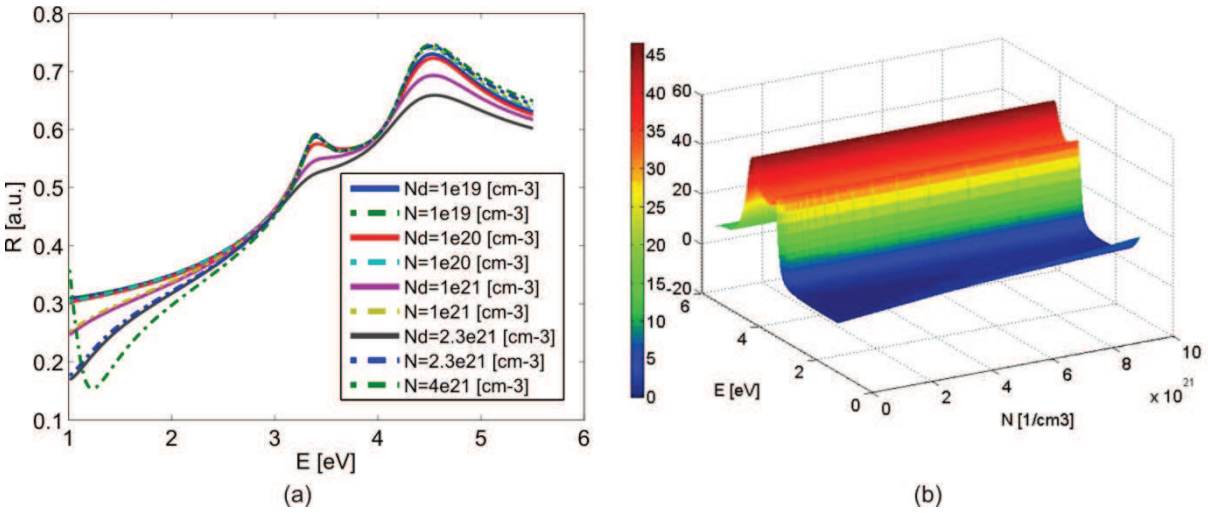

Figure III.14. Simulated reflectivity *R* (a) for different P-doping concentrations (solid curves) and corresponding density of excited free-carriers (dot-dashed curves). Simulated response of Im(ε) for free-carrier densities covering the range from intrinsic to near-metallic (b).

Reflectivity changes due to appearance of an additional free–carrier population are described in detail in the following chapters of this work.

3. Transition Matrix Approximation. Simulation of a 1D layered structure.

There are many optical models that allow rigorous treatment of electromagnetic wave propagation through different types of media. The most widely used approaches are the Finite Difference Time Domain (FDTD) method [23,24], the Beam Propagation Method (BPM) [25], the Rigorous Coupled Wave Analysis (RCWA) [26] and the Transition Matrix Approximation (TMA) [27,28]. In most cases, those models are designed to accurately address the problem of field distribution and wave propagation in dielectrics and weakly absorbing media, but with some modifications they are also capable of treating complex problems in highly conductive media [29].

While most of those approaches are capable of analyzing EM propagation in one, two and three dimensions, transitions to higher dimensions do not often come in pair with optimization for dedicated purposes. Since we are mainly concerned with layered structures with no obvious distinctive features inside each layer, our problem can be reduced to electromagnetic

wave propagation through a 1D structure. MINDs, apart some scattering effects that occur on the surface and at interfaces, are plain layered structures and can be accurately modeled with such 1D approach.

As a numerical tool we have chosen the TMA, and we will follow the introduction presented in highly renowned work of P. Yeh [27], with some slight modifications suitable for our case. Let us start by introducing the expression for a wave propagating inside a thin, homogeneous layer:

$$E(x,z) = E(x)e^{i\beta z} \tag{III.3.1}$$

The electric field distribution in each homogeneous layer (see figure III.15) can be expressed as the sum of the incident and reflected plane waves. As a result, the amplitudes of the field inside the n^{th} layer can be represented as a column vector:

$$\begin{bmatrix} A_n \\ B_n \end{bmatrix} \tag{III.3.2}$$

We designate the amplitudes at the beginning of the layer with prime, while non-primed amplitudes mark the field at the end of a layer. As a result, the field distribution in the same layer can be written as:

$$E(x,z) = \left(A'_n e^{ik_{x,n}x} + B'_n e^{-ik_{x,n}x}\right)e^{i\beta z} \tag{III.3.3}$$

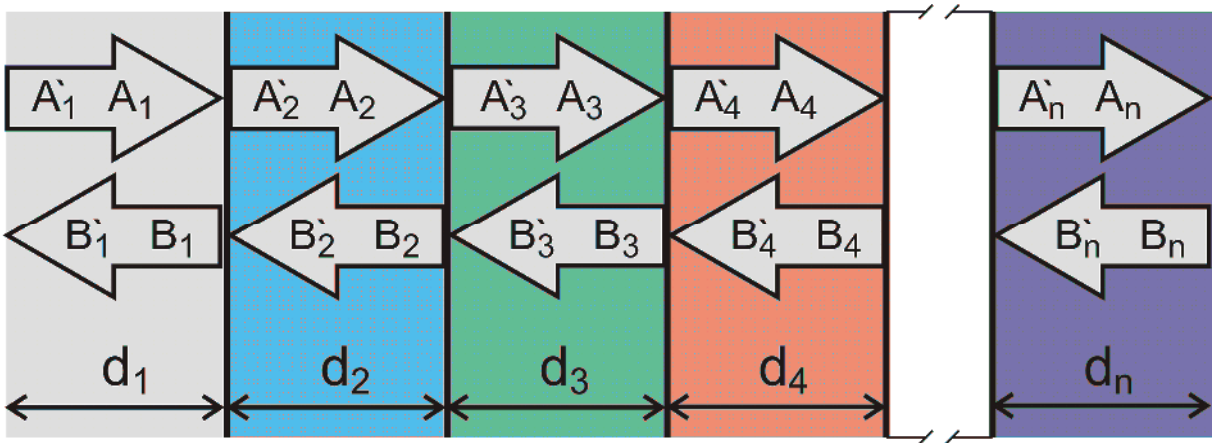

Figure III.15. Schematic representation of a stationary electromagnetic field propagating in a 1D medium composed of *n* arbitrary layers.

with:

$$k_{x,n} = \left\{\left[\left(\frac{\omega}{c}\right)\tilde{n}_n\right]^2 - \beta^2\right\}^{1/2} \tag{III.3.4}$$

and the following relation between vectors *A', B'* and *A, B* due to propagation in one layer is:

$$A_n + B_n = A'_n e^{ik_{x,n}d_n} + B'_n e^{-ik_{x,n}d_n} \tag{III.3.5}$$

The column vectors are not independent of each other, but are related through the continuity equations at the interfaces. In fact, only one vector can be chosen arbitrarily. In the case of TE waves (*s* polarization, *E* vector in *y*-*z* plane), imposing continuity of *E* and $\partial E/\partial x$ at the interface leads to:

$$\begin{aligned} A_n + B_n &= A'_{n+1} + B'_{n+1} \\ ik_{x,n}(A_n - B_n) &= ik_{x,n+1}(A'_{n+1} - B'_{n+1}) \end{aligned} \tag{III.3.6}$$

By eliminating the primed vectors A` and B`, a matrix equation:

$$\begin{pmatrix} A_{n+1} \\ B_{n+1} \end{pmatrix} = M_n \begin{pmatrix} A_n \\ B_n \end{pmatrix} = \begin{pmatrix} a & b \\ c & d \end{pmatrix} \begin{pmatrix} A_n \\ B_n \end{pmatrix} \tag{III.3.7}$$

is obtained. The M matrix elements are as follows:

$$a = \frac{e^{ik_{x,n}d_{n+1}}}{2e^{ik_{x,n+1}d_{n+1}}} + \frac{k_{x,n}e^{ik_{x,n}d_{n+1}}}{2k_{x,n+1}e^{ik_{x,n+1}d_{n+1}}} \tag{III.3.8a}$$

$$b = \frac{e^{-ik_{x,n}d_{n+1}}}{2e^{ik_{x,n+1}d_{n+1}}} - \frac{k_{x,n}e^{-ik_{x,n}d_{n+1}}}{2k_{x,n+1}e^{ik_{x,n+1}d_{n+1}}} \tag{III.3.8b}$$

$$c = \frac{e^{ik_{x,n}d_{n+1}}}{2e^{-ik_{x,n+1}d_{n+1}}} - \frac{k_{x,n}e^{ik_{x,n}d_{n+1}}}{2k_{x,n+1}e^{-ik_{x,n+1}d_{n+1}}} \tag{III.3.8c}$$

$$d = \frac{e^{-ik_{x,n}d_{n+1}}}{2e^{-ik_{x,n+1}d_{n+1}}} + \frac{k_{x,n}e^{-ik_{x,n}d_{n+1}}}{2k_{x,n+1}e^{-ik_{x,n+1}d_{n+1}}} \tag{III.3.8d}$$

The link between amplitudes in the first and last layer, represented by their column vectors is given by a matrix TM:

$$\begin{pmatrix} A_n \\ B_n \end{pmatrix} = M_1 M_2 \ldots M_n \begin{pmatrix} A_1 \\ B_1 \end{pmatrix} = TM \begin{pmatrix} A_1 \\ B_1 \end{pmatrix} \tag{III.3.9}$$

In most cases, it is more convenient to declare only the amplitude of the incident wave in the first layer A_1, and to set the amplitude of the reflected wave in the last layer to zero $B_n = 0$, which equals semi-infinity. In such case, the relations between the new column vectors are as follows:

$$\begin{pmatrix} A_n \\ B_1 \end{pmatrix} = \begin{pmatrix} s_1 & s_2 \\ s_3 & s_4 \end{pmatrix} = SM \begin{pmatrix} A_1 \\ B_n \end{pmatrix} \tag{III.3.10}$$

where the matrix SM is related to the matrix TM by:

$$SM = \begin{pmatrix} a - \dfrac{b \cdot c}{d} & \dfrac{b}{d} \\ -\dfrac{c}{d} & \dfrac{1}{d} \end{pmatrix} \tag{III.3.11}$$

At this point total reflectivity and transmittance of a given structure can be calculated by relating the amplitudes of waves propagating in the first and last layer to reflection and transmission coefficients. Then, the field reflection and transmission coefficients are equal to:

$$r = \left|\frac{B_1}{A_1}\right| \tag{III.3.12a}$$

$$t = \left|\frac{A_n}{A_1}\right| \tag{III.3.12b}$$

and associated power reflection and transmission coefficients are:

$$R = r^2 \tag{III.3.13a}$$

$$T = \frac{\tilde{n}_n}{\tilde{n}_1} t^2 \tag{III.3.13b}$$

Column vectors representing amplitudes of the field in each layer of the structure can be calculated by going back to the step described by equation (III.3.9).

In the case of TM waves, elements of the M_{TM} matrix are significantly different from those in the TE case:

$$a_{TM} = \frac{e^{ik_{x,n}d_{n+1}}}{2e^{ik_{x,n+1}d_{n+1}}} + \frac{\varepsilon_{n+1}k_{x,n}e^{ik_{x,n}d_{n+1}}}{2\varepsilon_n k_{x,n+1}e^{ik_{x,n+1}d_{n+1}}} \tag{III.3.14a}$$

$$b_{TM} = \frac{e^{-ik_{x,n}d_{n+1}}}{2e^{ik_{x,n+1}d_{n+1}}} - \frac{\varepsilon_{n+1}k_{x,n}e^{-ik_{x,n}d_{n+1}}}{2\varepsilon_n k_{x,n+1}e^{ik_{x,n+1}d_{n+1}}} \tag{III.3.14b}$$

$$c_{TM} = \frac{e^{ik_{x,n}d_{n+1}}}{2e^{-ik_{x,n+1}d_{n+1}}} - \frac{\varepsilon_{n+1}k_{x,n}e^{ik_{x,n}d_{n+1}}}{2\varepsilon_n k_{x,n+1}e^{-ik_{x,n+1}d_{n+1}}} \tag{III.3.14c}$$

$$d_{TM} = \frac{e^{-ik_{x,n}d_{n+1}}}{2e^{-ik_{x,n+1}d_{n+1}}} + \frac{\varepsilon_{n+1}k_{x,n}e^{-ik_{x,n}d_{n+1}}}{2\varepsilon_n k_{x,n+1}e^{-ik_{x,n+1}d_{n+1}}} \tag{III.3.14d}$$

By definition, the Poynting vector is given by:

$$\boldsymbol{S} = \boldsymbol{E} \times \boldsymbol{H} \tag{III.3.15}$$

and its time-averaged value is given by the following:

$$\langle \boldsymbol{S} \rangle = \frac{1}{2} Re\left(\tilde{\boldsymbol{E}} \times \tilde{\boldsymbol{H}}^*\right) \tag{III.3.16}$$

The energy density in non-magnetic materials is given by:

$$U = \frac{1}{2}(\boldsymbol{E} \cdot \boldsymbol{D} + \boldsymbol{H} \cdot \boldsymbol{B}) \tag{III.3.17}$$

The above formalism was implemented in the Matlab code which allows throughout analysis of 1D dielectric-semiconductor structures composed of an arbitrary number of layers. The core of the code, responsible for the TMA formalism, is presented below:

```
% ------------------------------------ %
% NUMBER OF LAYERS - modify also parameter d
m=4;
% ------------------------------------ %
% Setting layer thickness
d=[100 100 100 100];
% Wavelength
l=300;
eps(1)=1;
eps(2)=2.25+0.1i;
eps(3)=4.5+2.2i;
eps(4)=1;
mi=1.0;

for j=1:m
% Refraction index
n(j)=sqrt((real(eps(j))+sqrt((real(eps(j)))^2+(imag(eps(j)))^2))/2)+1i*sqrt
((-real(eps(j))+sqrt((real(eps(j)))^2+(imag(eps(j)))^2))/2);
% Speed of Light in each layer
c(j)=3.0e8/real(n(j));
% Angular frequency
w(j)=2*pi*c(1)/l;
end

% Resolution
res=100;
% Amplitude of waves in each layer, known only A(1,1)&A(2,m) = incident
% wave & outgoing wave
for j=1:m
A(1,j)=0.0;
A(2,j)=0.0;
tetha(j)=0.0;
end
% Amplitude of the incident wave
A(1,1)=1.0;
% Incident angle (in degrees)
tetha(1)=15*pi/180.0;

% Mode selection
reply=input('Choose mode TE=1, TM=2 ');
disp(' ')
if reply==1
    mode=1;
else
    mode=2;
end

% Wavevector calculation
for j=1:m
k0(j)=2*pi*n(j)/l;
end
kx(1)=k0(1)*cos(tetha(1));
kz(1)=k0(1)*sin(tetha(1));
```

```
% Determining if there is total internal reflection and further calculation
% of wavevector components
for j=1:m-1
         k0(j+1)=2*pi*n(j+1)/l;
         kz(j+1)=kz(j);
         if ((n(j)*sin(tetha(j))/n(j+1))>1)
            kx(j+1)=sqrt(k0(j+1)^2-kz(j+1)^2);
            disp('TIR')
         else
            tetha(j+1)=asin(kz(j+1)/k0(j+1));
            kx(j+1)=k0(j+1)*cos(tetha(j+1));
            disp('NOR')
         end
end
% Boundary points for layers
xb(1)=0.0;
       for j=1:m
         xb(j+1)=xb(j)+d(j);
       end
% Matrix element calculation for each layer transition
for j=1:m-1
    if mode==1
%      A
TM(1,1,j)=exp(i*kx(j)*xb(j+1))/(2*exp(i*kx(j+1)*xb(j+1)))+kx(j)*exp(i*kx(j)
*xb(j+1))/(2*kx(j+1)*exp(i*kx(j+1)*xb(j+1)));
%      B
       TM(1,2,j)=exp(-i*kx(j)*xb(j+1))/(2*exp(i*kx(j+1)*xb(j+1)))-
kx(j)*exp(-i*kx(j)*xb(j+1))/(2*kx(j+1)*exp(i*kx(j+1)*xb(j+1)));
%      C
       TM(2,1,j)=exp(i*kx(j)*xb(j+1))/(2*exp(-i*kx(j+1)*xb(j+1)))-
kx(j)*exp(i*kx(j)*xb(j+1))/(2*kx(j+1)*exp(-i*kx(j+1)*xb(j+1)));
%      D
       TM(2,2,j)=exp(-i*kx(j)*xb(j+1))/(2*exp(-
i*kx(j+1)*xb(j+1)))+kx(j)*exp(-i*kx(j)*xb(j+1))/(2*kx(j+1)*exp(-
i*kx(j+1)*xb(j+1)));
    else
%      A
TM(1,1,j)=exp(i*kx(j)*xb(j+1))/(2*exp(i*kx(j+1)*xb(j+1)))+eps(j+1)*kx(j)*ex
p(i*kx(j)*xb(j+1))/(2*eps(j)*kx(j+1)*exp(i*kx(j+1)*xb(j+1)));
%      B
       TM(1,2,j)=exp(-i*kx(j)*xb(j+1))/(2*exp(i*kx(j+1)*xb(j+1)))-
eps(j+1)*kx(j)*exp(-
i*kx(j)*xb(j+1))/(2*eps(j)*kx(j+1)*exp(i*kx(j+1)*xb(j+1)));
%      C
       TM(2,1,j)=exp(i*kx(j)*xb(j+1))/(2*exp(-i*kx(j+1)*xb(j+1)))-
eps(j+1)*kx(j)*exp(i*kx(j)*xb(j+1))/(2*eps(j)*kx(j+1)*exp(-
i*kx(j+1)*xb(j+1)));
%      D
       TM(2,2,j)=exp(-i*kx(j)*xb(j+1))/(2*exp(-
i*kx(j+1)*xb(j+1)))+eps(j+1)*kx(j)*exp(-
i*kx(j)*xb(j+1))/(2*eps(j)*kx(j+1)*exp(-i*kx(j+1)*xb(j+1)));
    end
end
% System matrix, calculating total field after all interfaces
B=[1 0;0 1];
for ii=1:m-1
    M=TM(:,:,ii)*B;
    B=M;
```

```
end
TM(:,:,m)=M;

T1=TM(1,1,m);
T2=TM(1,2,m);
T3=TM(2,1,m);
T4=TM(2,2,m);
SM=[T1-T2*T3/T4 T2/T4; -T3/T4 1/T4];

% Amplitude after all interfaces
% Auxiliary vectors
A1m=[A(1,1);A(2,m)];
Am3=SM*A1m;
% Amplitudes after computation
A(2,1)=Am3(2);

for ii=1:m-1
    A(:,ii+1)=TM(:,:,ii)*A(:,ii);
end
Ap=A;
for j=2:m
   A(1,j)=A(1,j)*exp(real(1i*kx(j)*xb(j)));
end
r=(abs(A(2,1)/A(1,1)));
R=abs(r)^2
t=(abs(A(1,m)/A(1,1)));
T=abs(n(m))/abs(n(1))*abs(t)^2
% Call field visualization subroutine
field
% End of code
```

Results of a typical simulation of any layered structure, and MIND structure in particular, can be performed for both monochromatic and/or for a given spectral range of incident wavelengths.

Simulation for a monochromatic incident illumination yields E field distribution as a result, power and field reflectivity and transmission, R, r, T, t respectively and Pointing vector distribution in space as well as energy density distribution in space.

Simulation for any given spectral ranges yields, in addition to data provided by monochromatic simulation, also spectral reflection and transmission coefficients.

Results of both types of simulations for test structure shown in figure III.16, are presented below. Test structure is composed of six layers that are made of, looking from the direction of incidence: air, amorphous SiO_2, crystalline Si, P-doped $N_d = 10^{20}$ cm^{-3}, amorphous Si, P-doped $N_d = 10^{18}$ cm^{-3} and two layers of crystalline Si, P-doped $N_d = 10^{16}$ cm^{-3}. The last 10 nm thick layer represents the base. Thicknesses of the layers are shown in figure III.16. Monochromatic simulations were performed for $\lambda = 500$ nm, while spectral simulations were performed for a wavelength range $\lambda = 250$ to 1250 nm. Results for both types of simulation for the test structure are shown in figures III.17, III.18 and III.19.

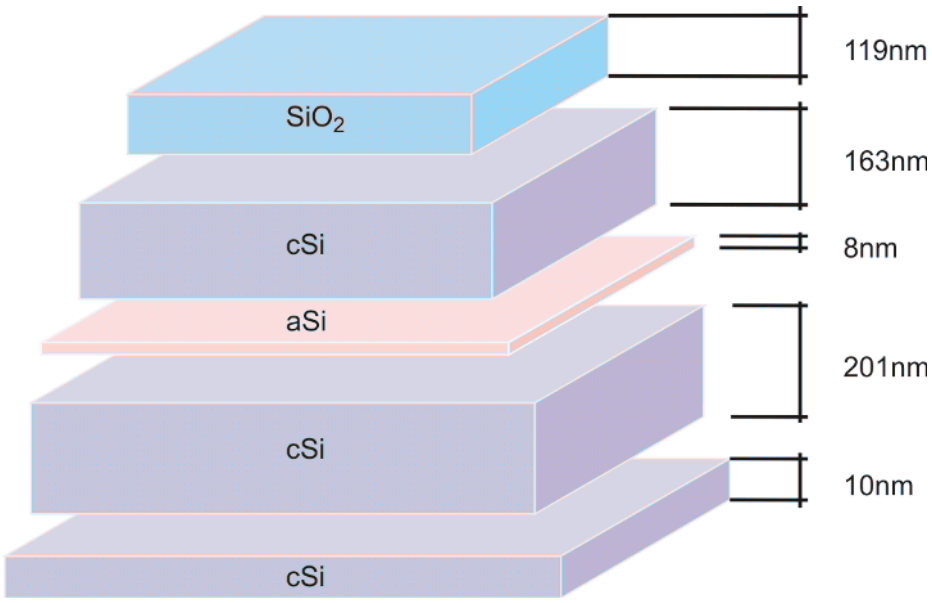

Figure III.16. An example of a simple MIND structure used for the test simulation. Layer thicknesses are shown for each of the layer, except for the layer of air (not shown), which has a thickness of zero. Light blue represents amorphous SiO_2, and shades of violet and rose represent crystalline and amorphous Si, respectively. The bottom layer of 10 nm thickness is in fact treated as semi-infinite and represents the substrate.

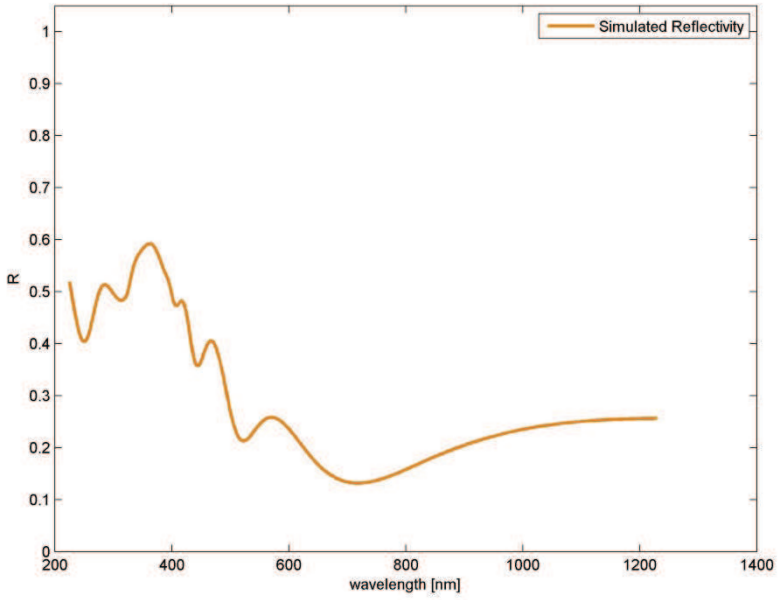

Figure III.17. Reflectivity R of the MIND test structure in the wavelength range $\lambda = 250$ to 1250 nm for normal incidence. Thanks to the passivation of Si, the reflectivity is reduced in regards to non-passivated Si. The peak at $\lambda = 370$ nm corresponds to the first direct band gap.

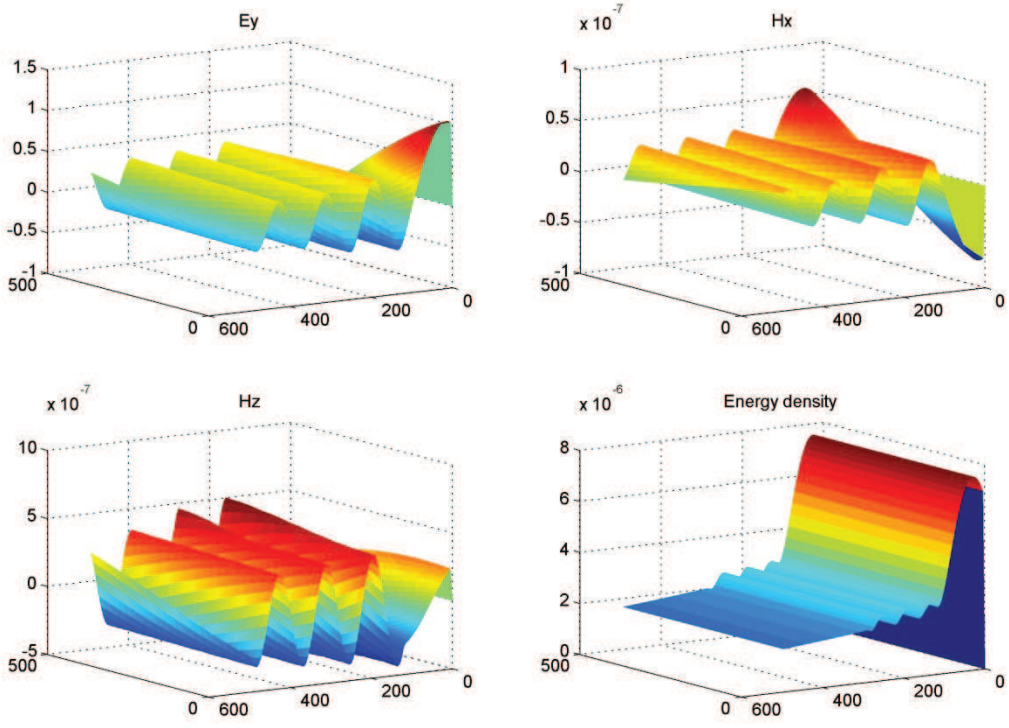

Figure III.18. Distribution of electric and magnetic fields E_y, H_z and H_x in test MIND structure shown in figure III.16 for $\lambda = 500$ nm. The energy density is shown in the lower right.

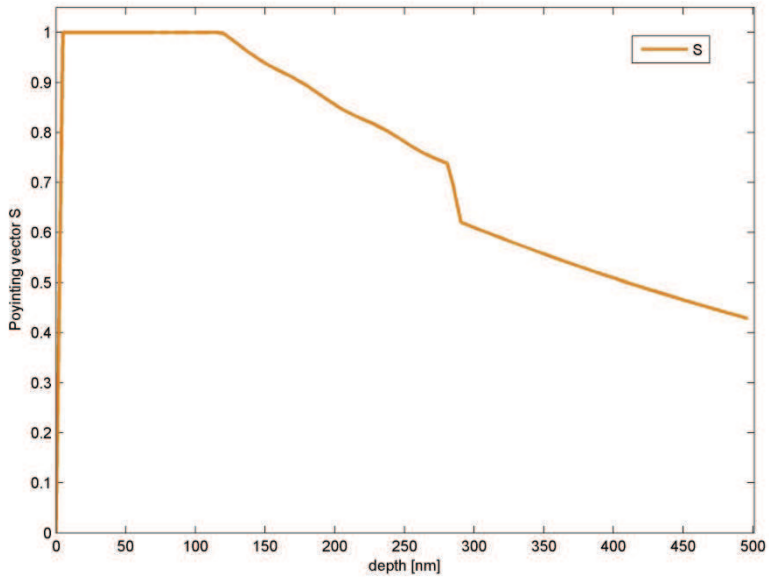

Figure III.19. Spatial distribution of the total time-averaged and normalized Poynting vector in MIND test structure for $\lambda = 500$ nm. Since the simulation is for the stationary case, the value of S decreases only in absorbing layers.

3.1. Interface between amorphous and crystalline Si. Effective Medium Theory.

Crystalline, optical and electrical properties of crystalline silicon (cSi) have been extensively reported in the literature for almost 40 years and were summarized in previous chapters of this work. Crystalline silicon forms regular crystals of diamond structure that have an indirect band gap of 1.12 eV, which changes as the Fermi level moves up with doping, reaching 1.17 eV for the heavily doped case, as was shown in Chapter I. Direct band gap in crystalline Si is equal to 3.4 eV, therefore every electron transition, such as resulting from photon absorption, between 1.12 and 3.4 eV has to be phonon-assisted.

Optical properties of cSi and their changes as a function of doping concentrations have been presented earlier in this chapter, as well as the electronic structure of both pure and heavily P doped cSi. Amorphous silicon (aSi) however, exhibits completely different optical, electrical and structural properties that transform it into a brand new semiconducting material. The interface between crystalline and amorphous silicon produces some properties that are linked with the specific features of both materials.

Even if amorphous silicon does not show a defined crystalline order, the placement of the atoms is not completely random. If we take crystalline Si as a starting material, there are many sites available for atoms in local energy minima, such as interstitial positions. These positions are usually unoccupied in good quality crystalline material, but when the crystal network is disturbed by doping or implantation, the foreign atoms cause some of the Si atoms to move to other positions, effectively distorting long range order and changing the phase of the material.

Amorphous silicon has an effective band gap ranging between 1.54 to 2.08 eV [30], which produces a mismatch in both the CB and VB for both materials. The interface between aSi and cSi has been extensively studied in the literature [31,32], but its exact properties depend strongly on the origin and features of the amorphous phase itself [33,34] and the doping in both the cSi and aSi [35,36]. In the case of MINDs, both crystalline and amorphous silicon are n type, which determines Fermi level in both materials. Resulting approximate band structure of the interface is shown in figure III.20.

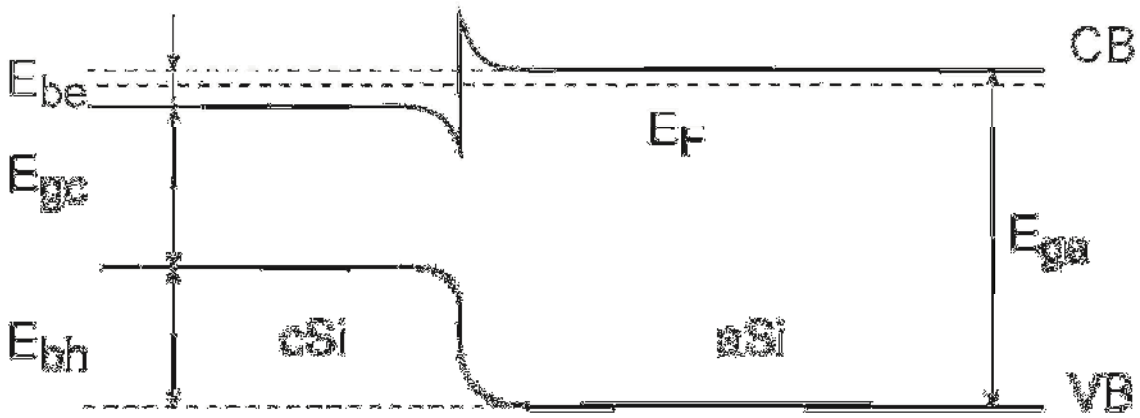

Figure III.20. Band structure of the aSi/cSi interface, after [37].

As can be seen on figure III.20, there is an effective barrier for holes caused by the aSi/cSi interface. The barrier height of $E_{bh} \approx 0.4$ eV is large enough to block transport of the minority carriers in the upper emitter in the junction direction. On the other hand, electrons experience a barrier of about $E_{be} \approx 0.15$ eV, which combined with the extremely high degeneracy of the emitter, giving raise to the Fermi level to a point above CB around 0.1 eV. In these conditions the low barrier for electrons can be crossed, thanks to the thermal energy at room temperature. Amorphous silicon has also a different dielectric function than crystalline Si, and therefore a different absorption coefficient. This property makes an amorphous/crystalline interface an optically active area, due to the change in the optical impedance. A comparison of dielectric functions for both amorphous and crystalline silicon is shown in figure III.21.

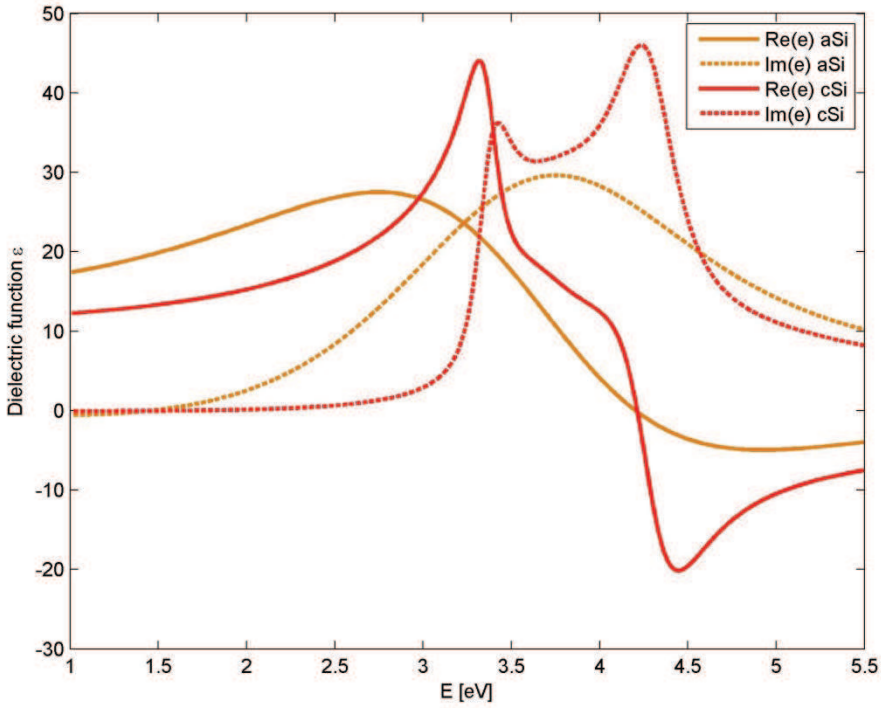

Figure III.21. Dielectric function of amorphous and crystalline silicon.

Amorphous silicon is created in MIND structures in a particular way, which results in a material somewhat different from the typical hydrogen-stabilized aSi:H. First of all, right after the amorphizing implantation there is no well-defined interface between the crystalline and amorphous phases; such an interface is created later by solid state epitaxy. Thermal processing sharpens the interface so that the transition between the crystalline phase and the amorphized phase becomes more distinct, however it is important to note that the positioning of the atoms in the aSi layer differs from those in stabilized aSi:H, and as a consequence one can assume that some electronic properties may be more sensitive due to abundance of the unsaturated and broken bonds (which would normally be saturated by hydrogen). Combination of above effects creates an extended aSi/cSi interface that does not exhibit the same properties over the same distance (for example strain or band structure) it is difficult to differentiate one material from the other. In such case, a material close to the interface does not have properties neither of crystalline nor amorphous silicon, but behaves as a medium that combines properties of both materials. The behavior of such materials can be approximated by the so-called Effective Medium Theory [38]. As the medium is composed of two different materials, one is treated as a host (described by a dielectric function ε_m) and other as an

inclusion phase (ε_i). In the literature, several mixing models can be found for the effective dielectric permittivity of such mixtures. Here we present only the ones that have gained the most attention.

For the case of circular or spherical inclusions, prediction of the effective permittivity of a mixture ε_{eff} according to the Maxwell-Garnett mixing rule is given by [39]:

$$\varepsilon_{eff} = \varepsilon_m + 2f\varepsilon_m \frac{\varepsilon_i - \varepsilon_m}{\varepsilon_i + \varepsilon_m - f(\varepsilon_i - \varepsilon_m)} \quad \text{(III.3.18)}$$

where f is the volume fraction occupied by the inclusion, that are randomly scattered in the matrix of the host material. The quasistatic nature of the mixture means that the wavelength is much larger that the inclusion diameter.

Another famous mixing approach was presented by Bruggeman [40], given by the following formula:

$$(1-f)\frac{\varepsilon_m - \varepsilon_{eff}}{\varepsilon_m + \varepsilon_{eff}} + f\frac{\varepsilon_i - \varepsilon_{eff}}{\varepsilon_i + \varepsilon_{eff}} = 0 \quad \text{(III.3.19)}$$

It is possible to gather both of the above formulas into one equation, by introducing a dimensionless parameter v [41]. The general formula is presented below:

$$\frac{\varepsilon_{eff} - \varepsilon_m}{\varepsilon_{eff} + \varepsilon_m + v(\varepsilon_{eff} - \varepsilon_m)} = f\frac{\varepsilon_i - \varepsilon_m}{\varepsilon_i + \varepsilon_m + v(\varepsilon_{eff} - \varepsilon_m)} \quad \text{(III.3.20)}$$

where for $v = 0$ we find Maxwell-Garnett formula, $v = 1$ gives the Bruggemann formula and $v = 2$ gives the Coherent potential approximation [42].

In modeling analysis power-law models are used quite often. These give the effective permittivity of a mixture as:

$$\varepsilon_{eff}^{\beta} = f\varepsilon_i^{\beta} + (1-f)\varepsilon_m^{\beta} \quad \text{(III.3.21)}$$

where β is a dimensionless parameter [43]. Different mixing models predict different effective permittivity values for a given mixture, and each has different range of validity. Therefore bounds for maximal and minimal values for effective ε exist, where the loosest are the so-called Weiner bounds [44]:

$$\varepsilon_{eff,max} = f\varepsilon_i + (1-f)\varepsilon_m \quad \text{(III.3.22a)}$$

and

$$\varepsilon_{eff,min} = \frac{\varepsilon_m \varepsilon_i}{f\varepsilon_m + (1-f)\varepsilon_i} \quad \text{(III.3.22b)}$$

For a statistically homogenous and isotropic mixture, other bounds have been generally accepted in the literature [45], based on a variational treatment of the energy functional for the mixture with the inclusions is distributed in three dimensions:

$$\varepsilon_{eff,min} = \varepsilon_m + \frac{f}{\frac{1}{\varepsilon_i - \varepsilon_m} + \frac{1-f}{3\varepsilon_m}} \quad \text{(III.3.23a)}$$

and

$$\varepsilon_{eff,max} = \varepsilon_i + \frac{1-f}{\frac{1}{\varepsilon_m - \varepsilon_i} + \frac{f}{3\varepsilon_i}} \quad \text{(III.3.23b)}$$

In the case of amorphous Si or the amorphous/crystalline interface, there might exist small areas where microcrystals of silicon are suspended in the amorphous matrix, giving validity to this kind of approximation [46].

3.2. Optical simulation of MIND structures.

MIND structures, as introduced in Chapter II of this work, all share a similar conceptual design that influences their architecture. In the most general description, a stack of layers with thicknesses in the range of nanometers is introduced on the top of a crystalline Si wafer. These layers are in most cases ordered as follows: a passivation layer, made of SiO_2, Si_3N_4 or Indium Tin Oxide (ITO), a heavily P-doped crystalline Si layer (cSi:P), a heavily P-doped amorphous Si layer (aSi:P) and a transition zone of P-doped crystalline Si.

When analyzing optical and electrical properties of such structures several factors have to be taken into account. It is convenient to begin with the optical properties when one intends to perform rigorous analysis/optimization of the solar converters, since the interaction of light and active areas occur first in the photovoltaic process, followed by subsequent carrier generation. In any solar cell, the ultimate goal for structure optimization is the following – if the total flux $\Phi = R + T + A$ can be decomposed into reflectivity, transmission and absorption components, an optimized, theoretical solar cell should minimize R and T while maximizing A, and all of A should be limited to the active area(s). In the case of MIND structures, the whole Si substrate is also an active area, and its total thickness is d_{tot} =1 mm exceeds the penetration depth for band gap energy photons several times. With the transmission $T = 0$, the remaining components R and A of the total flux can be estimated. It is easy to see that minimizing R will directly impact A and therefore the overall power conversion efficiency of the cell.

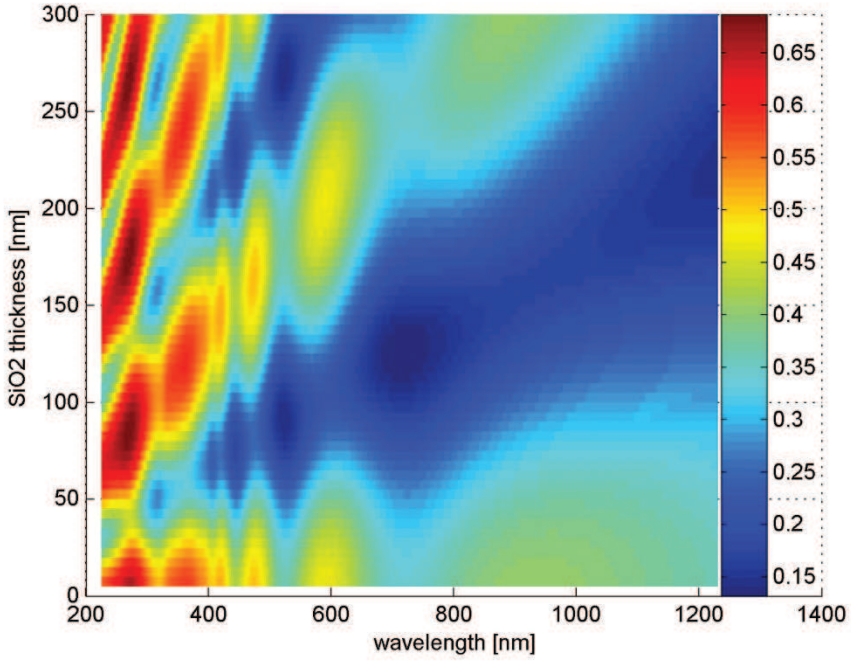

Figure III.22. Reflectivity of a typical MIND structure for different passivation thicknesses. The passivation layer is made of amorphous SiO_2.

Total reflectivity of a MIND structure can be dependent on two major factors: the geometry of the layers and the fraction of surface covered by the top electrodes. Electrodes cause an effect called shading, which reduces cell performance by creating inactive areas in the cell, directly below them. Apart from shading, the reflectivity of the electrodes affects the experimental value of total *R*, which is also strongly dependent on sample positioning and spot size. This effect can lead to serious systematic errors in the further analysis.

The part of the reflectivity related to the structure geometry can be then influenced by the passivation layer, the emitter thickness and amorphous layer thickness. We performed various simulations involving varying thicknesses and composition in each of those layers. If it is not stated otherwise, the thicknesses are as follows: passivation – 119 nm, upper emitter – 163 nm, aSi – 10 nm and substrate which in simulation is assumed to be semi-infinite. We have found that the passivation layer reduces the value of R in comparison with non-passivated Si, but does not shift the interference fringes. Results for both amorphous SiO_2 and Si_3N_4, for thicknesses d = 5-300 nm, are shown in figure III.22 and III.23.

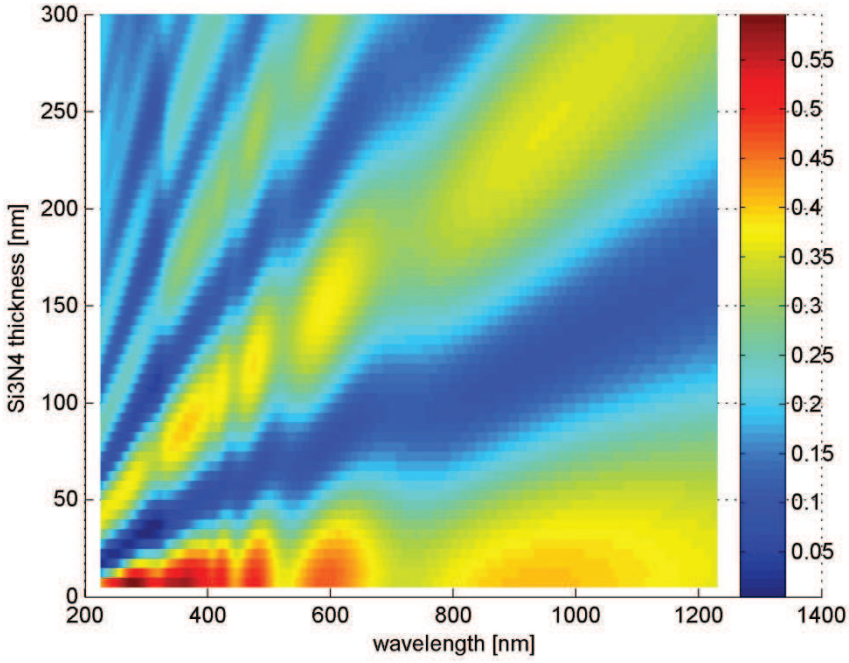

Figure III.23. Reflectivity of a typical MIND structure for different passivation thicknesses. The passivation layer is made of amorphous Si_3N_4.

The optimal passivation thickness is dependent on the material used, and for $aSiO_2$ it was found to be between 95 and 115 nm. In the case of Si_3N_4, the optimal passivation thickness was thinner, between 80 and 100 nm.

The influence of emitter thickness and amorphous layer was found to be completely different. As the emitter thickness increases, the interference fringes do not change their intensity but are shifted towards longer wavelengths. It is difficult to estimate the optimal thickness for an emitter, because of the complex requirements that need to be met in order to create the photovoltaic metamaterial, as introduced in chapter II. The emitter induces the strain field necessary for the PV metamaterial to form, the entire emitter area is inactive due to the barrier for holes that comes along the aSi layer. Nevertheless, putting all those complex connexions aside, from optical point of view the lowest reflectivity is obtained for thicknesses between 150-170 nm, for the visible spectral range.

The amorphous layer, which is the key component in PV metamaterial formation, has the strongest influence on the interference fringes and is in fact the reason behind their appearance. If an aSi layer is absent, R has exactly the same value as regular, heavily doped Si.

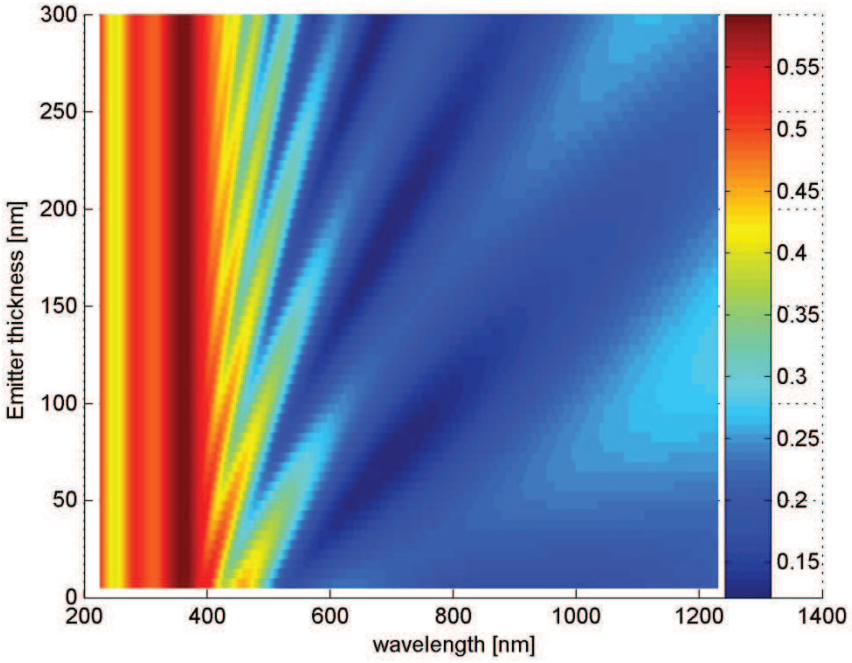

Figure III.24. Reflectivity of a typical MIND structure for different emitter thicknesses. An optimal thickness lies between 150 and 170 nm, if reflectivity only is taken into account.

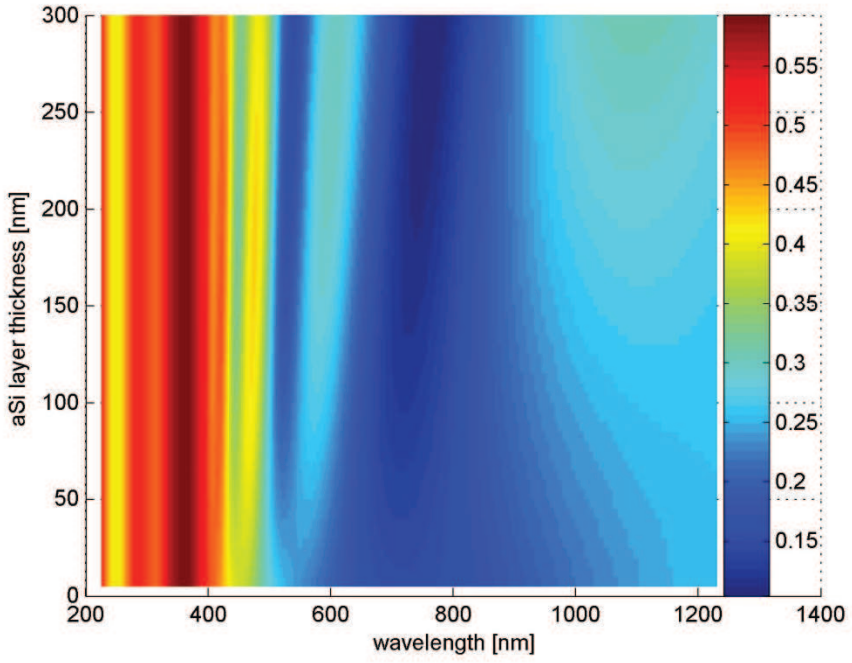

Figure III.25. Reflectivity of a typical MIND structure for different amorphous layer thicknesses. Interferences amplitudes increase very rapidly as the aSi thickness increases.

Changes in total R that depend on aSi thickness are the most complex of all layers. As the layer becomes thicker and better defined, the interferences increase in amplitude and are slightly shifted towards longer wavelengths. Interestingly, they oscillate around the mean value that is equal to the reflectivity of regular Si:P with equal doping. There is no easy answer regarding the optimal thickness of the amorphous layer, since the disadvantage resulting from increased reflectivity for some wavelengths can be compensated by more efficient secondary generation. This effect will be studied in more detail in the following chapters of this work.

3.3. Influence of sample positioning on reflectivity. Role of the electrodes.

The top electrode fingers are necessary for efficient charge collection in a solar cell, but from the optical point of view their presence is a drawback to the device overall performance. The average thickness of a silver electrode is around 500 nm, making it completely opaque for the UV-VIS-NIR photons (see figure III.26). The whole area of the cell that lies below is then inactive. There are ideas to either redirect the light so that it does not strike the electrode, or to completely replace the metal by a conductive glass. Both concepts have proven useful in certain cases, but the first one only copes well for the normal incidence and also increases the uneven energy concentration in the active layer, therefore leading to even greater dependency on the intensity of the incident light. Replacing metal electrodes by conductive a glass copes well with the problem of dispersed light, but conductive oxides such as ITO are much more expensive that typical, non-conducting passivation layers and also involve a lot of dangerous chemicals during manufacture. Another problem is their worse electron transport properties in comparison to metals that lead inevitably to resistance losses and the presence of absorption in such layers. In order to reduce absorption losses, conductive glasses used as a passivation layers must be kept thin, which in turn increases their sheet resistance. Another problem is the work function mismatch, which is often less well aligned with the conduction band in Si as in the case of well fabricated silver contacts.

On most of our MIND structures silver electrode fingers were used as top contacts, and for some test structures the SiO_2 passivation layer was replaced by ITO conductive glass. For couple of structures, gold fingers were fabricated.

We have shown earlier that the reflectivity of the structure can be accurately modeled, and the knowledge of the optical properties allows us to analyze the energy distribution inside the

structure. From this information more data can be derived, such as the Quantum Efficiency and short-circuit current. However, the simulation must take into account all parts of the device and be also comparable with the experiment. Therefore the influence of the electrodes on the measured reflectivity cannot be underestimated.

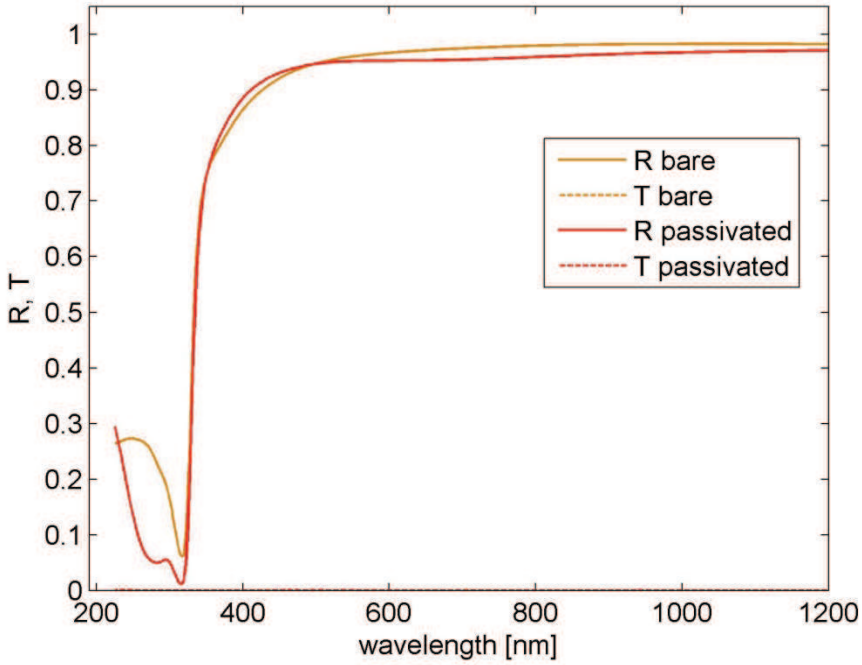

Figure III.26. Reflectivity *R* and transmission *T* for a silver electrode deposited on Si. Red curves show the case when the electrode is non-passivated, orange curves show the case where the electrode was passivated with 119 nm SiO_2. The thickness of the electrodes is 500 nm.

As can be seen in figure III.26, silver electrodes are completely opaque but their reflectivity is not always close to 100%, so the resulting measured reflectivity of the sample is dependent on two values of *R*, the structure and the electrodes, weighted by their surface ratio and light intensity distribution. In the simplest case, if the whole sample is uniformly illuminated, the weight ratio depends only on the ratio of the surface covered by the electrodes to the surface of the sample. For all MIND structures, the electrodes are always 100µm wide and 900µm apart. In more complex case, where the spot is smaller but the light intensity is still constant over entire illuminated area, the surface ratio changes. In figure III.27 (a) and (b), two white spots are shown that were used to measure the reflectivity of the samples with the help of integrating sphere. It is clear that the spot shown in figure III.27 (a) will yield a different R than that in (b), because the area covered by the electrodes is greater for the first one. Figure III.27 shows the difference in reflectivity obtained for different positioning of the spots. From

figures III.26 and III.27, it can be clearly seen that the electrodes increase the overall reflectivity for wavelengths longer than $\lambda = 350$ nm, but decrease the value of R by about 10% for UV ($\lambda > 350$ nm).

Figure III.27. Different spot sizes and their influence on the measured reflectivity. The same spot can produce different response, depending on the orientation (a and b) and also on the distribution of the intensity in the spot (c) which is particularly important for laser spots.

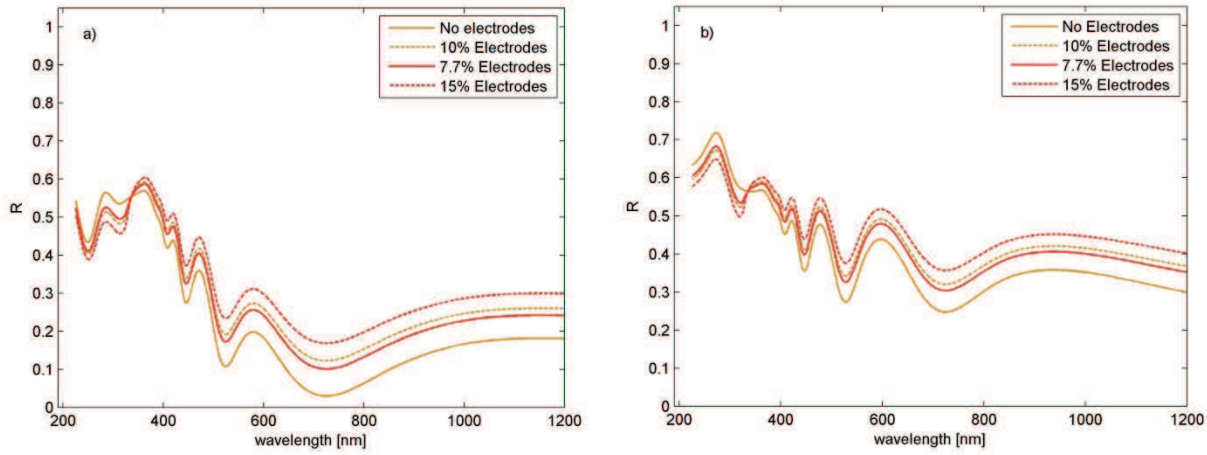

Figure III.28. Simulated reflectivity of a MIND structure for normal light incidence and for different fractions of surface covered by electrodes. The sample passivated with 119 nm SiO_2 (a) and non-passivated (b) is shown.

Let us now consider the situation when the sample is illuminated by a light beam with an inhomogeneous intensity distribution, such as a laser beam. In such case, the influence of the electrodes on the measured reflectivity will be more complex, because the light intensity at any given point in space will add to the surface ratio to produce highly intensity-dependent and very position-sensitive result. In our simulation we assumed that the laser beam has Gaussian distribution of the intensity, described by the following equation:

$$I = I_0 exp\left(-\frac{(x-c)^2}{2b^2}\right) \quad \text{(III.3.24)}$$

where I_0 is the amplitude, c is the position of the beam on the cell and b is the beam width at half maximum. We simulated reflectivity maps for monochromatic illumination in which the reflectivity of the electrodes was 100% and the structure reflected only 30% of the incident light. In the simulation, electrodes are 100 µm wide and are set 500 µm apart.

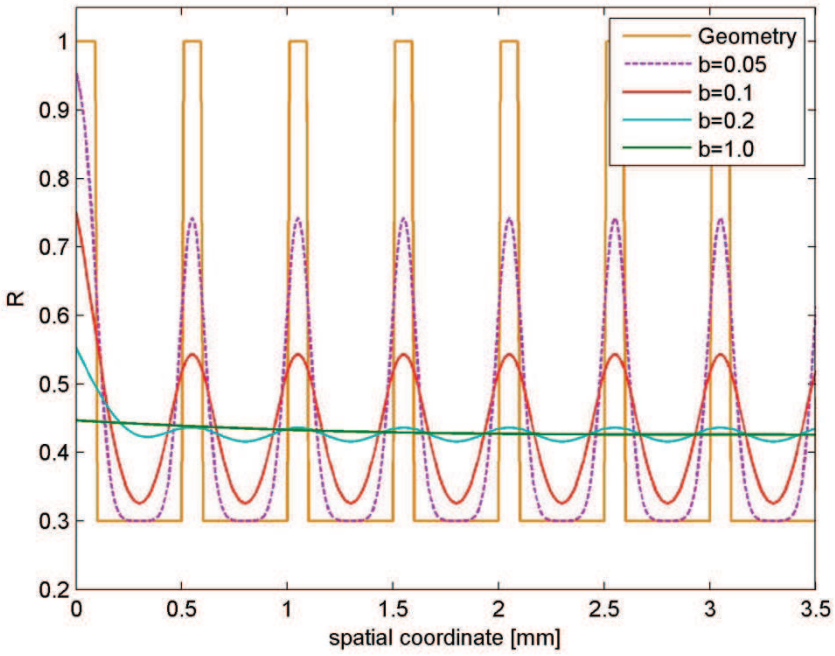

Figure III.29. Simulated reflectivity maps for monochromatic illumination for different width of a Gaussian intensity distribution in a beam. It can be clearly seen that even quite focused beams (with b > 0.1) are not able to correctly determine the reflectivity of the structure itself and get parasitic increase from electrodes.

For very large spots, obtained averaged reflectivity is constant, indicating that it can be approximated by a simple weight ratio dependent only on the relative surface covered by electrodes. For smaller spots however, the situation is more complex. Medium size spots show very strong sensitivity on the position on the sample, by are not able to properly probe neither the reflectivity of the structure nor the electrodes themselves, therefore analysis of experimental results obtained by such spots can prove to be challenging. Very focused spots can provide the information about the reflectivity of the structure and therefore information on the energy distribution inside the structure can be precisely modeled, which is of utmost importance for the Collection Efficiency (CE) calculation.

4. Collection Efficiency and energy distribution. Poynting vector.

Having determined the overall structure reflectivity and transmission, we modeled the exact field distribution inside the structure as was mentioned in point 3 of this chapter. This allows us to estimate the Poynting vector, given by equation (III.3.16), which in turn contains information about the rate at which photons are absorbed in the structure. In the case of layered structures, this is not the simple coefficient of absorption of each layer, because internal reflectivities from the interfaces also add to the effect. The Poynting vector also provides information about absorption in each layer, which can be then used to estimate the amount of carriers generated in a given region of the device. In figure III.30, a distribution of the Poynting vector (S) and energy density U is shown for the test structure used in previous examples. It can be clearly seen that S in the first layer (SiO_2) reproduces the reflectivity curve show in figure III.26. Also, the drop along y – axis (depth) occurs only in absorbing layers. It is important to stress that the absorption is more complex in such structure that it would have been in the absence of amorphous layer.

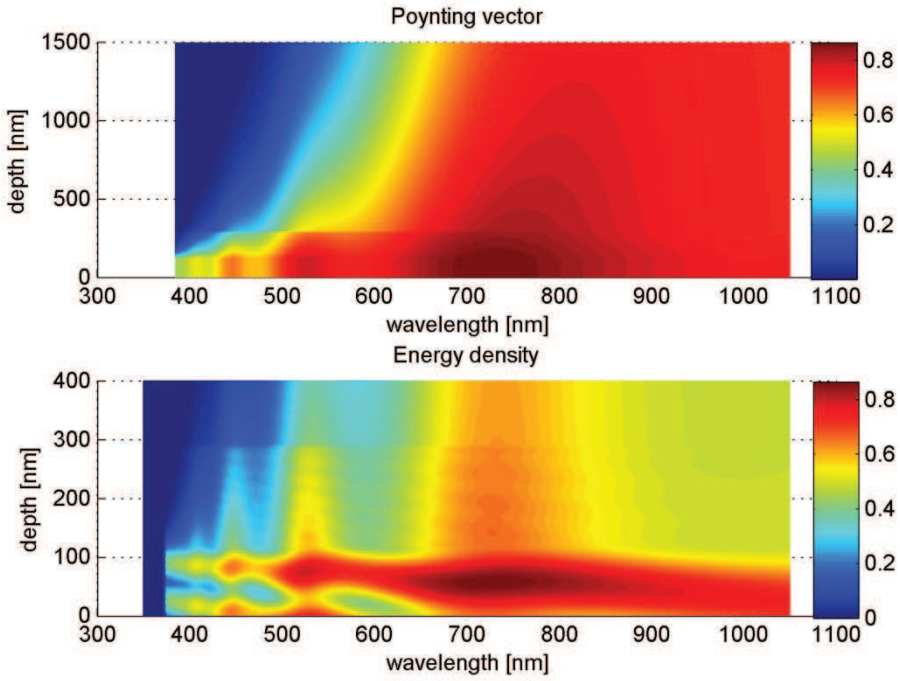

Figure III.30. Normalized Poynting vector S (upper) and energy density U (lower) in the simulation area of the test MIND structure. U is zoomed to the emitter region.

The energy density distribution U gives even clearer insight into the influence of the internal reflectivities on the absorption, but it shows also in which layers the energy is concentrated.

From figure III.30 it is easy to see that the highest energy concentration occurs in the SiO_2 layer for $\lambda = 750$ nm.

The information that can be extracted from the *S* vector distribution in space is the absorption *A* for any given area of the structure. The absorption for the first active layer, the amorphous layer and the upper emitter are shown in figure III.31

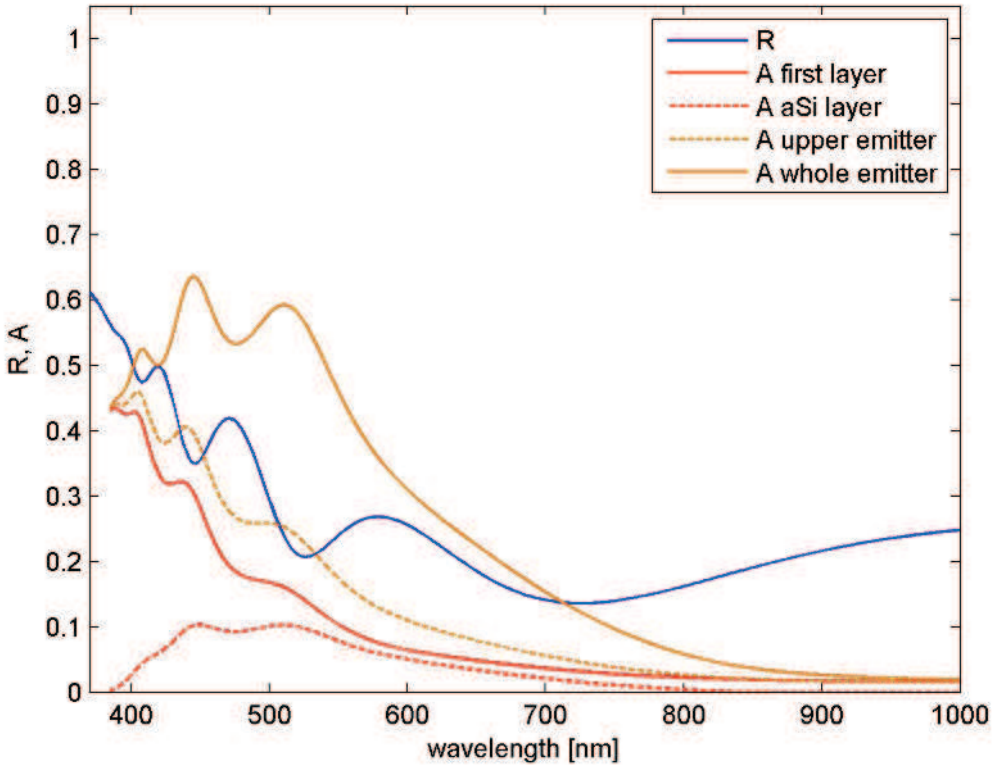

Figure III.31. Reflectivity *R* and absorption *A* for various regions of the test MIND structure. Note that absorption curves are not normalized but are diminished by the value of *R*, so that $1 = R+T+A$.

The same curves normalized to show only the light that penetrates inside the structure are shown in figure III.32. As can be seen for very short wavelengths ($\lambda < 460$ nm), all the light is absorbed in the emitter. However the maximum absorption occurs for 450 and 530 nm. Most, if not all, of the electron-hole pairs generated in the upper emitter (area above the aSi layer) do not contribute to the total photocurrent generated by the cell due to the potential barrier across the cSi/aSi interface. As can be seen in figures III.31 and III.32, this loss constitutes an important fraction of overall absorption. On the other hand, the amorphous layer absorbs only around 10% of the whole light, which corresponds to a maximum of 18% of the light that

penetrates inside the structure (for $\lambda = 470$ nm). As will be shown later, this area is capable of creating of additional e-h pairs that constitute second generation.

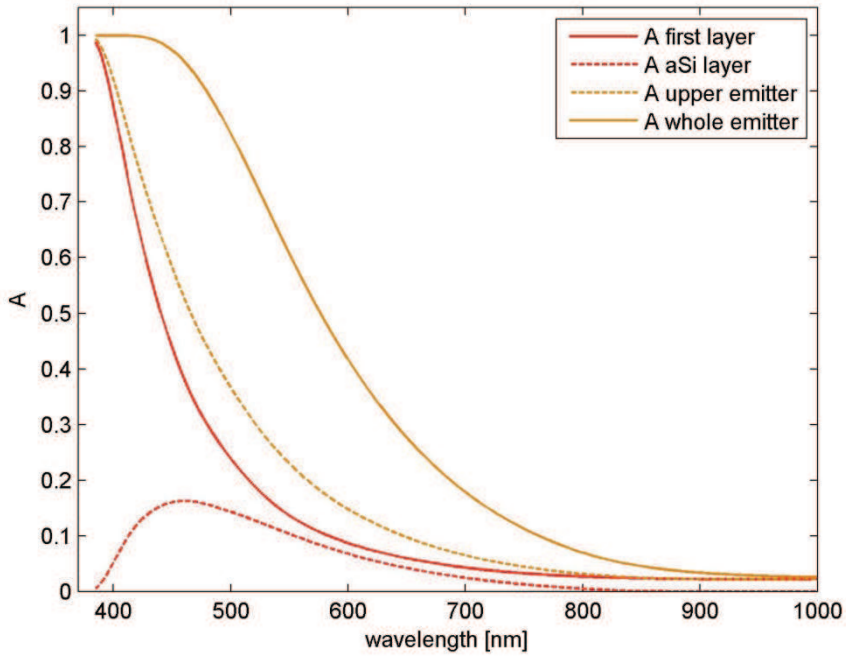

Figure III.32. Reflectivity *R* and absorption *A* for various regions of the test MIND structure. All curves are normalized to show only the light that penetrated inside the structure.

The information about the light absorption and its distribution in space provided by the S vector is usually not sufficient to estimate the spectral response of the solar cell, or the Quantum Efficiency (QE). Another parameter that comes into play is the so-called Collection Efficiency (CE). In a classical, monocrystalline solar cell, in which the absorption coefficient is constant and there are no buried interfaces, QE is linked to CE by the following relation:

$$\eta_{QE}(\lambda) = \frac{1}{\alpha}\int_0^{X_d} \exp(-\alpha x) CE(x)\big(1 - R(\lambda)\big)\, dx \qquad \text{(III.4.1)}$$

where X_d is the cell thickness [47]. This equation holds for any cell thickness, as long as above conditions are kept. In this approximation no internal reflections are allowed. In the case where the absorption coefficient is a function of spatial coordinate $\alpha(x)$, or internal reflections become non-negligible, relation (III.4.1) has to be expressed in more explicit way. By introducing the generation rate *G*, which in the most general approach is linked to the S vector by the following relation:

$$G(\lambda, x) = -\nabla \cdot S(\lambda, x) \qquad \text{(III.4.2)}$$

the equation for η can be rewritten as:

$$\eta_{QE}(\lambda) = q \int_0^{X_d} G(\lambda, x) CE(x)\, dx \qquad \text{(III.4.3)}$$

if G is normalized for each wavelength, the result is the Internal Quantum Efficiency (IQE). The External Quantum Efficiency (EQE) can be then obtained by applying the following relation:

$$\eta_{EQE}(\lambda) = \eta_{IQE}(\lambda) \cdot \big(1 - R(\lambda)\big) \qquad \text{(III.4.4)}$$

It can be clearly seen from equations (III.4.1-4) that the accurate estimation of CE is the key parameter in the process of analyzing Quantum Efficiency. There are several analytical formulas allowing recreation of CE for single junction, monocrystalline cells [47], but in case described by equation (III.4.3) none of them is directly applicable.

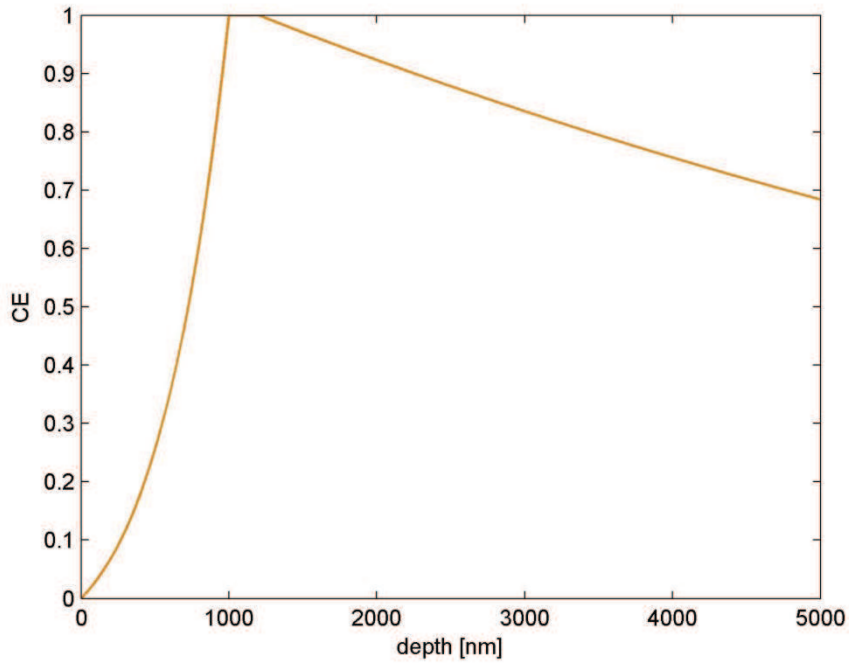

Figure III.33. CE for a typical single PN junction solar cell. CE = 1 only for the depletion region, in this example located 1000 nm from the surface.

However, to deploy even a numerical solution, certain assumptions have to be made. These assumption usually fall into determining three main regions of the cell: the depletion region, at which CE = 1, the emitter and the base. In both the emitter and the base, one can expect that there will be at least two key parameters determining the CE curve, namely diffusion

length L_d and surface recombination velocity V. A more detailed study has been done by some authors [48], which allows determination of the CE curve accurately by solving the diffusion equation and using the reciprocity theorem. A typical CE curve for a PN junction solar cell is shown in figure III.33.

The determination of CE is the key point in finding the quantum efficiency. CE can also be reproduced from experimental data if quantum efficiency and photogenerated charge distribution is known. In any case, the determination of CE can prove to be quite challenging for more complex systems. Usually, for good quality monocrystalline solar cells, the diffusion length in the base L_B is several hundreds of micrometers while L_E for the emitter is usually less than 10 micrometers. Surface recombination velocities V can range from several hundred for the base to 10^6 of cm/s for the emitter. A reconstructed QE curve for the MIND structure used in our example is shown in figure III.34. The diffusion lengths were set to $L_E = 300$ nm and $L_B = 300$ μm and the surface recombination velocities V were set to 0 on both sides.

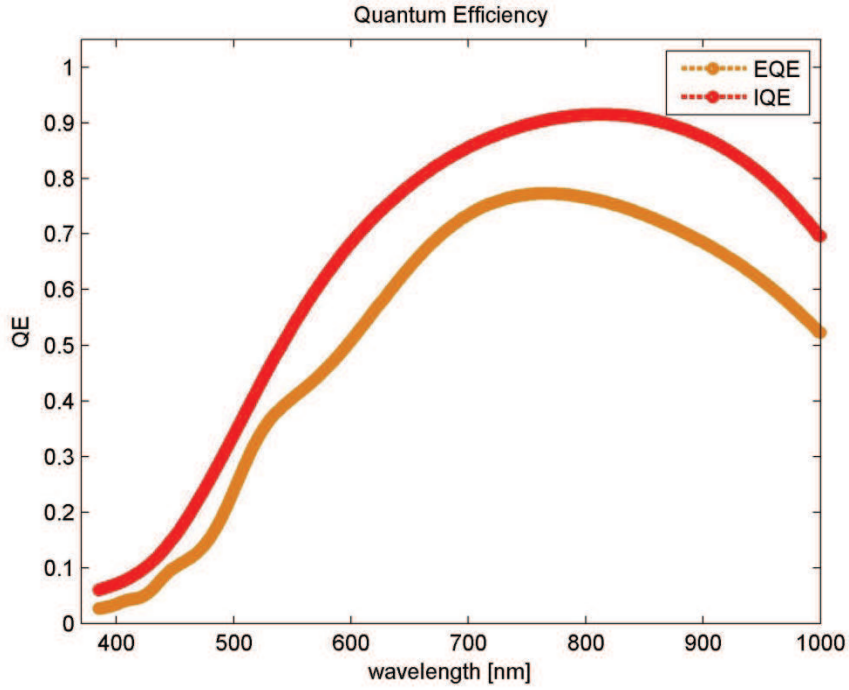

Figure III.34. Reconstructed Internal Quantum Efficiency and External Quantum Efficiency for a typical MIND sample with passivated surface.

Determination of Quantum Efficiency or spectral response allows further analysis, leading to predicting current density under given illumination, for example AM1.5.

We have shown that using combined efforts of several different approximations such as Drude-Lorentz, used to determine the dielectric function for each layer, Transition Matrix

Approximation, used to assemble all the layers into a structure of desired shape, and reciprocity theorem used to determine Collection Efficiency, we are able to calculate the Quantum Efficiency and from it, the first point on I-V curve, namely the short-circuit current. The IV curve can be then modeled using equation (I.4.33) and (I.4.47) introduced in Chapter I.

References:

[1] X. Gonze, B. Amadon, P.-M. Anglade, J.-M. Beuken, F. Bottin, P. Boulanger, F. Bruneval,' D. Caliste, R. Caracas, M. Cote, T. Deutsch, L. Genovese, Ph. Ghosez, M. Giantomassi, S. Goedecker, D.R. Hamann, P. Hermet, F. Jollet, G. Jomard, S. Leroux, M. Mancini, S. Mazevet, M.J.T. Oliveira, G. Onida, Y. Pouillon, T. Rangel, G.-M. Rignanese, D. Sangalli, R. Shaltaf, M. Torrent, M.J. Verstraete, G. Zerah, J.W. Zwanziger, *ABINIT : First-principles approach of materials and nanosystem properties*, Computer Phys. Commun. 180, 2009, 2582-2615.

[2] X. Gonze, G.-M. Rignanese, M. Verstraete, J.-M. Beuken, Y. Pouillon, R. Caracas, F. Jollet, M. Torrent, G. Zerah, M. Mikami, Ph. Ghosez, M. Veithen, J.-Y. Raty, V. Olevano, F. Bruneval, L. Reining, R. Godby, G. Onida, D.R. Hamann, and D.C. Allan. Zeit. *A brief introduction to the ABINIT software package*, Kristallogr. 220, 2005, 558-562.

[3] P. Hohenberg, W. Kohn, *Inhomogeneous electron gas*, Phys. Rev. 136, 1964, 864-871.

[4] W. Kohn, L. Sham, *Self-Consistent Equations Including Exchange and Correlation Effects*, Phys. Rev. A 140, 1965, 1133.

[5] L. Hedin, *New Method for Calculating the One-Particle Green's Function with Application to the Electron-Gas Problem*, Phys. Rev. 139 (1965) A796.

[6] R.M. Martin, *Electronic Structure. Basic Theory and Practical Methods*, Cambridge University Press, Cambridge, U.K., 2004.

[7] http://www.abinit.org/downloads/psp-links.

[8] N. Troullier and J. L. Martins, *Efficient pseudopotentials for plane wave calculations*, Phys. Rev. B 43, 1991, 1993-2006.

[9] http://webelements.com, University of Sheffield.

[10] J. C. Maxwell, *A Treatise on Electricity And Magnetism, Vols 1 and 2*, Oxford University Press, Oxford, U.K., 1954.

[11] K. Sierański, M. Kubisa, J. Misiewicz, J. Szatkowski, *Półprzewodniki i struktury półprzewodnikowe*, Oficyna Wydawnicza PWr, 2002.

[12] G. F. Knoll, *Radiation Detection and Measurement*, 2nd edition, New York: John Wiley and Sons, 1989.

[13] G. Bertolini and A. Coche, *Semiconductor Detectors*, North Holland Publishing Co., 1968.

[14] F.S., Goulding and R.H. Pehl, *Semiconductor Detectors*, Section IIIA, *Nuclear Spectroscopy and Reactions*, J. Cerny, Ed. Academic Press, 1974.

[15] K. Sokolowski – Tinten, D. von der Linde, *Generation of dense electron-hole plasmas in silicon*, Phys. Rev. B 61, 2000, 2643-2650.

[16] J. Leng, J. Opsal, H. Chu, M. Senko and D.E. Aspnes, *Analytic representations of the dielectric functions for device and structural modeling*, Thin Solid Films 313-314, 1998, 132-136.

[17] B.G. Martin, R.F. Wallis, *The dielectric constant associated with interband transitions in germanium*, Solid State Commun. 21, 1977, 385.

[18] M. Erman, J.B. Theeten, P. Chambon, S.M. Kelso, D.E. Aspnes, *Optical properties and damage analysis of GaAs single crystals partly amorphized by ion implantation*, J. Appl. Phys. 56, 1984, 2664.

[19] Jellison G. E., Jr., Withrow S. P., McCamy J. W., Budai J. D., Lubben D. and Godbole M. J., *Optical functions of ion-implanted, laser –annealed heavily doped silicon*, Phys. Rev. B 52, 1995, 14607-14614.

[20] M. Basta and Z.T. Kuznicki, *Dielectric functions and optical parameters of heavily doped and/or highly excited Si:P*, Optica Applicata, XLII, 2012, 713-724.

[21] R. Huber, F. Tauser, A. Brodschelm, M. Bischler, G. Abstreiter, A. Leitenstorfer, *How many-particle interactions develop after an ultrafast excitation of an electron-hole plasma*, Nature 414, 2001, 286-289.

[22] P. D. Altukhov, E. G. Kuzminov, *The self-compression of injected electron-hole plasma in silicon*, Physica Status Solidi 232, 2002, 364-379.

[23] K. Yee, *Numerical solution of initial boundary value problems involving Maxwell's equations in isotropic media*, IEEE Trans. Anten. Prop. 14, 1966, 302–307.

[24] A. Taflove, *Application of the finite-difference time-domain method to sinusoidal steady state electromagnetic penetration problems*, *IEEE Trans. El. Comp.* 22, 1980, 191–202.

[25] C. L. Xu and W. P. Huang, *Finite Difference Beam Propagation Method for Guide-Wave Optics*, Prog. Electromag. Research, PIER 11, 1995, 1-49.

[26] M. G. Moharam and T. K. Gaylord, *Rigorous coupled-wave analysis of planar-grating diffraction,* J. Opt. Soc. Am. 71, 1981, 811-818.

[27] P. Yeh, A. Yariv, Chi-Shain Hong, *Electromagnetic propagation in optical stratiefied media. I. General theory*., J. Opt. Soc. Am., 67, 1977.

[28] P.C. Waterman, *Symmetry, Unitarity and Geometry in Electromagnetic Scattering*, Phys. Rev. D, 3, 1971.

[29] T. Schimielau, G. Manzke, D. Tamme and K. Henneberger, *T-Matrix Approach to the Linear Optical Response of Highly Excited Semiconductors*, Phys. Stat. Sol (b), 221, 2000, 215-221.

[30] J. Tauc, *Optical properties and electronic structure of amorphous Ge and Si*, Mat. Res. Bulletin, 3, 1968, 37–46.

[31] N. Bernstein, *Atomic scale structure and dynamics of amorphous-crystal interfaces in silicon: simulations with empirical and quantum-mechanical approaches*, PhD thesis, Harvard University, 1998.

[32] C. G. Van de Walle, L. H. Yang, *Band discontinuities at heterojunctions between crystalline and amorphous silicon*, J. Vac. Sci. Technol. B 13(4), 1995, 1635-1638.

[33] M. P. Ali, P. A. Tove, H. Norde, *Junctions between amorphous and crystalline silicon*, Physica Scripta, 24, 1981, 399-400.

[34] R. Stangl, A. Froitzheim, W. Fuhs, *Thin film silicon emitters for crystalline silicon solar cells, epitaxial, amorphous or microcrystalline? A simulation study,* PV in Europe, Rome 2002, Italy.

[35] J. P. Kleider, R. Chouffot, A. S. Gudovskikh, P. Roca, I. Cabarrocas, M. Lebrune, P.-L. Ribeyron, R. Bruggemann, *Electronic and structural properties of the amorphous/crystalline silicon interface*, Thin Solid Films 517, 2009, 6386-6391.

[36] B. Bahardoust, D. Yeghikyan, S. Costea, R. B. Gangadhar, N. P. Kherani, S. Zukotynski, *Characterization of amorphous-crystalline silicon heterojunction using constant photocurrent method*, 20th EU PVSEC, Barcelona 2005, Spain, 1099-1103.

[37] J. P. Kleider, R. Chouffot, A. S. Gudovskikh, P. Roca, I. Cabarrocas, M. Lebrune, P.-L. Ribeyron, R. Bruggemann, *Electronic and structural properties of the amorphous/crystalline silicon interface*, Thin Solid Films 517, 2009, 6386-6391.

[38] T. C. Choy. *Effective Medium Theory* (1st ed.), Oxford University Press, Oxford, U.K., 1999.

[39] J. C. M. Garnett, *Colors in metal glasses and metal films*, Trans. Roy. Soc. 53, 1904, 385–420.

[40] D. A. G. Bruggeman, *Berechnung verschiedener physikalischer konstanten von heterogenen substanzen, i. dielektrizitätskonstanten und leitfähigkeiten der mischkörper aus isotropen substanzen*, Ann. Phys., 1935, 636–664.

[41] A. Sihvola, *Self-consistency aspects of dielectric mixing theories*, IEEE Trans. Geo. Rem. Sens. 27, 1989, 403–415, 1989.

[42] R. J. Elliott, J. A. Krumhansl, and P. L. Leath, *The theory and properties of randomly disordered crystals and related physical systems*, Rev. Mod. Phys. 46, 1974, 465–543.

[43] K. K .Karkkainen, A. H. Sihvola, K. I. Nikoskinen, *effective permittivity of mixtures: Numerical Validation by the FDTD method*, IEEE Trans. Geo. Rem. Sens. 3 (38), 2000, 1303-1308.

[44] O. Wiener, *Zur theorie der refraktionskonstanten*, Berichteüber Verhandlungen Königlich-Sächsischen Gesellschaft Wisseschaften Leipzig, 1910, 256–277.

[45] Z. Hashin and S. Shtrikman, *A variational approach to the theory of the effective magnetic permeability of multiphase materials*, J. Appl. Phys. 33, 1962, 3125–3131.

[46] S. Adachi, H. Mori, *Optical properties of fully amorphous silicon*, Phys. Rrev. B 62, 2000, 10158-10164.

[47] C. Donolato, *Reconstruction of the charge collection probability in a solar cell from internal quantum efficiency measurements*, J. Appl. Phys. 89, 2001, 5687-5695.

[48] P. Kittidachachan, T. Markvart, D.M. Bagnall, R. Greef, G.J. Ensell, *A detailed study of p–n junction solar cells by means of collection efficiency*, Sol. En. Mat.: Sol. Cells 91, 2007, 160–166.

Chapter IV

Experimental characterization of MIND test structures

Contents

Abstract

The experimental analysis of MIND structures presented in this chapter has been divided into four major parts i.e. structural, optical, quantum efficiency and electrical. The whole set of analyses is based on the chosen, representative samples. Structural measurements have confirmed the formation of a buried substructure and estimated the influence of etching on surface properties. Optical measurements were conducted in order to understand the dielectric functions of the samples and the propagation of the electromagnetic (EM) wave. Quantum Efficiency measurements were performed in order to compare the effects occurring in two different types of structures and to estimate the generation rate of e-h pairs. At last, the electrical measurements were employed in order to understand the physical parameters that shape the device performance and to identify possible channels for improvements.

Taken together, our measurements and analyses have created a complete picture of mechanisms behind light to electricity conversion in MIND structures.

1. Structural measurements.

Structural and morphological characterizations are usually the first step to understand properties of a given physical system. For solar cells, the knowledge of morphology of the device and the surface is of utmost importance, because it is a limiting factor for the device performance. For MIND structures, this type of measurement is particularly important because it provides necessary information to estimate material properties in the active zone. To fully access this information we have employed several different experimental techniques, such as Scanning Electron Microscopy (SEM) and Backscattered Electron Microscopy (BSE), Atomic Force Microscopy (AFM) and Optical Surface Profiler.

1.1. Backscattered Electron Microscopy.

We focused on two complementary methods: Backscattered Electron (BSE) and Scanning Electron Microscopy (SEM) that allowed us to fully characterize morphology and architecture of the buried internal structure without reducing the internal strain (as in case of Transmission Electron Microscopy (TEM)) and to analyze the surface of the samples via SEM. SEM is a method that produces images of a sample by scanning it with a focused beam of electrons. Electrons interact with a sample, producing various types of signals, in our case secondary electrons for SEM and backscattered electrons for BSE [1]. Both passivated and etched samples were characterized. We studied mainly the samples of N7 and LP families. Measured samples were taken from the edges of the wafer therefore we expect some thickness variations of the layers throughout the wafer, especially for the passivation layer, which is deposited by LPCVD. This type of measurement requires breaking off a small piece of wafer and taking a snapshot of the edge. Potential results concerning internal multi-layered structure may be, and often are, influenced by the topography of the cleavage itself, because the intensity of the back-scattered electros, which corresponds to the density of the material, depends on their trajectory in the sample.

1. LP01 sample

This sample was exposed to two different implantation processes, amorphizing at 180 keV and complementary at 20 keV, and passivated by SiO_2. The amorphous layer was designed to be buried at ~170 nm below the surface of silicon.

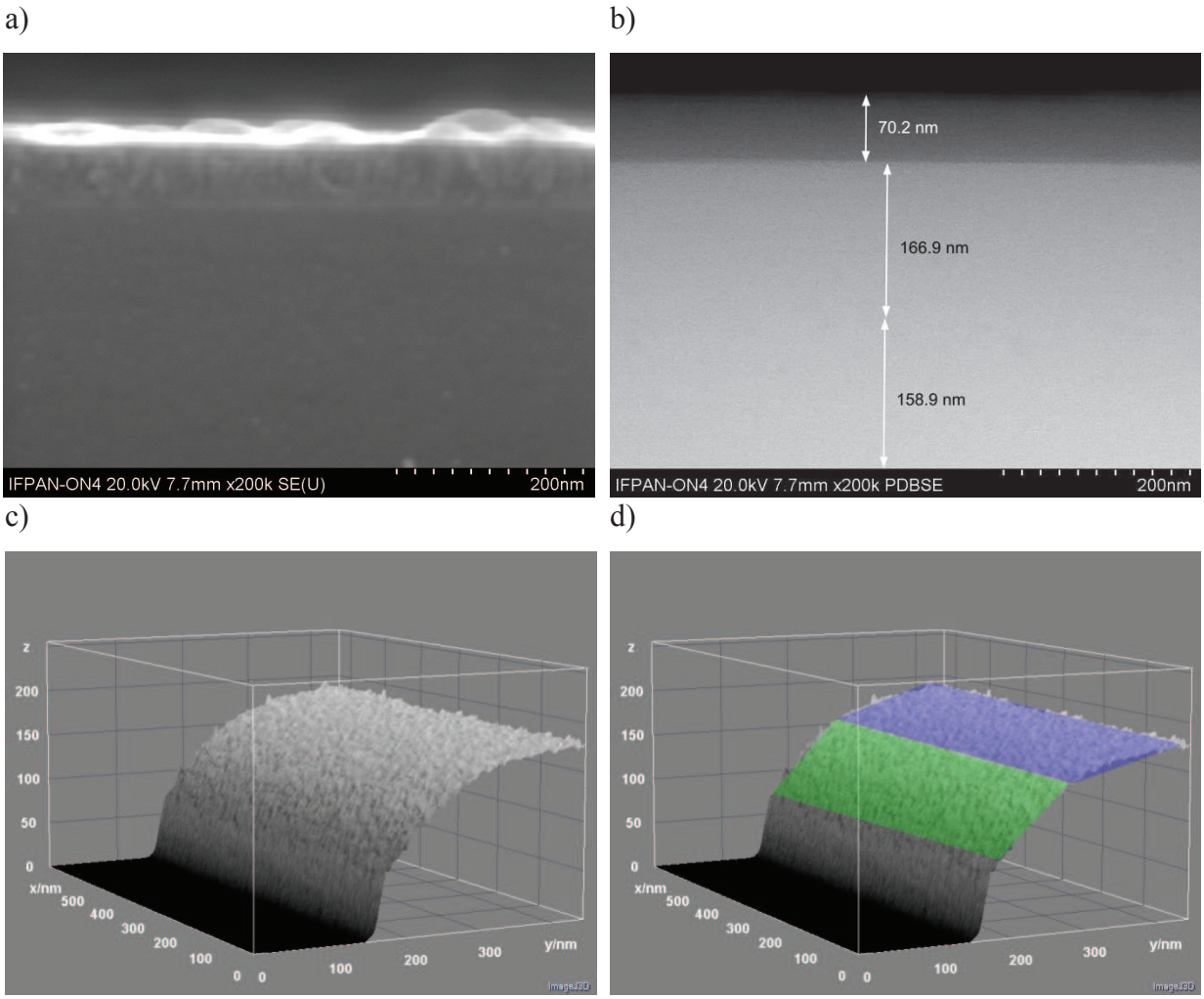

Figure IV.1. Electron microscopy images of the LP01 sample. SEM image of the sample edge (a) shows very uneven passivation thickness and clear SiO_2/cSi interface. BSE images of the same spot (b, c and d) show two different regions of silicon, with thicknesses 167 and 159 nm respectively.

The LP01 sample shows one distinct interface between two different regions of silicon, buried 167 nm below the surface. This interface lies very close to the intended 170 nm, but no other interface is visible. Because of this it is difficult to estimate the potential thickness of the amorphized region. This effect might be explained by the fact that the measurement was made on the edge of the wafer (where recrystallization induced by thermal annealing was faster and the implantation dose could have been smaller) on that the topography of the cleavage influenced BSE image, effectively scattering the electrons carrying information about the sub-structure.

2. LP02 sample

Double implanted structure, passivated by SiO_2 shows good quality interfaces between SiO_2/cSi and cSi/aSi, buried about 170 nm below the surface of the silicon. A distinctive region of damaged Si just below SiO_2 layer is also visible.

a) b)

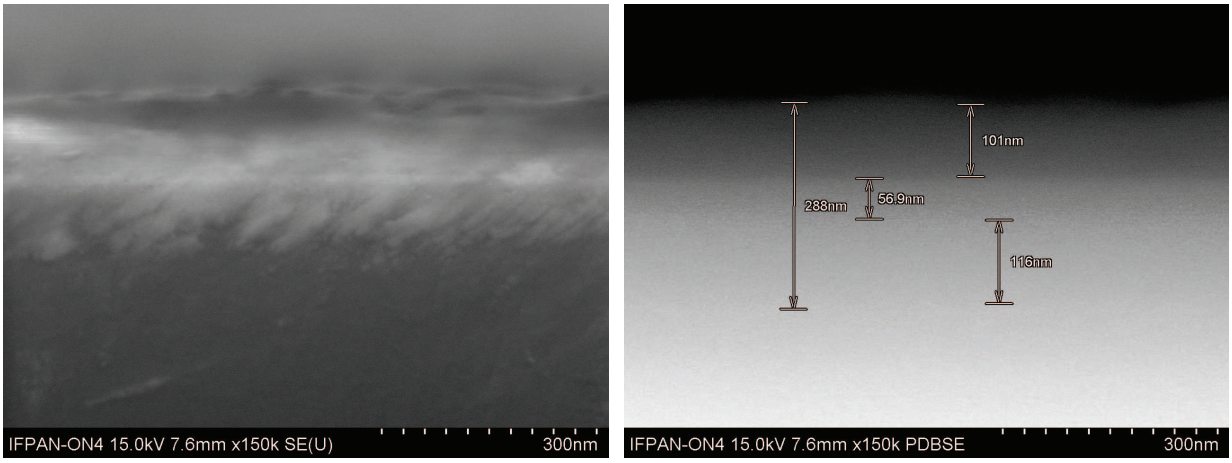

c) d)

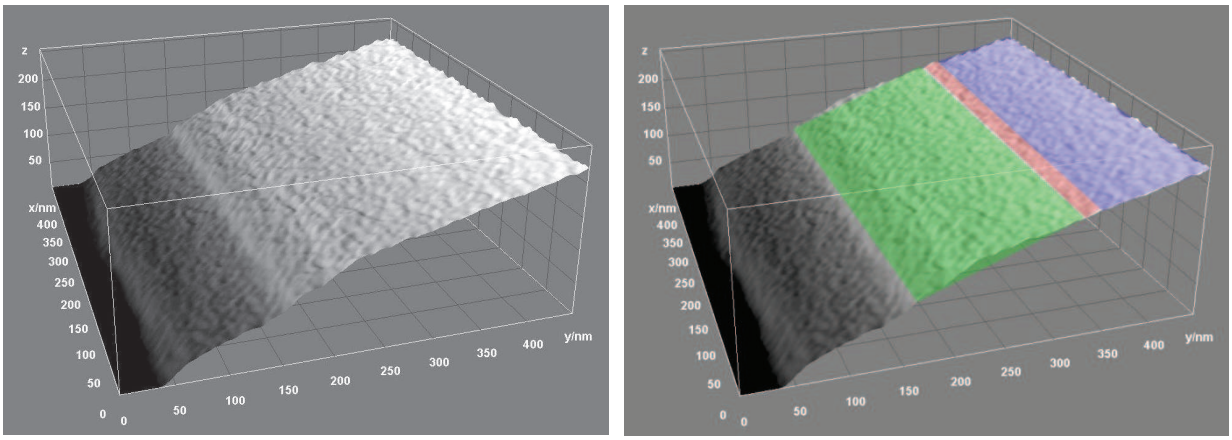

Figure IV.2. Electron microscopy images of the LP02 sample. SEM image of the sample edge (a) shows features on the surface, indicating cracks and crevices on the side. BSE images (b, c and d) show several different regions of silicon, with the deepest located 172 nm below the surface of Si.

The LP02 sample shows several buried interfaces in its structure. A very thin amorphous region is visible on the 3D BSE image (Figure IV.2 c), around 170 nm below the SiO_2/cSi interface, with a thickness between 8 and 10 nm.

3. LP03 sample

Double implanted structure, passivated by SiO_2 shows good quality interface between SiO_2/cSi and very well defined amorphous region, buried 132 nm below the surface of silicon.

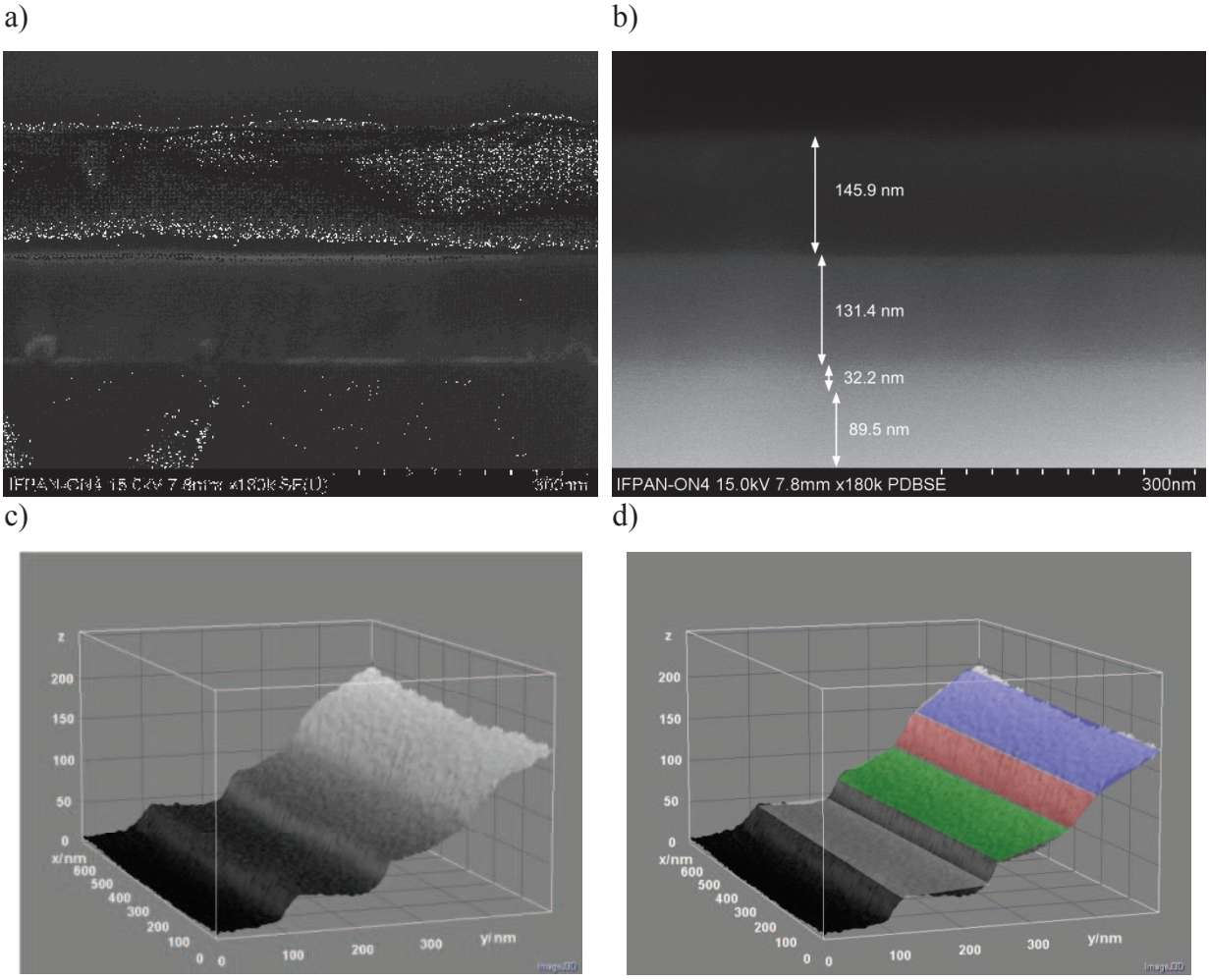

Figure IV.3. Electron microscopy images of the LP03 sample. SEM image of the sample edge (a) shows several different layers, which is confirmed by BSE images (b, c and d). An amorphous region is also clearly visible.

This sample shows very clearly defined amorphous region, and two aSi/cSi interfaces. Amorphous region is approximately 30 nm thick, however it is localized around 132 nm below the surface of Si, which is much closer to the surface than in other samples of LP family. The interface between SiO_2 and cSi is also quite sharp, indicating good quality electronic passivation, which is also much thicker than in other samples of this family.

4. LP04 sample

The LP04 is a double implanted structure, passivated by SiO_2 which shows good quality interface between SiO_2 and cSi. Passivation layer is uniform and around 94 nm thick. There are two distinctive regions just below the surface of silicon, indicating high concentration of P atoms and/or rather high disorder after the implantation. No other region can be distinguished and there is no evidence of any buried sub structure in the studied piece.

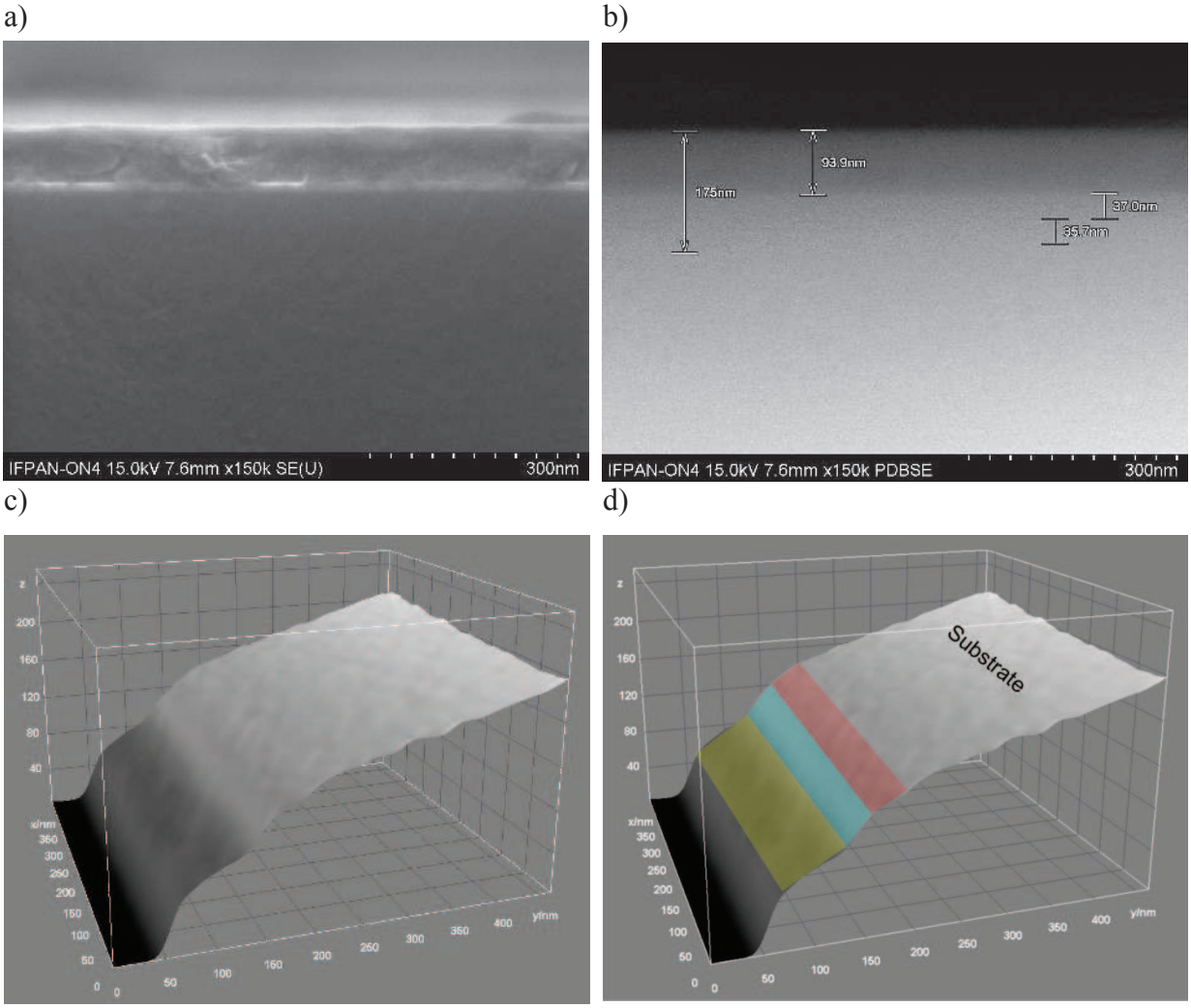

Figure IV.4. Electron microscopy images if the LP04 sample. SEM image of the sample edge (a) and BSE images of the internal geometry (b, c and d).

5. LP05 sample

The LP05 sample is a double-implanted structure passivated by SiO_2. Passivation thickness is rather low, reaching around 77 nm at most in the taken images of the analyzed wafer piece. There are also two distinct regions in the upper emitter, one about 89 nm thick, and the other 96 nm thick. This is in agreement with doping distribution measured by SIMS, where also two regions were distinguished. The amorphized region, and the cSi/aSi interface is localized somewhere at 185 nm below the surface of silicon, and the transition region is around 20 nm thick, which is a good approximation of a thickness of the amorphous layer.

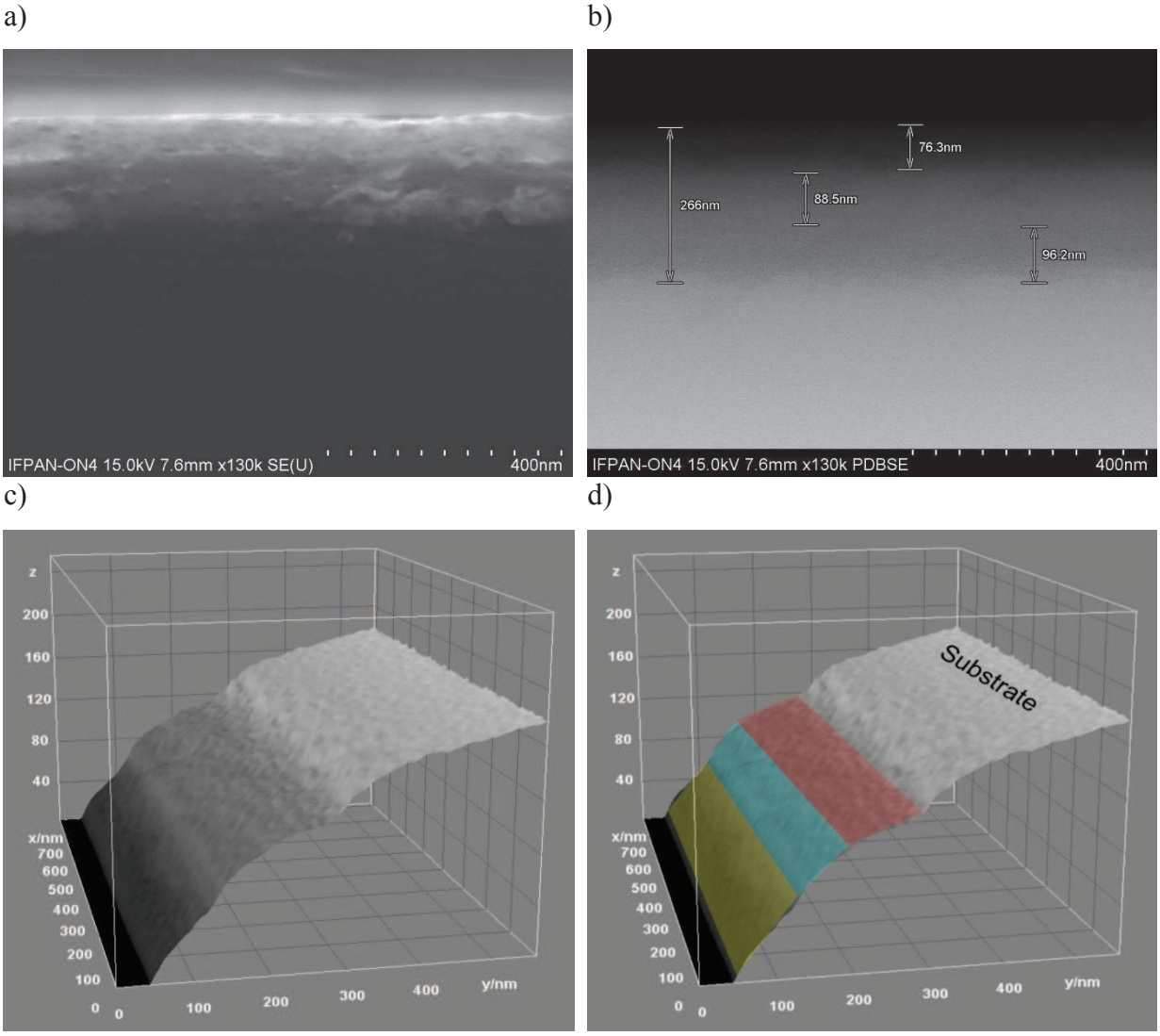

Figure IV.5. Electron microscopy images of the LP05 sample. SEM image of the sample edge (a) and BSE images of the internal structure (b, c and d). Several different density regions are visible, a heavily damaged silicon on the surface (blue), heavily P-doped Si (red) and amorphous region (above red).

6. LP07 sample

The LP07 sample is a diffused-implanted structure passivated by SiO_2. Passivation thickness is close to intended 100 nm and in the analyzed wafer piece reached values close to 90 nm. There are three distinctive crystalline regions in the upper emitter and one amorphous region. Total upper emitter thickness is estimated to be ~200 nm. First crystalline region is close to the surface of Si, damaged by implantation crystalline Si, around 47-50 nm thick. Region just below it is a better quality crystalline Si, with high concentration of phosphorous. Below lies another cSi region, with lower P concentration, bordered by amorphous region. Amorphous Si

is sandwiched by two transition layers of strained cSi/aSi extended interface of total module thickness reaching 50 nm.

a) b)

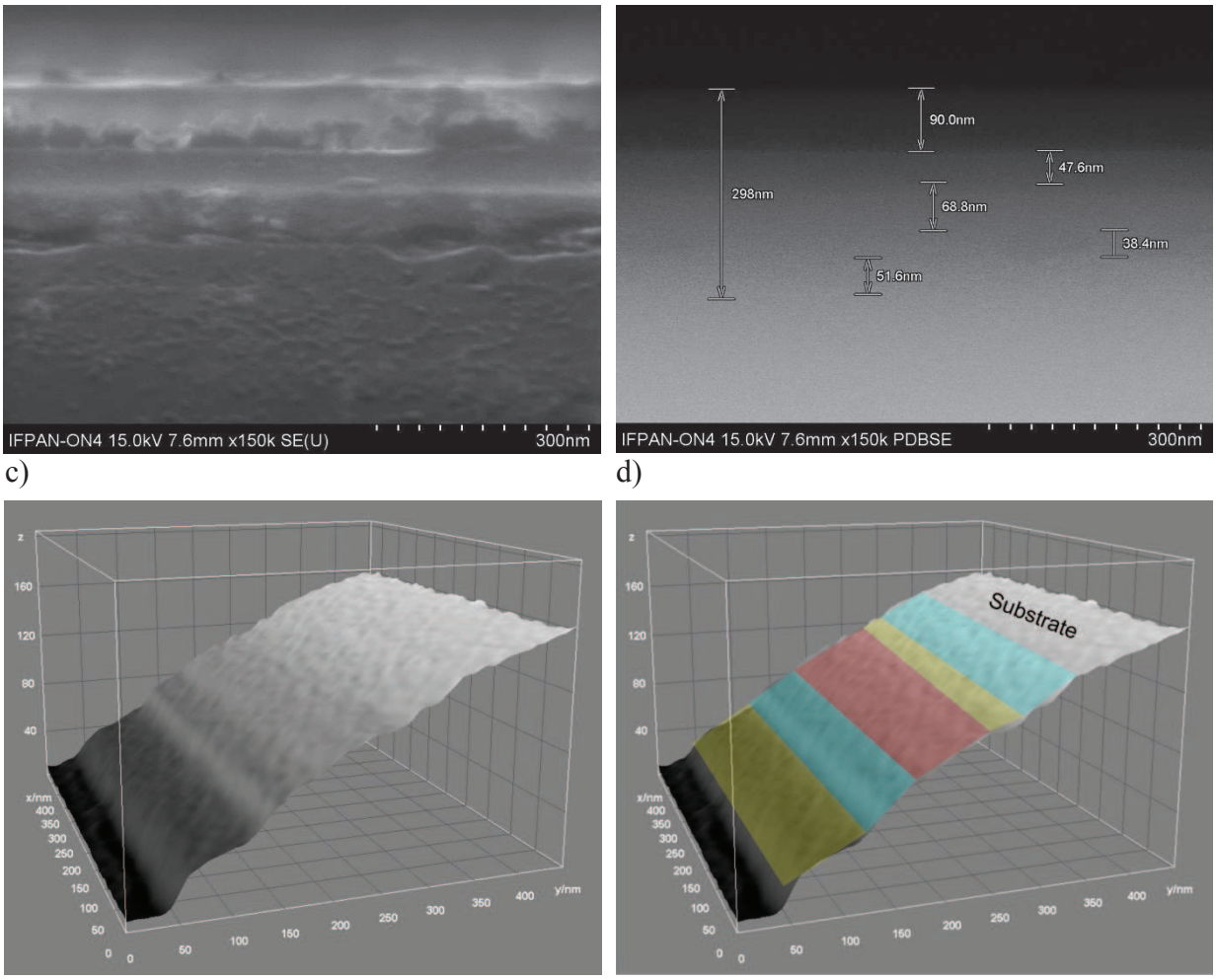

c) d)

Figure IV.6. Electron microscopy images of the LP07 sample. SEM image of the sample edge (a) and BSE images of the internal structure (b, c and d). Several different density regions are visible, with an amorphous region and transition zones clearly visible.

7. N2 sample

The N2 is a first sample of the second generation diffused-implanted structures. Those structures were developed after LP family, and featured clearer aSi/cSi interface thanks to improved annealing process. This sample was measured at the moment where it was passivated by 260 nm thick SiO_2, however the final structures were also passivated with the indium tin oxide conductive glass. This structure featured much thicker passivation than previous LP samples. Details of the architecture can be seen on the Figure IV.7.

a) b)

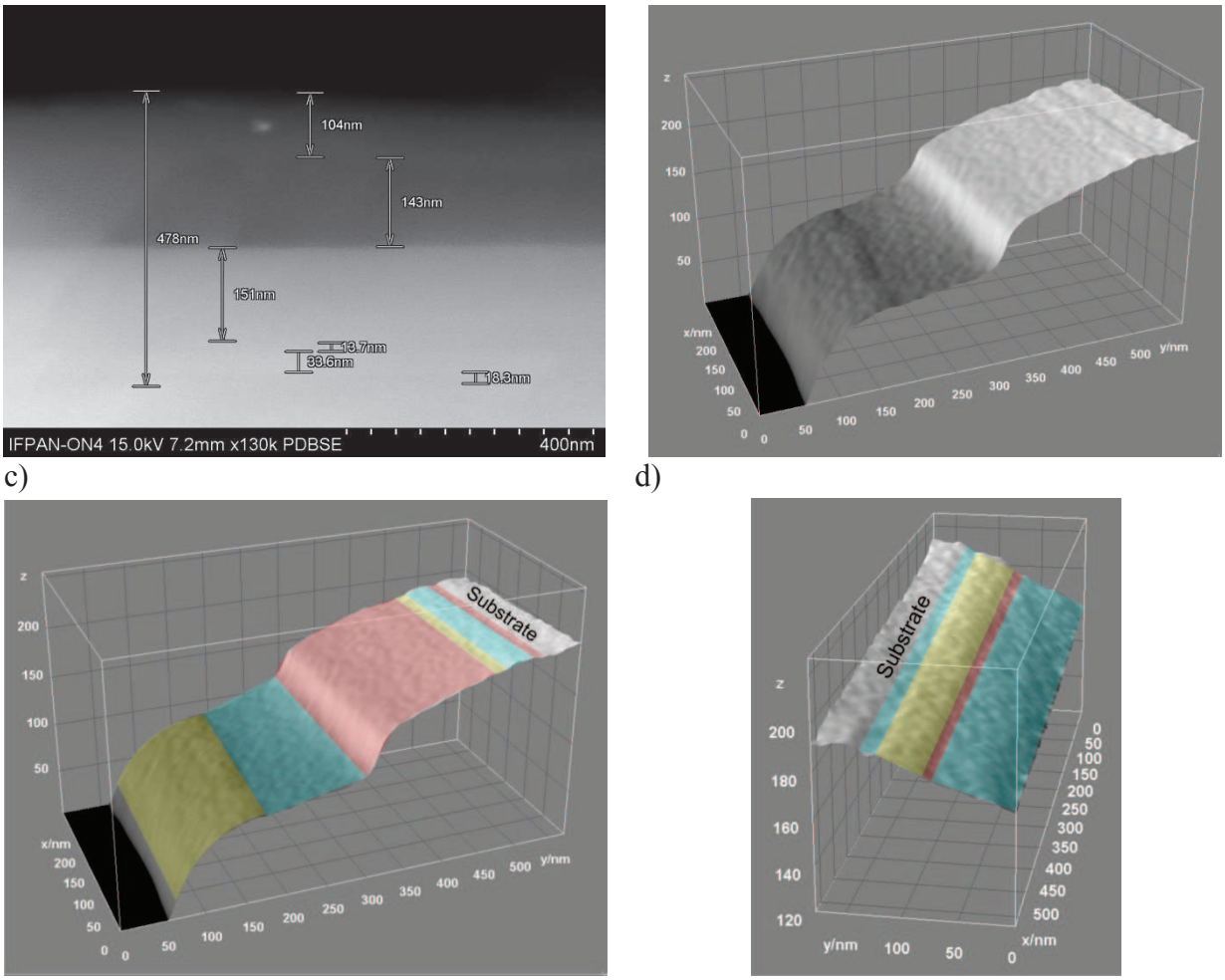

c) d)

Figure IV.7. Electron microscopy images of the N2 sample. SEM image of the sample edge (a) and BSE images of the internal structure (b, c and d). Amorphous layer along with neighboring interface is clearly visible and well-defined.

The N2 sample has a unique quality of the aSi layer and aSi/cSi interface, which is very clear and well defined. The strained transition zones can be clearly visible on the both sides of aSi layer. Upper emitter area is about 165 nm thick, rather homogeneous and does not show any regions of different density, except the edge surface region.

8. N3 sample

The N3 is another representative sample of the second generation diffused-implanted structures (Figure IV.8). It features thinner passivation of about 65 nm, relatively thicker emitter reaching 189 nm and well defined, thin amorphous layer. Thickness of the amorphized region is close to 16 nm, including the transition zones. Upper emitter area is also very homogeneous and uniform.

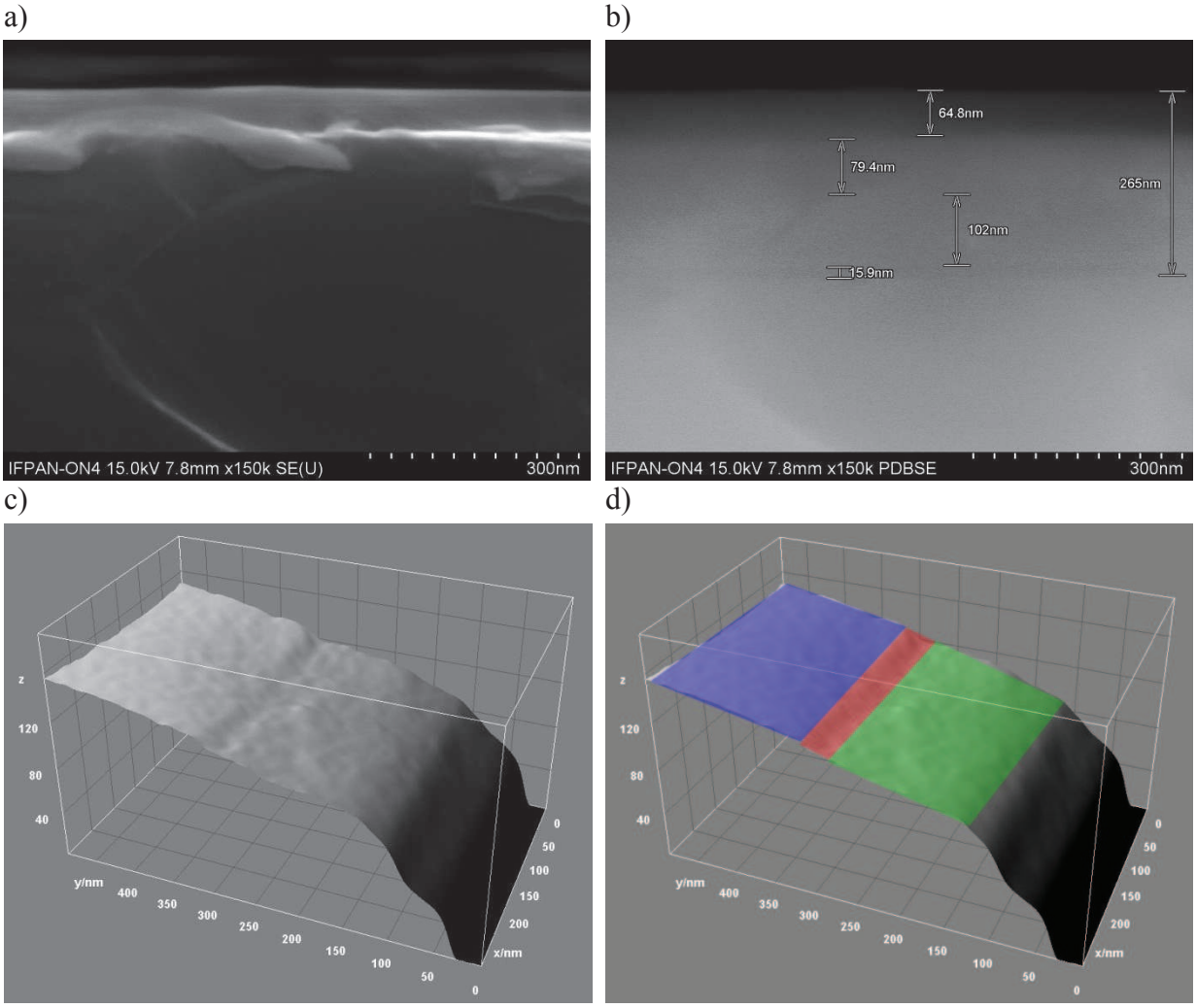

Figure IV.8. Electron microscopy images of the N3 sample. SEM image of the sample edge (a) and BSE images of the internal structure (b, c and d). A 16nm thick amorphous region and transition zone (red) is visible, buried 180nm below the surface of silicon.

9. N4 sample

The N4 sample features thin passivation of about 75 nm and rather thick upper emitter, reaching 180 nm. The emitter is inhomogeneous in density, with several different, distinctive regions visible. Surface region of about 22 nm is clearly damaged by the implantation/diffusion process. The area below is about 80 nm thick, crystalline heavily P-doped Si. The transition zone between lightly defined amorphized region and crystalline zone is about 85 nm thick. The fact that the aSi/cSi interfaces are not sharp in this particular structure might be due to the extensive annealing process that might have formed microcrystalline regions in aSi layer, therefore changing its properties to semi-amorphous. An estimated thickness of aSi layer in this structure is 20 nm, but the crystallinity factor is much

higher than in the N2 sample, indicating rather hypocrystalline layer instead of fully amorphous one.

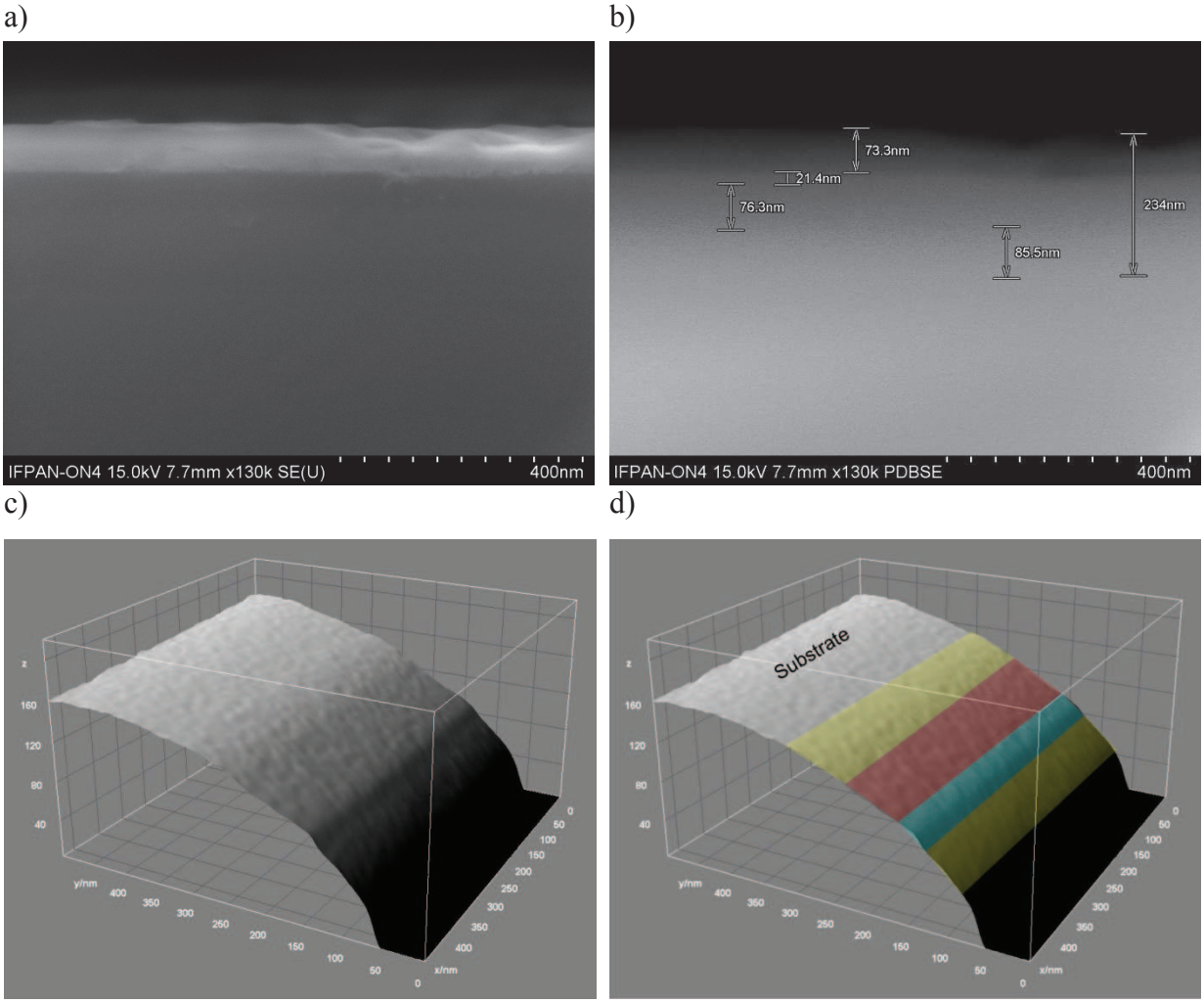

Figure IV.9. Electron microscopy images of the N4 sample. SEM image of the sample edge (a) and BSE images of the internal structure (b, c and d). Very wide transition zone and amorphized area is visible, indicating high fraction of microcrystals in the aSi region (yellow).

10. N7 sample

The N7 sample features very good quality passivation made of SiO_2, which is around 108 nm thick. It has thin emitter, where purely crystalline region extends to about 155 nm below the surface of Si. Below lies an amorphized region along with the transition zone, which is about 38 nm thick.

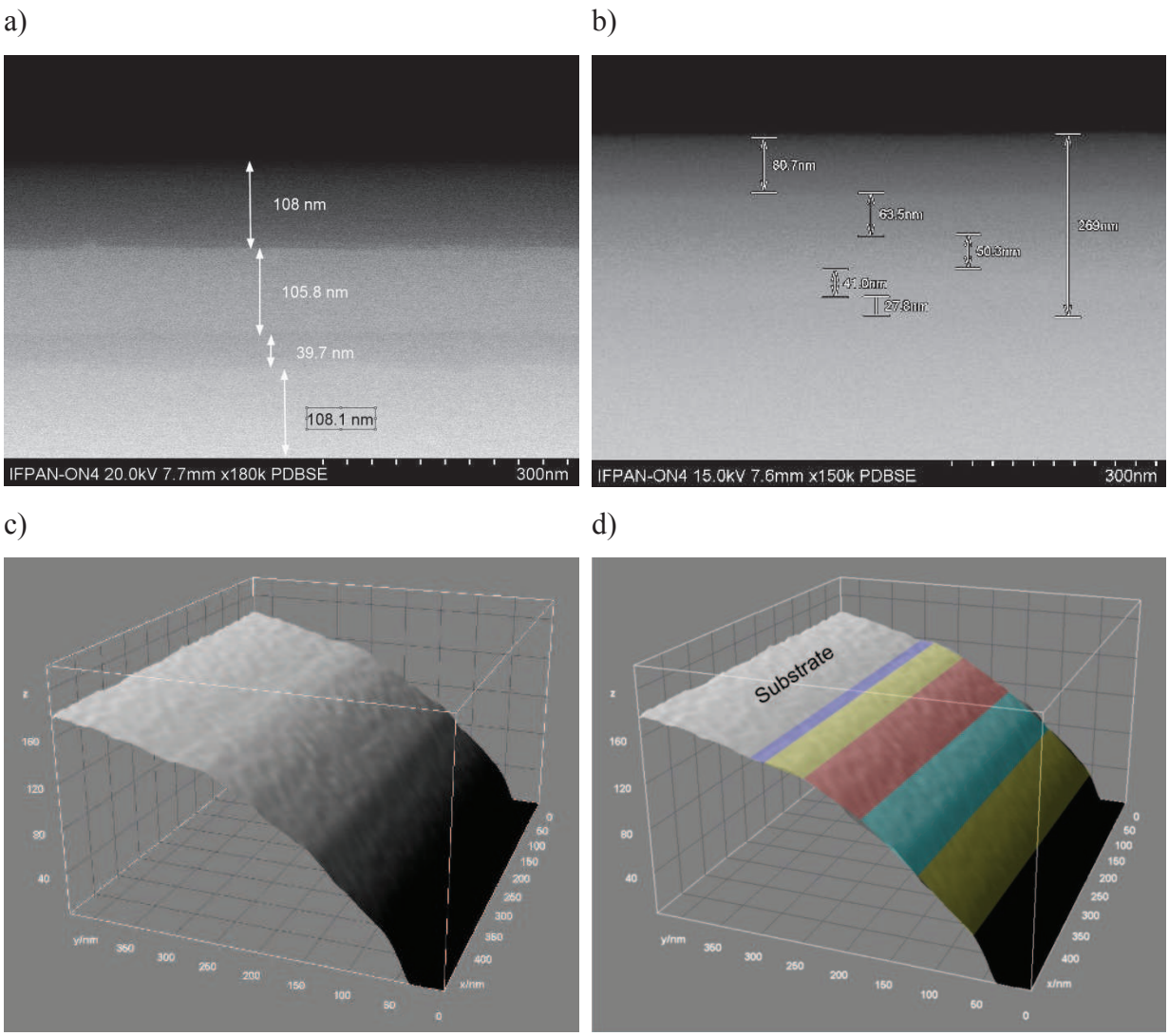

Figure IV.10. Electron microscopy images of the N7 sample. SEM image of the sample edge (a) and BSE images of the internal sample structure (b, c and d). Three different zones are clearly visible, with amorphized region lying in the middle, and about 40 nm thick (marked in red).

However, those values are valid only for the measured piece. The measurement was performed on an edge of the wafer; therefore thicknesses of the layers in the samples cut from the middle of the wafer might have slightly different values (usually thicker). This is especially true for the emitter.

11. N8 sample

Sample N8 is passivated by rather thin layer of SiO_2, reaching 90 nm at maximum in the measured piece. It exhibits very well-defined upper emitter with extremely sharp aSi/cSi interfaces. Total upper emitter thickness varies around 175 nm, below lies a sinusoidal amorphous layer, which along with the strained transition zones, is 18 nm thick.

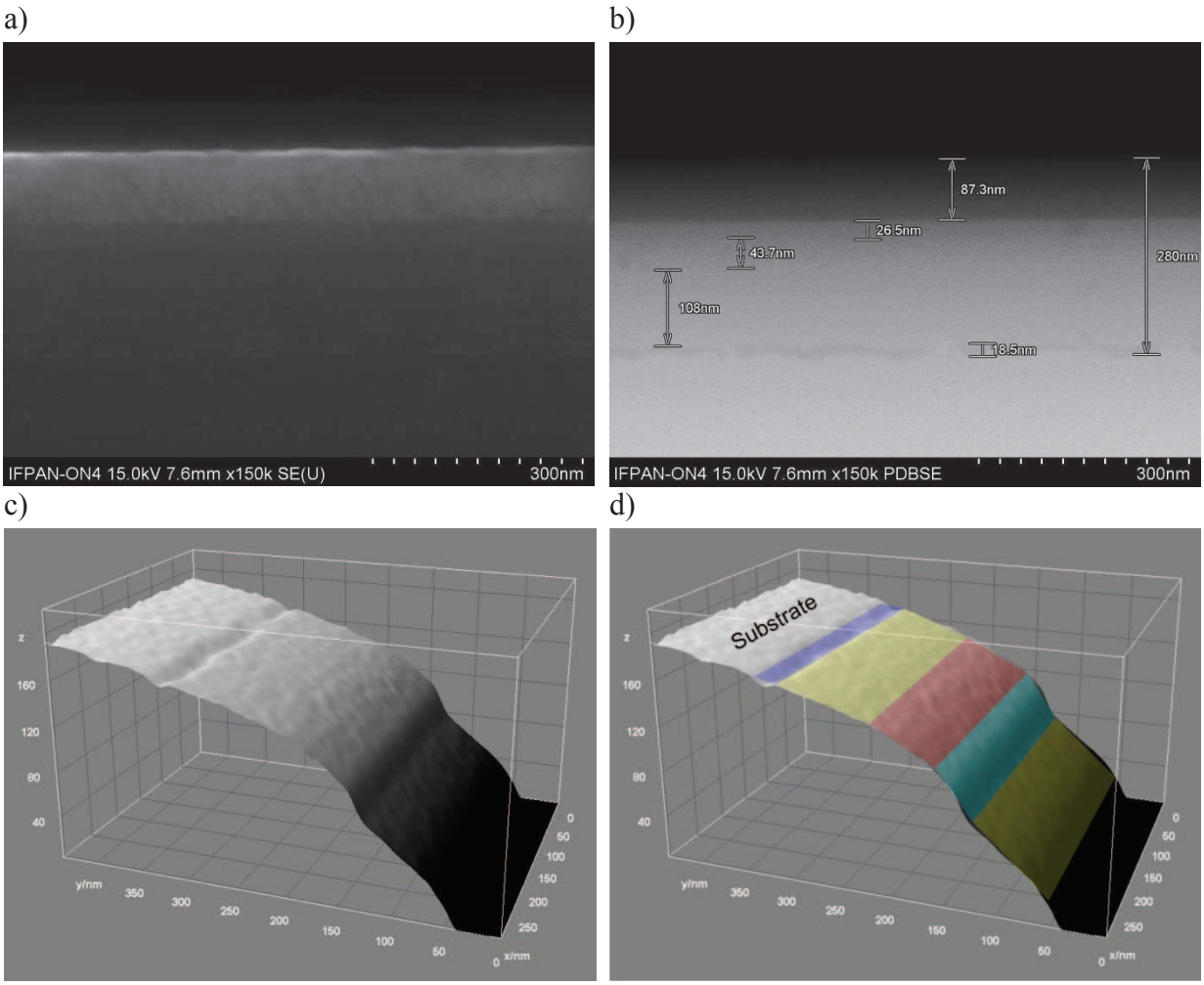

Figure IV.11. Electron microscopy images of the N8 sample. SEM image of the sample edge (a) and BSE images of the sample internal architecture (b, c and d). Extremely well-defined aSi later (marked in blue) is also visible on the figure d.

All Electron Microscopy measurements were performed at Institute of Physics, Polish Academy of Sciences in Warsaw, in the group of Professor Marek Godlewski. The author would also like to acknowledge the help of Bartłomiej Witkowski, who participated in SEM measurements.

1.2. Surface morphology.

To analyze morphology of the top surface as well as the influence of the passivation of the surface smoothness, we employed several experimental techniques. One such is Atomic Force Microscopy (AFM), which relies on sensing the interaction between a sharp tip and the surface of a sample. Various types of interactions might be sensed via AFM, such as mechanical, electrostatic, magnetic, chemical bonding, but in our case we measured van der Waals forces. Another technique used to analyze the surface of chosen samples was 3D optical surface profiling, which uses fringe projection to estimate the shape of the surface.

We studied two samples, N79 and N72, which were parts of the same wafer N7. Both of the samples show very good optical response from the buried nanostructure and differ only by the quality of the passivation, which was etched off the N72 sample. This feature greatly influences both electrical and optical properties of our structures.

To assign a numerical value to the properties of a measured surface and to quantitatively express the surface roughness we introduce the roughness factor R_a, defined as:

$$R_a = \frac{1}{n}\sum_{i=1}^{n}|S_i - S_{av}| \qquad \text{(IV.1.1)}$$

where S_i is the height of a given point on the surface, S_{av} is the arithmetic mean of all the points and n is the number of points on the surface.

Sample N79 is a passivated sample with a very smooth surface. We characterized it with the optical surface profiler, based on white light interferometry. Results showing two views of the surface are presented in Figures IV.12 and IV.13. Measuring on a different spot of sample N79 revealed also a smooth surface, but with a higher roughness factor R_a = 1.0467 nm, which is about 45% higher than the one measured at the other spot.

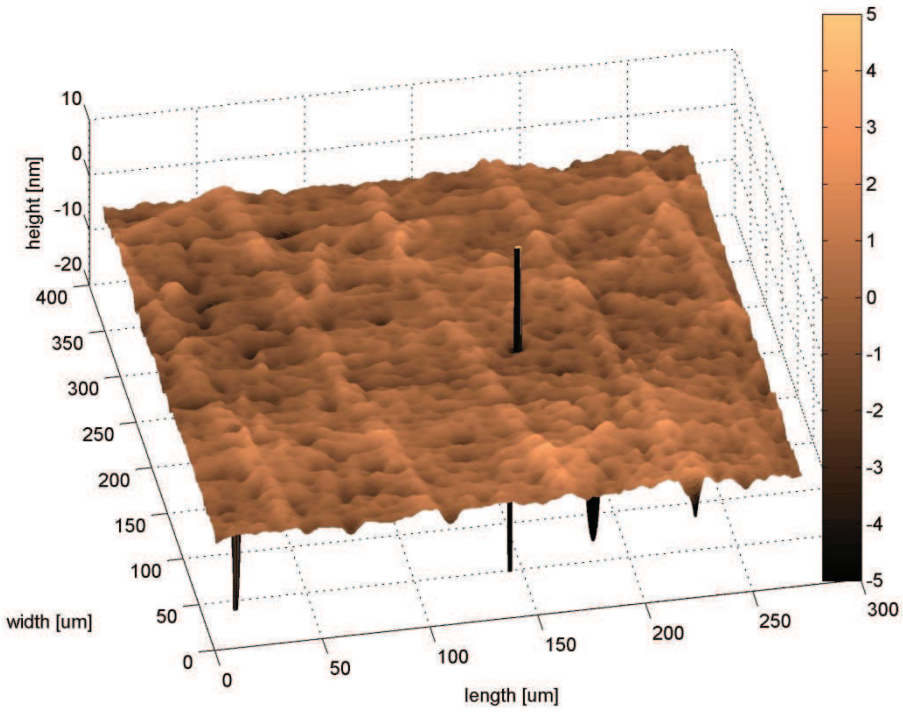

Figure IV.12. Surface of the N79 sample measured by the 3D optical surface profiler. The roughness factor was calculated to be R_a = 0.7214 nm.

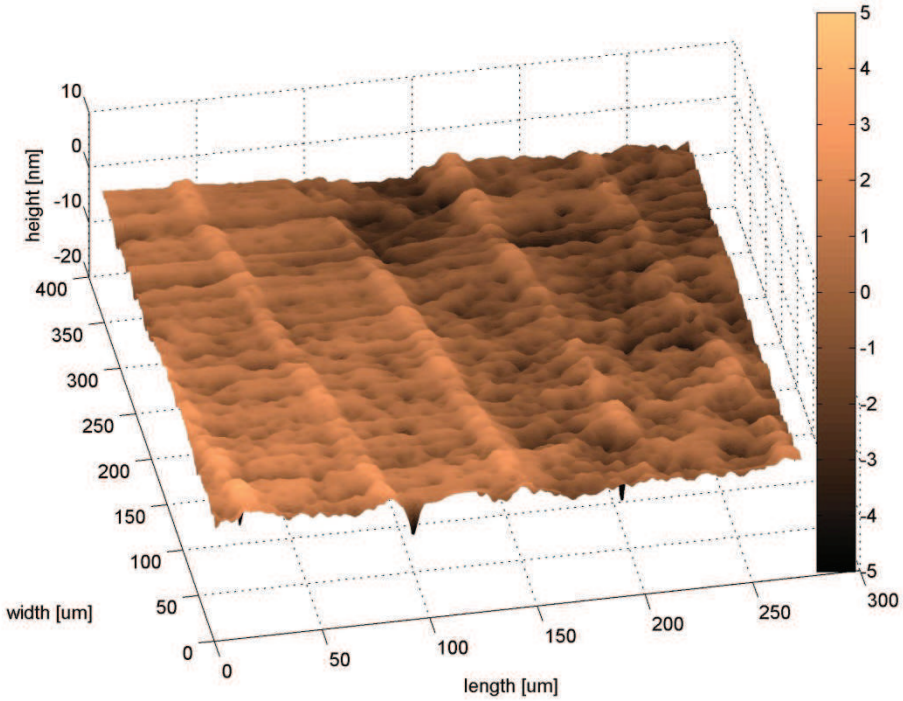

Figure IV.13. Surface of another spot of N79 sample measured by the 3D optical surface profiler. The roughness factor was calculated to be R_a = 1.0467 nm.

The overall conclusion of this measurement is that the sample is well passivated with SiO_2 and 90% of the points are confined between ± 5 nm around the mean value.

Sample N72, unlike its sister structure, was not passivated by SiO_2 for the second time, therefore it should retain its original, very rough surface with potentially very thin thermal coating about a few nanometers thick. We have employed two methods to analyze this structure i.e. 3D optical surface profiling and AFM.

The N72 shows much higher roughness factor, ranging between R_a = 4.24 to 6.4 nm, and 90% of the points is confined in between ± 10nm around the mean value. Optical profiling shows very uneven surface with plenty of craters and mountains that exceed R_a by an order of magnitude. These features are probable remnants of the reactive ion etching process that removed the SiO_2 layer. The area scanned by optical profiling was the same for both samples and was a rectangular spot by 360 x 275 μm.

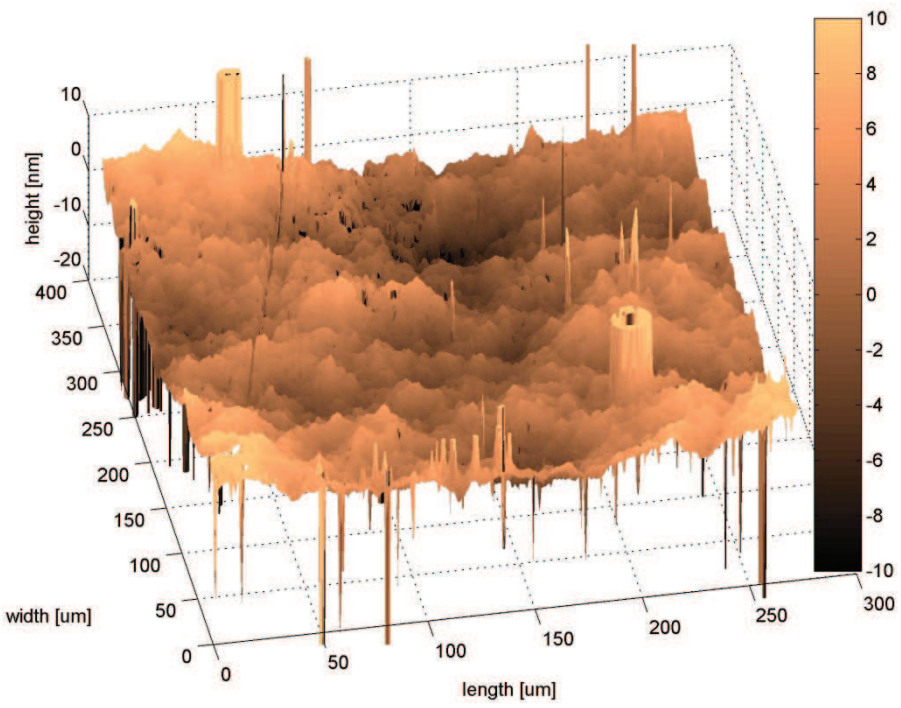

Figure IV.14. Surface of the etched N72 sample measured by the 3D optical surface profiler. The roughness factor was R_a = 4.2406 nm for this particular spot.

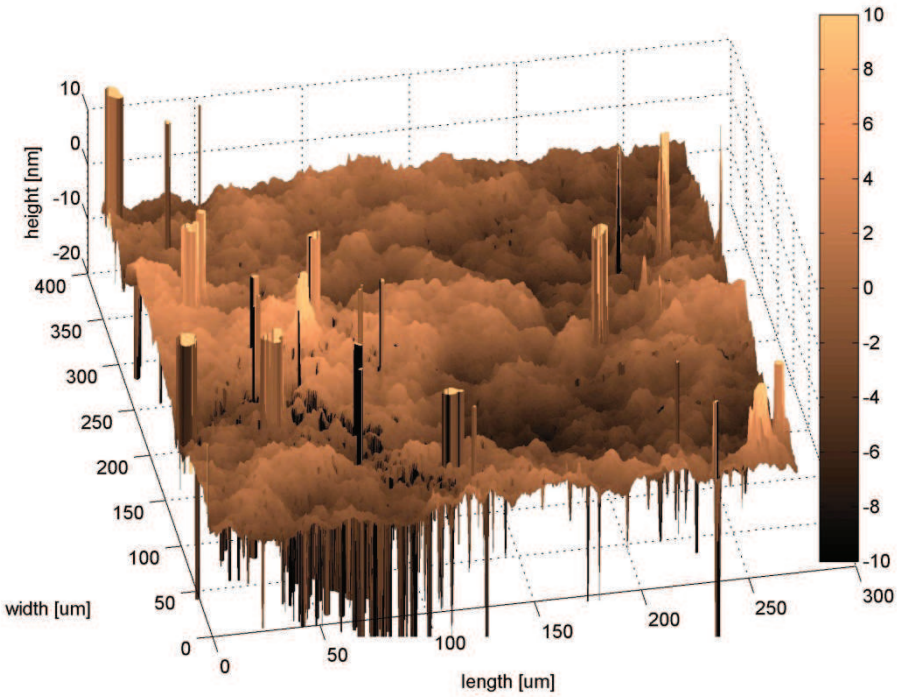

Figure IV.15. Another spot of the etched N72 sample measured by the 3D optical surface profiler. Roughness factor was R_a = 6.4080 nm for this particular spot.

a) b)

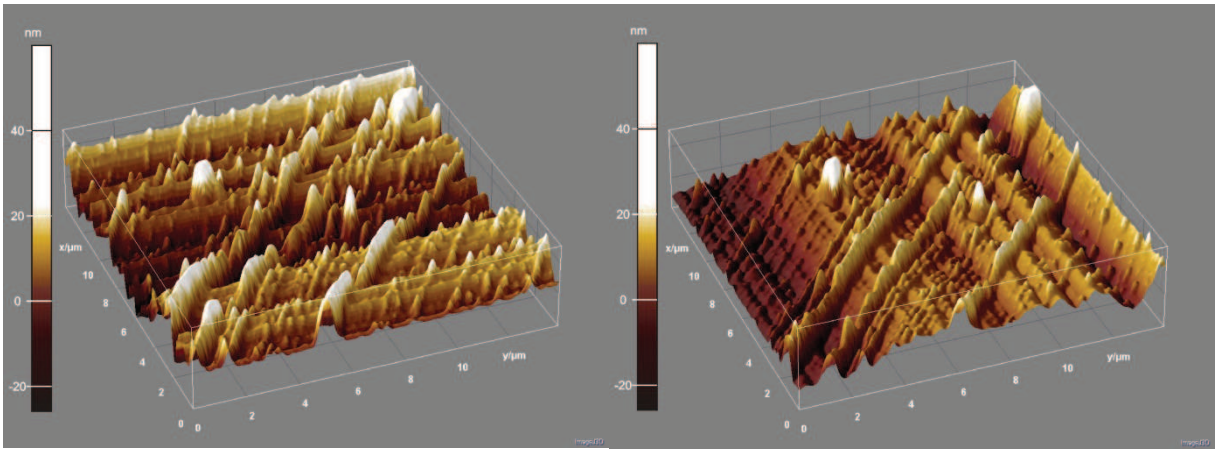

Figure IV.16. Surface of the etched N72 sample measured by AFM. Two scans were taken, along y-axis (a) and x-axis (b).

For the AFM measurements two scans of the same spot were taken, with much greater spatial resolution than with the optical profiler. Measured surface was a square of a side equal to 14 µm. Since it was not performed in vacuum, the measurement was sensitive to the movement of the air in the chamber, as well as it proven to be very sensitive to the vibration of the floor. Artefacts can seriously degrade the quality of measurements thus to limit their

incidence during the experiment, we performed two scans along perpendicular axes (figure IV.16). Due to the fact that we were not able to fully remove artefacts produced by the scan only height of the features lying on the respective line should be considered, i.e. along *y*-axis for results shown in Figure IV.16b and along x-axis for Figure IV.16a.

2. Optical measurements.

Optical properties are one of the most important factors that determine the overall performance of any optoelectronic device, and solar cells in particular. Light-matter interaction is the first stage of the complex process of light to electricity conversion, and therefore proper estimation and control of optical properties is crucial for understanding, determination and estimation of all the other processes that take part in the whole process. It is not only important because of the potential losses related to reflectivity of the cell, but it also allows more detailed control of where the light is absorbed and where the power is generated in the structure. Such knowledge is particularly important for any structured cells that are not simple one junction cells, especially tandem cells. In the case of MIND structures, we can study the exact amount of photons that could have been used to generate hot electrons in the active sub-structure. We will analyze this process in detail in Chapter IV.
We have employed two different optical methods i.e. reflectivity measurement in the integrating sphere and ultrafast spectroscopy.

2.1. Reflectivity measurements in the visible and near infrared.

Reflectivity is one of the most important parameters describing a solar cell. It represents the first possible interaction between the light and the device and is also the first limiting factor for the efficiency. Combined with structural measurements and SIMS profiles, one can extract the spatial dielectric function, which in turn allows determination of the exact distribution of the Poynting vector and energy density in the structure. We have performed our measurements using an integrating sphere to ensure that the entire reflected flux will be directed towards the detector. Transmission measurements were not possible because of the back surface mirror made of Al.
Several families of MIND samples were measured, that are based on two possible SIMS profiles (implanted or diffused) but differ when it comes to thickness of the emitter and/or amorphized region, and also were passivated with different materials, such as silicon dioxide

(SiO_2), silicon nitride (Si_3N_4) and indium tin oxide (ITO). We have analyzed samples from both LP and N generations.

2.1.1. N7 samples.

Samples N79 and N72B are the most extensively analyzed by several different experimental techniques, due to their unique features that will be discussed later. Both samples are squares of approximately 2 x 2 cm, and differ only by the state of passivation and the surface roughness, as was shown earlier in this chapter. This unique difference allows us to extract vital information about the overall performance of the structure as well as analyze and study several interesting effects. Apart from reducing the optical impedance of the structure, the SiO_2 passivation layer also acts as an electronic passivation, reducing the density of surface states through which Auger recombination takes place, a process that usually negatively influences electronic properties of any semiconductor device.

Sample N79.

We expect to observe interferences in the optical response of N79 sample, due to the existence of the buried amorphous layer and rather low surface roughness factor. (figure 2.1). As was shown by the BSE measurements, the internal structure of N79 sample is well-defined, but the exact values of the thickness for the upper emitter and amorphous layer are not well known (see Figure IV.10). We will therefore assume in the first approximation that the structure can be modeled by the simplest architecture possible, consisting only of five layers: passivation, upper cSi emitter, thin amorphized region and the substrate.

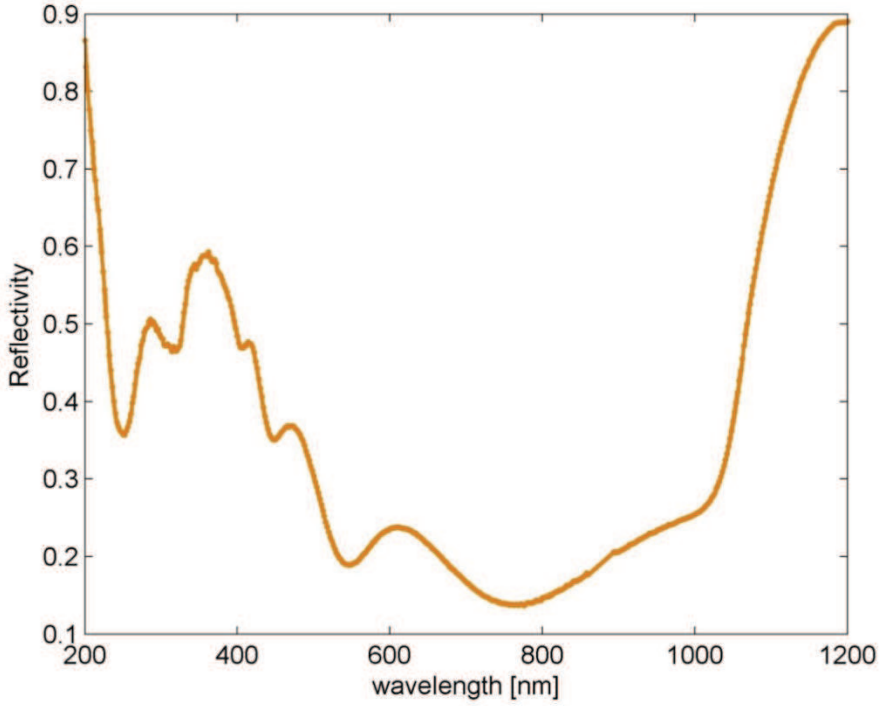

Figure IV.17. Reflectivity of the N79 sample. Interference maxima are visible for 420, 500 and 650 nm, respectively. For wavelengths longer than 1050 nm R raises dramatically due to the back surface aluminum mirror. Characteristic peaks at 275 and 360 nm are also visible.

For the moment we neglect the influence of the inhomogeneous doping and assume that the structure has the intended geometry, where layer thicknesses are as follows:

- passivation 119 nm
- upper emitter, thickness 163 nm, P concentration $N_P = 10^{20}$ cm^{-3}
- amorphous layer, thickness 8 nm, P concentration $N_P = 10^{18}$ cm^{-3}
- substrate, P concentration $N_P = 10^{16}$ cm^{-3}

The modeled structure is shown in Figure IV.18a. This simple structure reproduces all the interferences and matches rather accurately their height, which is quite remarkable considering used approximation (Figure IV.18b).

The real strength of the model presented in chapter III of this work lies not only in the ability to simulate macroscopic optical properties such as reflectivity, transmission and absorption of the sample and compare them with experimental measurements, but in the possibility to extract the quantities that are not available through non-destructive measurements, such as absorption of each layer and the energy distribution.

a) b)

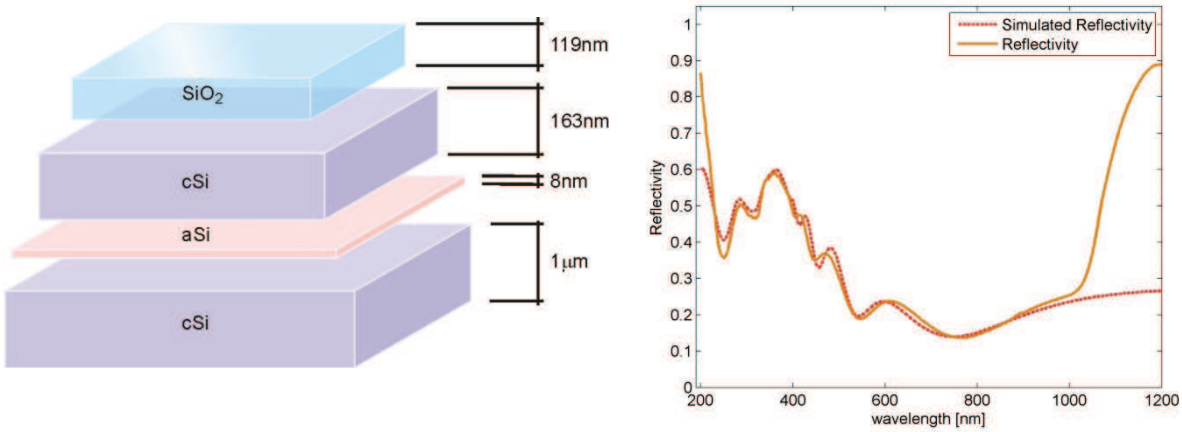

Figure IV.18. Schematic representation of the simple model multilayer structure (a) and the both simulated and experimental reflectivities for N79 sample (b). Interference maxima and minima are reproduced quite accurately.

a) b)

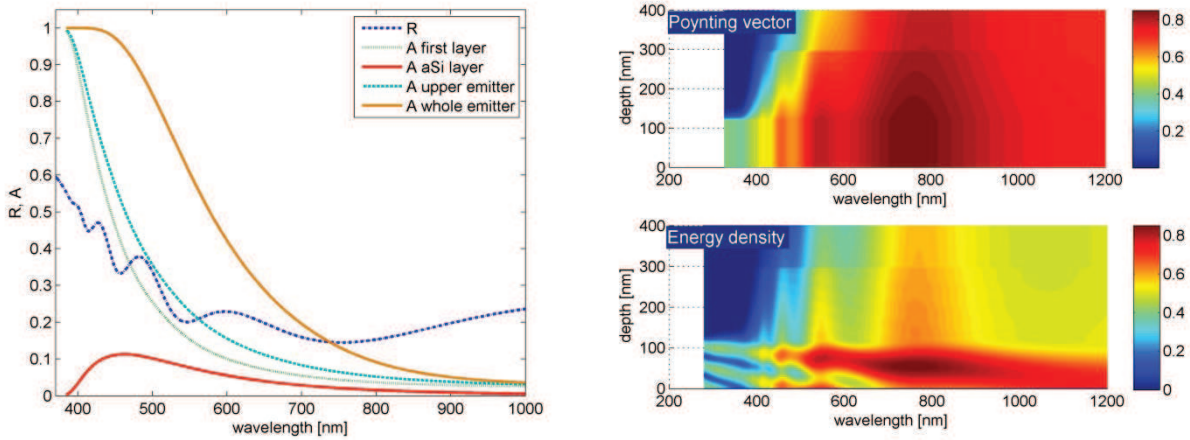

Figure IV.19. Normalized absorption curves for each layer in the emitter and the sample reflectivity (a) and Poynting vector $|S|$ distribution as well as energy density U (b) inside the upper emitter.

As can be seen in Figure IV.19, only a fraction of total incident flux is absorbed in the upper emitter, and only relatively small amount is absorbed in the aSi layer. Photons up to 600 nm are quite efficiently absorbed in the emitter, with only about 50% penetrating deeper into the structure, however lower energy photons, for wavelengths 700 nm and greater, are weakly absorbed in the emitter, with more than 80% penetrating to the base. The amorphous layer, in this particular model cell, absorbs only small fraction of the total incident flux, peaking 10% for 450 nm. We can therefore expect that the low-energy multiplication phenomenon, even if it was very efficient, would not have huge impact on the overall cell performance.

However such a simplistic approach cannot be expected to truthfully reproduce effects observed in a real cell. On one hand, the architecture of N7 wafer was measured by BSE microscopy, clearly indicating that the amorphized region is much thicker, between 25 and 40 nm thick, while the upper emitter thickness oscillates around 155 nm. On the other hand, we have to take into account the inhomogeneous P doping distribution that can vary by two orders of magnitude over a distance of 200 nm for implanted-diffused samples. Another thing we took into consideration is the percentage of the activated dopants. P doped silicon up to concentrations of $N_d = 10^{18}\text{cm}^{-3}$ are considered fully activated in room temperature [2], and this is the usual value of P concentration in the emitter of good quality cSi cells.

However, for higher doping concentration, often only a fraction of the introduced P atoms are activated. We calculated an approximate number of active dopants from the density of states obtained through DFT and a subsequent calculation of the Fermi energy (see chapter I and III for details). The results indicate that for the highest P concentration, reaching $N_d \sim 10^{21}\text{cm}^{-3}$ only a small fraction of phosphorous is active (about 6%), and the number of active dopants increase as the overall P density decreases, deeper into the structure. This fact has a direct implication when dielectric function is considered, because for very high doping densities changes in dielectric function become important, both due to carrier and lattice contribution terms. Those two effects can greatly influence optical properties of the structure in several ways, changing reflectivity only slightly, but significantly rearranging power distribution in each layer.

a) b)

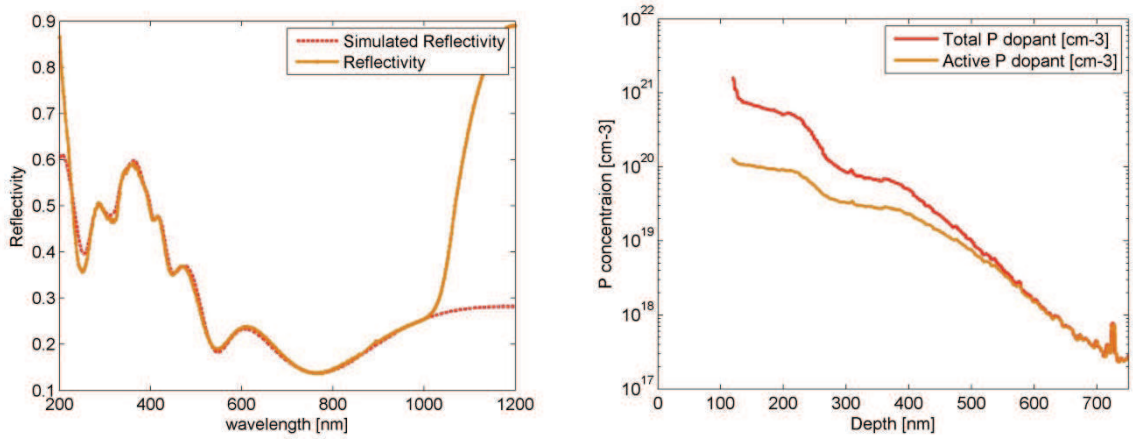

Figure IV.20. Reflectivity curves for accurate model structure (a) and comparison of active dopant versus total P concentration in the emitter. The structure is shown in Figure IV.21.

We have performed a much more accurate simulation, where the model structure incorporated all the above components. We have also included the possibility that the amorphized region can be in fact an amorphous matrix in which micro- and nanocrystallites might have formed.

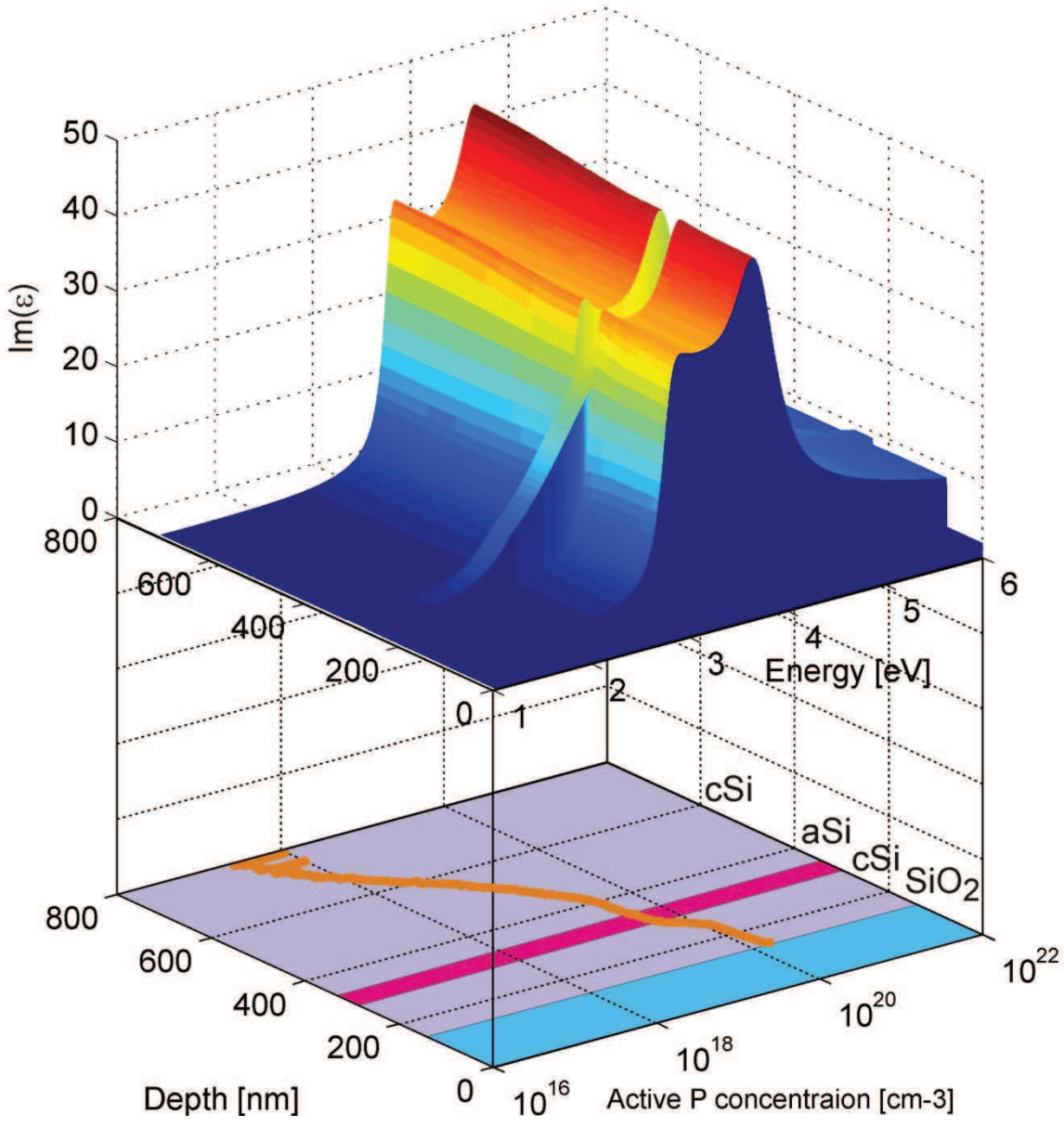

Figure IV.21. Imaginary part of the dielectric function vs sample depth for accurate structure model (upper) and the active P distribution in each layer (lower). Thicknesses for each region in this model were: SiO2 – 117 nm, upper cSi – 158 nm, amorphized Si – 40 nm, lower cSi – 400 nm (for precise doping simulation).

This effect is often observed in hydrogen-stabilized amorphous Si, and it can be expected that due to the fabrication process employed for MIND structures it was even more emphasized [3]. In Figure IV.20 we present results of this simulation. It can be seen that the interference

fringes are much more accurately reproduced both in terms of position and value. Also, the energy density is distributed in a different way in comparison with the simple model, especially in the upper emitter (first cSi region), forming several peaks for wavelengths around 750 nm. Figure IV.21 shows schematic representation of all the features of the accurate model structure as well as the doping distribution in the crystalline and amorphized regions. It is clearly visible that the dielectric function changes dramatically due to doping and that the amorphized region has different optical impedance, and is therefore responsible for the interferences.

Two main conclusions become apparent from the more accurate simulation. First, the absorptive properties of the structure changed dramatically, even if the reflectivity remained more or less the same and preserved the same characteristic interferences. Second, we were able to extract the dielectric function of the amorphized region with the help of Effective Medium Approximation (EMA), and can roughly estimate the fraction occupied by crystalline inclusions in amorphous matrix. Comparison of the dielectric function of the amorphized region with that of the hydrogen – stabilized aSi is shown in Figure IV.22 (c). The striking increase in the absorption of the aSi layer in this approximation, which is almost threefold, would allow for more efficient energy manipulation during multiplication process, therefore making the whole phenomenon more plausible.

We were able to uncover all the parameters describing optical properties of the measured N79 sample with satisfying accuracy. Experimental and simulated reflectivity show very good agreement, lying in the range of systematic measurement error. Thanks to good coherence between structural and reflectivity measurements, we managed to extract the properties of amorphized region as well as estimate the total power absorbed there, which in turn can be used to calculate the potential strength of low energy multiplication process.

a)

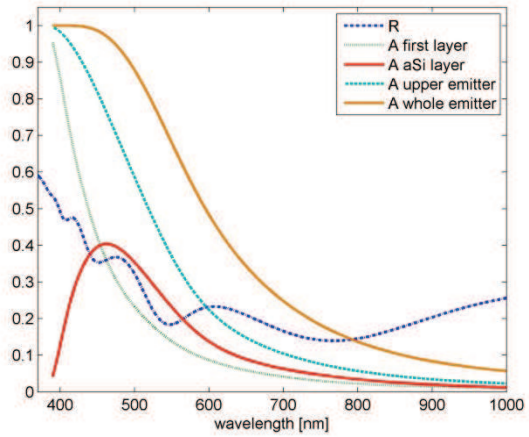

b)

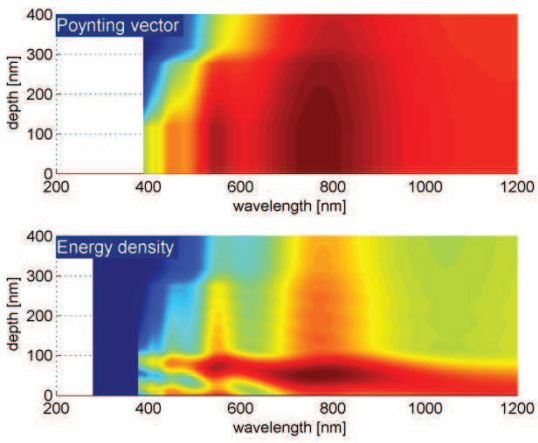

c)

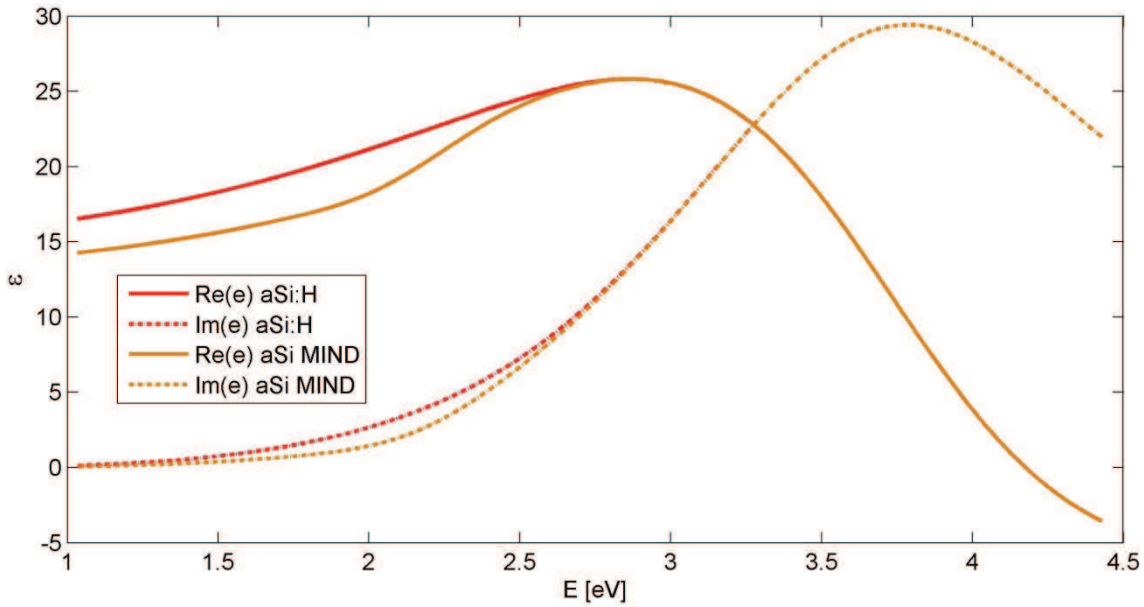

Figure IV.22. Normalized absorption curves for each zone in the accurate model structure (a) and Poynting vector $|S|$ and energy density U (b) inside the upper emitter. Figure (c) compares the dielectric function of hydrogen stabilized amorphous silicon aSi:H with the one present in N79 sample. Influence of crystalline inclusions is clearly visible, for which the volume fraction was estimated to be f_c = 0.2–0.5.

Sample N72B.

N72B and N79 are parts of the same wafer, therefore they should have exactly the same internal structure. However the state of its surface is vastly different because of the surface damages induced by the Reactive Ion Etching (RIE) (see Figure IV.14). The thermal oxide was etched and the sample was never again passivated, unlike in the case of other samples. Comparison between experimental R for N79, N72 before and N72B after RIE is shown in Figure IV.23.

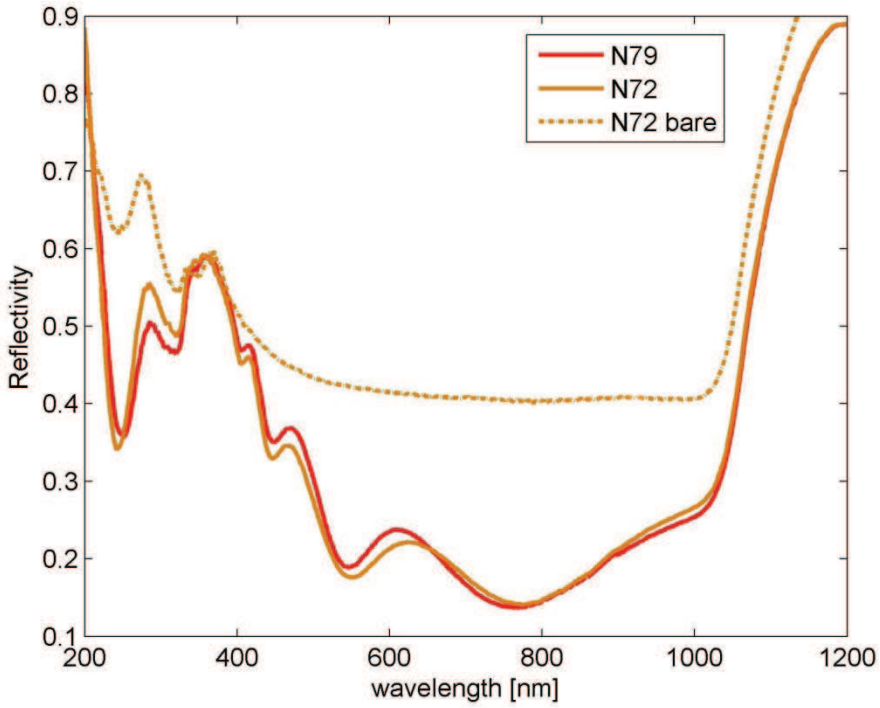

Figure IV.23. Experimental reflectivity of N79, N72 (before) and N72B (after RIE).

As was already presented in the subsection dedicated to the morphology, the roughness factor is about 4-9 times higher than the one for N79. We therefore expect that the optical properties of this sample should show different features: interferences are unlikely to be seen because of high surface scattering and the overall amount of reflected light should be higher, due to the lack of an optical passivation layer/antireflection coating. This is indeed the case, and the reflectivity of N72B is very close to the one of moderately doped Si, (see Figure IV.24). Interferences in N72B are not visible because of high surface scattering, however it can be clearly seen that for simulated N72B sample, interferences are localized around mean value measured experimentally.

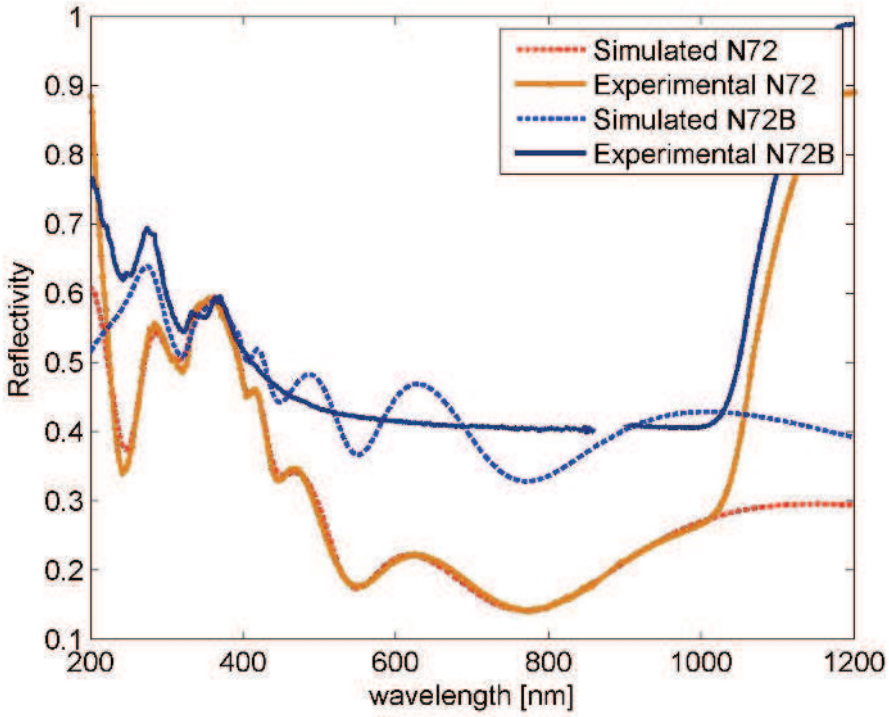

Figure IV.24. Reflectivity of N72 with SiO_2 passivation and N72B compared with the simulation. There is good agreement between experimental and simulated R for the passivated sample, however the fringes predicted by simulation for etched one are absent in experiment, due to surface scattering.

The passivated N72 sample has similar optical response as N79, with slightly thinner effective thickness of passivation layer and slightly different properties and thickness of the aSi region. The region thicknesses were estimated to be as follows: SiO_2 112 nm (for passivated), first cSi layer 157 nm and amorphized region 42 nm. Properties of the amorphous layer are also slightly different than in N79 sample, as is shown in Figure IV.25. Absorptive properties are similar and thanks to the estimation of energy density and Poynting vector, we can determine the number of electrons generated in the active sub-structure and in the whole upper emitter, which will be discussed in the following paragraphs.

a)

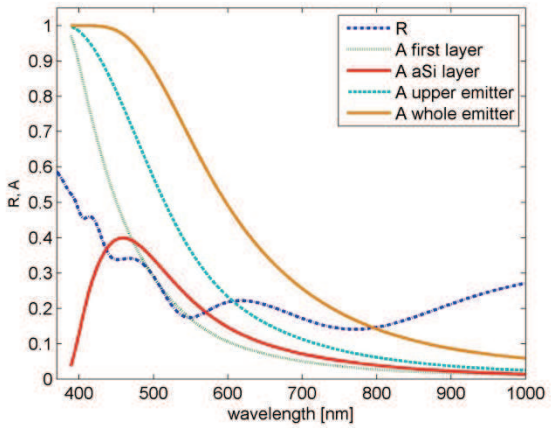

b)

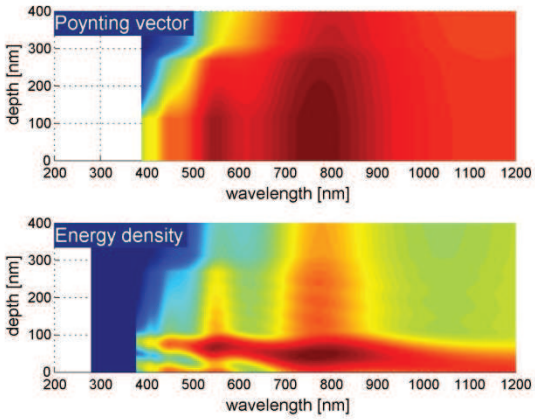

c)

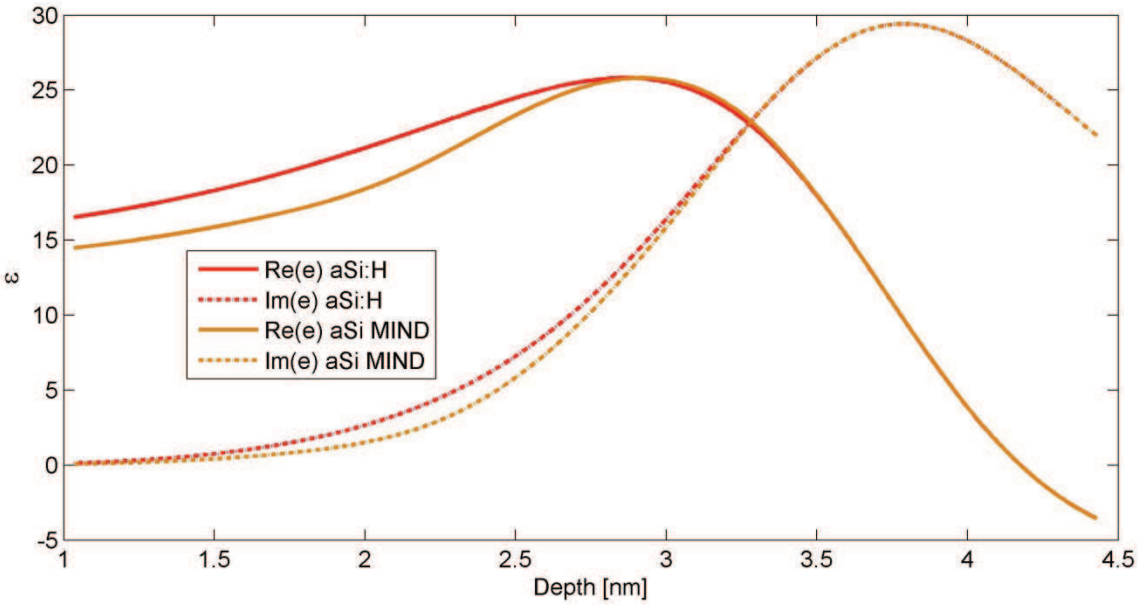

Figure IV.25. The normalized absorption curves for each zone in the accurate model structure (a) and Poynting vector $|S|$ and energy density U (b) inside the upper emitter. Figure (c) compares the dielectric function of hydrogen stabilized amorphous silicon aSi:H with the one present in the N72 sample. The influence of crystalline inclusions is clearly visible, for which the volume fraction was estimated to be f_c = 0.2–0.45.

Estimated properties of the N72 sample indicate that it a has slightly higher absorptivity, especially in the active region. The amorphized region seems to have fewer crystalline inclusions, and it has an extended thickness in comparison with N79. However the overall properties match well the properties of N79, which gives evidence that the fabrication process was reliable and produced homogeneous structures along the wafer.

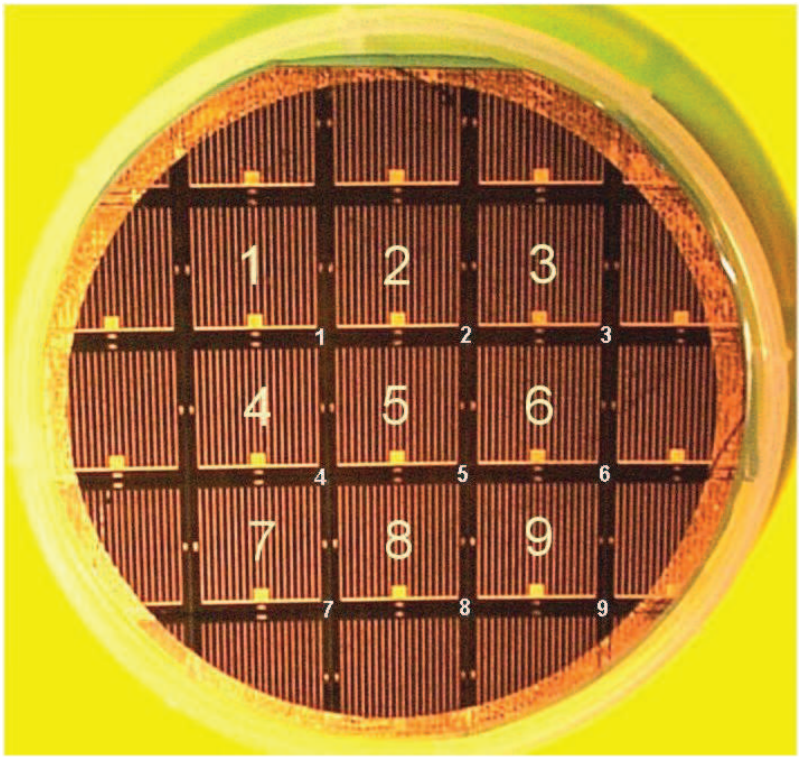

Figure IV.26. Photo of a N7 wafer. Square parts numbered 1, 2, 3… 9 were named after cutting N71, N72, N73… N79 respectively.

2.1.2. N2 samples.

Second generation N2 samples are another type of diffused-implanted MIND structures. As can be seen in Figure IV.7, they feature a well-defined amorphized region, clearly visible in the SEM measurements. N2 structures feature a rather thick passivation, ranging from 210 to 250 nm of SiO_2, which was intended as a better electronic passivation for the surface, however due to its thickness it deteriorated the optical properties by increasing the reflectivity, and does not fulfill well its role as an anti-reflective coating. Reflectivity of a N24 sample, which is a representative specimen of the whole family, is shown in Figure IV.27 along the structure used in the modeling. We based the thicknesses of each region in the model on direct BSE measurement shown in Figure IV.7, with the possible deviation of the actual optical path length from geometric layer thickness below 2%. The model reproduces optical properties of N24 with satisfying accuracy, correctly predicting the position and value of every interference fringe.

a) b)

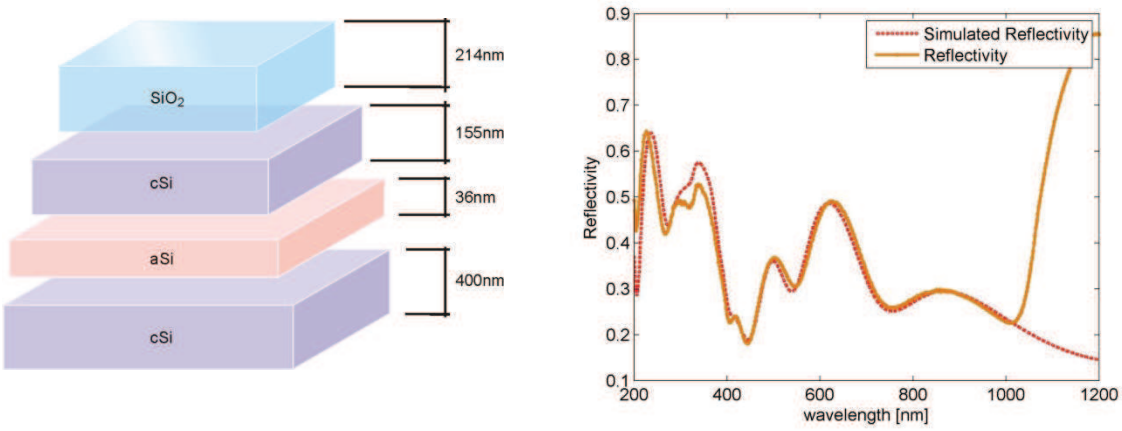

Figure IV.27. Schematic representation of the model structure (a) and comparison between experimental and simulated R for N24 sample. Slight offset at 370 nm is due to the surface scattering and increased number of defects in the passivation layer.

Since the doping procedure for the N2 wafer was the same as for the N7 wafer, we assumed that N24 would have the same P profile as N7 samples, and therefore we simulated the spatial dielectric function distribution according to the SIMS data we used for N79 and N72. The P concentration in both types of structures would be the same in the range of the systematic fabrication error.

Results indicate that the N24 features relatively few crystalline inclusions in the amorphized region in comparison to N7 samples, reaching only $f_c = 0.2$. It shows also a slightly smaller absorbance in the active sub-structure in comparison to N7 samples, peaking at 38% for 460 nm. We were able to extract the effective dielectric function of the amorphized region, which is shown in Figure IV.28.

We can see clearly that the energy density in the structure is comparatively much smaller than in N7 samples, which is a direct result of the thicker passivation layer. Amorphized region shows fewer crystalline inclusions, which decreases the absorption coefficient of the aSi layer and the active sub-structure as a whole. However the shape of ε implies that μc-Si inclusions are much better defined and with sharper interfaces than it was in the case of N7 samples, which can be seen thanks to the remaining characteristic peaks close to the critical energies in Si (3.34 and 4.3 eV).

a) b)

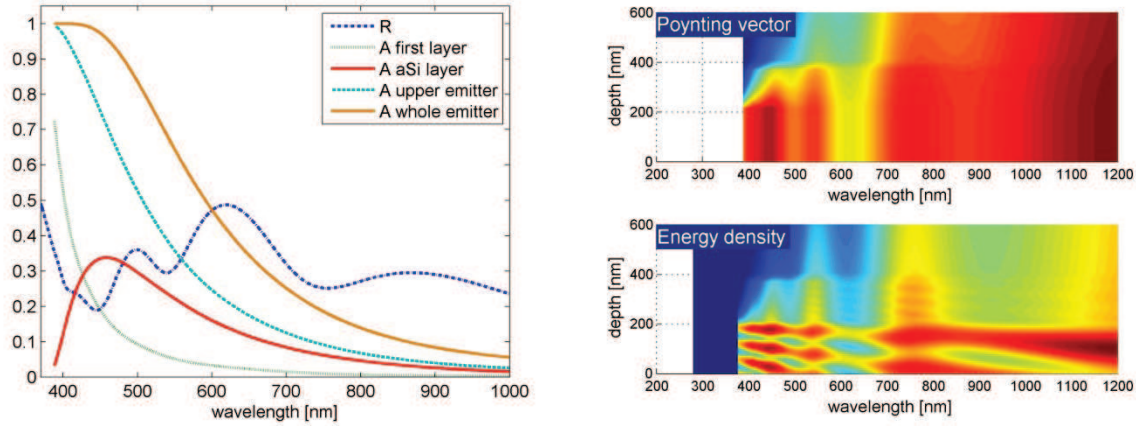

c)

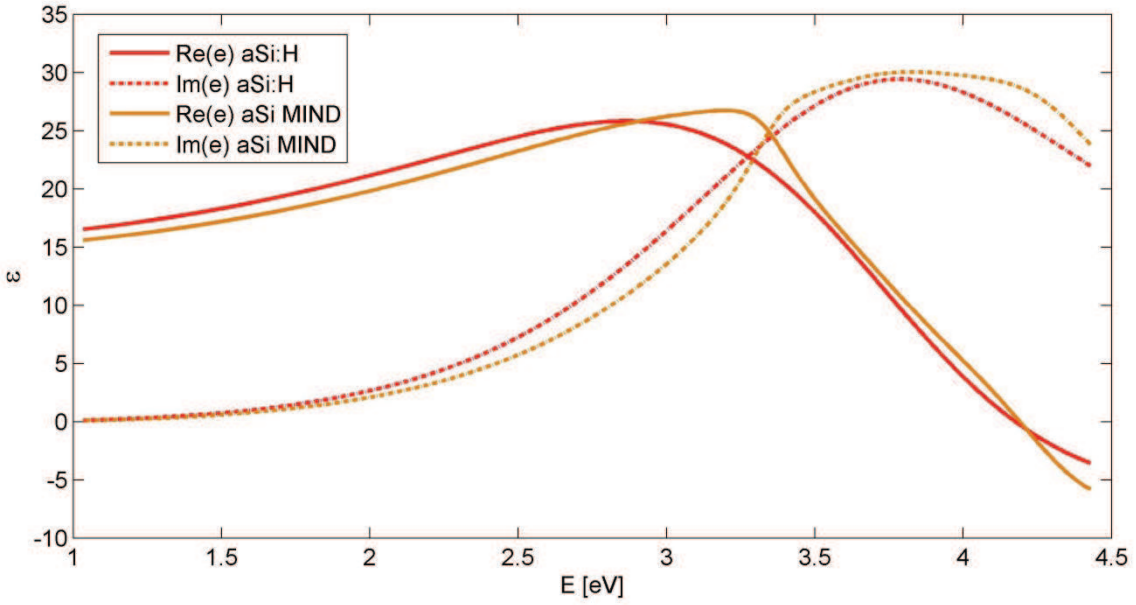

Figure IV.28. Normalized absorption curves for each zone in the accurate model structure (a) and Poynting vector $|S|$ and energy density U (b) inside the upper emitter. Figure (c) compares the dielectric function of hydrogen stabilized amorphous silicon aSi:H with the one present in the N24 sample. Percentage of crystalline inclusions is smaller than in N7 samples, and reaches $f_c = 0.2$ at maximum.

2.2. Ultrafast spectroscopy of chosen MIND structures.

Free-carrier dynamics is one of the most important parameter of a solar cell and it has a direct impact on the overall cell performance. One way to access that information is to study the changes in optical properties in a material after excitation by a fast perturbation like a pulsed electric field or an optical excitation. In that context, femtosecond laser spectroscopy is a powerful technique for investigating the fundamental mechanisms responsible for the

modification of the dielectric response function in silicon nanostructures. Here we present some of the results of a pump-probe experiment that summarize the data to be published in our article [4]. Femtosecond carrier dynamics in silicon have been investigated using pump-probe techniques over the past two decades [5,6]. Although several researchers have worked on bulk silicon, the continuous improvements in semiconductor nanotechnology have emphasized the importance of understanding the carrier dynamics on an increasingly shorter timescale and over a large spectral range in nanostructured and layered material.

In our case we have investigated two representative samples, N72B and N79. Time-resolved measurements of the carrier dynamics were carried out using a femtosecond pump-probe technique, in which a short pump pulse excites carriers and a time-delayed probe pulse measures the resulting change in reflectivity as a function of the pump-probe delay time. The optical pulses were generated using an amplified Titanium:Sapphire laser system operating at a repetition rate of 5 kHz. The pump beam, 150 fs in duration, has a central frequency doubled at 397 nm (about 3.12 eV) using a beta barium borate (BBO) nonlinear crystal. The probe pulses with broad band spectrum were produced by femtosecond white light continuum generation on a thin sapphire plate. The probe beam reflected from the sample, was dispersed by a grating in a monochromator and detected by a CCD camera. A band pass filter was placed in front of the detector in order to suppress all the side contributions from the pump and the fundamental beams. Because the supercontinuum pulse is chirped, the recorded reflectivity data have been time-corrected by performing a conformal mapping in the time frequency plane. To determine the chirp in the continuum pulse we performed two-photon absorption on ZnSe using the same pump and probe pulses. The optical pumping remained below the melting threshold. A precise control of the spot size of the pump beam (diameter 100 μm) on the sample during the measurements allowed for an accurate determination of the absorbed fluence. The maximum power of the beam was 2.2 mW

We recorded reflectivity spectra every picosecond up to $t = 20$ ps after the excitation, and for longer times for $t = 100$, 200 and 400 ps. As a quantity of analysis we determined the differential reflectivity defined by the following formula:

$$dR = \frac{R_{exc} - R_{base}}{R_{base}} \qquad \text{(IV.2.1)}$$

where R_{exc} denotes reflectivity of the sample at a given time after the excitation and R_{base} denotes the reflectivity in the static case and under weak illumination. N72B has a typical

response of bulk silicon under weak excitation, reflectivity first decreases slightly and recovers over time as the photogenerated population of carriers recombines [7].

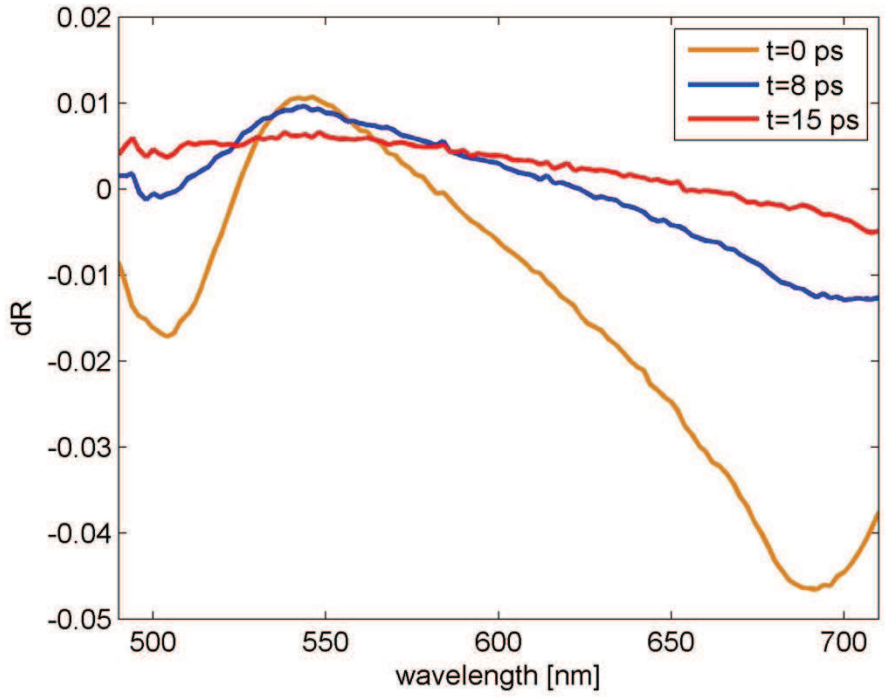

Figure IV.29. Experimental differential reflectivity of N79 for $t = 0$, 8 and 15 ps after excitation.

As can be seen in Figure IV.29, N79 exhibits interesting response where two minima and one maximum are visible, which decay over time for short times. After 15 ps the reflectivity reaches almost the value for static case. For long times we observe an inverse of this behavior, where the central peak at 550 nm becomes a minimum, neighbored by two maxima at 510 and 690 nm. The decay process is much slower in this case, and after 400 ps the change in *dR* is still quite strong, as can be seen in Figure IV.30.

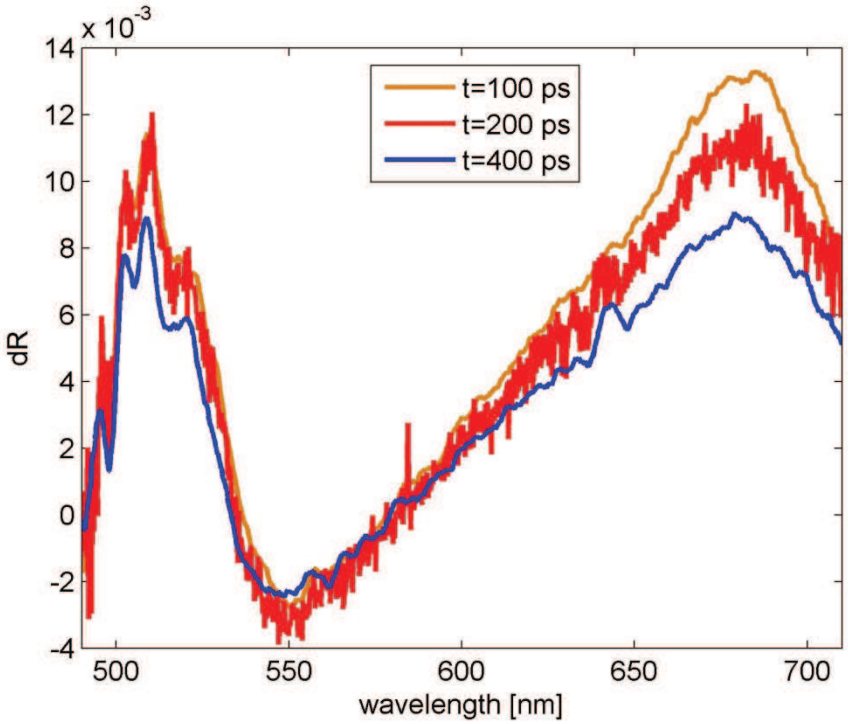

Figure IV.30. Experimental differential reflectivity of N79 for t = 100, 200 and 400 ps after excitation.

In bulk non-polar semiconducting materials, the dependence of reflectivity on carrier concentration is predicted quite accurately by the Drude's equation, introduced in chapter III:

$$\varepsilon(\omega, N_d) = \varepsilon_{HMO} - \frac{N_{e-h}e^2}{\varepsilon_0 m_{opt} m_e \omega^2} \frac{1}{1 + i\frac{1}{\tau_D \omega}} \tag{IV.2.2}$$

$$\varepsilon(\omega, N_d) = (n + ik)^2 \tag{IV.2.3}$$

$$R = \frac{(n-1)^2 + k^2}{(n+1)^2 + k^2} \tag{IV.2.4}$$

As can be seen from above equations, for low extrinsic carrier concentrations the reflectivity decreases in comparison to the unexcited material and for very dense e-h plasma, increases rapidly. The break point for this increase is commonly attributed to the plasma frequency, which is related to the density in the following way: $\omega_p = \sqrt{\frac{N_{e-h}e^2}{\varepsilon_0 m_{opt} m_e}}$. The change in absolute and differential reflectivity is shown in Figure IV.31.

a) b)

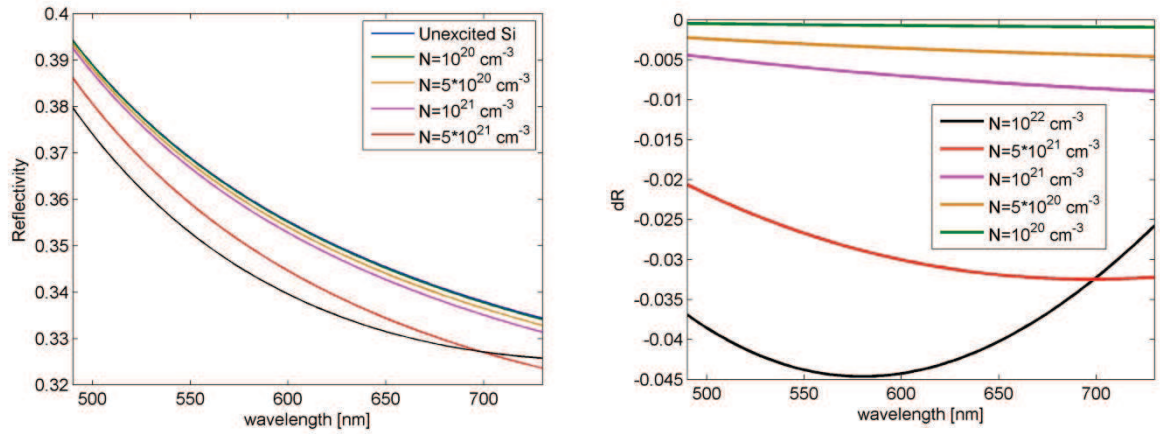

Figure IV.31. Simulated absolute (a) and differential (b) reflectivity for bulk Si under excitation for λ = 490 to 710 nm. For the highest free-carrier concentration the minimum in R corresponds to ω_p.

Unlike in bulk materials, we expect that the changes in *dR* in the N79 sample are due to two overlapping effects: nonlinear change in optical properties of the surface region of the structure and interferences caused by the buried aSi region.

To analyze the quality of changes introduced by the pump, we first estimated the initial photon distribution in the sample delivered by the pump beam, which is analogous to the |*S*| for 397 nm. We assume that for times comparable with the pulse duration after excitation (t > 150 fs), the carrier distribution follows the exact shape of photon distribution, because diffusion processes have not yet started. As can be seen in Figure IV.32, more than 90% of the initial photons are absorbed in the first Si layer. Estimating that the total number of photons in a single exciting pump beam was $N \sim 10^{20}$ cm^{-3}, we performed simulations of the N79 sample, based on the model established in previous paragraph, where carrier distribution follows the exact shape of |*S*|. Simulation reproduces correctly the general behavior of the differential reflectivity, predicting right changes in the maxima and minima attributed to interferences visible in the stationary case. However, the concave shape of *dR* predicted by the simulation for λ = 510-670 nm is not observed in the experiment. This might be explained either by the laser chirp or insufficient correction of the optical path for the probe beam for longer wavelengths in the experiment, or by some additional effects not taken into account in the simulation, such as carrier diffusion.

a) b)

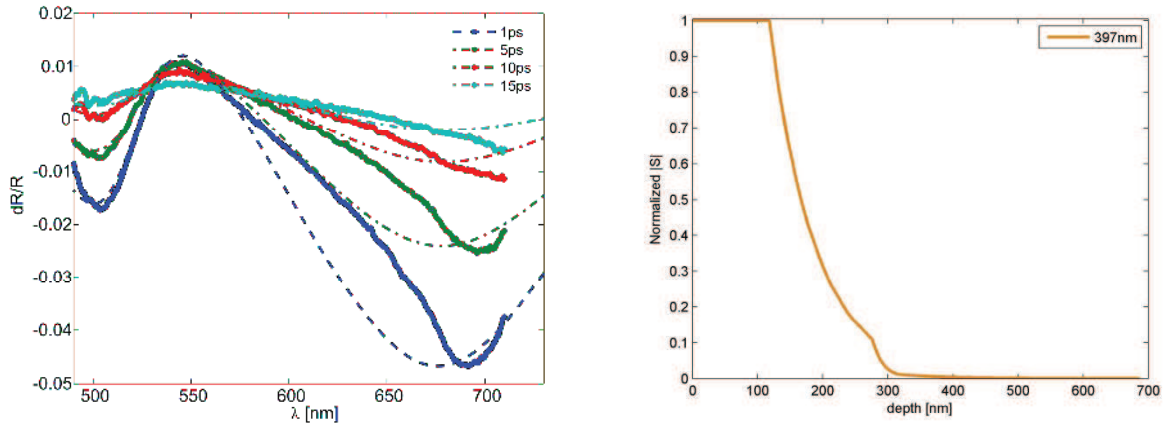

Figure IV.32. Simulated (dashed line) and experimental (points) changes in reflectivity for short times in N79 (a) and estimated $|S|$ for the pump beam in the sample (b).

a) b)

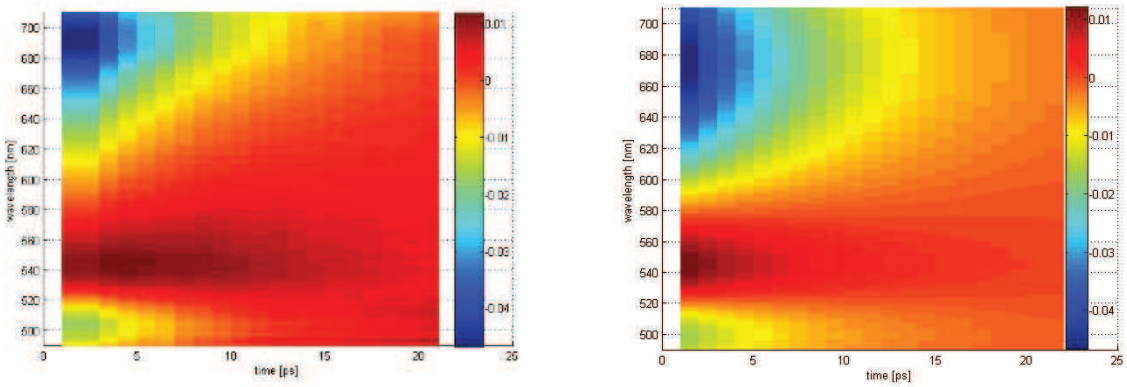

Figure IV.33. Simulated (a) and experimental (b) changes in reflectivity for short times in N79 for t = 1 to 21 ps.

For longer times i.e. $t > 15$ ps, diffusion effects are no longer negligible and significantly alter the experimental response in comparison to the simulated dR. In spite of this fact, we were able to estimate the lifetimes of excited carriers by reproducing dR for times up to 15 ps and extrapolating the exponential decay, which resulted in lifetime $\tau = 130$ fs (see figure IV.34). This lifetime is comparative but smaller than the usual value obtained in bulk Si, which may be attributed to the amount of defects and the quality of the materials [7].

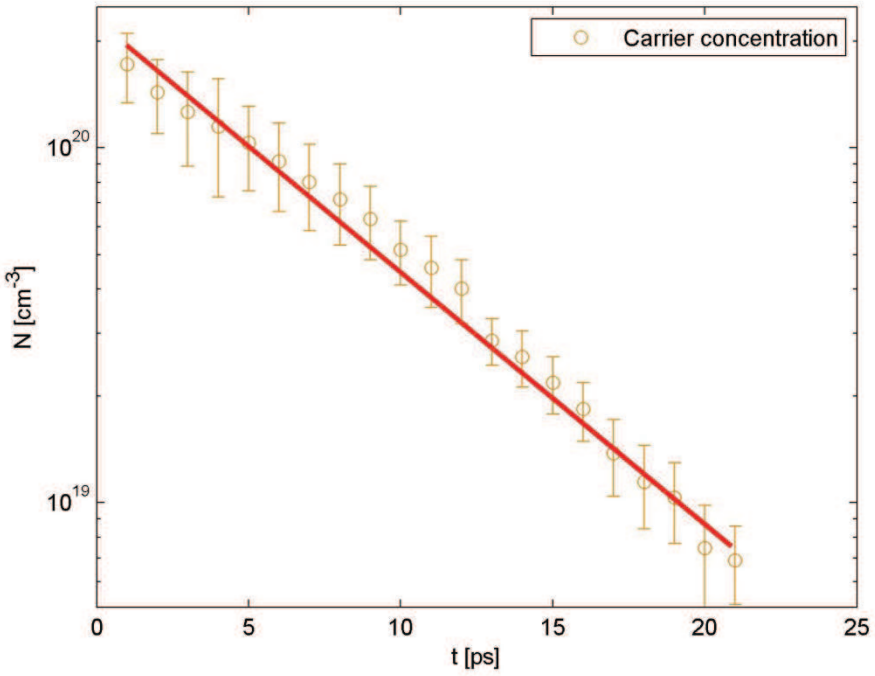

Figure IV.34. Carrier concentration in the N79 sample after excitation by the pump beam for short times. An exponential decay can be clearly seen, with lifetime $\tau = 130$ fs.

The carrier dynamics in N79 for short times produce an interesting response, which in combination with buried nanostructure produce changes in *dR* not observed in the bulk materials. Those changes however, when the phase response of the material is taken into account, are nevertheless quantitatively similar to those obtained by other authors [6]. Changes observed for longer times ($t > 100$ ps) are not so easily explained (Figure IV.30). In bulk material, we would expect that all the electrons have already thermalized and the sample has reverted to its original state, therefore *dR* should remain at 0. However, since the pump beam carries a lot of energy, we might also consider that the sample heats up locally, therefore changing its properties. This process is much slower than the carrier dynamics and could be potentially responsible for the inverse behavior of *dR* in the N79 sample. The absolute upper limit for the increased temperature has been estimated to be T = 300 K. [4] The real temperature increase is probably much smaller, because we do not take into account electron diffusion and electron-electron scattering, however this assumption allows us to estimate the level and type of changes induced by the temperature increase. Changes in the dielectric response of Si were analyzed experimentally by other authors [8] and for a temperature range applicable in our case are known to be centered on critical points (see Figure IV.35a).

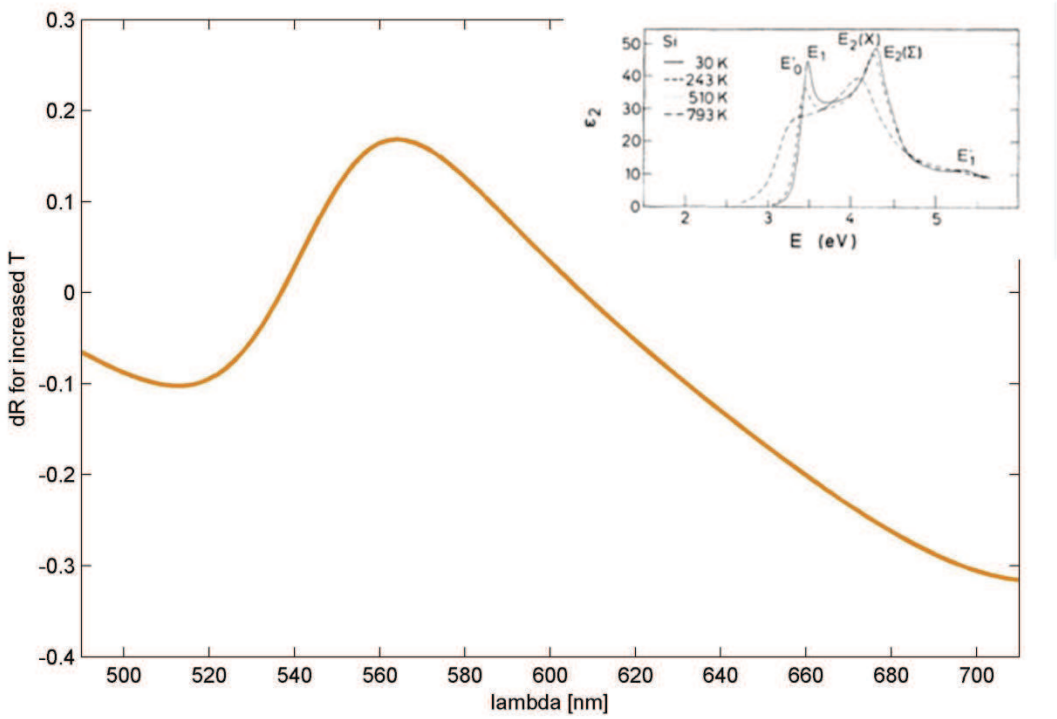

Figure IV.35. Simulated response of the N79 sample with T increased to 510 K in the first layer. Inset shows changes in Im (ε) for different temperatures. After [8].

The simulation of the optical properties of N79 for increased temperature have yielded an effect exactly opposite to the one observed in our experiment. This can be explained, on one hand, by the fact that the changes in ε were reported for good quality monocrystalline Si, which is not our case. On the other hand, the obvious shape of the Im(ε) for increased temperatures indicate that the majority of the changes come from the band structure renormalization due to an increased perturbation of the periodicity of the crystal, caused by increased vibrations of the ions in the lattice. The effect is mainly visible for the critical points, and negligible for longer wavelengths ($\lambda > 620$ nm), since the free-carrier population increase for T = 510 K is still small (see chapter I) and has no effect on optical properties. However, qualitative the same effect is observed for highly doped Si, as it is in our case (see chapter III). One can therefore make the two following assumptions:

- temperature-related changes in critical point are negligible for heavily doped/defected Si, since the perturbation of the periodic potential induced by temperature is smaller than the one induced by doping.
- scattering cross-section for the ions will be increased due to vibrations and might affect high intrinsic free-carrier population resulting from the doping.

In the case of the N79 sample, the intrinsic carrier population in the emitter is close to $N = 10^{20}$ cm^{-3}, which already has an impact on the optical properties of the structure. With increased T, one can expect changes in optical mass m_{opt}, which in this case might be regarded as the parameter describing the effective ease at which carriers are allowed to propagate in the material. Increase in T will result in higher scattering, effectively increasing m_{opt}.

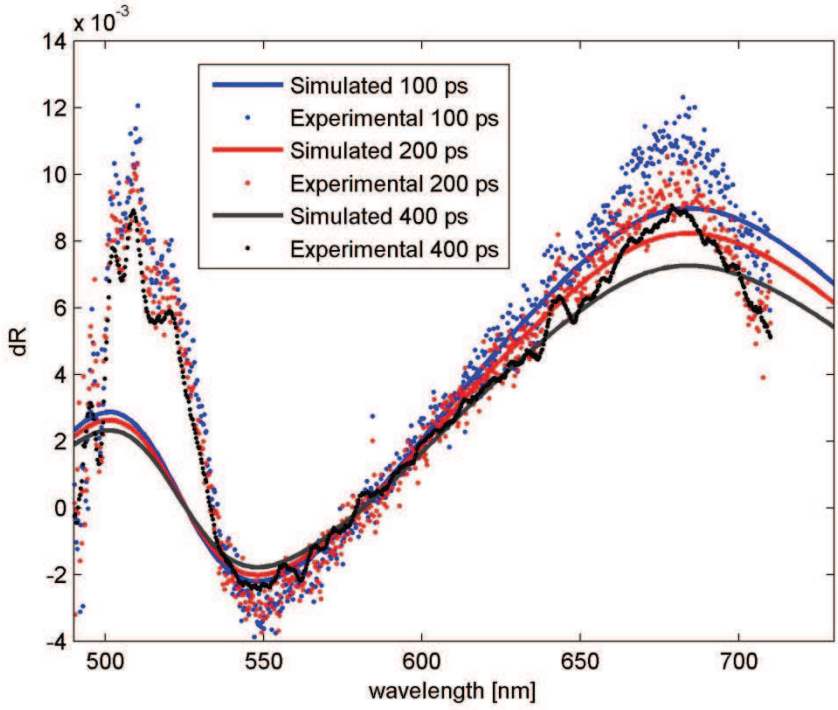

Figure IV.36. Simulated (line) and experimental (points) changes in reflectivity for long times in N79. The estimated evolution of the optical mass m_{opt} with time was quasi-linear in the studied time domain and varied between $m_{opt} = 0.9$ for $t = 100$ ps to $m_{opt} = 0.65$ for $t = 400$ ps.

We have performed simulations in which we allowed m_{opt} to change in a monotonic way with time for $100 < t < 400$ ps (Figure IV.36). As can be seen, the changes in m_{opt} can provide quantitative and qualitative changes in dR as observed in experiment, and can be linked to physical processes that might be taking place in the device after excitation.

3. Quantum efficiency measurements.

One of the parameters that characterize any solar cell and describe its capability to effectively convert light into electricity is Quantum Efficiency (QE). It connects the amount of photons that are striking the surface of the converter with the amount of electrons collected in an external circuit. If both numbers of particles are equal, then the QE is unity. One can distinguish two types of quantum efficiencies, i.e. an External Quantum Efficiency (EQE) is described when all of the incident light particles are taken into account and an Internal Quantum Efficiency (IQE) when only the photons that were absorbed inside the cell are taken into account. Both types of QE describe slightly different thing i.e. EQE provides information about how efficient a converter is in converting incident photons to electrons, while the IQE focuses more on the transport properties of the converter.

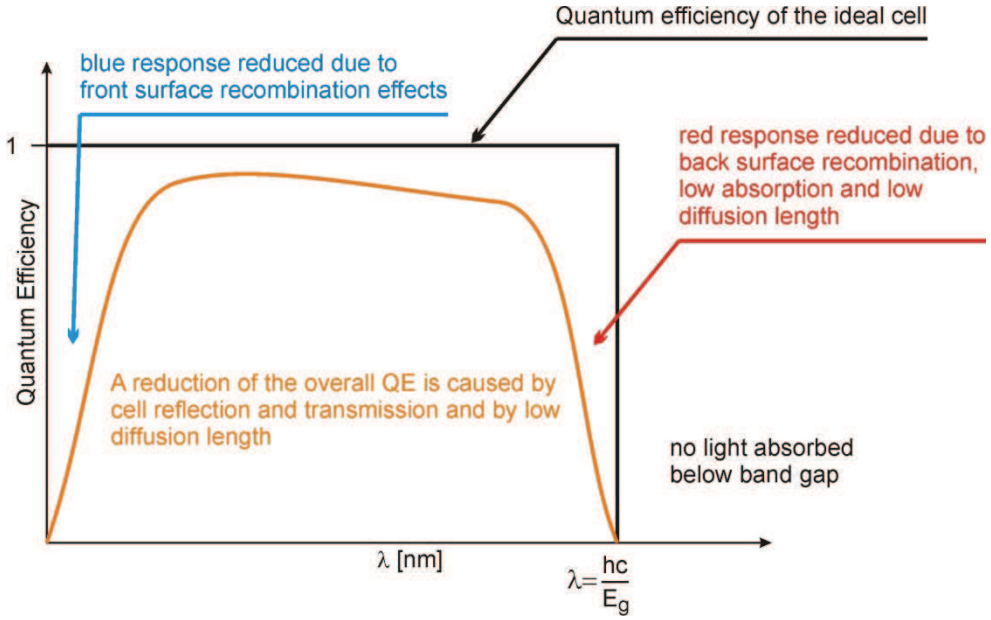

Figure IV.37. Quantum Efficiency of an ideal cell and the basic mechanisms responsible for reduction in real devices. Note that QE > 0 only for $E > E_g$, which does not necessarily correspond to zero absorption.

While the QE ideally has the square shape (see Figure IV.37), the quantum efficiency for most solar cells is reduced due to the recombination effects. The same mechanisms which affect the collection probability also affect the quantum efficiency. For example, front surface passivation affects carriers generated near the surface, and since blue light is absorbed very close to the surface, high front surface recombination will affect the "blue" portion of the quantum efficiency. Similarly, green light is absorbed in the bulk of a solar cell and a low

diffusion length will affect the collection probability from the solar cell bulk and reduce the quantum efficiency in the green portion of the spectrum. The quantum efficiency can be viewed as the collection probability due to the generation profile for a single wavelength, integrated over the device thickness and normalized to the number of incident photons.

The EQE of a silicon solar cell includes the effect of optical losses such as transmission and reflection. However, it is often useful to look at the quantum efficiency of the light left after the reflected and transmitted light has been lost. The IQE refers to the efficiency with which photons that are not reflected or transmitted out of the cell can generate collectable carriers. By measuring the reflection and transmission of a device, the external quantum efficiency curve can be corrected to obtain the internal quantum efficiency curve.

The Collection Efficiency (CE) describes the probability that a light-generated carrier in a certain region of the device will be collected by the *p-n* junction and therefore contributes to the light-generated current. CE depends on the distance that a light-generated carrier must travel compared to the diffusion length. Collection efficiency also depends on the surface properties of the device. The collection efficiency of carriers generated in the depletion region is unity as the electron-hole pairs are quickly swept apart by the electric field and are collected. Away from the junction, CE drops and if the carrier is generated more than a diffusion length away from the junction, then the collection efficiency of this carrier is quite low. Similarly, if the carrier is generated closer to a region such as a surface with higher recombination than the junction, then the carrier will recombine. The impact of surface passivation and diffusion length on collection efficiency in a single junction cell can be approximated by the following equation:

$$CE(x) = \begin{cases} \dfrac{1 + V_{FR} \cdot x}{1 + V_{FR} \cdot b} \exp\left(\dfrac{x - b}{L_e}\right), & \text{for } x < b \\ 1, & \text{for } b \le x \le b + W \\ \dfrac{1 - V_{BR} \cdot x}{1 - V_{BR} \cdot (b + W)} \exp\left(\dfrac{-x - (b + W)}{L_b}\right), & \text{for } x > b + W \end{cases} \quad \text{(IV.3.1)}$$

where V_{FR} and V_{BR} are recombination velocities of front and back surface respectively, b is the emitter thickness, W is the depletion zone length, L_e and L_b are diffusion lengths of carriers in emitter and base.

At this point we will analyze two representative MIND structures, N79 and N72B. They represent two parts of the same wafer, and differ only by the state of the surface. N79 is covered with 117 nm of LPCVD deposited SiO_2, while in N72B the passivation layer was

etched and the surface was damaged by the process, as shown in the previous paragraphs. We therefore expect from the classical point of view, that N72B should have its QE in the blue region strongly reduced by the state of the surface, resulted in an increased recombination velocity V_{FR}. On the other hand, we have shown before that the existence of the amorphized region creates a barrier for holes, which will also cause CE in the emitter area to decrease, leading to decrease in QE for the blue region. Experimental measurements of both IQE and EQE for N79 and N72B are presented in Figure IV.38.

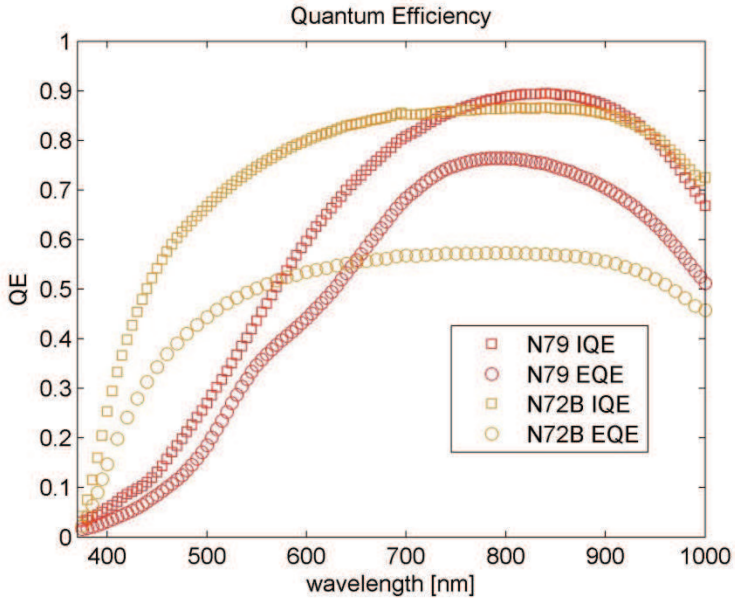

Figure IV.38. Measured Quantum Efficiencies for N7 samples. N79 (red) shows a strong decrease in the blue region due to surface effects/potential barrier at the cSi/aSi interface. N72B (orange) shows overall increase in both EQE and IQE for blue region in comparison to N79, however its EQE does not exceed 55% due to high reflectivity.

In a classical approach, we would expect both samples to have a similar collection efficiency in the base area, while in the emitter area N72B should have CE reduced due to a higher recombination velocity. The Quantum Efficiency of the N79 passivated sample fits well to the prediction based on the aSi/cSi barrier hypothesis, however N72B features an increase in both external and internal quantum efficiency in the blue region. This effect is exactly the opposite to the expected influence of removing passivation [9]. In the red region, EQE is decreased due to increased reflectivity of the sample, which is expected. Before we try to analyze the origin of this unexpected increase in EQE for short wavelengths, we will estimate the CE for N79 sample, assuming that it features only classical effects, includes potential barrier for holes at the cSi/aSi interface and has good surface passivation, resulting in a low recombination

velocity. The emitter was also divided into three different mobility regions, analogous to the areas specified in the optical simulation. These assumptions allowed for correct prediction of the CE and QE curves for N79 (Figure IV.39). Reconstructed collection efficiency features rather low mobility in the whole emitter area: specifically in the first layer $L_e = 1.8 \cdot 10^{-1}$ [µm], the amorphized zone $L_{amo} = 2.5 \cdot 10^{-1}$ [µm] and the second crystalline region $L_e = 3.7 \cdot 10^{-1}$ [µm], while the surface recombination velocity $V_{FR} = 10^{-2}$ [cm/s] was kept low to reproduce good quality of passivation. Any significant decrease in CE caused by the potential barrier at the aSi/cSi interface is invisible due to the already low collection efficiency in the neighbouring area.

a) b)

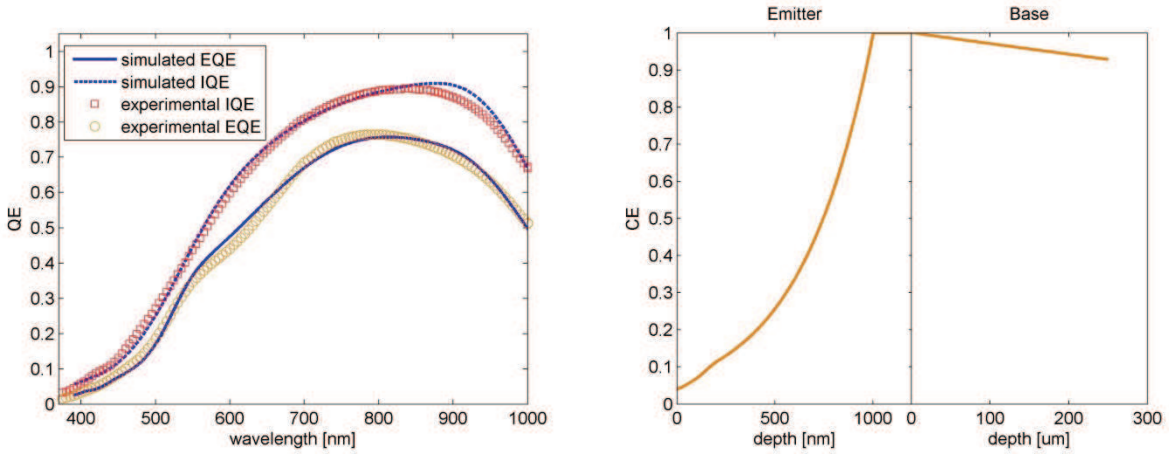

Figure IV.39. Simulated quantum efficiencies for the N79 sample (a) and reconstructed collection efficiency (b).

The base of the cell shows a high diffusion length, i.e. $L_b = 5 \cdot 10^{3}$ [µm], which is expected from a high quality substrate. The back surface recombination velocity was estimated to be $V_{BR} = 2.8 \cdot 10^{-2}$ [cm/s]. The simulated QE for N79 reproduces rather accurately the general shape and values of the experimental data; however differences at 480 and 600 nm indicate that either collection probability results from more complex transport properties, different physical effects take place or can be attributed to the systematic incertitude of the measurement. Slight overshoot of IQE at 900 nm is probably due to the mismatch of the absorption coefficient in the base.

The interesting increase in blue region for N72B for both EQE and IQE, shown in Figure IV.38 poses a complex problem that so far has no straightforward answer. From the completely classical point of view, assuming that the etching has not damaged the active area of the cell, one should see almost no change in IQE in comparison to N79, which already has a small CE in the front surface region. However, if we assume that the passivation layer was

non-absorptive and the active area remains the same, an increase in IQE or EQE in any area is unlikely. An analysis of the collection efficiency needed to reproduce the experimental QE of N72B, while keeping all the structural parameters the same as they were estimated before etching is shown in Figure IV.40. Thus, to explain the increase in IQE and EQE for the blue region classically, the diffusion length in the whole emitter has to be increased; moreover the front surface recombination velocity could be decreased only slightly, down to the value $V_{FR} = 10^{-1}$ [cm/s].

a) b)

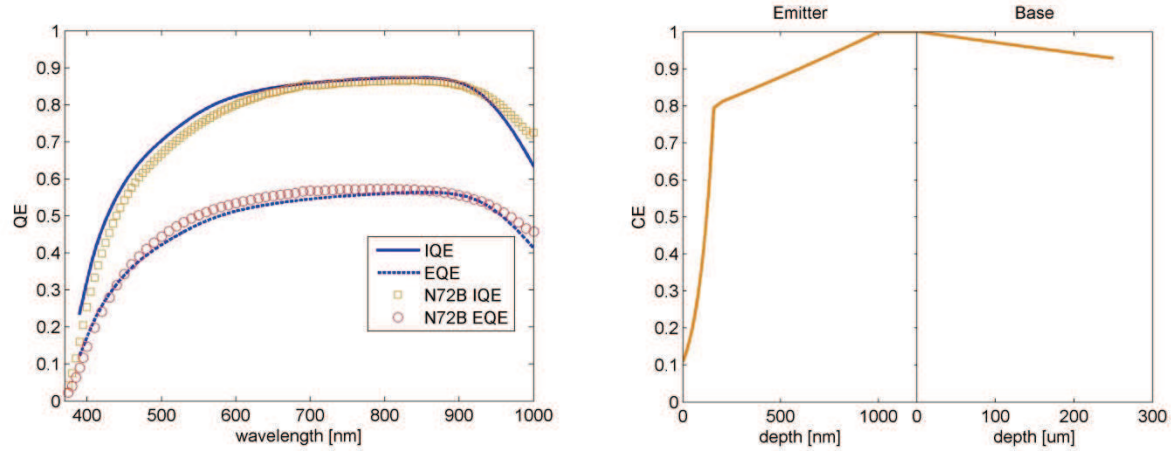

Figure IV.40. Simulated quantum efficiencies for N72B sample (a) and reconstructed collection efficiency (b).

It might be argued that the potential barrier for holes, which impact on collection efficiency is clearly visible in the case of N72B, can act as a protective barrier from the surface effects on the deeper laying regions of the sample. This would explain the high value of CE in the second crystalline zone of the structure, lying below amorphous layer at 200 nm and below. However the necessary increase in the mobility in the emitter area up to the value $L_e = 6$ [µm] is difficult to explain. Another interesting result is that the effective CE at the surface is higher than the one for N79, which also works against the effect of removing the passivation. The state of the surfaces of N72B and N79 samples was shown in figures 1.12-1.15 of this chapter, and the effect that would explain an increase in both CE and QE has not yet been observed for solar cells [10]. It is also important to stress that the increase in EQE after removal of passivation layer could be explained by the means of classical collection efficiency. It would be even more unexpected and uncommon observation than electron multiplication.

One of the possible classical explanations behind the increase in IQE for the N72B sample after removal of the SiO_2 passivation layer is that the deposited amorphous silicon dioxide

possessed mild absorptive properties that were accidently tuned just to cut off the blue part of the incident flux. In this scenario, the collection efficiency of N79 would remain either the same or better than the N72B, and the resulting difference in QE would have to be attributed to parasitic absorption in the first, inactive layer. By analyzing the differences between the experimental IQE for the blue region, shown in Figure IV.41, one can try to estimate the fraction of the flux that would have to be absorbed in the passivation layer.

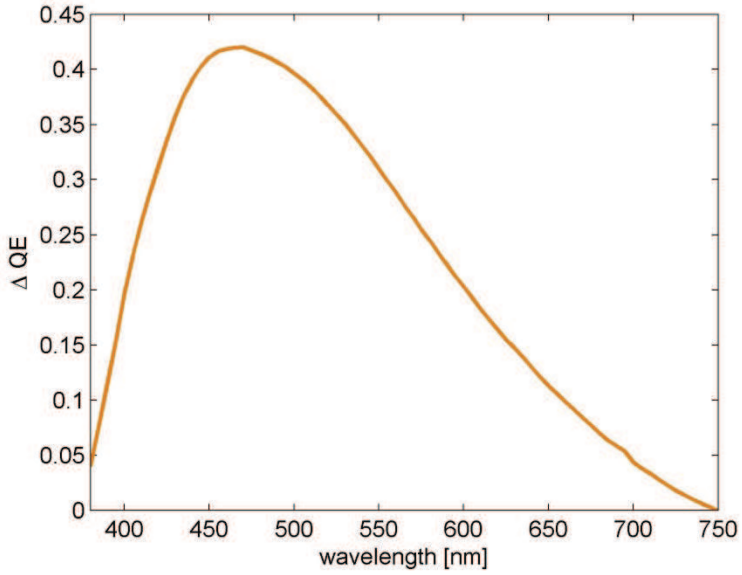

Figure IV.41. Difference in experimental IQE between N72b and N79 samples. The strongest increase of about 43% is located at 480 nm.

The slope between 500 and 700 nm gives good indication of the potential shape of the necessary absorption coefficient of the SiO_2 passivation layer, essential to reduce the flux penetrating into the cell sufficiently to achieve changes in QE observed in the experiment. For a moment we neglect the impact the extinction coefficient would have on the reflectivity of the structure and take into consideration only changes in the energy distribution and the resulting changes in the generation function *G*. We retain the same structure and distribution of the layers as was estimated by both SEM measurements and optical analysis in paragraphs 1 and 2 of this chapter. For the purpose of this estimation, we assume that the real part of the refraction index does not change significantly, and we only add extinction coefficient high enough to precisely cut off the amount of the flux responsible of the increase in the IQE for N72B. The resulting dielectric function does not fulfill Kramers-Kronig relations, but in the first attempt we will neglect that also. The collection efficiency was also kept exactly the same as was shown in Figure IV.40b. The results of this simulation are shown in Figure

IV.42. An introduction of rather high extinction coefficient can cause a decrease in EQE which fits well the experimental data (Figure IV.42a); however it is impossible to reproduce both EQE and IQE due to differences in reflectivity of the sample (Figure IV.43b).

a) b)

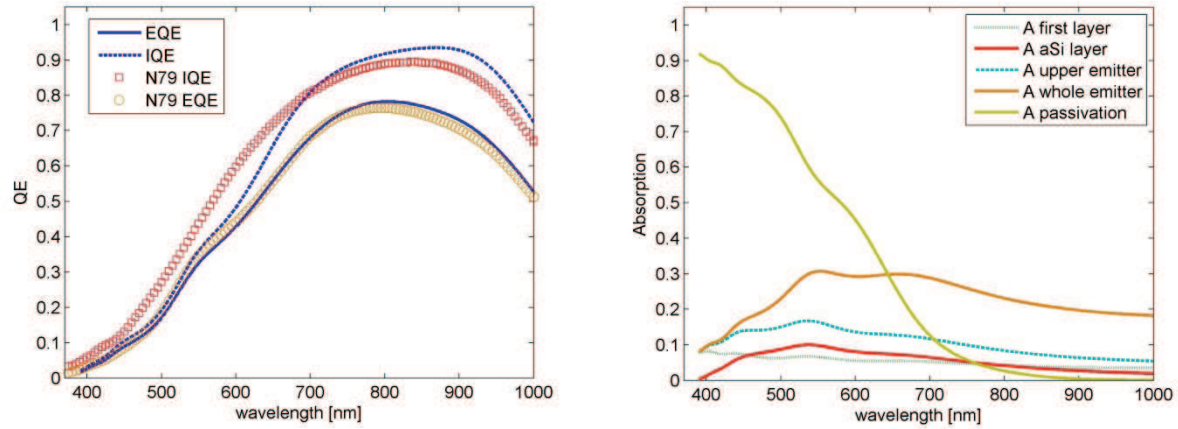

Figure IV.42. Simulated quantum efficiencies for N79 sample passivated with an absorbing SiO_2 layer (a) and normalized absorption in each area of the emitter (b).

a) b)

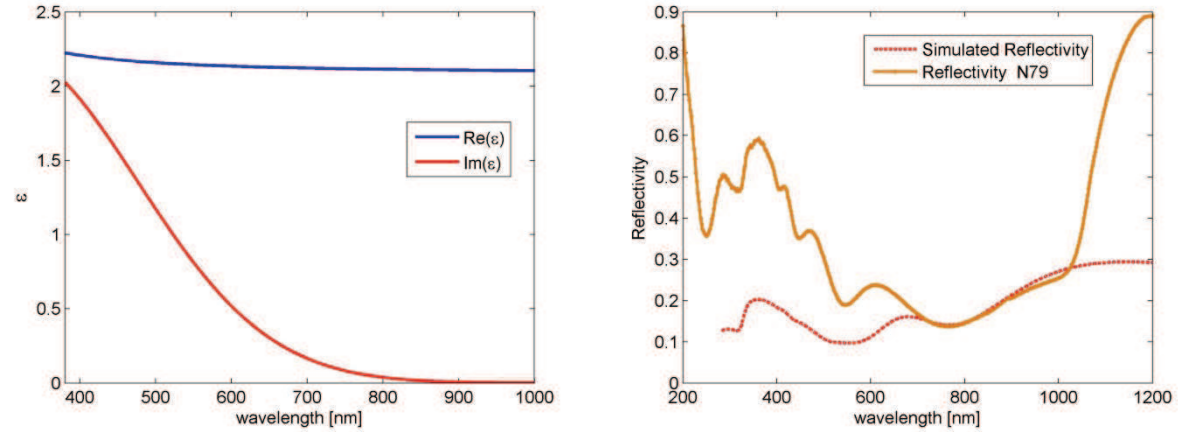

Figure IV.43. Dielectric function of the hypothetical absorbing SiO_2 layer deposited on the N7 samples (a) and reflectivity of the whole structure covered with 117 nm of such material, compared with the experimental result (b).

Such a highly absorptive passivation layer also completely reorganizes the power distribution in the emitter, allowing only small amount of the incident flux to penetrate into the active layer, (Figure IV.42b). The dielectric function of the passivation layer is shown in Figure IV.43a together with a comparison of the resulting reflectivity in the broad spectral region with the experimental data (Figure IV.43b). There is absolutely no coherence between the experimental reflectivity of N79 and the simulated R with the absorbing passivation layer, which is caused mainly by the changes of refraction index and resulting optical impedance.

The overall value of R for wavelength up to 700 nm is far below the experimental data and none of interferences are visible. In fact, the appearance of the interferences for the wavelengths just below the first critical energy is a good indication that the passivation layer (which was confirmed to be about 110 nm thick by SEM measurements) is non-absorptive, because in the opposite scenario the incident flux would be completely absorbed in the passivation layer, and would not penetrate deeper into the structure and produce the interferences. This effect is confirmed by the simulations presented in figures 2.4a and 3.7b. The resulting conclusion is that even if the shape of the EQE curve could be theoretically explained by the absorption in the passivation layer, none of the remaining optical properties of the structure support this theory.

Being unable to explain the sudden increase in both EQE and IQE for N7 samples not covered with the passivation layer, in spite of the inherent increase in the surface recombination velocity and no particular reason that would explain necessary increase in the diffusion length, as was needed in the classical approach (figures 3.3b and 3.4b), we will now try to implement the effect of electron multiplication in the structure.

As was indicated earlier, the existence of suspended nano- and microcrystallites in the amorphous matrix may produce an effect similar to the already observed Multiple Exciton Generation (MEG) or electron multiplication [11,12]. Before we try to validate this theory quantitatively, for this hypothesis to be correct we would have to explain why the hypothetical multiplication effect is only observed or is significantly stronger in samples with removed passivation. We will take into consideration two multiplication mechanisms: MEG and Low Energy Electron Multiplication (LEEM) as proposed by Kuznicki et al. [13]. In the MEG case, one of the possible scenarios is that the initial multiplication process is equally efficient in both structures, since it depends only on the properties of the amorphized region, which is the same in both samples, even if the relative collection efficiency for secondary generation carriers is not the same. A multiplication could be attributed to the reduced density of free-electrons in the etched sample, which in conjunction with the potential barrier introduced by cSi/aSi/cSi interfaces could help the MEG generated e-h pairs to dissociate. In the opposite case, passivated samples have reduced density of surface states that must significantly increase the lifetime of the light-generated e-h pairs. Holes generated in the first cSi region would accumulate at the barrier and induce changes in the potential, reducing the dissociation rate and collection probability of the extra e-h pairs generated in the active sub-

structure. This effect would lead to overall decrease in the CE for second generation carriers in passivated samples.

In the case of LEEM, the energy conservation principle would require the generation states to be constantly recharged by the electrons coming from any source but the light generation for the process to be efficient, and to generate also an extra hole in the valence band somewhere. In the first moments after the sample is exposed to the external flux of photons, at room temperature all the second generation centers are charged (located 0.274 eV below the CB), but once the extra electrons are created the positively charged states are left. If these are not recharged rapidly with a thermal excitation of an electron from the valence band, the secondary charge will eventually recombine and occupy its origin state, producing no increase in short-circuit current. Passivated samples have much lower recombination rate which results in slower dynamics of the thermal generation/recombination processes. This might cause the secondary generation centers to regenerate at a much slower rate than it would happen in a sample with an increased density of surface recombination states, as in the case of etched structures.

We tried to validate both theories by performing a simulation of the quantum efficiency in the assumption that the first generation collection efficiency is exactly the same as estimated for the N79 sample, in which the secondary generation effect is either non-existent or has no significant impact on the experimental value of QE curves. Collection Efficiency for secondary (and higher tiers) carriers is then localized only in the proximity of the active sub-structure and is energy dependent, as was introduced in the chapter II of this work.

There are many challenges behind an approach to validate the existence and strength of a multiplication process. If in the present experiment, neither EQE nor IQE overshot 100% efficiency, there always some sort of classical explanation to be found. On the other hand, the step-like increase predicted by the general multiplication theory has not yet been observed in the experiment, even if the existence of extra exciton or even free electrons was confirmed experimentally [11,14], as can be seen in Figure IV.44.

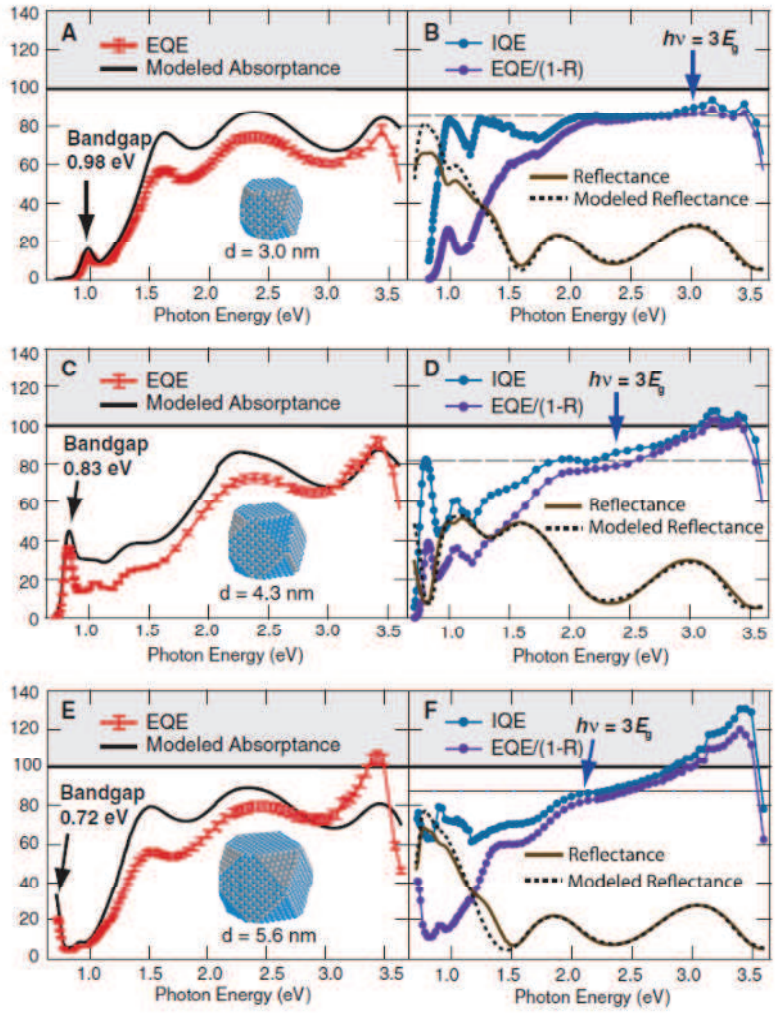

Figure IV.44. Multiplication in quantum dots from reference [11]. This work is one of the first in which the existence of extra e-h pairs was measures in the external circuit; nevertheless the step-like shape of EQE is not visible.

Those two facts make the task of detecting an electron multiplication significantly harder, and as such it can only be addressed by a very rigorous comparative analysis. We have experimentally observed an increase in EQE, which equals an increase in total, unmodified number of carriers generated by the same spectrum, despite an increase in the reflectivity. Having run out of classical explanations, which based either on the improvement of Collection Efficiency or the absorbance in the passivation layer, we turn our attention to the multiplication process. We are aware that simple implementation of multiplication mechanisms in our analysis will neglect any effects related to energy smearing, shifting of the energy states where multiplication occurs and fraction of active multiplication centers, which have an important effect on the macroscopic result, as can be seen in ref [11].

a) b)

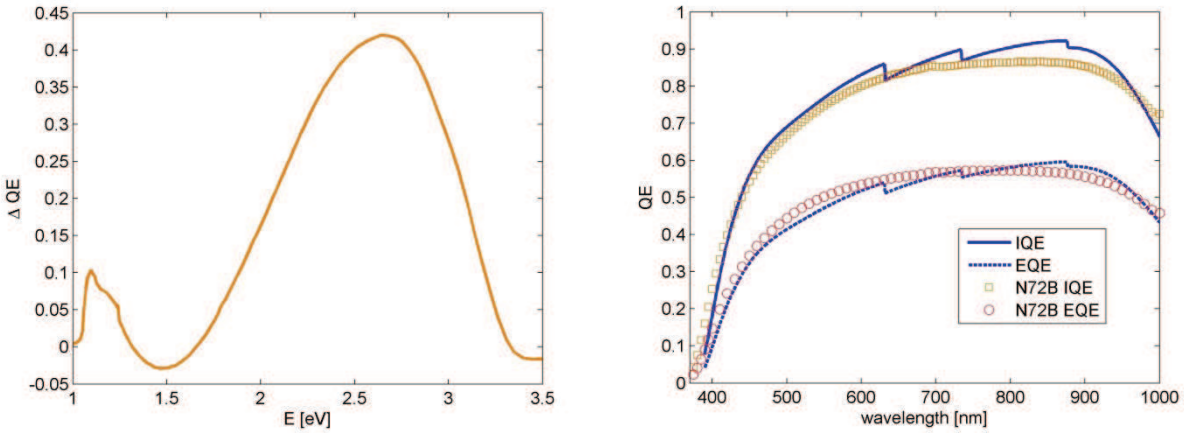

Figure IV.45. Differences in experimental IQE for N72B and N79 samples (a) and simulation of both IQE and EQE for the structure where multiplication is active (b).

As can be seen in Figure IV.45, a simple simulation in which low-energy carrier multiplication is allowed can reproduce the experimental value of IQE quite accurately. In this particular case, the fit parameters i.e. multiplication probability $p = 0.8$, and the active area where multiplication could occur was assumed to be only the interface between the amorphized and crystalline layers, lying close to the PN junction. However, we also allow some of the hot carriers to move in the emitter before their energy is homogenized with the electron cloud and assumed that they would follow a similar mechanism as in the case of e-h pairs, that is an exponential decay in probability with a specific diffusion length, $L_m = 15$ nm. It was also assumed that multiplication can generate no more than three extra carriers due to the physical limiting factors, such as energy conservation principle and state filling. The simulation reproduced well the general shape and the tendency of the IQE increase; however as mentioned before, we do not observe the step-like shape in the experiment. This might be the caused by the energy smearing, surface scattering or other effects. We have tried to implement an approximation of this effect in the simulation by introducing Gaussian smearing of the energy states responsible for multiplication. This resulted in much smoother shape of the IQE curve, that resembles the experimental result. For the case in which energy smearing is allowed the Quantum Efficiency assumes a much smoother shape and the simulation approaches the experimental result. For the low-energy multiplication case, we assumed that the multiplication energy is $E_m = 0.274$ eV and the probability was $p = 0.56$, which seems reasonable.

a) b)

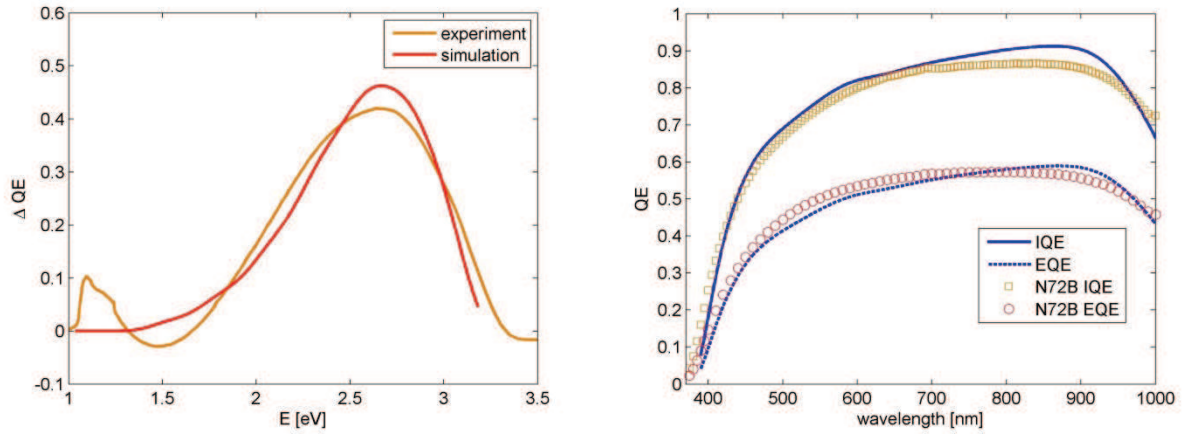

Figure IV.46. Comparison between experimental (orange) and simulated (red) increase in IQE for N7 samples (a). Simulation of both IQE and EQE for the structure where multiplication is active (b) and energy smearing is allowed.

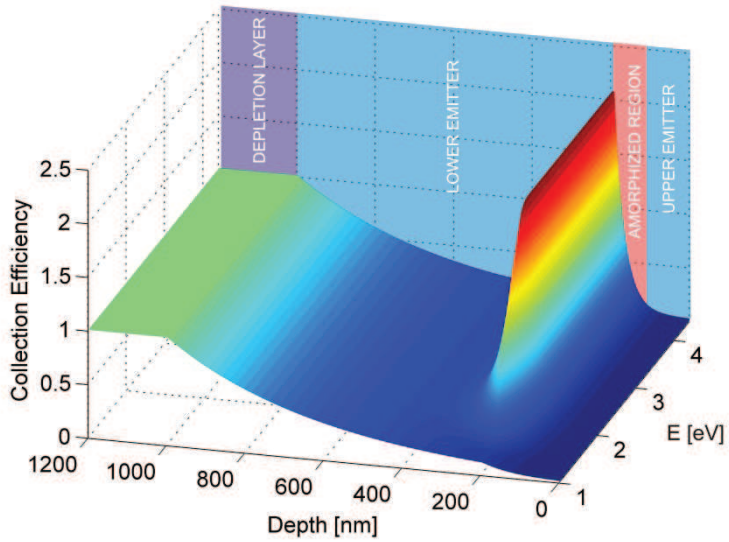

Figure IV.47. Collection Efficiency of the structure where low-energy multiplication is allowed and energy smearing of $E_s = 0.08$ eV was assumed. Both IQE and EQE for this structure are shown in Figure IV.46 (b).

In the case of MEG, we assumed that the multiplication is localized in the amorphized region and can perhaps extend a little bit into the crystalline region. The maximum increase in the experimental ΔIQE is localized around 2.5 eV, as can be seen in Figure IV.45. This fact fits well into the hypothesis that the multiplication might occur in cSi nanocrystals embedded in the amorphized matrix, since the expected multiplication energy in such case would be close to $E_m = 1.2$ eV above the band gap, which would yield the energy $E > 2.3$ eV. This predicts almost precisely the maximum increase in IQE, however, as in the case of other works, the

step-like shape of the IQE curve, predicted by theory, is not observed in the experiment. Our simulation is not able to reproduce such a linear increase, even with the assumption that the multiplication states are not very well defined in the band structure.

a) b)

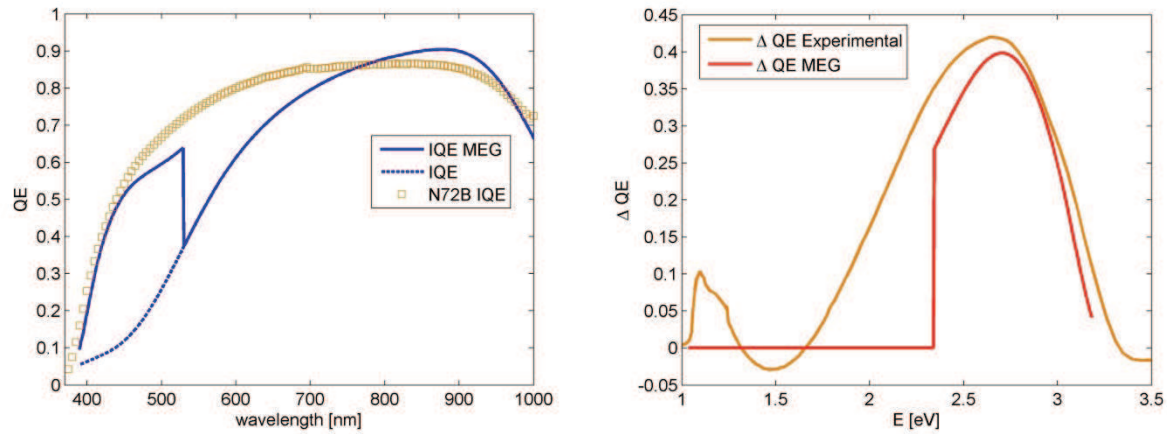

Figure IV.48. Simulated IQE for N72B sample with MEG enabled (a) and comparison of the experimental (orange) and simulated (red) increase in IQE for MEG case (b).

As can be seen in Figure IV.48, the MEG implementation in our simulation cannot well reproduce experimental QE results. An increase for short wavelengths, up to 550 nm is predicted by the simulation, but the region between 550 and 700 nm is not well reproduced. However the comparison of the difference in the IQE of both N79 and N72B as measured and predicted by the simulation shows good agreement for high energies, notably after the first multiplication step. This effect, while not completely ruling of the MEG hypothesis, shows clearly that our model cannot grasp all the physical phenomena behind this process.

4. Electrical measurements.

A current–voltage characteristic or I–V curve is a relationship, typically represented as a chart or graph, between the electric current through a device or material and the corresponding voltage across it. Solar cells and solar converters are electronic devices that use P-N junctions to directly convert sunlight into electrical power. As was shown in Chapter I, the P-N junction has a complex relationship between voltage and current. As both voltage and current are functions of the light falling on the cell, the relationship between insolation (sunlight) and output power is complex. The current-voltage relation of the ideal quality junction is given by the equation I.4.28 of Chapter I, while the current-voltage characteristic of a real solar converter based on a single junction is usually well described by the Shockley equation,

introduced in Chapter I, equation I.4.47 (shown below). Some parameters such as the fill factor η_{FF}, series and shunt resistance R_s and R_{sh}, respectively, and ideality factor n, that describe the solar converter were introduced in chapter I. An additional parameter that is used to describe the quality of the device are characteristic resistance $R_{ch} = V_{max}/I_{max}$, which is the output resistance of the solar cell at its maximum power point. If the resistance of the load is equal to the characteristic resistance of the solar cell, then the maximum power is transferred to the load and the solar cell operates at its maximum power point.

4.1. Analysis of the existing structures.

We have performed several measurements of I–V characteristics of N7 samples and estimated all the parameters in the Shockley equation:

$$\ln\left(\frac{I+I_L}{I_0}-\frac{V-IR_s}{I_0R_{sh}}+1\right)=\frac{q}{nk_BT}(V-IR_s) \qquad \text{(IV.4.1)}$$

In all our fitting we used a single diode model. Estimated resistances R_s and R_{sh} were then used to calculate the efficiency of the cells under an AM1.5G spectrum. Results of the measurements performed under AAA class solar simulator are shown in the Table 1 and in the Figure IV.49. The intensity of the radiation was not always equal to that of the AM1.5G spectrum during the measurement; therefore we applied a correction coefficient C_{corr} to properly estimate the parameters of the cells. We have also performed dark measurements to estimate the resistances and the dark saturation current I_0 for every sample. It is worth noting that the theoretical light current I_L calculated using the AM1.5G spectrum and simulated EQE was always equal to the measured I_{sc}. This implies that our solar simulator was indeed a very good class and that our simulation can accurately reproduce the experimental results.

	η %	V_{oc} [V]	I_{sc} [mA]	I_0 [A]	n	η_{FF}	R_s [Ω]	R_{sh} [Ω]	R_{ch} [Ω]	C_{corr}
N72B	5.6508	0.4699	75.2	$4\cdot10^{-7}$	1.5	0.5841	1.08	210	5.0252	0.91
N79	6.5690	0.4494	74.4	$2.37\cdot10^{-7}$	1.38	0.6892	0.1	100	5.518	0.875

Table 1. Parameters used in the fit of I-V characteristics measured under the solar simulator. Correction coefficients were applied to match the intensity of the illumination with the AM1.5G spectrum. Cell area was 4 cm^2.

Interestingly, N72B shows higher open circuit voltage than N79 as well as a higher shunt resistance, which could probably be explained by the non-uniformity of the doping distribution throughout the wafer and reproducibility of the process. However, an order of

magnitude higher series resistance for the N72B sample is an expected result of increased sheet resistance of the emitter, caused by the missing passivation layer.

a) b)

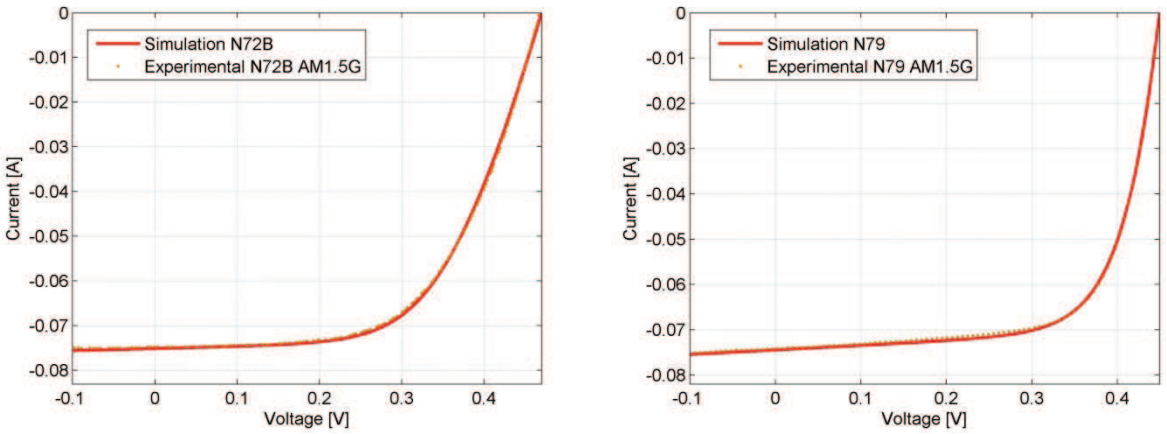

Figure IV.49. I-V curves for both N72B (a) and N79 (b) samples measured under solar simulator.

Both cells unfortunately feature low efficiency η caused on the one hand by a non-optimized external quantum efficiency and rather low fill factor, ranging from $\eta_{FF} = 0.58$ to 0.68. Another decreasing parameter is a surprisingly low shunt resistance, which does not exceed $R_{sh} = 250\ \Omega$. These results could be expected since all the optimization procedures were omitted and the emphasis was on detecting the possible multiplication effect. We will nevertheless try to estimate the efficiencies of those structures under optimized parameters later in this chapter.

Using parameters extracted from the I-V measurements under the solar simulator and the External Quantum Efficiency, we calculated the I-V characteristics of both N72B and N79 samples under an exact AM1.5G spectrum, as well as their theoretical, "improved" counterparts, free of resistance losses and with optimized ideality factors, however yielding the same I_{sc} and V_{oc}. The results of these simulations are shown in Figure IV.50. It is evident that assuming the same EQE, the main losses come from resistive effects and low fill factors of N7 cells.

a) b)

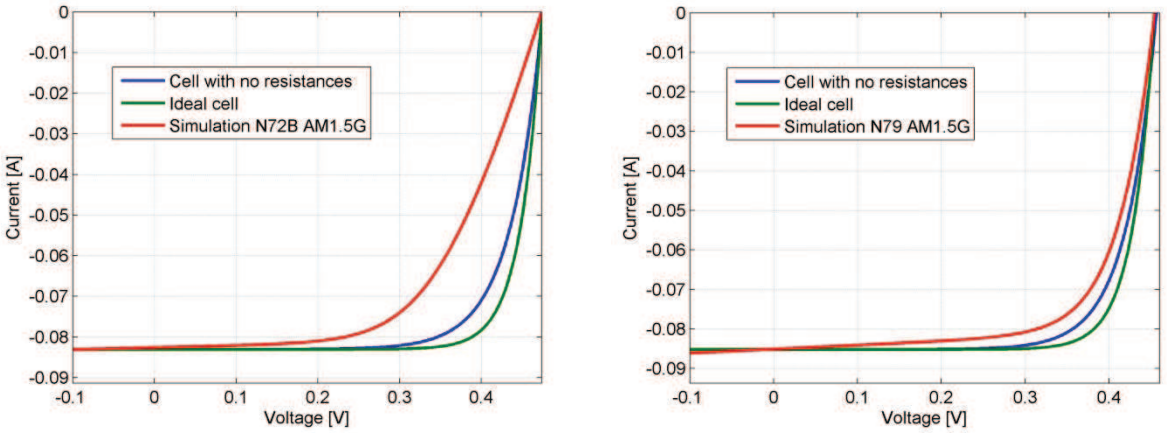

Figure IV.50. Simulated I-V curves for both N72B (a) and N79 (b) samples for AM1.5G spectrum (red curves) and theoretical improved counterparts without resistive effects and the same ideality factor (blue curves) and for an ideal solar cell (green curves).

As could be expected, the high series resistance of N72B resulted in a slight decrease of both efficiency to $\eta = 5.6055$ % and fill factor to $\eta_{FF} = 0.5748$ under AM1.5G spectrum. However, in the case of the N72B sample there is room for significant improvement in both efficiency and fill factor, if the resistive effects had been diminished. The cell without any resistances, but the same ideality factor $\eta_{FF} = 1.5$ yielded $\eta = 7.1826$ % and fill factor $\eta_{FF} = 0.7365$, while the ideal cell showed even higher efficiency of $\eta = 7.8082$ % and fill factor of $\eta_{FF} = 0.8007$. In the case of the N79 cell, the resistive effects were weaker. Under AM1.5G spectrum the cell has estimated efficiency $\eta = 6.6812$ % and fill factor $\eta_{FF} = 0.6932$. The idealized cells, the one without any resistive effects but the same ideality factor n = 1.38 shows some improvement in both efficiency $\eta = 7.1574$ % and fill factor $\eta_{FF} = 0.7426$, while the ideal cell showed even higher efficiency $\eta = 7.612$ % and fill factor $\eta_{FF} = 0.7891$. Surprisingly lower efficiency and fill factor for the ideal N79 (thus, having the same I_{sc} and V_{oc} as real cell) in comparison with the N72B cell is an effect of lower open circuit voltage. Any further improvements in efficiency of these structures would have to be linked to higher external quantum efficiency.

References:

[1] D. McMullan, *Scanning electron microscopy 1928–1965, Scanning* 17**,** 2006, 175.

[2] S. M. Sze, *Physics of Semiconductor Devices, 2nd edition,* Wiley 1981.

[3] S. Adachi, H. Mori, *Optical properties of fully amorphous silicon*, Phys. Rrev. B 62, 2000, 10158-10164.

[4] A. Sieradzki, M. Basta, P. Scharoch, Z. T. Kuznicki and J.-Y. Bigot, *Ultrafast dynamics of dense electron gas in silicon nanostructures*, in preparation, 2013.

[5] A. Othonos, *Probing ultrafast carrier and phonon dynamics in semiconductors*, J.Appl. Phys. 83, 1998, 1789-1830.

[6] J. R. Goldman, J. A. Prybyla, *Ultrafast dynamics of laser-excited electron distributions in silicon*, Phys. Rev. Lett. 72, 1994, 1364-1367.

[7] K. Sokolowski-Tinten, D. von der Linde, *Generation of the dense electron-hole plasmas in silicon*, Phys. Rev. B 67, 2000, 2643-2650.

[8] P. Lautenschlager, M. Garriga, L. Vina and M. Cardona, *Temperature dependence of the dielectric function and interband critical points in silicon*, Phys. Rev. B 36, 1987, 4821–4830.

[9] C. Leguijta, P. Lölgen, J.A. Eikelboom, A.W. Weeber, F.M. Schuurmans, W.C. Sinke, P.F.A. Alkemade, P.M. Sarro, C.H.M. Marée, L.A. Verhoef, *Low temperature surface passivation for silicon solar cells*, Sol. En. Mat: Sol. Cells, 40, 1996, 297-345.

[10] A. A. Aberle, *Surface Passivation of Crystalline Silicon Solar Cells: A Review*, Prog. Phot: Research and Application, 8, 2000, 473-487.

[11] O. E. Semonin, J. M. Luther, S. Choi, H.-Y. Chen, J. Gao, A. J. Nozik, M. C. Beard, *Peak external photocurrent quantum efficiency exceeding 100% via MEG in a Quantum Dot Solar Cell*, Science 334, 2011, 1530-1533.

[12] M. C. Beard, K. P. Knutsen, P. Yu, J. M. Luther, Q. Song, W. K. Metzger, R. J. Ellingson, A. J. Nozik, *Multiple exciton generation in colloidal silicon nanocrystals*, Nano Letters 7, 2007, 2506-2512.

[13] Z. T. Kuznicki, J.-J. Grob, J.-C. Mueller, H. E. Strazynska-Kuznicki, French patent 94 98885, 13th June 1994.

[14] Z. T. Kuznicki, L. Wu, and J. C. Muller, *Towards realization of a delta-BSF solar cell: Infrared improvements*, 12th EU PVSEC, Amsterdam 1994, Netherlands.

Résumé en français.

Notre travail s'est principalement porté sur la compréhension de l'origine et l'analyse des effets de la multiplication de faible énergie. Ce phénomène de multiplication de porteurs intervient dans des métamatériaux spécialement conçus et essentiellement constitués de silicium, au sein de cellules solaires multi-interfaces (cellule MIND). En plus de dominer le marché actuel des circuits intégrés et des semi-conducteurs en général, la technologie silicium joue également le premier rôle dans le photovoltaïque (PV), couvrant environ 90% du marché mondial. La limite de Shockley-Queisser, qui fixe l'efficacité théorique maximale, est d'environ 33% pour une cellule monojonction en silicium sous un spectre solaire AM 1.5, tandis que les 67% restants ne sont pas convertis en énergie électrique mais sont perdus par recombinaison, par thermalisation et par d'autres mécanismes. Bien que beaucoup d'efforts aient été consacrés à la réduction des coûts de production et au développement des couches minces, voire ultra-minces, ces technologies réduisent encore les rendements. Il faut noter que même si il existe des solutions pour obtenir des conversions lumière-électricité de plus de 40%, aucune d'entre elles n'est adaptée à la production à grande échelle, en raison de la nécessité d'utiliser des matériaux exotiques et souvent extrêmement rare. Ainsi, il a n'y a pour le moment pas de candidats pour remplacer le silicium (Si) à grande échelle dans le marché PV. La multiplication de porteur est une stratégie prometteuse pour les cellules solaires de troisième génération. L'énergie des photons très énergétiques, principalement perdue sous forme de chaleur dans les conceptions classiques, est ici utilisée pour générer des porteurs supplémentaires. Une fois collectés, ces porteurs supplémentaires produisent un surplus d'énergie électrique, ce qui peut conduire à la réalisation de cellules solaires dont les rendements dépassent les limites théoriques classiques de Shockley-Queisser.

Plusieurs mécanismes de multiplication ont déjà été observés expérimentalement comme l'ionisation par impact ou encore la multi-génération d'excitons (MEG) dans les nanocristaux. L'ionisation par impact dans le silicium massif apparaît dans la pratique pour des photons de longueurs d'onde inférieures à 320 nm, ce qui correspond à environ 3,5 fois la largeur de bande interdite (Eg). Par conséquent, une partie seulement du spectre solaire est concernée et le gain de conversion de puissance est assez faible. L'utilisation de nanocristaux peut réduire cette énergie minimale requise des photons pour démarrer le processus. Il a notamment déjà été observé un seuil d'énergie des photons dans les nanocristaux de silicium de 2,4 eV pour une largeur de bande interdite Eg = 1,20 eV efficace. Mais la dissociation des excitons et leur

collection sont difficiles et constituent encore un domaine de recherche actif. Une autre approche du problème consiste à modifier la structure du matériau à l'échelle nanométrique par d'intenses transformations locales en jouant sur les niveaux de dopage ou sur les contraintes mécaniques internes, jusqu'à un point où les matériaux commencent à exposer des propriétés qui n'étaient pas présentes auparavant. Cette approche peut être exploitée dans la création d'états par ingénierie de bande, ce qui pourrait éventuellement permettre la multiplication de porteur pour des énergies de photon beaucoup plus faibles que l'énergie de bande interdite.

Nous présentons un nouveau processus de multiplication à faible énergie où l'énergie du photon seuil peut être inférieure à 2 Eg. Dans nos travaux précédents, nous avons présenté une méthode de fabrication du dispositif ainsi que les applications potentielles et les effets observés. Dans notre approche, des états électroniques sont introduits à une énergie 0.274 eV en dessous de la partie inférieure de la bande de conduction d'un émetteur hautement dégénéré. Grâce à la grande densité de population de porteurs intrinsèques permettent une meilleure conversion des photons très énergétiques grâce à l'ionisation par impact. Comme les centres de multiplication ne sont pas aussi localisé que les nanocristaux par exemple, nous définissons le segton comme la plus petite partie du matériau qui permet la multiplication des électrons et qui possède la capacité de se recharger une fois le processus terminé. Les propriétés des segtons dérivent des contraintes mécaniques au niveau des interfaces entre le silicium cristallin et silicium amorphe, et le fort dopage au phosphore. De plus, étant donné que les segtons sont noyés dans des matériaux conducteurs, les porteurs de deuxième génération sont généralement collectables, si aucun autre obstacle n'est présent. Ici, nous démontrons une augmentation jusqu'à 40% de l'efficacité quantique interne (IQE) pour un pic centré autour de 450 nm. C'est la première fois qu'un phénomène de multiplication d'électrons est observé sur une nanostructure 1D de silicium. Une représentation typique de la structure MIND est donnée à la figure 1.

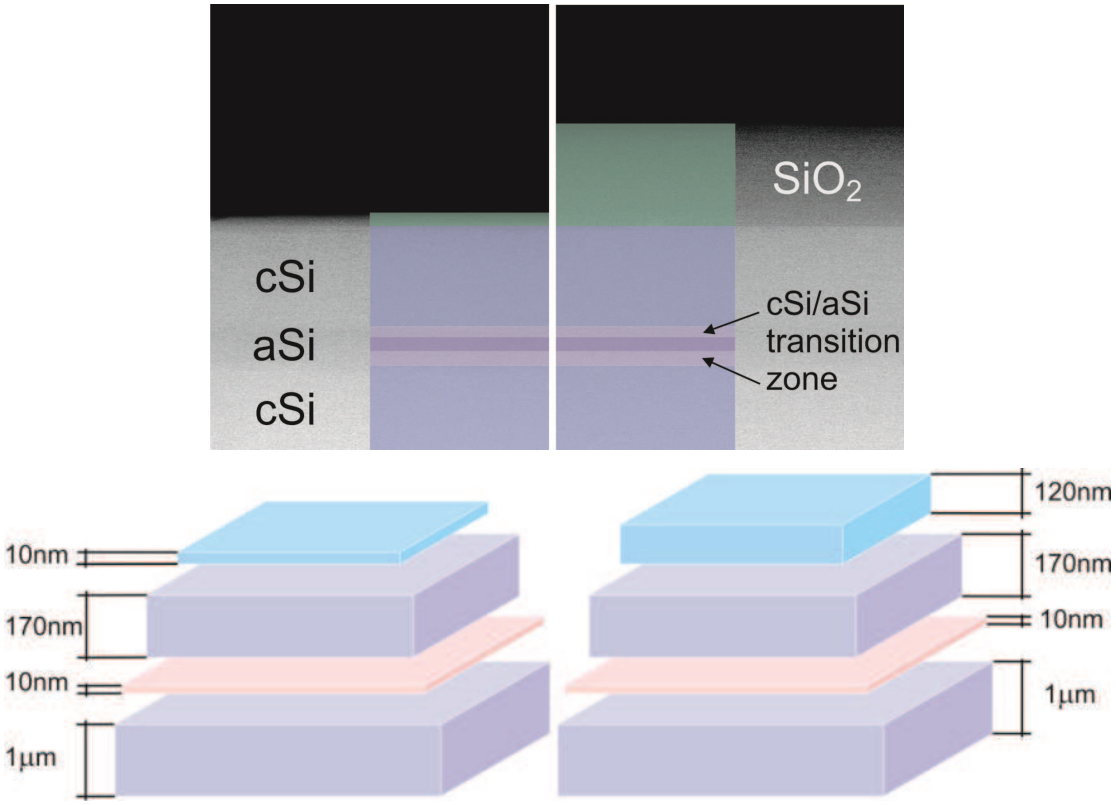

Figure 1: Mesures MEB montrant l'architecture de deux échantillons. La couche de passivation de l'échantillon de gauche a été réduite à environ 5-10 nm par gravure. La géométrie finale des deux échantillons est la suivante: couche de passivation (~ 10 nm pour la cellule gravée, ~ 120 nm pour cellule passivée), 170 nm silicium cristallin (cSI), ~ 10 nm amorphe de Si (aSi) et une jonction pn à la profondeur de 1,0 µm.

Les propriétés optoélectroniques spécifiques de semi-conducteurs fortement dopés ou très excités, qui diffèrent de diverses manières des cas parfaitement connus des matériaux non dégénéré, conduisent à de nouvelles applications souvent imprévues. Les propriétés de ces matériaux sont appréciées dans des circuits électroniques spécifiques et vont probablement apparaître dans les futures applications optiques et photoniques tout silicium. Plusieurs effets ont été découverts dans les matériaux pour produire des propriétés souvent imprévus ou l'amélioration des propriétés connues. Malgré des études approfondies au cours des vingt dernières années, il y a plusieurs questions non-élucidées sur les fonctionnalités optiques.

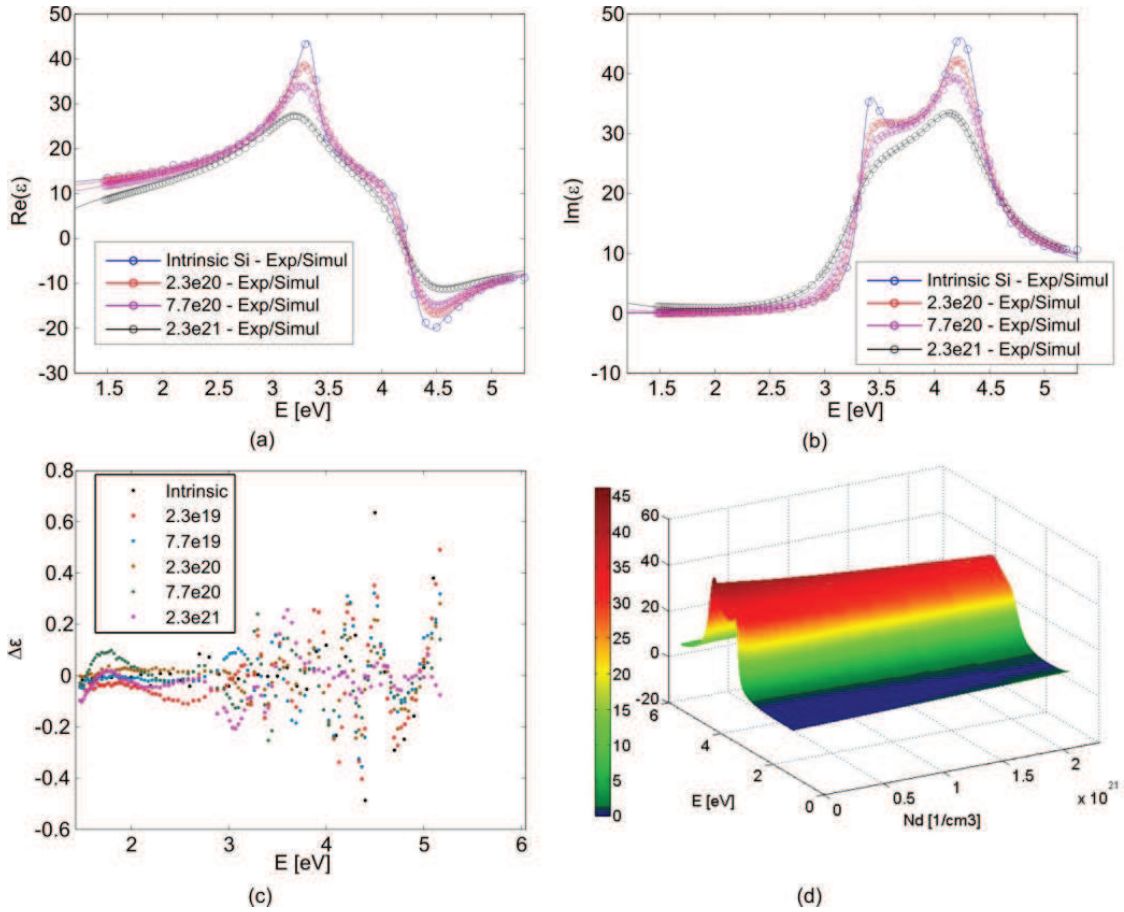

Figure. 2. Simulées (ligne continue) et expérimentales (points) de données pour différentes concentrations de dopage phosphore. (a) Re (ε), (b) Im (ε), (c) tracé des valeurs résiduelles pour la partie imaginaire de la fonction diélectrique (ε Δ) et (d) Im (ε) de Si pour toutes les densités de dopage phosphore possibles.

Nous proposons une méthode de prédiction des fonctions diélectriques de Si fortement dopé (Si:P) et de Si fortement dopé sous excitation élevée (par exemple par la lumière incidente) qui conduisent toutes deux à une grande densité de population de porteurs libres extrinsèques. Le modèle d'oscillateur harmonique (HMO) a été largement étudié au cours des années et certains problèmes classiques et les désaccords entre les données expérimentales et la théorie de Si ont été identifiés comme une représentation inexacte de la limite d'absorption associée à la bande interdite directe. De simples extensions au modèle classique pourraient résoudre le problème, mais elles conduisent à la perte de généralité du modèle lui-même. Pour l'analyse des fonctions diélectriques des matériaux qui varient peu, on a besoin d'un outil qui est adapté à une application particulière et à une gamme spectrale, plutôt qu'un modèle plus générique mais moins exacte. Ces extensions ont été développées pour le silicium intrinsèque et les matériaux dérivés du silicium dans le passé. Ils fonctionnent bien lorsque le paramétrage

d'une fonction diélectrique donnée est effectué, mais ils ne sont pas capables de prédire les propriétés optiques lorsque des changements structurels se produisent. Des changements structurels, une équation de modèle introduit par Aspnes groupe a été élargie par l'ajout d'une dépendance fonctionnelle possible de ses paramètres au sujet de changer la densité de dopage, et ensuite combiné avec une prolongation de Drude qui mène à l'ensemble d'équations suivant:

$$\varepsilon(\omega,N_d)=\left(\begin{array}{l}\varepsilon_\infty+\sum_j\frac{C_{0j}(N_d)}{\omega^2}\left\{\begin{array}{l}\exp\left[i\beta_j(N_d)\right]\times\left[\omega_{gj}(N_d)-\omega-i\Gamma_j(N_d)\right]^{\mu_j(N_d)}\\+\exp\left[-i\beta_j(N_d)\right]\times\left[\omega_{gj}(N_d)+\omega+i\Gamma_j(N_d)\right]^{\mu_j(N_d)}\\-2\,\mathrm{Re}\left\{\exp\left[-i\beta_j(N_d)\right]\times\left[\omega_{gj}(N_d)+i\Gamma_j(N_d)\right]^{\mu_j(N_d)}\right\}\\-2i\mu_j(N_d)\omega\,\mathrm{Im}\left\{\exp\left[-i\beta_j(N_d)\right]\times\left[\omega_{gj}(N_d)+i\Gamma_j(N_d)\right]^{\mu_j(N_d)-1}\right\}\end{array}\right.\\-\frac{N_{e-h}e^2}{\varepsilon_0 m_{opt}m_e\omega^2}\frac{1}{1+i\frac{1}{\tau_D\omega}}\end{array}\right) \quad (1)$$

où C_0 et ω_g sont, respectivement, l'amplitude et la fréquence de l'oscillateur Lorenz, Γ est un coefficient d'élargissement, N est la densité des porteurs, τ_D est le temps d'amortissement de Drude, m_{opt} la masse optique des porteurs, μ est l'ordre de pôle et β est le facteur de phase de pole. Le reste des paramètres ont leurs significations habituelles. La précision de l'ajustement pour les différentes concentrations de dopage est donnée dans la figure 2. La représentation de la fonction diélectrique pour chaque couche est ensuite combinée par approximation de la matrice de transition (TMA), ce qui nous permet d'extraire des informations complètes sur la propagation du champ électromagnétique à l'intérieur de la structure.

La présence d'interface enterrées amorphe/cristallin induit un obstacle pour les porteurs minoritaires dans l'émetteur supérieur dopé n. Donc nous supposons qu'une diminution significative de l'efficacité quantique externe et interne (EQE et IQE) doit être présente pour courtes longueurs d'onde. En tenant compte de cela et en supposant de plus que l'efficacité de collecte (CE) est égal à 1 seulement à proximité de la jonction, nous avons pu reconstruire CE pour l'échantillon B. La figure 2 montre l'ensemble du spectre EQE (courbe bleue) et de réflexion (courbe vert) ainsi que la réflectivité simulée (noir) pour deux échantillons étudiés (gravé en haut et passivé en bas). Aux plus hautes énergies de photons, EQE pour l'échantillon avec la surface endommagée dépasse les valeurs d'EQE pour les échantillons passivés malgré un plus grand taux de recombinaison de surface et l'absence de tout revêtement antireflet. La surface de l'échantillon est suffisamment endommagée pour que, en

raison de la diffraction de lumière, les pics d'interférence ne soient plus observés dans les spectres de réflexion. Ces pics sont clairement visibles pour l'échantillon passivés et nous permettent d'attester de l'existence et de la qualité des sous-structures enterrées qui en sont l'origine (à comparer avec le modèle). L'augmentation du QE est encore plus visible sur la figure 3, montrant des spectres IQE. IQE a été calculé en utilisant l'équation suivante:

$$IQE=EQE/(1-R) \quad (2)$$

Nous prenons en compte toute la lumière qui pénètre à l'intérieur de la structure. Les résultats sont paradoxaux parce que malgré le fait que la surface soient endommagée et l'absence de revêtement anti-reflet, l'EQE de l'échantillon A est plus élevée que l'EQE de l'échantillon B pour des énergies de photons élevées (figure 2). L'IQE est même supérieur pour la cellule A pour presque la totalité de la gamme spectrale (figure 3). Les efficacités de collecte pour les échantillons A et B devraient être presque les mêmes étant données les architectures internes identiques des deux échantillons, les différences résultant uniquement de la surface endommagée dans le cas A. Parce que nous avons déjà supposé que presque toutes les paires électron-trou générées dans l'émetteur supérieur sont perdus à cause de la barrière à l'interface ASI/CSI, ces efficacités de collecte ne devraient pas présenter de différences majeures. La différence de réflectivité due à l'absence de la couche antireflet dans le cas A, ne peut pas expliquer la différence dans l'efficacité quantique parce que la cellule la plus efficace est aussi celle présentant la plus grande réflectivité. Nous avons exclu toutes les explications classiques pouvant mener à ce comportement et, par conséquent, nous supposons que le métamatériaux introduit doit être responsables des changements observés.

Pour résoudre le problème de façon plus détaillée, nous avons décidé de comparer les résultats d'IQE avec la simulation. Nous avons considéré deux cas possibles: l'une entièrement classiques pour les deux échantillons A et B, et l'autre où nous avons supposé que le métamatériau a réussi à créer des électrons supplémentaires disponibles autorisant le phénomène de multiplication. Dans le premier cas, l'efficacité de collecte pour l'échantillon gravé devait être bien meilleure que pour l'échantillon passivé pour réaliser une bonne compatibilité entre l'IQE expérimental et celui simulé. Il était également nécessaire de négliger partiellement la barrière introduite par la couche d'aSi pour l'échantillon gravé. Étant donné que ce type de comportement n'a jamais été observée et les cellules solaires sont bien connus pour être très sensibles à la qualité de la passivation, nous considérons que cette approche ne rend pas bien compte de la réalité. Dans le second cas, nous avons supposé que

pour l'échantillon passivé, l'effet de multiplication n'a pas lieu à cause du confinement des porteurs dans l'émetteur supérieur qui augmente leurs durées de vie et bloque le processus de rechargement des centres.

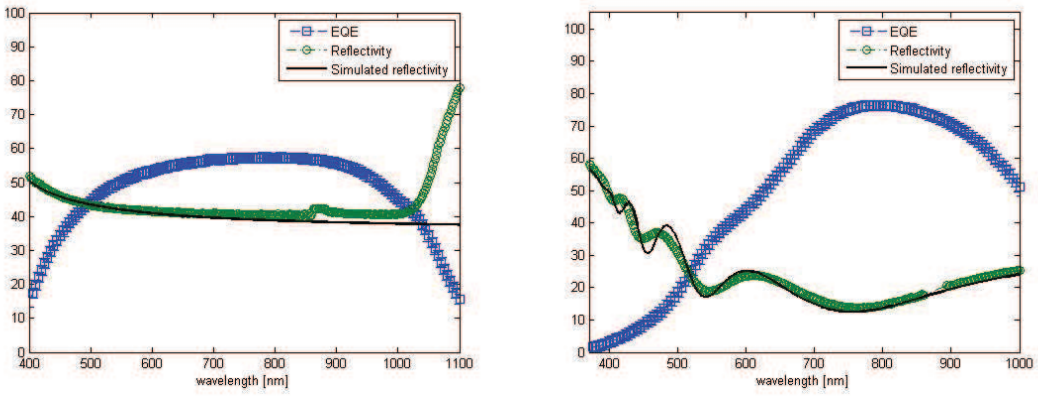

Figure 3: EQE expérimental (bleu) pour l'échantillon gravé (gauche) et l'échantillon passivé (droit). Nous estimons l'incertitude de ces courbes à être inférieure à 1,5%. Une comparaison de la réflectivité mesurée (cercles verts) et modélisées (ligne noire) est également présentée.

Par conséquent, nous supposons que l'échantillon B peut être très précisément modélisé en supposant que les caractéristiques prédominantes sont celles d'une cellule solaire classique Si passivée avec une barrière de potentiel enterrée pour les porteurs minoritaires. Notre analyse semble confirmer l'affirmation selon laquelle l'ionisation par impact à faible énergie des électrons supplémentaires est possible dans les milieux semi-conducteurs spécialement préparés. Dans notre cas, nous avons effectué une analyse de deux échantillons contenant une sous-structure enterrée de métamatériaux. Dans cette étude, un échantillon avec une meilleure structure de passivation montre de moins bonnes propriétés électriques globales, tandis que l'échantillon sans passivation présente une nette amélioration de ses propriétés électriques et en particulier de son efficacité quantique. La structure des deux échantillons a été étudiée par microscopie électronique à balayage et par des mesures de réflectivité. Les propriétés optiques des deux échantillons sont expliquées par des moyens classiques et sont facilement associables à la géométrie des échantillons. Les propriétés électriques des deux échantillons montrent exactement la tendance inverse, de façon prévisible, le comportement classique peut être observé que pour l'échantillon passivé. Pour l'échantillon gravé, la seule explication serait l'hypothèse que l'augmentation actuelle de recombinaison de surface annule la barrière enterrée pour des porteurs minoritaires. Un tel effet n'a jamais été observé et ne trouve aucune explication physique.

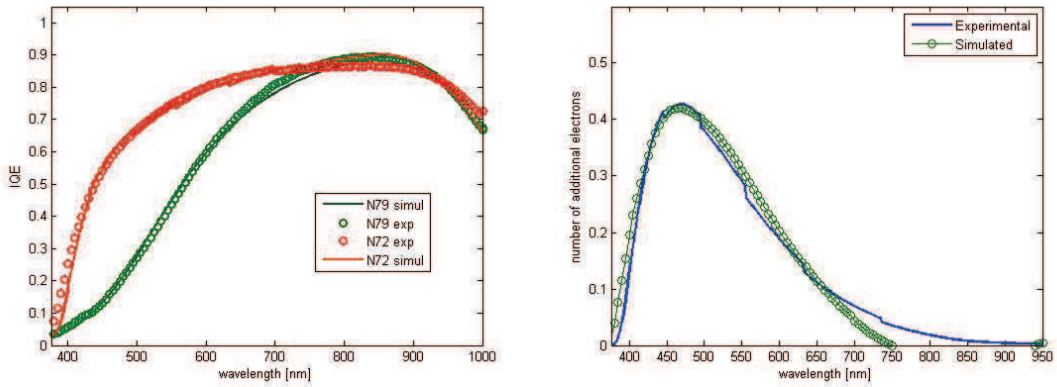

Figure 4: (à gauche) IQE pour l'échantillon passivé (en vert) et l'échantillon grave (en rouge). Les cercles correspondent aux mesures expérimentales et les courbes en trait plein au simulations. (à droite) Augmentation de l'IQE due à une multiplication de porteurs aux interfaces de la couche amorphe. Les cercles verts correspondent au mesures et le trait plein à la simulation pour une probabilité de multiplication p=0.7 et une énergie d'activation E_t=0.274 eV.

L'hypothèse plus acceptable est que l'augmentation du nombre d'états de recombinaison de surface réduit la durée de vie des porteurs majoritaires dans l'émetteur supérieure et augmente le taux de recharge de centres de multiplication, ce qui les rend plus efficaces. Cela s'intègre bien dans l'effet désiré et explique les résultats expérimentaux de façon très précise. Ici, nous avons constaté que la probabilité de multiplication est p = 0,7 pour l'énergie E = 0.274eV. Plusieurs problèmes et des questions restent ouverts et d'autres recherches sont nécessaires pour comprendre comment: (1) accroître la CE primaire dans l'émetteur supérieure, se débarrasser de la partie électroniquement inactive, (2) induire une transition de PV en métamatériaux Si massif et sous quelles conditions exactes le métamatériau peut être réparti uniformément sur l'ensemble de la zone active, (3) résoudre le problème actuel où la formation métamatériau est liée à l'introduction d'une barrière pour les porteurs minoritaires qui limite l'efficacité de l'ensemble du dispositif et (4) augmenter la mobilité des porteurs et de réduire le nombre de défauts nécessaires pour que le métamatériau puisse se former. Si ces questions peuvent être résolues, l'introduction de ce type de métamatériaux dans les cellules solaires de silicium peut conduire à surmonter la limite de Shockley-Queisser et à accroître considérablement le rendement énergétique des cellules solaires de silicium.

Low Energy Photovoltaic Conversion in MIND structures

Photovoltaic devices of today convert solar energy into electricity in a clean, renewable and inexhaustible way and represent a possible replacement for the fossil fuels. However, in order to compete with classical energy sources a significant increase in the conversion efficiency is inevitable. In this work, we concentrate on the aspects able to raise the conversion efficiency above the limitations of present cells. The first part of the study is devoted to new theoretical ideas considered as 3rd generation photovoltaics, while the most interest is kept at studying the possible benefits of electron multiplication at low-energies. In the second part of the study, we develop a model that allows a precise treatment of optical and transport properties of silicon structures with buried interfaces. Extensive theoretical and experimental analyses of existing MIND structures are then conducted. By studying the exact flux and power distribution inside several structures in conjunction with their geometry, we estimate the possible quantum efficiencies and compare them with experimental results. Through the means of numerical simulations coupled with experimental characterization, we extract the carrier collection efficiency of studied cells. New effects are being observed, such a possible increase in collection efficiency above unity. A deeper analysis of the experimental results coupled with the numerical study analyzes several classical and non-classical explanations of the increase in collection efficiency or the resulting increase in the quantum efficiency. With most of the classical explanations ruled out, we conclude that the most probable, but not definitive explanation of this effect can be interpreted as the result of a low-energy carrier multiplication.

Conversion photovoltaïque en basse énergie dans les structures MIND

Dispositifs photovoltaïques d'aujourd'hui convertissent l'énergie solaire en électricité de manière propre, renouvelable et inépuisable et représentent un remplacement possible pour les combustibles fossiles. Toutefois, afin de rivaliser avec les sources d'énergie classiques une augmentation significative de l'efficacité de conversion est inévitable. Dans ce travail, nous nous concentrons sur des aspects pouvant propulser le rendement de conversion au-dessus des limites de cellules présentes. La première partie de l'étude est consacrée à de nouvelles idées théoriques considérés comme le photovoltaïque de 3ème génération, alors que le plus d'intérêt est maintenu à étudier les avantages possibles de la multiplication d'électrons faible seuil. Dans la deuxième partie de l'étude, nous développons un modèle qui permet un traitement précis des propriétés optiques et de transport des structures de silicium avec des interfaces enterrées. Les analyses théoriques et expérimentales approfondies des structures existantes MIND sont ensuite effectuées. En étudiant le flux exacte et la distribution d'énergie à l'intérieur de plusieurs structures dans le cadre de leur géométrie, nous estimons les rendements quantiques possibles et les comparer avec les résultats expérimentaux. Grâce aux moyens de simulations numériques couplées avec caractérisation expérimentale, nous extrayons l'efficacité de la collecte de porteur de cellules étudiées. De nouveaux effets sont observés, une telle augmentation possible de l'efficacité de la collecte au-dessus de l'unité. Une analyse plus approfondie des résultats expérimentaux couplés avec l'étude numérique suit quelques explications classiques et non classiques de l'augmentation de l'efficacité de la collecte ou l'augmentation résultante de l'efficacité quantique. Avec la plupart des explications classiques exclu, nous concluons que l'explication la plus probable, mais non définitive de cet effet peut être interprété comme le résultat d'une multiplication des porteurs faible seuil.

Keywords: solar cell, electron multiplication, high efficiency. Silicon, 3rd generation